Beta Decay Studies of Heavy Neutron-Rich Nuclei Around A=190

Nasser Alkhomashi

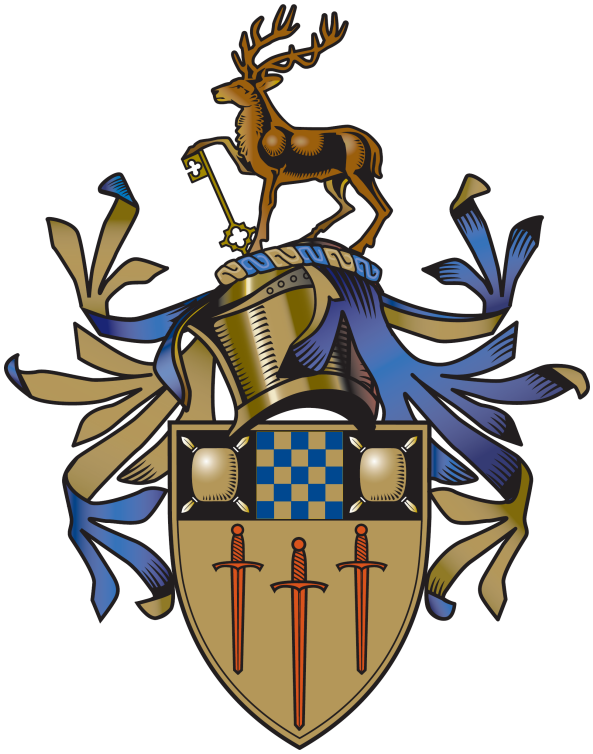

Department of Physics,
School of Electronics and Physical Sciences,
University of Surrey,
Guildford, Surrey, GU2 7XH

Submitted for the degree of Doctor of Philosophy

January 2010

Abstract

Heavy neutron-rich nuclei with A$\sim$190 have been investigated following their production by the relativistic projectile fragmentation of a ^{208}Pb primary beam on a 2.45 g/cm^2 ^{9}Be target. The secondary beam of radioactive fragmentation residues was separated using the in-flight FRagment Separator (FRS) at GSI and stopped in the RISING active stopper detector. The active stopper consisted of three 5cm x 5cm Double Sided Silicon Strip Detectors (DSSSDs), each pixellated into 16 strips in both the horizontal and vertical directions. The DSSSDs were used to measure the position of the implanted ions and correlate these with subsequent β-decays detected in the same or neighbouring pixels. Gamma-ray decays from previously reported isomers in ^{188,189}Ta, ^{190,191}W and ^{192,193}Re, together with previously unreported isomeric states in ^{190}Ta and ^{187}Hf have been measured using the 15 germanium cluster detectors of the RISING γ-ray detection array. Time and position correlations between implanted ions of ^{188,190,192}Ta and their subsequent β-decays to ^{188,190,192}W were also determined. Beta decay half lives of ^{188,190,192}Ta of 19.6(20)s, 5.3(7)s and 2.2(7)s respectively were established and γ rays from respective states in the W daughter isotopes were measured using the β-delayed coincidence technique afforded by the RISING active stopper. The results of these investigations are consistent with experimental information reported from previously reported in-beam and isomer-decay studies of ^{188}W and ^{190}W respectively. Evidence is presented from the β-decay of ^{190}Ta to provide a first measurement for the energy of the γ bandhead $I^{\pi}= 2^{+}$ state in ^{190}W and excitation energy of the yrast 2^{+} state in ^{192}W thus providing spectroscopic information on the heaviest tungsten observed to date. The evolution of ground state structure along the W isotopic chain is discussed as evidence for a possible proton sub-shell effect for the A $\sim$190 region and the maximisation of the γ-softness of the triaxial nuclear potential in this region at N $\sim$116. The experimentally deduced level schemes are compared with theoretical predictions using the Interacting Boson Approximation (IBA) and microscopic/macroscopic calculations of the nuclear shape. Beta decay half lives for the neutron-rich nuclei ^{187,188,189}Hf, ^{188,189,190,191,192}Ta, ^{191,192,193,194}W and ^{193,194,195}Re are also established for the first time in this work.

Acknowledgements

This research project would not have been possible without the support of many people. In the first place I would like to record my gratitude to Prof. Paddy Regan for his supervision, advice, and guidance from the very early stage of this research. I would like to thank him for giving me the opportunity to do my PhD thesis work in the field of nuclear physics. In addition to the scientific part, I really enjoyed our discussions about cultures, religions, histories and sometimes our country politics. I understand a lot of things concerning these subjects which seemed to me before unclear or hidden and I hope Paddy also got similar understanding from me!

I also gratefully acknowledge Zsolt Podolyák for his advice and supervision. He gave me incredible attention and more understating of the experimental details. In addition, my thanks to Prof. W.Gelletly for his advice throughout my studies, answering my questions and his encouragement to calculate the beta efficiency!

Special thanks also to all my graduate colleagues and postdoctorates at the department of Physics. They have provided me an enjoyable working atmosphere and helped me to solve a lot of hard problems. Especially, I would like to thank Gregory Farrley who was my partner in all the early stages of my PhD and during the experiment work; Steve Steer for his technical support for someone who knew nothing in computing; Nawras Al-Dahan for his encouragement and not forgetting our talks in our native language, Arabic; Aje Deo for his patience while answering my questions and Ian Cullen for his support in solving my Latex problems. In addition, thanks to my friends Alkhorayef, Alzimami, Alnafea, Alghamdi and to all of the Saudi students in the University of Surrey.

I wish to express my love and gratitude to my family for their understanding and endless love, through the duration of my studies. I am deeply and forever indebted to my parents for their love, moral support and encouragement throughout my entire

life. Further thanks go to to my wife Mai for her long-standing support and love. This PhD was impossible to complete without her encouragement and patience. In addition, thanks to my son Abdulrahman who has been a great source of strength all through this work. Also thanks goes to my brothers and sisters for their support to finish this PhD. Finally, I am grateful to my scholarship sponsor King Abdulaziz City for Science and Technology (KACST) for financing this study.

Contents

List of Figures

List of Tables

Chapter 1

Introduction

There are about 280 species atomic nuclei which are sufficiently stable to exist naturally on earth, having decay lifetimes of more than 10^{15} years. However, it is predicted that there approximately 7,000 another possible nuclear species which are unstable against radioactive decay [1, 2] and have significantly shorter half-lives. About 3,000 have been experimentally synthesized and investigated in the laboratory to date [2, 3].

Figure 1.1 shows the nuclear chart (also called Segré chart) which provides a schematic map of all possible nuclear species by plotting proton number, Z, against neutron number, N [4]. The black squares on the figure represent the radioactively stable nuclei. By adding more neutrons or protons to such nuclei, unstable nuclei are produced until the neutron and proton drip lines are reached. At this point the nuclear binding forces which arise from the strong nuclear force interaction are no longer strong enough to hold nuclei together and the least bound nucleon (i.e. either proton or neutron) is no longer energetically attached [5]. The blue, red, yellow, orange and green squares represent those nuclei that have been observed and studied experimentally.

This thesis focuses on the structure study of the heaviest neutron-rich tungsten isotopes studied to date. The study of heavy (A >170) nuclei with a neutron excess compared to the stable isotopes of a given element represents one of the major challenges in current nuclear physics research. Such nuclei can not be produced with stable-beam-target fusion-evaporation reactions and they are too heavy to be populated significantly via spontaneous fission reactions. In order to investigate such nuclei experimentally, they must be studied using either heavy-ion deep-inelastic colli-

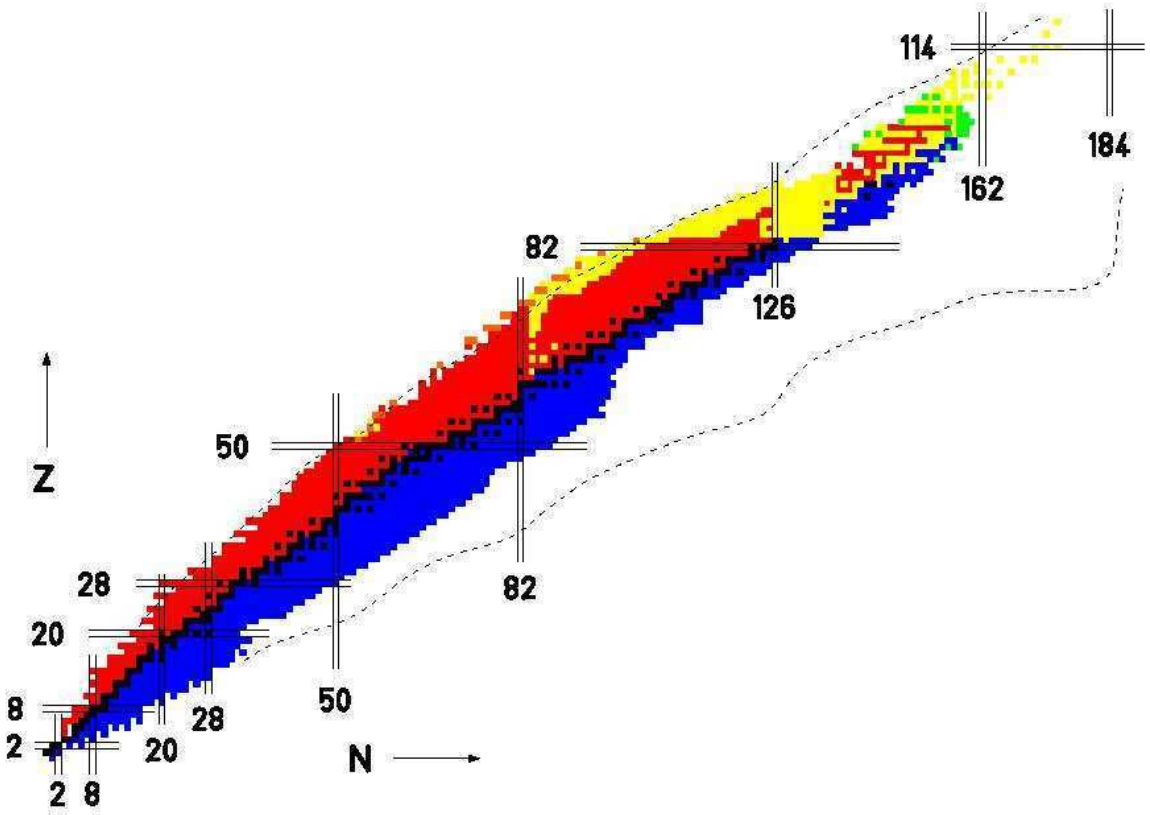

Figure 1.1: The chart of the nuclides showing the stable nuclei in black squares. The red, blue, yellow, orange and green squares represent radioactive nuclides that have been identified experimentally (taken from ref. [4]).

sions [6, 7, 8] and/or projectile fragmentation reactions [9, 10, 11, 12]. Deep-inelastic collisions provide only a limited access to nuclei far from stability and have general difficulties in the selection of the ions of interest [13, 14]. The projectile fragmentation mechanism has however been found to be an efficient tool for populating such nuclei far from stability [9, 11, 15, 16, 17]. In such reactions, a fast, heavy, stable-element beam is fragmented on a fixed, thick target, leading to the production of a wide variety of secondary ion species lighter than the primary beam [18]. The secondary fragmentation reaction residues are then separated and identified using a fragment separator before being brought to rest in a stopper which is surrounded by a γ-ray spectrometer array. Such a set up often allows the first spectroscopic studies in such exotic nuclear systems [11, 19].

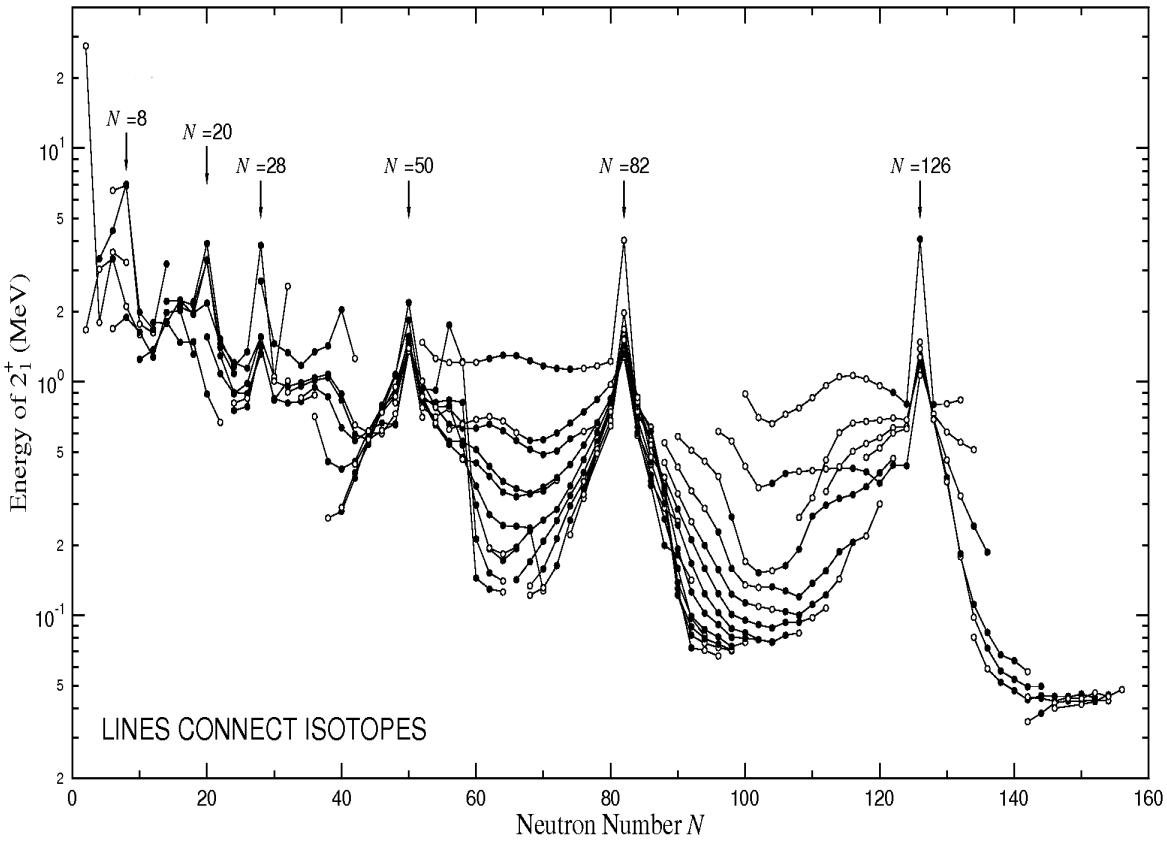

Figure 1.2: Excitation energies of the first $I^{\pi}= 2^{+}$ state versus the neutron number, N, for even-even nuclei (taken from reference [21]).

1.1 Basic Considerations of Nuclear Structure

For a mathematical description of the total number of inter-nucleon interactions, the number of nucleons in the nucleus is too large to be treated individually (except for very low-mass nuclei). Truncation schemes are needed and thus the nucleus can be considered as two limited systems: (i) the core (or closed shell) and (ii) the valence nucleons. For nuclei with only a few ($\sim$4) valence nucleons, the single particle motion and residual interactions between these nucleons can be used to make a prediction of the nucleus' excitation energies. The low-lying nuclear properties arise from the motion of these few individual valence nucleons. However, for nuclei with significant numbers of valence nucleons, such treatments prove unsuccessful. The collective model approach [20] exhibits the coherent motion of many nucleons and considers the nucleus as a single object which is responsible of all the nuclear properties. Nuclear 'collective' motions can be summarised either as vibrational or rotational excitations.

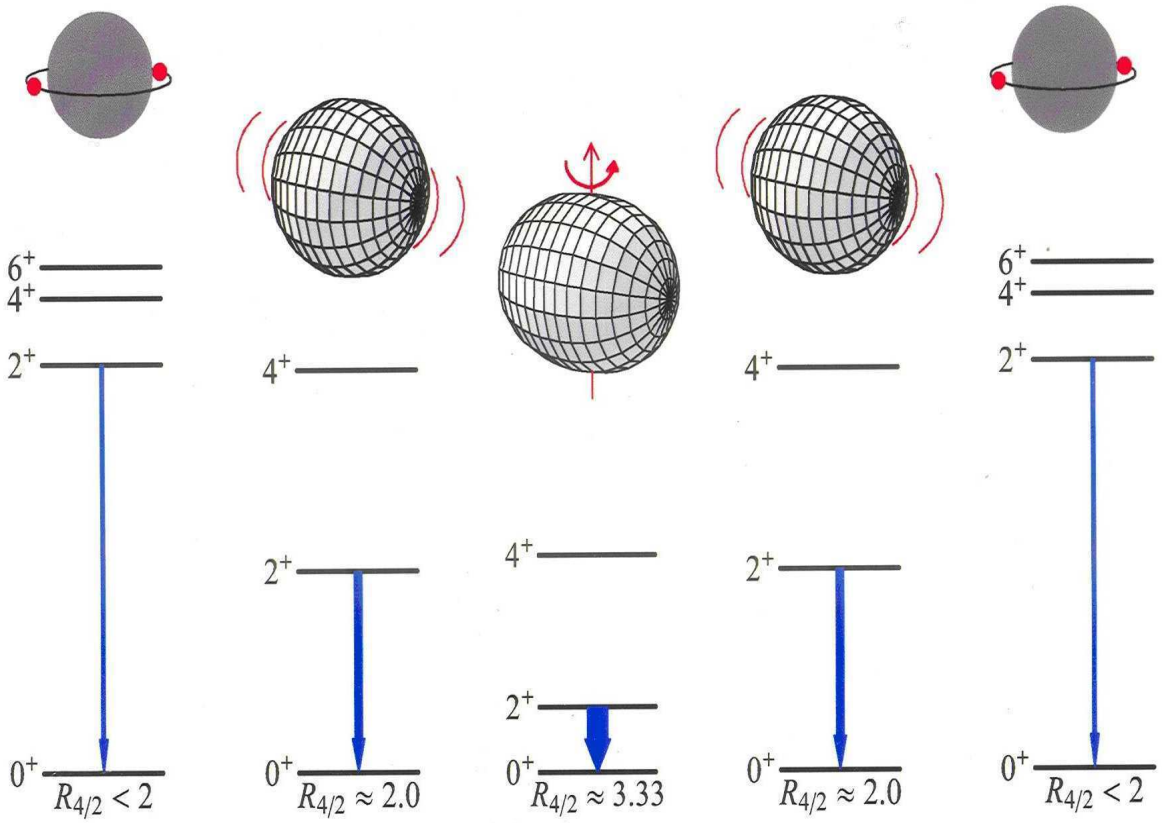

Figure 1.3: Schematic illustration of the evolution of structure from a near closed shell to a deformed midshell and then again to a near closed shell [23].

Collective characteristics of nuclear structure for even-even nuclei can be revealed by two simple signatures of the excitation energy spectrum, namely the energy of the first 2^+ excited state and the ratio R(4/2)= E(4^+)/E(2^+) of the excitation energies of the lowest-lying 4^+ and 2^+ states [22]. In general, the energy of the first excited state 2^+ decreases smoothly with increasing mass number A (except the regions around the closed shells). Figure 1.2 shows data for the first $I^\pi = 2^+$ state of even-Z, even-N nuclei as a function of the neutron number, N, as reported in reference [21]. The values of the ratio R(4/2) across the nuclear chart tend to fall into three ranges as illustrated schematically in Figure 1.3. The even-even nuclei close to the magic nuclei, closed shells, have values below 2 while the nuclei further away have a ratio value between 2 and 2.4. The energy ratio R(4/2) has an idealized characteristic value for the perfect harmonic vibrator of exactly 2.0 [24, 25]. The region around the midshell, valence maximum regions tend to approach the idealised axially symmetric rotor limit of 3.33, suggesting a near-perfect axially symmetric deformed rotor at low spins for these nuclei

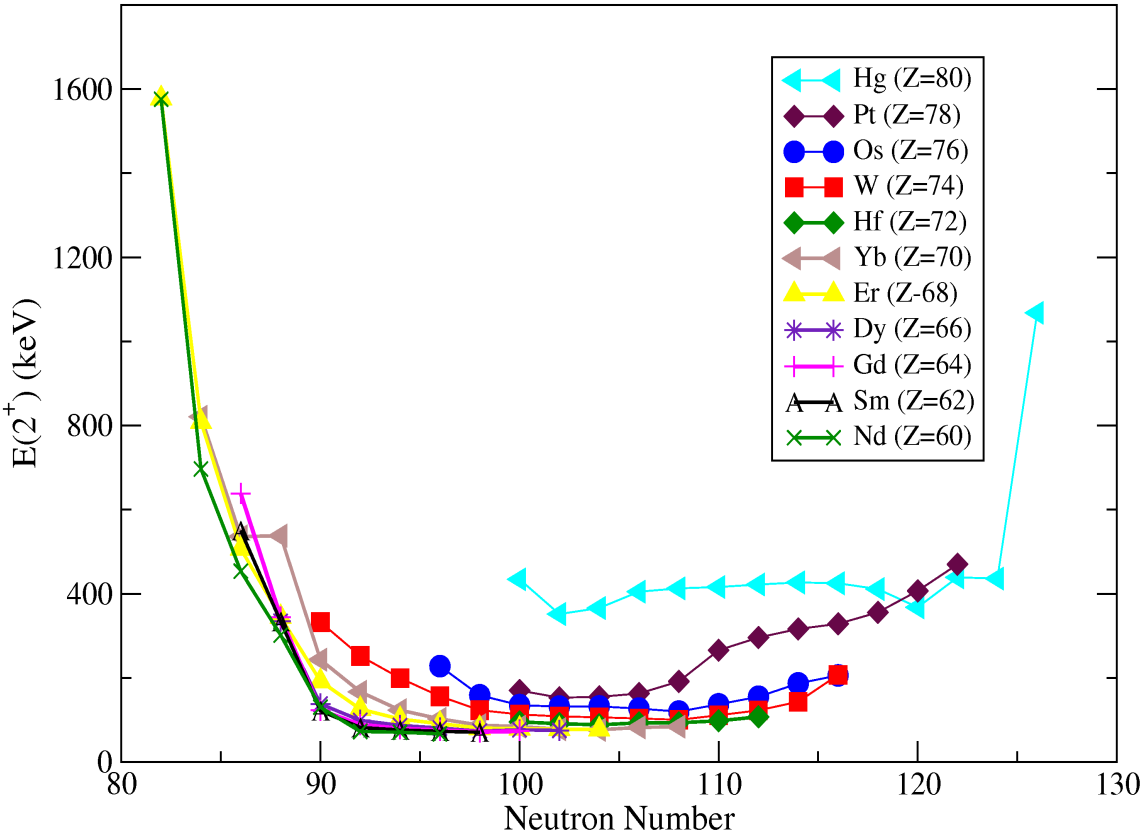

Figure 1.4: The energy of the first excited state, E(2^+), versus the atomic mass number (A∼150-206) for even-even nuclei between Nd and Hg. These data are taken from reference [3].

[26, 27] (see Chapter 2).

1.2 Overview of A≈170-190 Region

The region of heavy neutron-rich nuclei with A≈170-190 is known to exhibit signatures of permanent ground state quadrupole deformation [21]. Figures 1.4 and 1.5 show the systematics of first E(2^+) exited state and the R(4/2) ratio as a function of neutron number, for even-even nuclei between Z=60 and Z=78. A near-constant E(2^+) value and values of R(4/2) approaching 3.33 are observed for N >90, implying low-lying collective rotational structures in such nuclei.

A particularly interesting phenomenon can be observed when plotting R(4/2) ratio as a function of the atomic number, Z, for this region (see figure 1.6). A smooth increase of the R(4/2) ratio toward a constant value approaching R=3.33 is observed

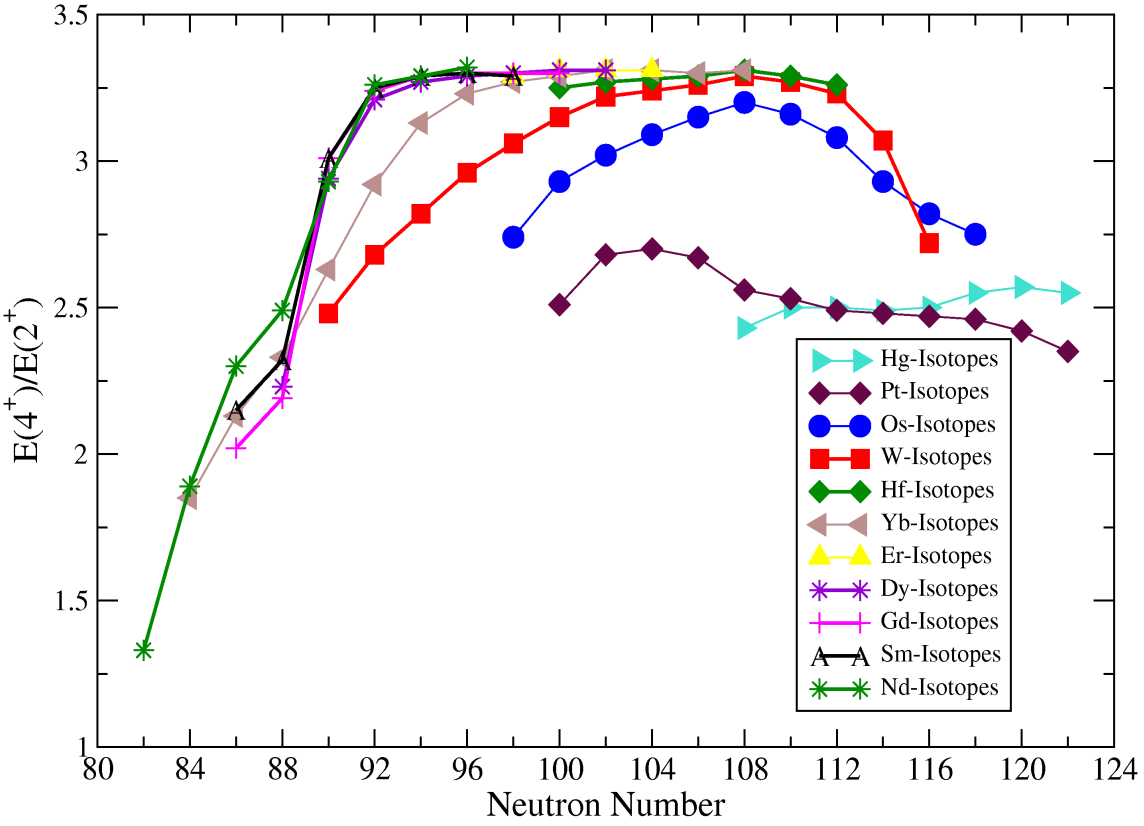

Figure 1.5: Ratio of the excitation energies of the first 4^+ and 2^+ states, R(4/2), for Nd-Hg (Z=60→80) even-even isotopes with A∼142-202. These data are taken from reference [3].

for N<116 with decreasing the atomic number Z (i.e. increasing the valence product). However, there is a notable discontinuity in the evolution of this quantity for the N=116 nucleus, ^{190}W [29]. This discontinuity was interpreted in reference [29] as possible evidence of the begining of the effect of a localised proton sub-shell closure. An alternative explanation proposed a phase transition corresponding to a change from a prolate to an oblate nuclear shape around $N = 116$ [30, 31, 32]. The region of nuclei between $^{180}Hf_{108}$ and $^{200}Hg_{122}$ has been suggested by Jolie and Linnemann [28] to exhibit prolate and oblate deformation competition as the N=126 closed shell is approached. Figure 1.7 shows results of axially symmetric, Hartree-Fock calculations for a series of even-even nuclei around ^{190}W, from reference [33]. This nucleus is predicted to exhibit two minima of near-equal energy depth (i.e. approximately equal prolate and oblate configurations). Other recent calculations by Robledo *et. al.* on the ground state nuclear shapes in this region using a Skyrme Hartree-Fock plus BCS

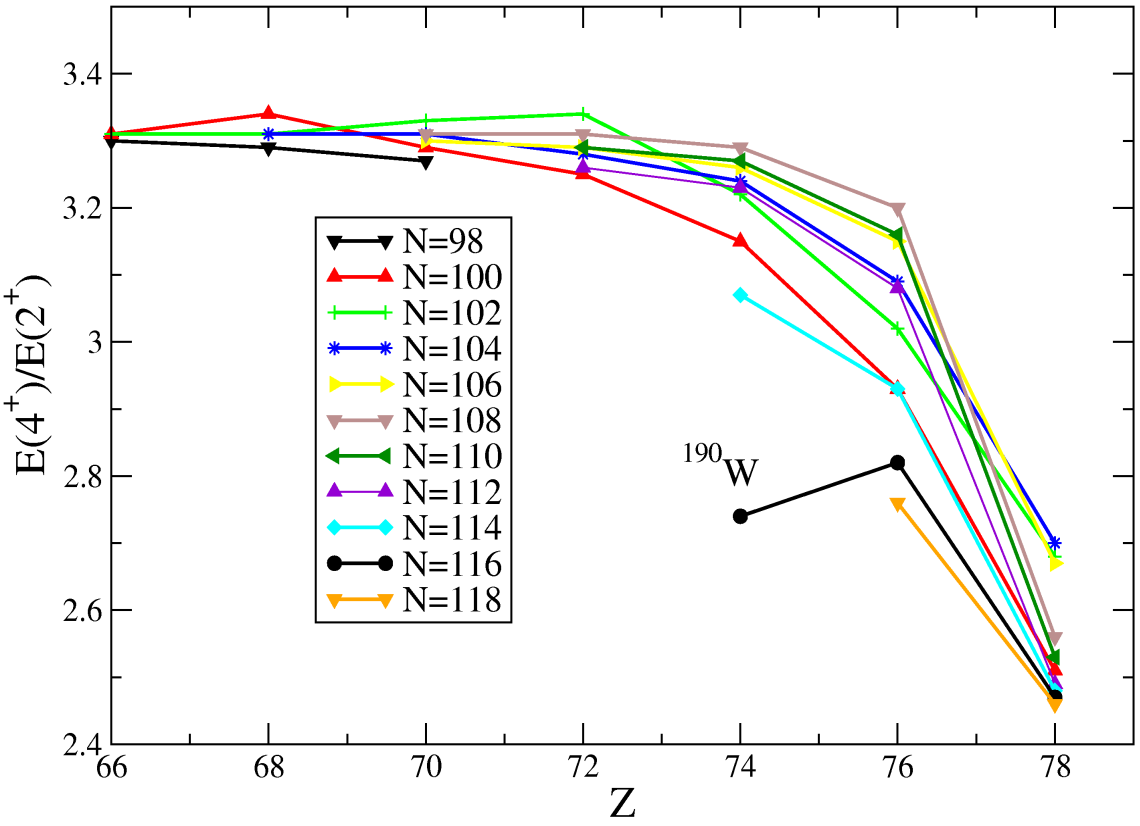

Figure 1.6: The R(4/2) ratio for the even-even as a function of Z for N=98 up to N=118. The discontinuity associated with the ^{190}W data point is notable in this figure.

pairing approach [34] were performed including the γ degree of freedom as shown in Figure 1.8. These calculations predict that ^{190}W lies on the near-critical point between prolate and oblate shapes and suggest this nucleus for a candidate of the O(6) symmetry in the Interacting Boson Approximation (IBA) [35, 36, 37, 38, 39] (see section 2 of Chapter 6). Experimental evidence of such behaviour has been reported in a number of nuclei in this region previously including ^{194,196}Pt [24, 40] and ^{192}Os [41]. These nuclei represent the "best cases" so far for the experimental realisation of the O(6) symmetry limit of the IBA.

This thesis presents results from an experiment performed at the GSI laboratory, Germany in March, 2007 to study the internal structures of the neutron-rich nuclei around A=190 populated using projectile fragmentation reactions. Figure 1.9 shows the limit (red line) of nuclei with identified excited states in this region prior to the current work [11, 17, 44, 45, 46, 47]. The nuclei represented by the blue squares

are those produced and discussed in this thesis. The specific goal of this work is to study the low-lying excitations in ^{188,190,192}W following the decay of their mother nuclei ^{188,190,192}Ta using the RISING active stopper [42]. Evidence is presented for the first observation of the second $I^{\pi}= 2^{+}$ state in ^{190}W and the yrast $I^{\pi}= 2^{+}$ state in ^{192}W. The experiment also provided the first measurements of β^{-} half lives in a number of neutron-rich nuclei in this region, specifically ^{187,188,189}Hf, ^{188,189,190,191,192}Ta, ^{191,192,193,194}W and ^{193,194,195}Re.

The remaining Chapters of this thesis are ordered as follows: Chapter 2 provides a theoretical background of related subjects discussed; Chapter 3 outlines the experimental techniques used in the current work; the experiment details are discussed in Chapter 4, with the experimental results and discussion of the low-lying nuclear structures of ^{188,190,192}W presented in Chapters 5 and 6. Finally, the main conclusions and perspectives of this work are presented in Chapter 7.

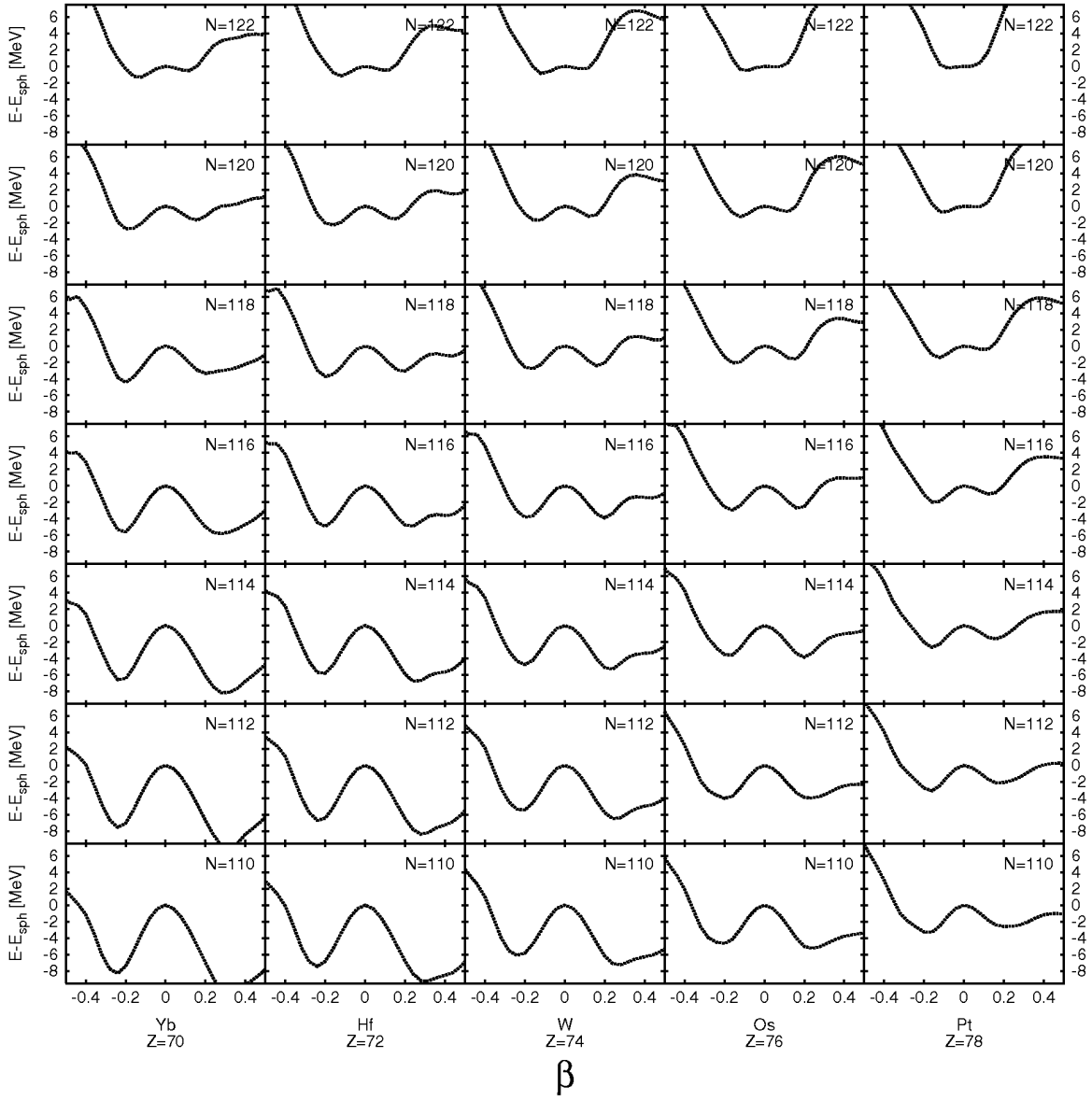

Figure 1.7: Potential energy as a function of quadrupole deformation from axially symmetric Hartree-Fock calculations for Yb, Hf, W, Os and Pt nuclei with neutron number between N=110 and 122, performed by Stevenson *et. al.*, and taken from reference [33].

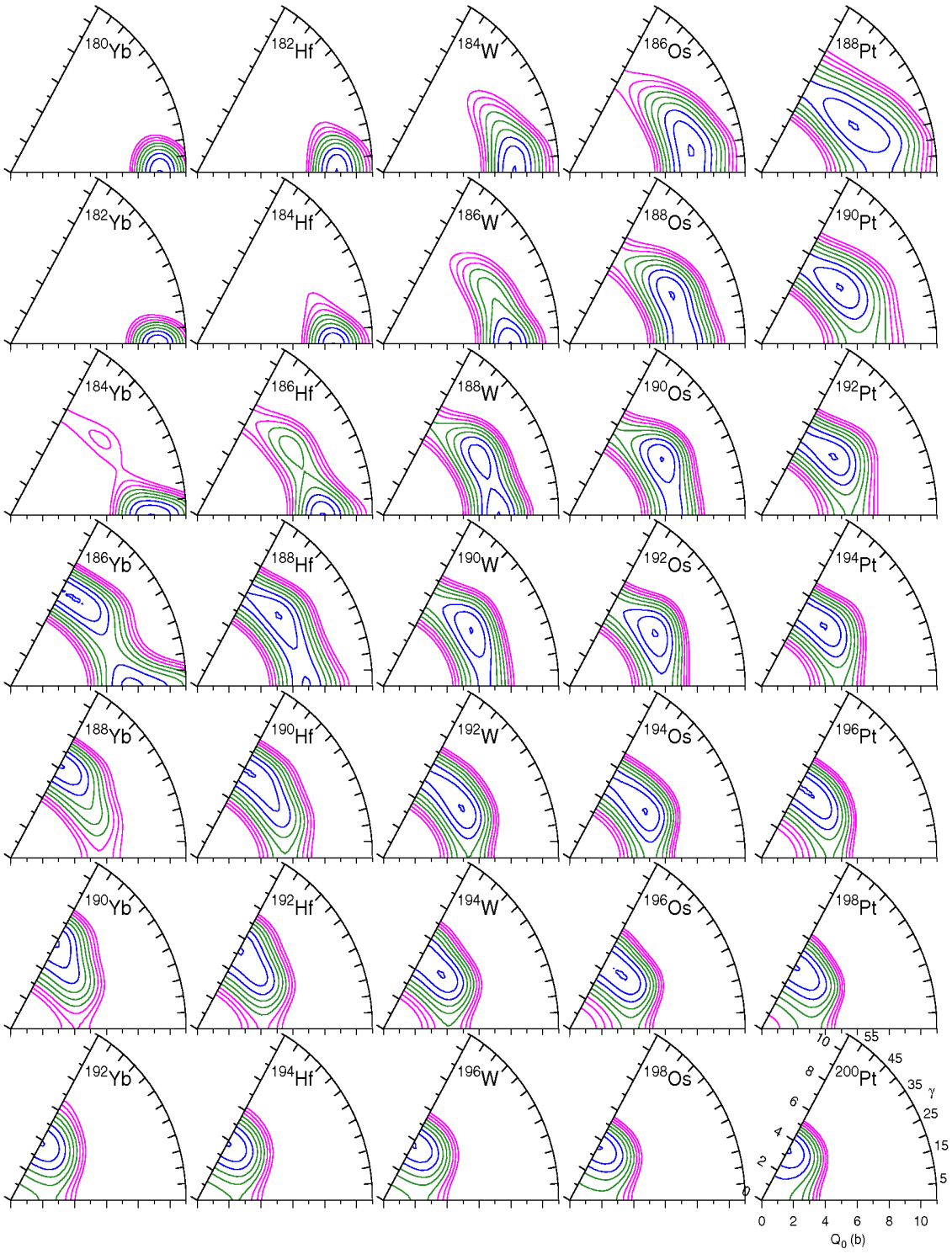

Figure 1.8: β (in term of axial quadrupole moment)-γ contour planes for Yb, Hf, W, Os and Pt nuclei ranging from N= 110 for the top row up to N= 122 for the bottom row, performed by Robledo *et. al.*, and taken from reference [34].

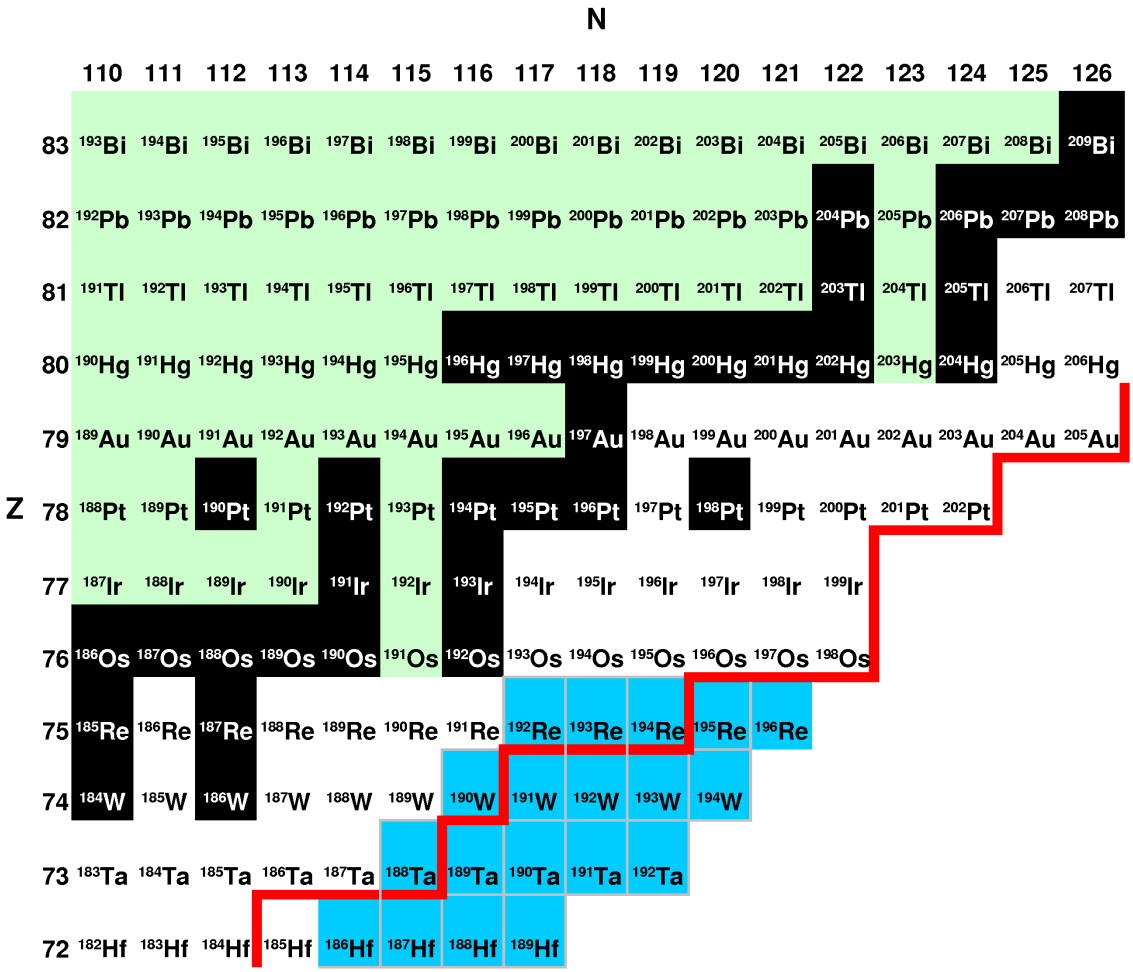

Figure 1.9: Partial nuclear chart highlighting the region of interest for the current work. The black squares represent the stable nuclei. The red line represents the experimental measured excited state limits prior to the current experiment [11, 17, 44, 45, 46, 47]. The blue squares represent the region of nuclei populated in the current work.

Chapter 2

Nuclear Structure and Decay

2.1 Nuclear Models

2.1.1 The Shell Model

The shell model is one of the important tools that helps scientists to understand nuclear properties and their internal structure. This model originated from different experimental results which suggested shell effects and closures in nuclei and could be connected to each other through this model. The concept behind the nuclear shell model is that a nucleon moves in a potential created by the other nucleons in the nucleus and the nucleons occupy well defined orbits. The nucleons (protons and neutrons) in unfilled shells (i.e. the valence nucleons) are responsible for most of the observed low-energy nuclear properties.

Additional evidence for shell structure includes sudden and discontinuous behaviour of the single and two nucleons separation energies for specific proton and neutron numbers. These nucleons numbers are called *magic numbers* and occur at N,Z= 2, 8, 20, 28, 50, 82 and 126 (see Figure 2.1) [48]. Nuclei with magic numbers of both Z and N (e.g. $^{208}_{82}\mathrm{Pb}_{126}$) are called doubly magic nuclei.

The first step in understanding the shell model and predicting the correct sequence of magic numbers is the selection of a suitable mean-field potential $V(r)$. The Shell Model Hamiltonian can be represented by [50]:

$$H = \sum_{i=1}^{A} \left[-\frac{\hbar^2}{2m} \nabla_i^2 + V(r_i) \right] \tag{2.1}$$

The first term represents the kinetic energy of each nucleon (i) of mass m and the

second term represents the potential. A simple potential which can be used to approximate the average nuclear potential is the Harmonic Oscillator potential, represented by the equation [49]:

$$V(r) = \frac{1}{2}m\omega^2 r^2 \tag{2.2}$$

where ω is the particle oscillator frequency and r is the orbital radius. The time independent Schrodinger equation for this motion is given by:

$$\left(-\frac{\hbar^2}{2m}\nabla^2 + V(r)\right)|\phi\rangle = E|\phi\rangle \tag{2.3}$$

$V(r)$ is the potential and $E|\phi\rangle$ is the wave function with eigenvalue of energy E. Solving this equation leads to the extraction of the energy eigenvalues, E, for the three dimensional harmonic oscillator which are given by [50]:

$$E_{nl} = \left(n + \frac{3}{2}\right)\hbar\omega \tag{2.4}$$

where n is the principal quantum number (= 1, 2, 3, ...). Thus, the energy does not depend on the orbital angular momentum quantum number, l. The left side of figure 2.1 shows the energy levels obtained from the harmonic oscillator potential. It is clear that the first three magic numbers (2, 8 and 20) are predicted correctly, but this model fails to correctly predict the nuclear magic numbers at 28, 50, 82 and 126.

The values of the orbital angular momentum quantum number, l, are 0, 1, 2, 3, 4, ... which are labeled using *spectroscopic notation* as s, p, d, f, g, ... respectively [50]. Each specific l-value has an energy degeneracy of $2(2l+1)$ neutrons or protons.

A realistic nuclear potential therefore should follow the size of the nucleus (nucleus radius $R = r_0 A^{\frac{1}{3}}$ [50]) and extend out to cover the range of the nucleon-nucleon interaction ($\approx$ 1fm). Such a potential is the *Woods-Saxon potential* [51]:

$$V(r) = \frac{-V_O}{1 + exp\left[(r-R)/a\right]} \tag{2.5}$$

where V_0 is the depth of the potential, r is the radius of the potential, R is the mean radius and a is called the surface diffusivity which represents how sharply the potential falls off to zero ($\approx$ 0.524 fm [50]). The depth of the well, V_0, can be adjusted to be

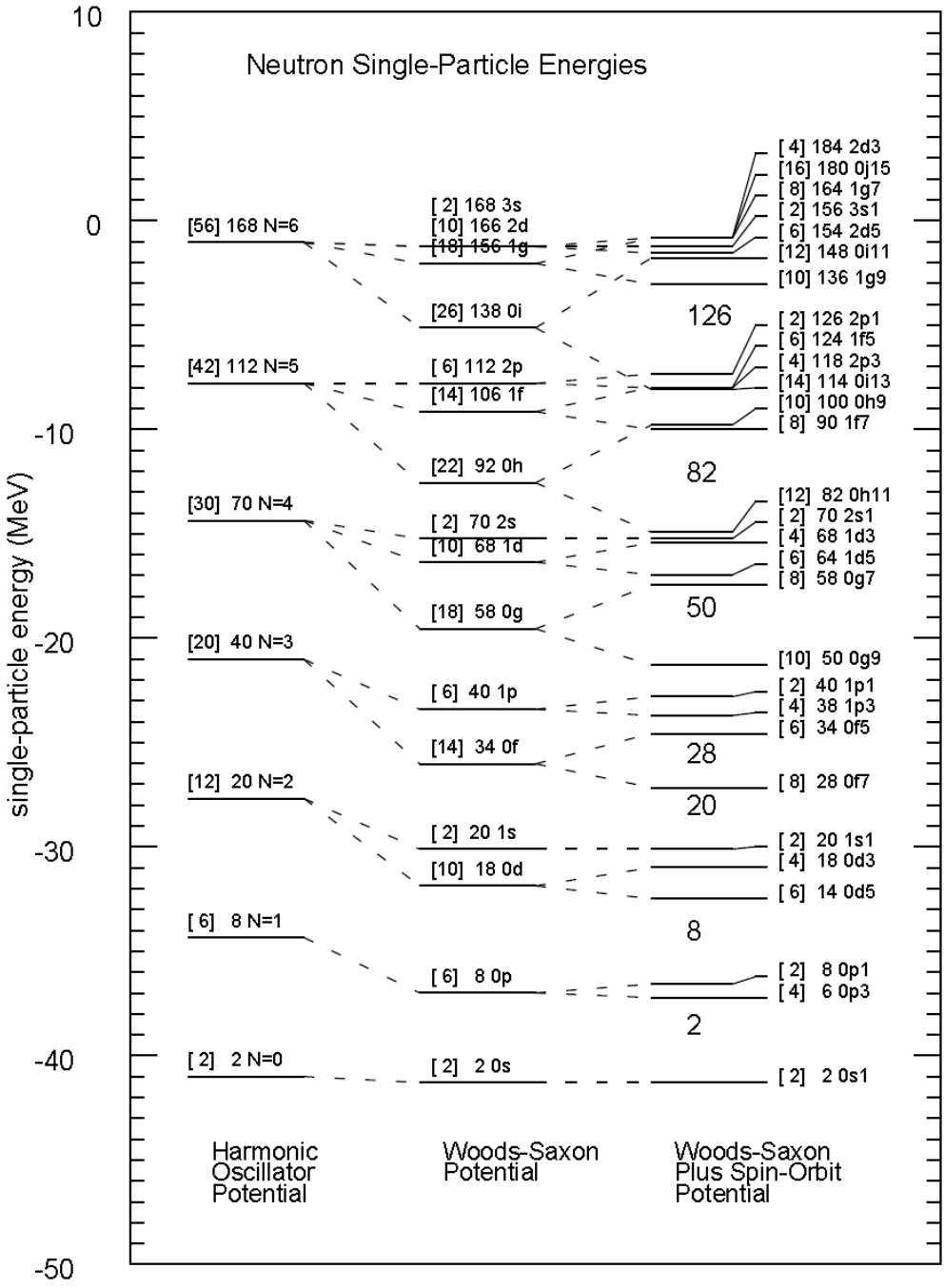

Figure 2.1: Single particle energy levels for three nuclear potentials: (left) the simple Harmonic Oscillator; (centre) Wood-Saxon potential and (right) the Woods-Saxon plus a spin-orbit interaction. The numbers in square brackets represent the maximum number of nucleons that can occupy each level. This figure is taken from [50]

.

the order of 50 MeV to reproduce the correct energy separation of the nucleons [50]. The effect of this correction in the potential can be seen in the central part of figure 2.1. This potential removes the l degeneracy of the major levels which are seen in the Harmonic Oscillator. The number of nucleons (protons or neutrons) allowed in each energy levels are:

$$2,\ 6,\ 10,\ 2,\ 14,\ 6,\ ...$$

While this modified potential also predicts correctly the smaller magic numbers (i.e. N, Z$\leq$20), it fails to reproduce the energy gaps which give the higher ones (N, Z$\geq$28).

The first model which reproduced the experimentally observed magic numbers was presented in 1948 by Mayer [52] and also by Haxel, Suess and Jensen [53] who suggested that by analogy with the atomic shell model, that there could be a finer structure of the nuclear energy levels arising from inclusion of a spin-orbit potential. This potential can be given by [53]:

$$V_{l_\bullet s} = -V_{ls}\frac{\delta V\left(r\right)}{\delta r} l_\bullet s \tag{2.6}$$

where s and l are the intrinsic spin and the orbital angular momentum vectors for the nucleon respectively and V_{ls} is a strength constant. This (strong) spin-orbit potential causes additional splitting of the energy levels and reproduces the correct magic numbers as shown on the right side of figure 2.1. This splitting of each level of a given l-value into two separate levels of $j = l \pm \frac{1}{2}$ is the important result of the inclusion of this potential. In the nucleus, the lower energy level of the two always takes the $j = l + \frac{1}{2}$ coupling state and the higher one has $j = l - \frac{1}{2}$.

The degeneracy of each orbital level is now given by $2j + 1$ which arises from the number of magnetic substates of angular momentum projection, m_j. Thus, when a given j orbit is filled with $2j + 1$ nucleons, the next higher lying orbit fills consistent with the Pauli principle, which states that no two identical fermions can occupy the same quantum state simultaneously [54].

For even-even nuclei, the ground state spin and parity are predicted by the spherical shell model to be $I^\pi = 0^+$. For odd-odd nuclei, the ground state spin and parity are determined by coupling of the spin and parity of the last two valence nucleons [50]. The allowed coupling rules in odd-odd nuclei are given by the Gallagher and Moszkowski selection rules [55], which can be summarized by:

$$\begin{aligned} I &= j_p + j_n \text{ if } j_p = l_p \pm \frac{1}{2} \text{ and } j_n = l_n \pm \frac{1}{2} \\ I &= |j_p - j_n| \text{ if } j_p = l_p \pm \frac{1}{2} \text{ and } j_n = l_n \mp \frac{1}{2} \end{aligned} \tag{2.7}$$

2.1.2 The Deformed Shell Model

The low-lying states in near closed-shell nuclei are assumed to have spherical shapes as predicted by the independent particle spherical shell model. However, nuclei with protons and neutrons number away from closed shells exhibit non-spherical shape effects [56, 57]. This deformation from spherical symmetry was inferred originally from experimental measurements of nuclear properties such as measurements of nuclear quadrupole moments [27].

The surface of a deformed nucleus of an average radius R_0 can be parametrised by [58]:

$$R = R(\theta, \phi) = R_0 \left(1 + \alpha_{00} + \sum_{\lambda=1}^{\infty} \sum_{\mu=-\lambda}^{\lambda} \alpha^*_{\lambda\mu} Y_{\lambda\mu}(\theta, \phi) \right) \tag{2.8}$$

where $\alpha^*_{\lambda\mu}$ are the coefficients of the spherical harmonics $Y_{\lambda\mu}$ of a nucleus with a volume V:

$$V = \frac{4}{3}\pi R_0^3 \tag{2.9}$$

The parameter α_{00} describes the change in the nucleus volume such that:

$$\alpha_{00} = -\frac{1}{4\pi} \sum_{\lambda \geq 1, \mu} |\alpha_{\lambda\mu}|^2 \tag{2.10}$$

For a quadrupole deformation ($\lambda = 2$), the expansion coefficients can be described by the Hill-Wheeler variables β and γ such that [59]:

$$\alpha_{20} = \beta_2 \cos\gamma \tag{2.11}$$

$$\alpha_{22} = \frac{1}{\sqrt{2}} \beta_2 \sin\gamma \tag{2.12}$$

In the same way, the nuclear deformation can be written for the octupole ($\lambda = 3$) and hexadecapole ($\lambda = 4$) shapes. The β coordinate represents the extent of the

quadrupole deformation where γ represents the degree of axial asymmetry. When $\beta_2 \geq 0$, the nucleus is described as having a prolate shape and when $\beta_2 \leq 0$ the nucleus has the flattened form of an oblate shape.

2.1.3 The Collective Model

The main limitation of the shell model is the assumption that the nucleons move independently in a paired fashion in a spherically symmetric potential. This assumption leads to the idea that valence nucleons are responsible of all the low-lying nuclear properties. However, it fails to explain some low-lying nuclear properties, particularly with regards to the structure of nuclei far from the closed shell boundaries (i.e. those nuclei with a significant number of valence protons and neutrons). These properties are known as the *collective properties*, in which the motion of many nucleons contribute to the nuclear excitation. The two main types of the collective motion in nuclei are quadrupole vibrations and rotation [27]. The vibrational mode can occur about the "average" spherical nuclear shape whereas the rotational mode implies a static deformation (i.e. permanently deformed, nonspherical nuclei).

Nuclear Vibrations

For nuclei with N and/or Z numbers near to the closed shells, where the shape is assumed to be near-spherical, the residual interaction of the few valence nucleons can cause the nucleus to vibrate in shape. The shape of a such nucleus was described previously by equation 2.8. A λ=1 deformation corresponds to a collective electric dipole excitation. This vibrational mode corresponds to a net translation of the centre of mass and therefore cannot result from the action of internal nuclear forces [50]. The next lowest order multipole mode is the quadrupole vibration (λ=2). The quantum energy unit of the (quadrupole) vibrational energy is called a *phonon*.

For the even-even nuclei, the lowest energy state is the spin/parity 0^+ ground state. By adding one phonon (two units of angular momentum), the first excited state is 2^+. For the two-quadrupole phonon double excitation, a triplet of levels with spins of 0^+, 2^+ and 4^+ are allowed. Figure 2.2 shows the low-lying excited states of multi vibrational phonon mode. The selection rule of the allowed transitions between the

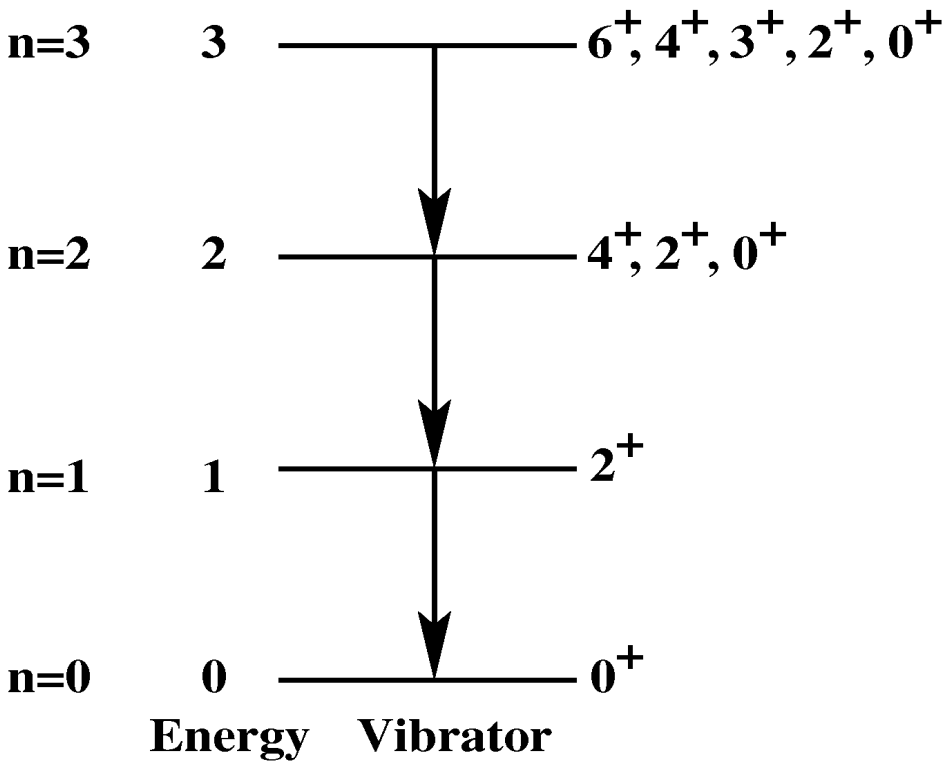

Figure 2.2: The low excited states of a perfect, idealised harmonic vibrator (figure modified from [27]).

phonon levels is that they must follow [27]:

$$\Delta N_{ph} = \pm 1 \tag{2.13}$$

where N_{ph} corresponds to the number of phonons associated with that particular state.

Nuclear Rotations

In an axially symmetric quadrupole deformed nucleus, the total angular momentum I (see figure 2.3) can be written as:

$$\boldsymbol{I} = \boldsymbol{R} + \boldsymbol{J} \tag{2.14}$$

where J is the vector sum of all angular momenta of the individual nucleons ($J = \sum_{i=1}^{A} \boldsymbol{j}$). The projection of the total angular momentum onto the axis of symmetry, K, is equal to the sum of angular momentum projection of all individual nucleons, Ω (i.e. $K = \sum_i \Omega_i$).

The Hamiltonian H of a rotating object is defined by [27]:

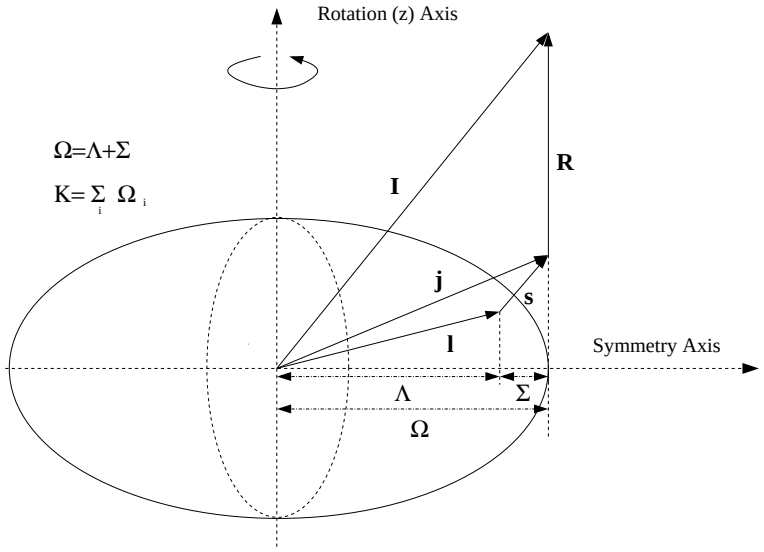

Figure 2.3: A diagram representing the quantum numbers associated with an axially symmetric deformed nucleus (taken from Ref [60]).

$$H = \frac{\hbar^2}{2\Im}\mathbf{R}^2 \tag{2.15}$$

where $\Im$ is the moment of inertia and $\mathbf{R}$ is the (collective) rotational angular momentum operator. If we consider even-even nuclei which have ground state of $I^\pi = 0^+$ and assume that all the angular momentum can be ascribed to rotation, then the total angular momentum $\mathbf{I}$=$\mathbf{R}$ and the excitation energy of states of the idealised rotor can be predicted by:

$$E_{rot}(I) = \frac{\hbar^2}{2\Im}I(I+1) \tag{2.16}$$

Increasing the quantum number I corresponds to adding more rotational energy to the nucleus. Therefore, for an idealized axially symmetric deformed even-even nucleus, the rotational levels take the following rotational energy values [27, 50]:

$$E_{0^+} = 0 \tag{2.17}$$

$$E_{2_1^+} = 6\frac{\hbar^2}{2\Im} \tag{2.18}$$

$$E_{4_1^+} = 20\frac{\hbar^2}{2\Im} \tag{2.19}$$

$$E_{6_1^+} = 42\frac{\hbar^2}{2\Im} \tag{2.20}$$

Thus, for a perfect, idealised axially symmetric rotor, the energy ratio $\mathrm{E}_{4_1^+}/\mathrm{E}_{2_1^+}$=20/6=3.33*.

2.1.4 The Davydov-Filippov Model for axially asymmetric Nuclei

The Davydov-Filippov model is one of the more successful models for describing deformed even-even nuclei [61]. It is particularly known as a model which describes of fixed stable asymmetry (triaxiality) deformation in nuclei. The potential V(γ) has the characteristics of a well-deformed and deep minimum at a particular value of γ; thus the nucleus has a rigid axial asymmetric shape in this model.

In the Davydov-Filippov triaxial model, there is no distinction between the ground state band (rotational band) and γ vibrational band. The levels of these two bands are simply described as "normal" and "anomalous" states of a new ground state band [27]. The energies of these states depend on the value of γ, which ranges between 0° (prolate symmetric) and 30° (maximum asymmetry). The 0_1^+, 2_1^+, 4_1^+,6_1^+ ... states are the normal ground state band levels. Figure 2.4 shows the lowest energy levels predicted by Davydov-Filippov model for even-even nuclei as a function of γ degree of freedom [62]. For γ=0°, the energy spectrum is identical to the axially symmetric deformed nucleus. As γ is increased, the nuclear shape becomes more flattened and thus those states with wave functions aligned into the direction of this flattening achieve lower energies. This effect is due to the short-range attractive nature of the nuclear force; the closer nucleon to the nuclear bulk, the lower the energy (i.e. greater binding energy) [27].

One of the main applications of Davydov-Filippov model is the potential to extract the γ degree of freedom from the energy ratio $E_{2_2^+}/E_{2_1^+}$, using the following expression [61]:

$$\frac{E_{2_2^+}}{E_{2_1^+}} = \frac{[1+X]}{[1-X]} \tag{2.21}$$

where X related to the triaxiality parameter γ by the following equation:

$$X = \sqrt{1 - \frac{9}{8} sin^2(3\gamma)} \tag{2.22}$$

2.1.5 The Wilets-Jean Model

The Wilets-Jean model assumes a deformed nucleus free to vibrate in the γ degree of freedom [63]. The nucleus can oscillate smoothly from γ=0° to 60°. Such a nucleus

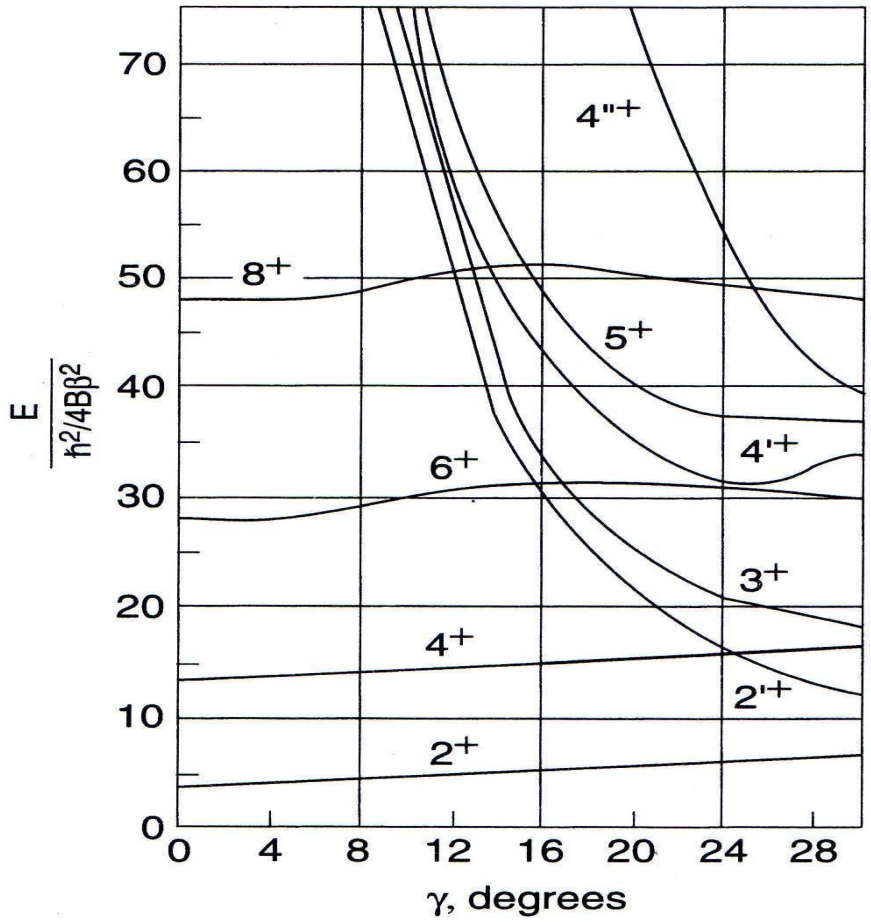

Figure 2.4: Low-lying energy states predicted by the Davydov-Filippov model of the nuclear triaxial rotor as a function of γ degree of freedom, taken from reference [27].

is called γ-soft. The rotational energies are given by [27]:

$$E(\Lambda) = \vartheta\Lambda(\Lambda + 3) \tag{2.23}$$

where Λ is the level quantum number and ϑ is a constant that is analogous to the $\hbar^2/2\Im$ term in the symmetric rotor model. The yrast states have I=2Λ and thus have energies $E(I\text{-yrast}) = (\vartheta/4)I(I+6)$. The state energies increase with I but are lower than the $I(I+1)$ relation predicted for the symmetric rotor. For example the energy ratio $E_{4_1^+}/E_{2_1^+}$ is predicted to have a value of 2.5 for a completely γ-soft nucleus compared to 3.33 for the symmetric rotor.

The $E2$ selection rule in the Wilets-Jean model matches the selection rule in the phonon vibration model. Allowed transitions follow a $\Delta\Lambda = \pm 1$ rule. For example, the $2_2^+ \rightarrow 2_1^+$ transition is allowed ($\Delta\Lambda = 1$) while the $2_2^+ \rightarrow 0_1^+$ is forbidden, since $\Delta\Lambda = 2$.

One of the main differences between the spherical vibrator and Wilets-Jean models is the triplet levels (0^+, 2^+ and 4^+) for the two-phonon excitation while there are only two analogous levels predicted in the Wilets-Jean model which have I^π=2^+ and 4^+. The first excited 0^+ state has $\Lambda = 3$. Figure 2.5 shows the γ soft level scheme from the Wilets-Jean model and the analogy levels of a typical symmetric rotor. In this figure, the energy levels of the γ band group according to (2^+), (3^+,4^+) and (5^+,6^+). This grouping is opposite to the Davydov-Filippov model where the γ bands tend to group into neighbouring spin doublets (i.e. (2^+,3^+), (4^+,5^+), ...).

2.1.6 The Interacting Boson Approximation (IBA)

The *Interacting Boson Approximation* (IBA) was invented in 1974 by F. Iachello and A. Arima [35]. It is suitable for describing the collective behaviour of intermediate and heavy atomic nuclei. The IBA is based on the nuclear shell model which becomes intractable far from closed shells [27].

The fundamental idea of the IBA is based on assuming that only the valence nucleons are responsible for the properties of the collective low-lying states. These valence nucleons couple in pairs to total angular momentum J =0 and 2, called s and d bosons respectively. In the IBA-1 model there is no distinction between proton and neutron bosons. The states of such an interacting boson system thus depend on the s and d boson energies and their interactions.

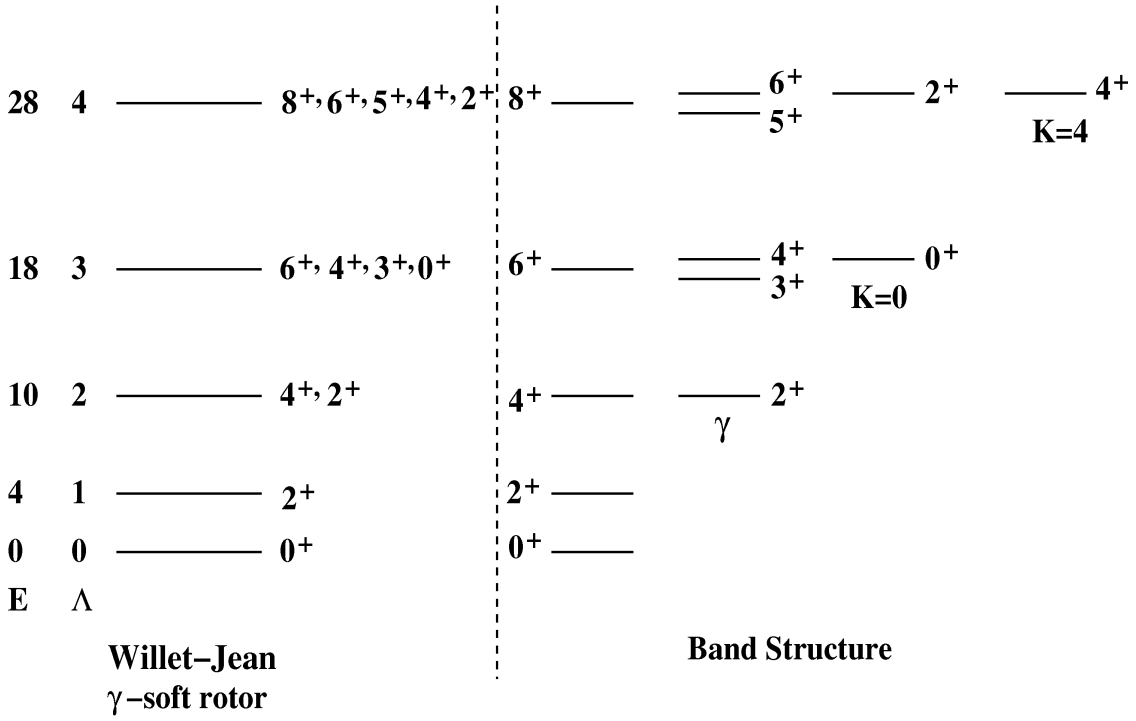

Figure 2.5: The Wilets-Jean model γ-soft level scheme (left) and the analogue band structure of a typical rotor (modified from [27]).

The number of available magnetic substates of such s-d boson configurations are 1 for an s boson ($J = 0$) and 5 for a d boson ($J = 2$), thus forming a six dimensional space. This system can be described mathematically in terms of the algebraic group $U(6)$. There are different subgroups of the $U(6)$ structure leading to different symmetries. The three most relevant groups of these symmetries for nuclear physics interpretations are labelled as $U(5)$, $SU(3)$ and $O(6)$. These subgroups are the theoretical representations of the three nuclear structure limits: quadrupole vibrator, axially symmetric rotor and gamma-soft rotor, respectively. The symmetry structure of the IBA model can be illustrated in term of the symmetry triangle as shown in figure 2.6.

2.1.7 The Nilsson Model

The spherical shell model, as described in Section 2.1.1, provides a reasonable description of the low-lying excitations in nuclei near to the closed shells. However, the existence of permanently deformed nuclei implies the need to introduce another model to describe the deformed potential. The Nilsson Model is one of most successful

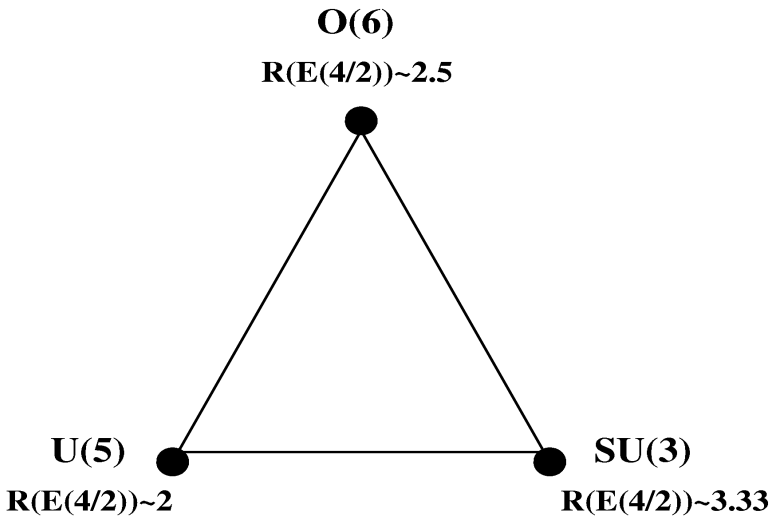

Figure 2.6: The symmetry triangle of the IBA model showing the three symmetry limits: $U(5)$, $SU(3)$ and $O(6)$ [27].

models which can be applied to deformed nuclei. In this model, Nilsson used a deformed harmonic oscillator potential [64] to predict the effect of core deformation on the relative energies of the single-particle levels. The total one-particle Nilsson Hamiltonian for a nucleus with axial symmetry ($\omega_x = \omega_y \neq \omega_z$) is given by [64]:

$$H = \frac{\mathbf{P}^2}{2m} + \frac{1}{2}m\left(\omega_x^2 x^2 + \omega_y^2 y^2 + \omega_z^2 z^2\right) + Cl \cdot s + Dl^2 \tag{2.24}$$

where the first term represents the kinetic energy of a single-particle of mass m and momentum p. The term $l \cdot s$ represents spin-orbit interaction and the term l^2 is a term introduced to simulate the flattening of the nuclear potential at the centre of the the nucleus. The coefficients C and D are defined in terms of the parameters κ and μ as follows [27]:

$$\kappa = \frac{C}{2\hbar\omega_0} \qquad \mu = \frac{2D}{C} \tag{2.25}$$

where ω_0 is the oscillator frequency; κ takes a value around 0.06 and μ takes a value which varies from 0 to $\approx$0.7 [65].

Figures 2.7 and 2.8 show the axially symmetric Nilsson single-particle digram for neutrons in the $82 \leq N \leq 120$ region and for proton region $50 \leq Z \leq 82$ respectively.

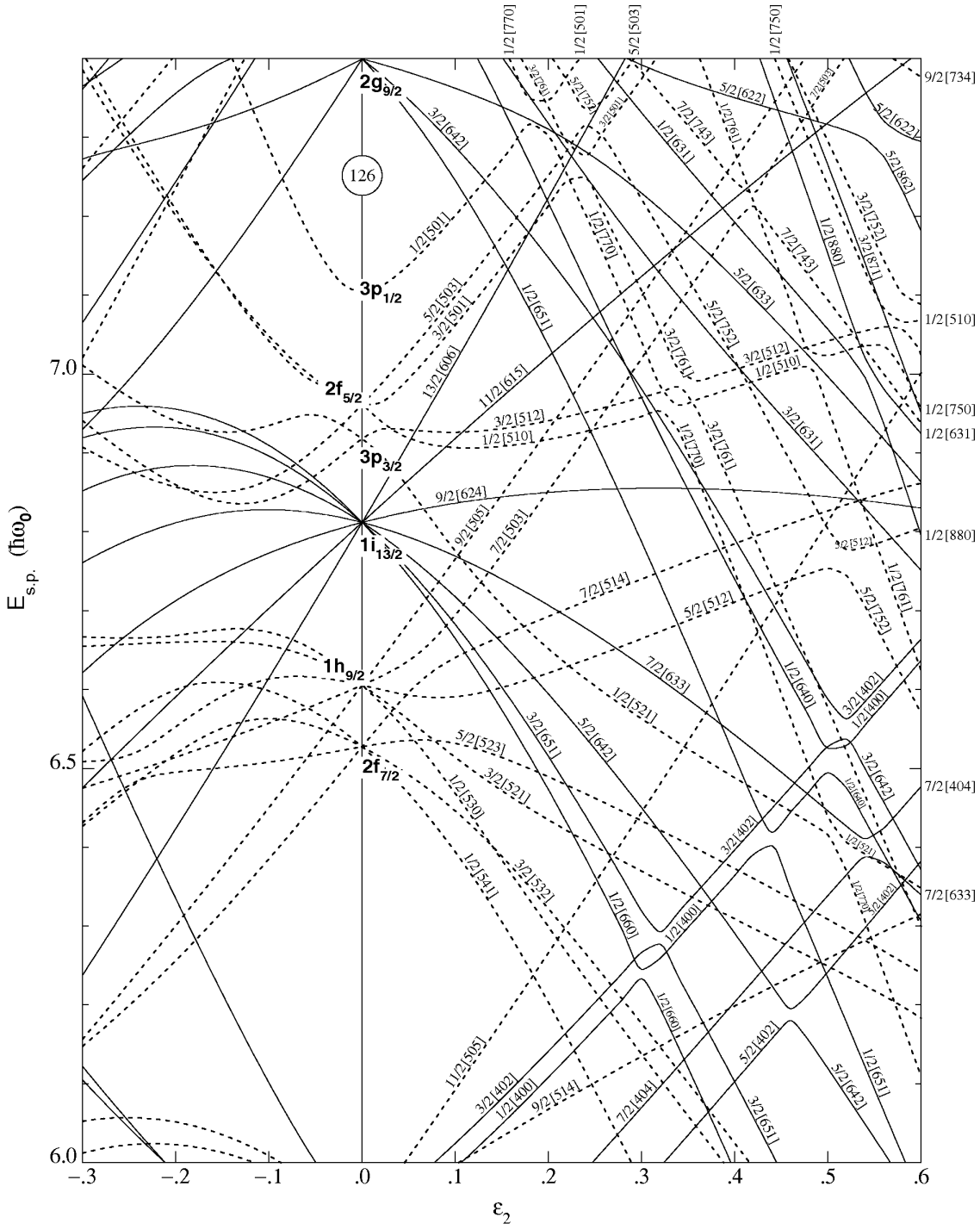

Figure 2.7: Nilsson diagram for neutrons 82< N <120 ($\varepsilon_4 = \varepsilon_2^2/6$), taken from reference [66].

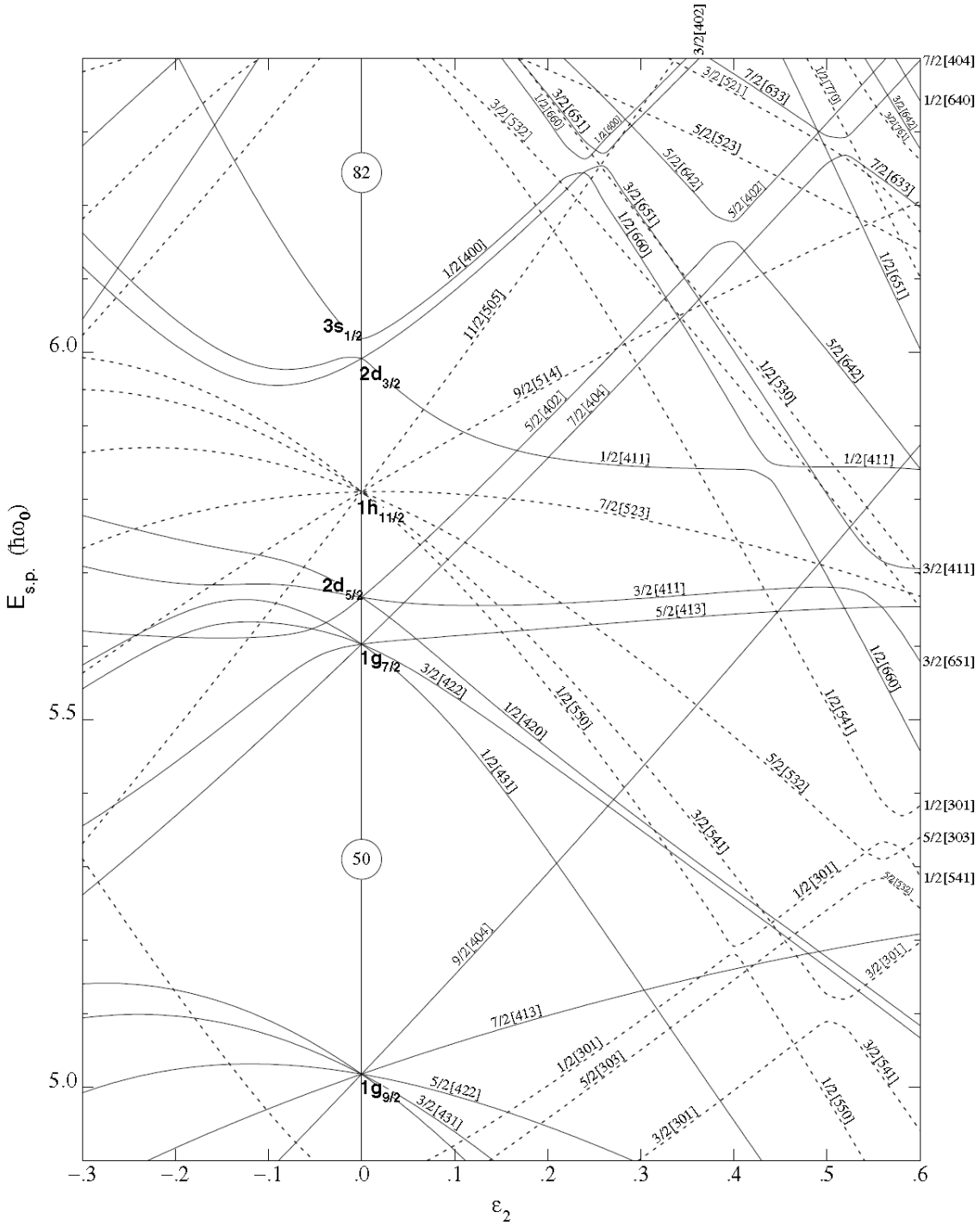

Figure 2.8: Nilsson diagram for protons 50< Z <82 ($\varepsilon_4 = \varepsilon_2^2/6$), taken from reference [66].

It can be seen in this diagram that at zero deformation, states with the same j are degenerate. Then, when the quadrupole deformation is introduced, the different j magnetic substates undergo a splitting in energy.

Each state of a given j is labeled according to its angular momentum projection onto the symmetry axis, K, as shown in figure 2.3. The upward or downward sloping of the orbital energies with respect to increasing deformation depends on the angle (θ) of the state relative to the main mass distribution of the nucleus. The nuclear force is considered to be short range and attractive, therefore the closer the orbital to the bulk nuclear matter, the higher the attractive force and the lower the single particle energy of the nucleon. As the deformation parameter (β) increases, the energy differences between each magnetic substate also increases.

The Nilsson orbitals can be characterized by the following quantum numbers:

$$\Omega^{\pi}[Nn_z\Lambda] \tag{2.26}$$

where N is the principal quantum number of the major shell, Ω is the particle projection, n_z is the number of nodes in the wave function in the z direction and Λ is the projection of the orbital angular momentum onto the symmetry axis ($\Omega = \Lambda \pm \frac{1}{2}$).

2.2 Nuclear Decay

2.2.1 Binding Energy

The mass of a nucleus of mass number A and atomic number Z is less than the sum of mass of the constituent protons and neutrons. This difference is related to the binding energy (BE) of the system which represents the total energy required to disassemble a nucleus into its constituent protons and neutrons:

$$BE = (M_N - ZM_p - (A - Z)M_n)c^2 \tag{2.27}$$

where M_N is the nuclear mass, M_p is the proton mass, M_n is the neutron masses and c is the speed of light.

The nuclear reaction process can be written as:

$$A + B \longrightarrow C + D \tag{2.28}$$

where A is the projectile nucleus, B is the target nucleus and C and D are the residual nuclei created by the reaction. The Q-value of a reaction is defined as the difference in total mass energy before and after the reaction and can be written as:

$$Q = (M_A + M_B - M_C - M_D)c^2 \tag{2.29}$$

If $Q \geq 0$ the reaction is called "exothermic" and if $Q \leq 0$ the reaction is called an "endothermic" reaction.

Attempts to understand the binding energy variation with A and Z led to the Weizsacher semi-empirical formula (SEMF) [72]:

$$BE(MeV) = a_v A - a_s A^{2/3} - a_c Z(Z-1)A^{-1/3} - a_{sys}\frac{(A-2Z)^2}{A} + \delta \tag{2.30}$$

The first term, $a_v A$, is the volume term due to the addition of each nucleon being responsible for approximately the same amount of increase in the total binding energy. The second term is the surface term and accounts for the nucleons at the surface being less bound than those in the interior of the nucleus. As the radius of the nucleus is proportional to $A^{1/3}$, then the surface area is proportional to R^2 (i.e. $A^{2/3}$). The reduction in binding energy due to the Coulomb repulsion between the protons in the nucleus is included via the third term. Since there are Z(Z-1)/2 pairs in the nucleus and each is on average $R_0 A^{1/3}$ apart (where R_0=1.2 fm), the Coulomb energy of the nucleus is approximately $Z^2e^2/2R_0A^{1/3}$. The fourth term incorporates the fact that stable nuclei have N≥Z and it is called the symmetry term. The final term is an empirical term which reflects that the nucleons tend to pair off with opposite spins and the nuclei tend to be correspondingly more stable than their odd N, Z partners. This term is usually expressed to be $-a_{sys}A^{-3/4}$ for odd Z, odd N; $+a_{sys}A^{-3/4}$ for even Z, even N; and 0 for A odd.

By using all the above terms, the semi-empirical mass formula can be written as:

$$M(A,Z) = ZM_H + (A-Z)M_n - a_v A + a_s A^{2/3} + a_c Z(Z-1)A^{-1/3} + a_{sys}\frac{(A-2Z)^2}{A} + \delta \tag{2.31}$$

For constant A, the SEMF formula represents a parabola of M *vs* Z. For odd-A one parabola is obtained but for even-A isobaric chains, two parabolas are obtained, separated by the 2δ arising from the pairing term. Figure 2.9 shows the mass parabolas of the A=188, 190 and 192 isobars of relevance to the work described in this thesis.

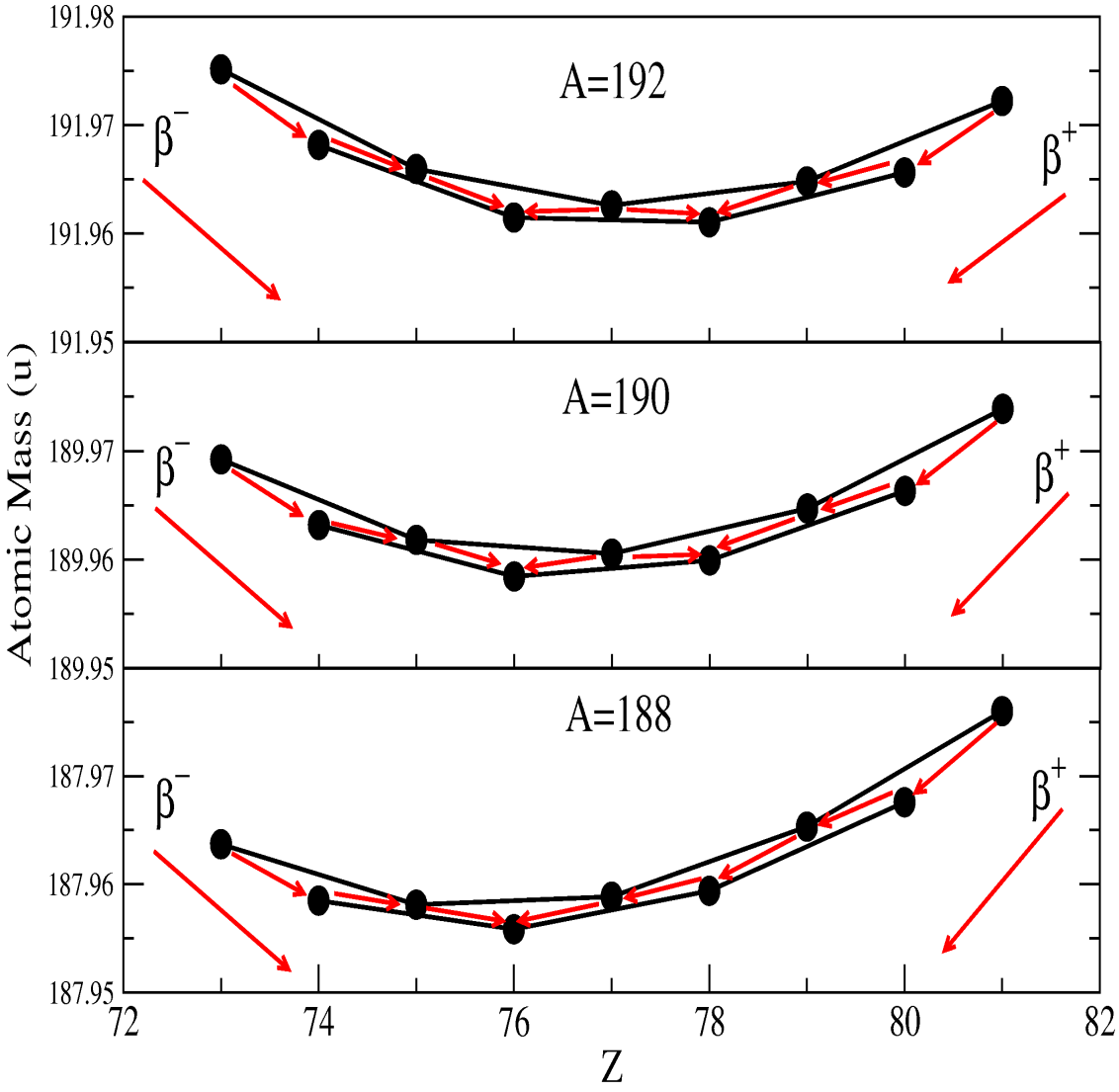

Figure 2.9: The mass parabolas for the A=188,190 and 192 isobaric chains calculated using the mass evaluation from reference [2].

2.2.2 Beta Decay

The term β decay involves three different modes of nuclear decay in which the atomic number, Z, changes by one unit while the mass number, A, remains constant. These three modes are β^-, β^+ and electron capture (EC). The basic decay process of each decay are:
For β^- decay

$$n \rightarrow p + e^- + \overline{\nu_e} \tag{2.32}$$

For β^+ decay

$$p \rightarrow n + e^+ + \nu_e \tag{2.33}$$

Electron capture is a process that competes with β^+ decay in which the nucleus captures an atomic electron (usually from the atomic K shell), resulting in the formation of a neutron and a neutrino:

$$p + e^- \rightarrow n + \nu_e \tag{2.34}$$

For β^- decay, the Q-value of the decay can be represented from equation 2.30 to be:

$$Q_{\beta^-} = [M(A,Z) - M(A,Z+1)]c^2 \tag{2.35}$$

where $M(A,Z)$ and $M(A,Z+1)$ are the atomic masses of the parent and the daughter nucleus respectively. The energy released is shared between the (small) nuclear recoil, kinetic energy of the emitted electron and the antineutrino. This three body process explains why the energy spectrum distribution of beta particles is a continuous spectrum.

Fermi Theory of Beta Decay

The basic assumption of Fermi theory is that the β-decay transition probability is caused by the weak interaction which is weaker than either the strong nuclear or the electromagnetic interactions [73]. The beta decay transition rate between the initial and final state is given by Fermi's Golden Rule [73, 74], which state that:

$$\lambda = \frac{2\pi}{\hbar}|M_{fi}|^2\rho(E_f) \tag{2.36}$$

Table 2.1: The selection rules of beta decay transitions with the $log_{10}ft$ expected values for each transition [50].

Category	$\triangle$I	$\triangle\pi$	Range of $\log_{10}$ft
(Super)Allowed, Fermi	0	no	2.9 - 3.7
Allowed, Gamow-Teller	0,1	no	4.4 - 6.0
First Forbidden, Fermi	0,1	yes	6 - 9
First Forbidden, Gamow-Teller	0,1,2	yes	8 - 10
Second Forbidden	2,3	no	10 - 13
Third Forbidden	3,4	yes	15

where $|M_{fi}|$ is the nuclear matrix element representing the interaction between the initial (i) and final (f) states and $\rho(E_f)$ is the density of final states.

The comparative half-life or $ft_{\frac{1}{2}}$ value provides a way to compare the β-decay probabilities in different nuclei [50]:

$$ft_{\frac{1}{2}} = 0.693\frac{2\pi^3\hbar^7}{g^2m_e^5c^4|M_{fi}|^2} \tag{2.37}$$

where g is the strength constant of beta decay ($g = 0.88 \times 10^{-4} MeV.fm^3$) and f in the left side originally is called the *Fermi integral* ($f = f(Z', E_0)$) which depends on the atomic number Z' of the daughter nuclei and the maximum electron energy, E_0 such that:

$$f(Z', E_0) = \frac{1}{(m_ec)^3(m_ec^2)^2}\int_0^{P_{max}} F(Z', p)p^2\left(E_0 - E_e\right)^2 dp \tag{2.38}$$

where p is the emitted electron momentum, E_e is the electron total relativistic energy and $F(Z', p)$ is the Fermi function which accounts for the influnce of the nuclear Coulomb field [75, 76, 77]. As there is enormous range of half lives of beta decay, a $log_{10}ft$ is usually used instead of ft [50, 78]

Selection Rules

During an allowed β-decay transition between two nuclear states, the total angular momentum and the parity of states are conserved. The two particles emitted (i.e. electron and antineutrino or positron and neutrino) each have an intrinsic spin $\frac{1}{2}\hbar$ and may carry away orbital angular momentum relative to the residual daughter nucleus. When the two particles are created at a point interaction (L=0), they cannot carry any orbital angular momentum (i.e. $\Delta J = |j_i - j_f| = 0$) and the change in the angular momentum between the mother and daughter nuclei (i.e the initial and final states) arises only from the coupling of the electron and neutrino spins. Such a transition is called an *allowed* decay and has two possibilities: (i) *Fermi* decay when the two particles have antiparallel spin, $S = 0$, and (ii) *Gamow-Teller* decay which corresponds to the parallel spin configuration, $S = 1$. For both modes of decay, the parity between the initial and final states will not change since this depends on the orbital angular momentum ($\pi = (-1)^l$) [50].

Other types of beta decays are called *forbidden* transitions. Such decays are not really forbidden but are much less probable than the allowed beta transitions. One group of such transitions occurs when there is a change in the parity of the nuclear states or when the spin $\Delta J \geq$0,1. The first classification of this transition is called first-forbidden, with L=1. The next order forbidden transitions are decays with L=2,3,4,... which are more rare. An indication of beta decay transitions selection rules with the expected values of the $log_{10}ft$ is given in Table 2.1. Figure 2.10 shows a summary of previously reported allowed and forbidden transitions plotted as a function of their respective $log_{10}ft$ values [79].

2.2.3 Electromagnetic Decays in Nuclei

Gamma Decay

A nucleus decaying via beta radiation can leave the daughter nucleus in an excited state. In this case, one or more gamma rays may be emitted by the residual daughter nucleus as it de-excites to its ground state. These electromagnetic emissions follow a specific set of selection rules derived from consideration of conservation of total mass-energy (E), parity (π) and angular momentum (L). If an excited state of excitation energy E_i, parity π_i and angular momentum I_i decays to a final state with E_f, π_f and

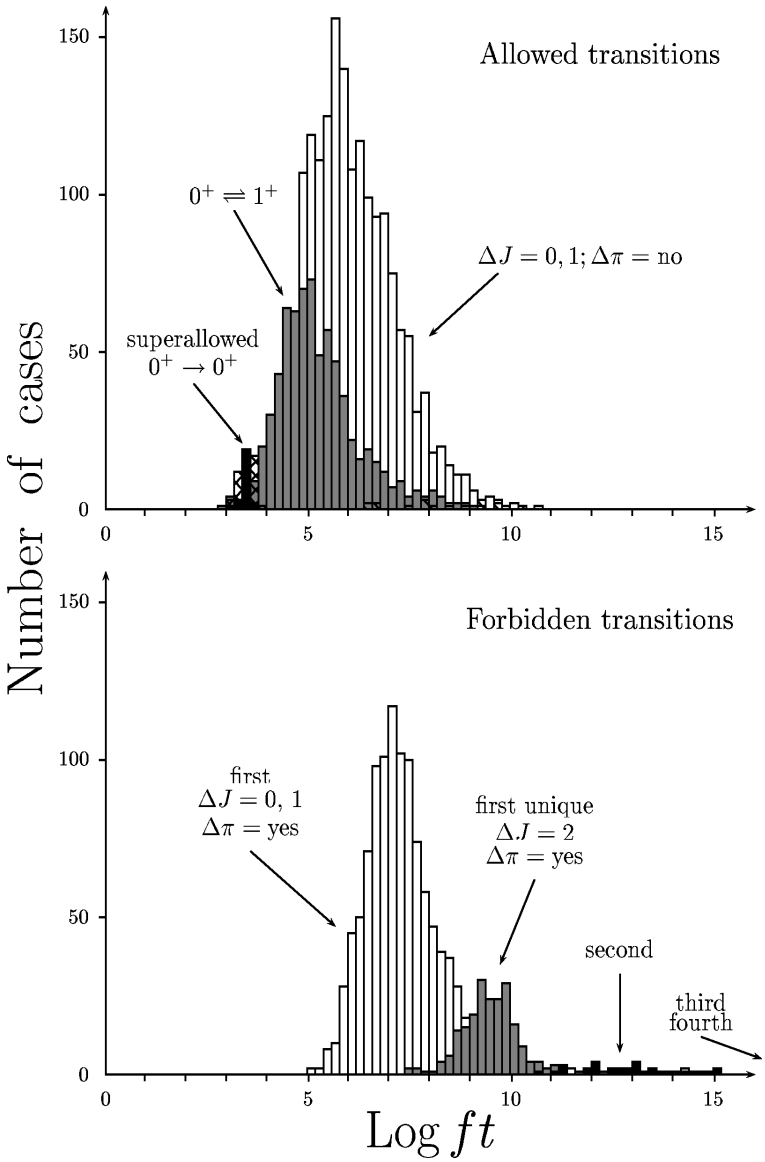

Figure 2.10: Numbers of known allowed (upper) and forbidden (lower) transitions plotted as a function of the $\log_{10} ft$ values. This figure is taken from [79].

I_f respectively, (neglecting the small effect from the energy of the recoiling nucleus), then the emitted gamma ray has an energy of [50]:

$$E_\gamma = E_i - E_f \tag{2.39}$$

By consideration of vector addition, conservation of angular momentum means that the angular momentum removed by the photon must be an integer value in the range:

$$|I_i - I_f| \leq L \leq I_i + I_f \tag{2.40}$$

There is an exception for transitions from spin/parity 0^+ to 0^+, which is forbidden to proceed by gamma decay due to the intrinsic spin of the photon being $1\hbar$. Such transitions can decay via internal conversion or internal pair formation if $E > 1.022MeV$ [80].

Considering the parity change associated with the transition, there is a distinction between electric and magnetic multipole natures of the decay. Therefore, for an electric transition, the parity change given by $\triangle\pi_E = (-1)^L$ and for the magnetic transition it is given by $\triangle\pi_M = (-1)^{L+1}$. The meaning of this distinction is that the radiation field of even parity would be M1, E2, M3 and E4 and for odd parity would be E1, M2, E3 and M4.

The probability of transition per unit time (i.e. the emission rate) of a multipole of order L and gamma energy E_γ is given by [81]:

$$T_{fi}(\sigma L) = \frac{8\pi(L+1)}{\hbar L((2L+1)!!)^2}\left(\frac{E_\gamma}{\hbar c}\right)^{2L+1} B(\sigma L : J_i \rightarrow J_f) \tag{2.41}$$

where the function $B(\sigma L)$ is called the *reduced transition probability* and σ represents electric (E) or magnetic (M) multipolarity. This function is essentially the square of the multipole transition matrix element, which requires a knowledge of the wave functions of the initial and final states. For electric radiation with an electric multipole operator (Q_L), the reduced transition probability is given by [82, 50]:

$$B(E\sigma : I_i - I_f) = \frac{1}{2I_i + 1}\left|\langle f|Q_L|i\rangle\right|^2 \tag{2.42}$$

For the magnetic radiation with a magnetic multipole operator (M_L), it is given by:

$$B(M\sigma : I_i - I_f) = \frac{1}{2I_i + 1} |\langle f|M_L|i\rangle|^2 \tag{2.43}$$

Weisskopf estimates

To simplify the calculation, the transition can be assumed to be based on a single proton transition from an initial orbital state to a final state. The estimates for the decay probabilities in such cases are known as *Weisskopf estimates* which give unit scales of electric (EL) and magnetic (ML) transition rates (λ) [82] as follows:

$$\lambda(EL) \approx \frac{8\pi(L+1)}{L\left[(2L+1)!!\right]^2} \frac{e^2}{4\pi\epsilon_0\hbar c} \left(\frac{E}{\hbar c}\right)^{2L+1} \left(\frac{3}{L+3}\right)^2 cR^{2L} \tag{2.44}$$

$$\lambda(ML) \approx \frac{8\pi(L+1)}{L\left[(2L+1)!!\right]^2} \left(\mu_p - \frac{1}{L+1}\right)^2 \left(\frac{\hbar}{m_p c}\right)^2 \left(\frac{e^2}{4\pi\epsilon_0\hbar c}\right) \times \left(\frac{E}{\hbar c}\right)^{2L+1} \left(\frac{3}{L+2}\right)^2 cR^{2L-2} \tag{2.45}$$

where m_p is the single proton mass and $R = R_0 A^{1/3}$. For the first four values of L, the Weisskopf estimates of electric transition rates are as follows [83]:

$$\lambda(E1) = 1.0 \times 10^{14} A^{2/3} E^3 \tag{2.46}$$

$$\lambda(E2) = 7.3 \times 10^{7} A^{4/3} E^5 \tag{2.47}$$

$$\lambda(E3) = 34 A^2 E^7 \tag{2.48}$$

$$\lambda(E4) = 1.1 \times 10^{-5} A^{8/3} E^9 \tag{2.49}$$

For the magnetic transitions, the Weisskopf estimates of the transition rates are as follows:

$$\lambda(M1) = 5.6 \times 10^{13} E^3 \tag{2.50}$$

$$\lambda(M2) = 3.5 \times 10^{7} A^{2/3} E^5 \tag{2.51}$$

$$\lambda(M3) = 16 A^{4/3} E^7 \tag{2.52}$$

$$\lambda(M4) = 4.5 \times 10^{-6} A^2 E^9 \tag{2.53}$$

where λ is in s^{-1}, E is in MeV and A is the atomic mass number.

Internal Conversion

Internal conversion is a competing process with gamma decay. In this process the nuclear electromagnetic field interacts with an atomic electron giving sufficient energy to eject it from the atom. The kinetic energy of this electron, T_e, is related to the energy difference between the two nuclear states such that:

$$T_e = \Delta E - BE \tag{2.54}$$

where BE is the electron binding energy and ΔE is energy difference between the two nuclear states (neglecting the effect from nuclear recoil). The binding energy of the electron varies with the atomic orbital and therefore there will be internal conversion from different atomic states with different binding energies. As a result, the internal conversion electrons are labeled according to their atomic shell from which the electron is emitted (i.e. K,L,M etc.).

The emission of an internal conversion electron leaves a hole in the atomic shell. The electrons from higher shells will directly fill this vacancy and the result of this process is the emission of a characteristic X-ray (with energy equal to the difference between the initial and final states) or an Auger electron where the excitation energy is transferred to one of the outer electrons which is then ejected from the atom.

The total decay probability, λ_t, of particular nuclear state is given by:

$$\lambda_t = \lambda_\gamma + \lambda_e \tag{2.55}$$

where λ_γ is the decay probability arising from gamma emission and λ_e is the decay probability arising from internal conversion emission. This formula leads to the definition of Internal Conversion Coefficient (α):

$$\alpha = \frac{\lambda_e}{\lambda_\gamma} \tag{2.56}$$

Thus, the total decay probability λ_t is given by:

$$\lambda_t = \lambda_\gamma(1 + \alpha) \tag{2.57}$$

The total internal conversion coefficient (α_{tot}) is defined to be the sum of all individual coefficients of all atomic shells:

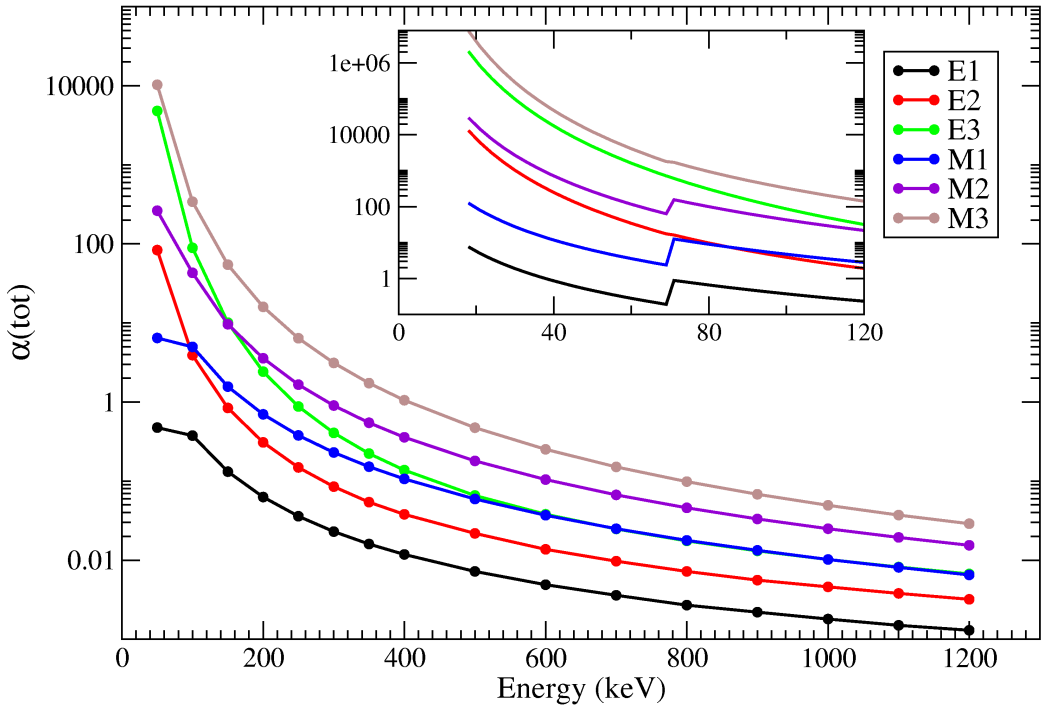

Figure 2.11: Calculated total internal conversion coefficients for different multipolarity transition in W (Z=74) as a function of γ-ray energy, using the equations from reference [84, 85].

$$\alpha_{tot} = \alpha_K + \alpha_L + \alpha_M + ... \tag{2.58}$$

The internal conversion coefficient for electric (E) and magnetic (M) multipole transitions can be calculated as follows [84, 85]:

$$\alpha(EL) \approx \frac{Z^3}{n^3}\left(\frac{L}{L+1}\right)\left(\frac{e^2}{4\pi\epsilon_0\hbar c}\right)^4\left(\frac{2m_ec^2}{E}\right)^{L+\frac{5}{2}} \tag{2.59}$$

$$\alpha(ML) \approx \frac{Z^3}{n^3}\left(\frac{e^2}{4\pi\epsilon_0\hbar c}\right)^4\left(\frac{2m_ec^2}{E}\right)^{L+\frac{3}{2}} \tag{2.60}$$

where Z is the atomic number, n is the principal quantum number of the electron shell, m_e is the electron mass, L is the multipolarity of the transition and E is the transition energy. Figure 2.11 shows the total internal conversion coefficients as a function of γ-ray energy for various multipolarity transitions in W nuclei (Z=74).

2.3 Nuclear Isomers

Excited states which are hindered in their decay are known as metastable or isomeric states. Such excited states can be hindered in their decay if there a small overlap in the wavefunction of the state and that to which it decays due to large change in shape or spin, or a small change in energy [86]. These excited states can decay by electromagnetic transitions (or conversion-electron emission), as well the modes that are available for ground-state decays [87, 88] allowed by the energetics of the specfic decay.

There are four main groups of isomer, namely shape, spin-trap, seniority and K-isomers. Shape isomers occur when there is a second minimum of the nuclear potential surface populated at large elongation of the nucleus [89]. A spin-trap isomer arises from conservation of angular momentum. The decay path of high-spin state with low excitation energy may require a relatively large change in nuclear spin (i.e. $\triangle I \geq 2$) and therefore a transition with a high multipolarity. Seniority isomers are important near nuclear closed shells [90]. Seniority (ν) is defined as the number of unpaired nucleons in a state of angular momentum J in a configuration j^n (n is the number of valence nucleons) [27, 90]. K isomers occur in near-axially symmetric deformed nuclei. This type of isomer depends on both the magnitude of the nuclear spin vector and its orientation relative to the nuclear axis of symmetry [87, 88].

2.4 The Interaction of Ions with Matter

The Coulomb force is the primary interaction of ions with matter. The positive charge of the ions interacts with the negative charge of the orbital electrons within the absorber atoms. When the charge particle interacts with the target electrons, part of its kinetic energy is transferred to the target atom electrons. This process raises the electrons to higher energy levels *(excitation)* or removes the electrons out of the atom *(ionization)*. From 2-body kinematics considerations, the maximum energy that can be transferred from the incident particle to an electron in a single collision is about 1/500 of the particle energy per nucleon [91]. Therefore, the incident particle requires many such interactions with the target electrons to decrease its energy continuously until it is finally stopped.

For those electrons which obtain a large amount of kinetic energy from the incident particle such that they are emitted from the parent atom, there is a high probability that they create further ionization. These electrons are called δ-electrons. The range of these electrons is small compared to the range of the high energy incident particles ($\sim$ 100 MeV per nucleon).

Stopping Power

The linear stopping power (S) for charged particles within a specific absorber can be defined as the ratio of the differential energy loss for the particles divided by the differential path length of these particles within the matter [91], i.e;

$$S = -\frac{dE}{dx} \tag{2.61}$$

For a specific energy loss of particles, *the Bethe-Bloch* formula is used [93, 94]:

$$-\frac{dE}{dx} = \frac{4\pi e^4 z^2}{m_0 \nu^2} NB \tag{2.62}$$

where

$$B = Z\left[ln\frac{2m_0\nu^2}{I} - ln\left(1 - \frac{\nu^2}{c^2}\right) - \frac{\nu^2}{c^2}\right] \tag{2.63}$$

and ν is the particle velocity, ze is the particle charge Q (where $Q = Z$ for fully stripped atoms), m_0 is the electron rest mass and Z is the atomic number of the absorber material. The parameter I represents the average excitation and ionization potential of the absorber. The parameter N is the electron density number of the absorber and can be calculated from [95]:

$$N = \frac{N_A.Z.\rho}{A} \tag{2.64}$$

where ρ is the density of the material, Z and A are the atomic number and mass number respectively and N_A is the Avogadro number (6.022×10^{23} Atoms/mol).

For a beam of charged particles with the same velocity interacting with a specific target material, the main factor that changes the loss of energy in Eq. (2.54) is z^2. Therefore, particles with highest charges will experience the largest energy losses per unit length.

Chapter 3

Experimental Techniques

This chapter describes the experimental techniques used to synthesise and measure the nuclei of interest described in the current thesis.

3.1 Primary Beam

In the current work a beam from the ion source at GSI (from the ^{1}H to ^{238}U) was initially accelerated by the Universal Linear Accelerator (UNILAC) to reach an energy of about 11.4 MeV/u at the output gate of this accelerator [96]. These ions can be then injected into the heavy ion SchwerIonen Synchrotron (SIS-18) accelerator which has a maximum bending power of 18 Tm from its 24 dipole magnets [97]. The ions are accelerated to relativistic energies which vary from 50 MeV/u to 1000 MeV/u. The beam is then extracted from the SIS to the focal plan of Fragment Separator (FRS) in order to generate secondary Radioactive Ion Beam (RIBs).

3.2 Projectile Fragmentation Reactions

A projectile fragmentation reaction can be described as a peripheral nuclear collision between the beam and the target nuclei. The reaction mechanism, as illustrated in figure 3.1, occurs in a two-stage process: abrasion and ablation with a distinct time difference between the two stages [98]. The abrasion stage is based on the participant-spectator picture where some nucleons (the participants) in the overlap region are abraded after the beam-target collision. The other nucleons are considered to be only spectators with respect to the moving nuclei. As a result of this reaction, both projec-

tile and target nuclei lose some nucleons with a given excitation energy proportional to the number of abraded nucleons in the overlap region (see figure 3.1).

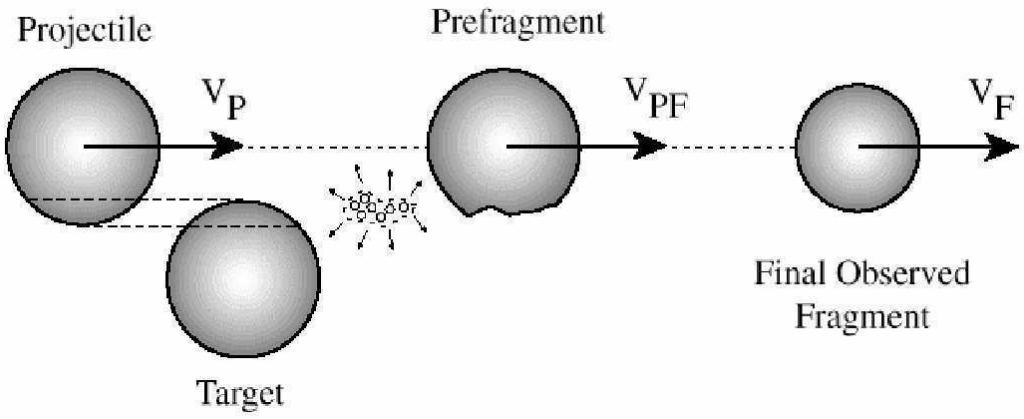

Figure 3.1: Schematic view of the projectile fragmentation reaction mechanism, taken from reference [100].

In the subsequent ablation stage, the rest of the projectile-like fragments are still travelling forward with similar velocity to the primary beam. These fragments attempt to compensate the loss of nucleons by forming a compound nucleus which de-excites and decays by light particle evaporation and (or) fission, followed by the emission of gamma rays.

3.3 The Fragment Separator at GSI (FRS)

To select certain ion species as a secondary radioactive ion beam with good isotopic separation, the Fragment Separator (FRS) is used. The FRS consists of four independent stages, each with a 30^o dipole (bending) magnet. There are also a set of quadrupole focusing magnets before and after each of the four dipole magnets to ensure the correct focusing of the secondary beam [99]. Each dipole magnet has an independent power supply in order to give maximum flexibility for different experiments to adapt the ion optical conditions. The maximum magnetic rigidity of these dipoles is about 18 Tm which makes it possible to analyse heavy-ion beams. The FRS length from the target to the final focal plane is about 69 m (see figure 3.2).

The spatial separation and identification of fragments in the FRS is based on mounting an energy degrader in the intermediate focal plane and then applying a

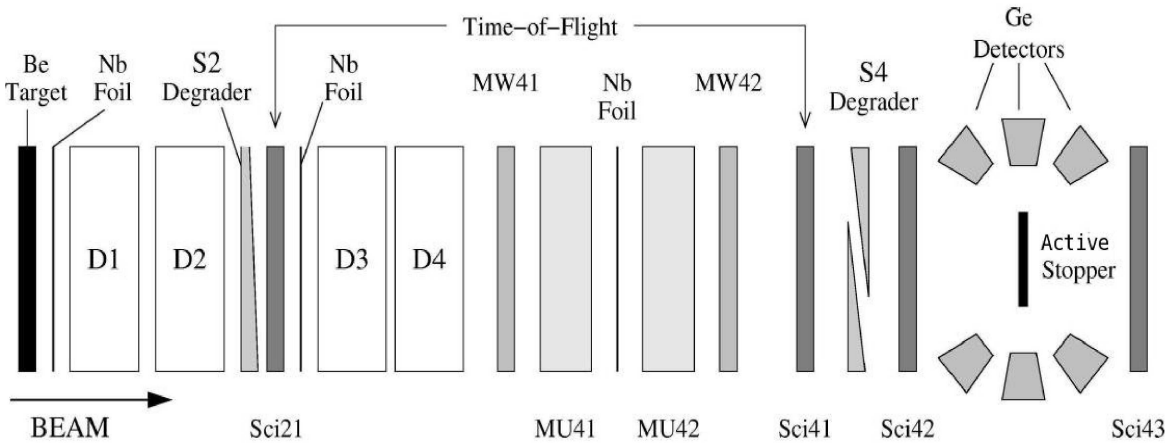

Figure 3.2: Schematic outline of the FRagment Separator (FRS) with the detectors using in the stopper RISING set-up at GSI, taken from reference [101].

magnetic field at the next two dipoles in the final focal plane with respect to the secondary beam direction. The movement of these heavy ions in a magnetic field strength, $\boldsymbol{B}$, is governed by the Lorentz force which is the force utilized on the particle in an electromagnetic field [102]:

$$\boldsymbol{F} = qe\,(\boldsymbol{E} + \boldsymbol{v} \times \boldsymbol{B}) \tag{3.1}$$

where $\boldsymbol{F}$ is the force, $\boldsymbol{E}$ is the electric field, q is the particle charge and $\boldsymbol{v}$ is the particle velocity. Hence, since the ions are deflected in the FRS magnetic field by the dipole magnets, the linear momenta of the ions (mv) is an effective way to separate the different ion species. The magnetic force depends on the charge q and the velocity $\boldsymbol{v}$:

$$F = qe(\boldsymbol{v} \times \boldsymbol{B}) \tag{3.2}$$

The circular motion of the ions as they bend through the dipole magnet is governed by $F = \dfrac{mv^2}{r}$ where r is the radius of the dipole magnet and m is the mass of the ions. Therefore, if (i) the bending radius ($r = \rho$) is known (or can be measured), (ii) the fragments are fully stripped of electrons (i.e. $q = Z$) and (iii) the mass (m) of the particles is given by γAu, then the mass-over-charge ratio $\frac{A}{Q}$ and velocity for a given value of the magnetic rigidity can be calculated to give information on the particle identification using the relation:

$$B\rho = \frac{A}{Q} \cdot \beta\gamma \cdot \frac{uc}{e} \tag{3.3}$$

where A is the mass number, Q ($\approx Z$) is the ionic charge, e is the electron charge, c is the speed of light in vacuum, u is the mass unit and the relativistic parameters β and γ are defined by:

$$\beta = \frac{v}{c} \quad and \quad \gamma = \sqrt{\frac{1}{1-\beta^2}} \tag{3.4}$$

The particle identification is achieved by measuring the time of flight (TOF) of the fragments through the FRS spectrometer to give a measure of their velocities. This is possible by assuming that the flight path of all particles is approximately equal to the distance between the target and the implantation point at the final silicon detector (see later). Thus, if the TOF is measured then the relativistic velocity parameters can be extracted using the following equation:

$$v = \frac{L}{TOF} \tag{3.5}$$

where L is the measured length of the ion path.

Another mechanism for particle identification is the fragment's energy loss as it passes through various detectors which can be used to infer the atomic number, Z, of the particles. This method requires a measurement of the energy loss in the Multiple Sampling Ionizing Chamber (MUSIC) detector. The energy deposited in the detector per unit path-length, $(\frac{-dE}{dx})$, depends on the momentum transfer to the detector electrons. From the Bethe-Bloch formula, the loss of energy is [103]:

$$\frac{-dE}{dx} = \frac{4\pi Z_1^2 e^4 N}{mc^2\beta^2}\left(ln\frac{2mc^2\beta^2}{I} + ln\gamma^2 - \beta^2\right). \tag{3.6}$$

where N is the number of target electrons per unit volume, Z_1 is the projectile atomic number and m_e is the electron rest mass. The parameter I represents the average excitation and ionization potential of the detector material, thus dE in a given thickness is proportional to Z^2.

3.4 The FRS degrader

The energy degrader is positioned in the intermediate focal plane of the FRS. It provides a reduction in the fragment energies and also can be used to measure the charge distribution of fragments between the first and second halves of the FRS. The characteristic shape of the degrader is designed in such a way that the momentum distribution is compensated after the first group of dipoles. The energy degrader system (see figure 3.3) consists of three main parts [99]:

1. A set of five plane plates of degrader.
2. A pair of wedged disc degraders.
3. A pair of wedged plate degraders.

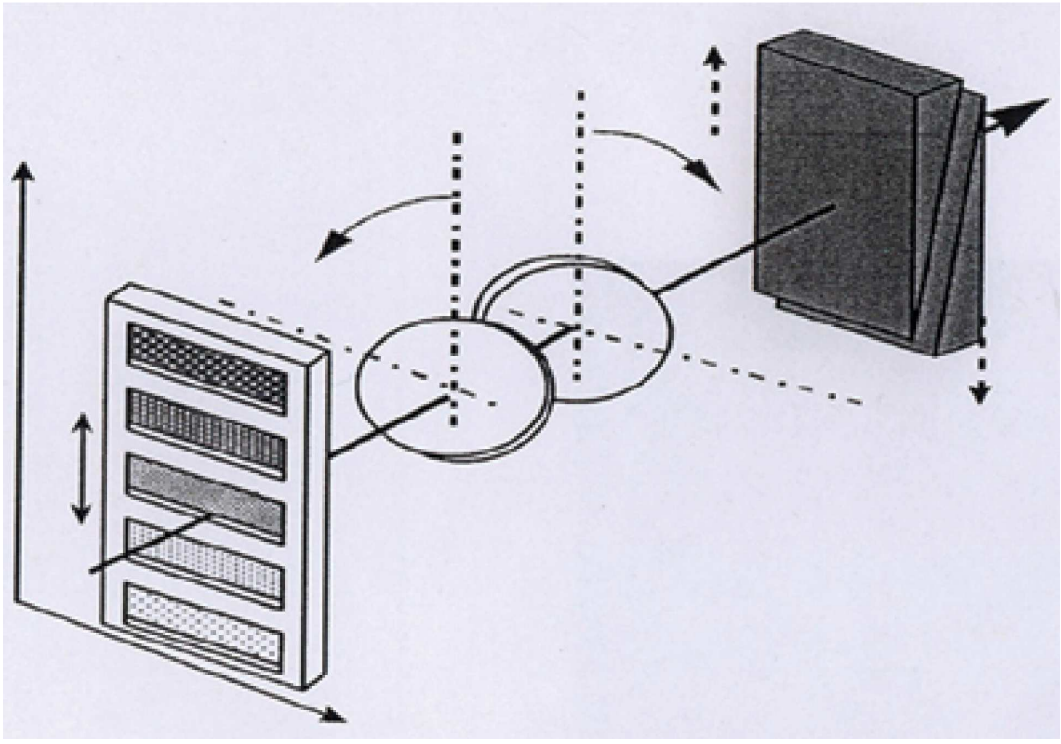

Figure 3.3: Schematic outline of the main components of the FRS degrader, taken from [104].

These three parts together form the aluminium wedge degrader which is adjustable in both thickness and angle of slope. The adjustments in the slope leads to different ion-optical conditions resulting in two operation degrader modes:

- **The achromatic degrader**

In the middle panel of the FRS, the fragment's momentum distribution is spread along the wedge. If the slope of the degrader is adjusted in such a way that the image is independent on the momentum of the ions, then the degrader acts in achromatic mode. For selected fragments the momentum decreases by a constant factor due to their energy loss in the degrader. This leads to a refocusing of the image in a small spot along the x-direction at the exit of the degrader.

- **The monoenergetic degrader**

In the monochromatic mode, the slope of the wedge whose thickness increases linearly along the direction of dispersion (x-axis) is adjusted in such a way that the difference in the thickness compensates for the momentum differences between the fragments. Therefore, all of the fragments are deflected by the second dipole stage in the same way and reach the exit of the separator with a similar energy. Figure 3.4 shows a measured example of phase-space imaging taken from reference [105]. In the experiment described in the current work, the monoenergetic mode was used to obtain the widest spatial implant distribution of the fragments with the same energy and maximum area dispersion along the active stopper detector (see Chapter 4).

In the example of the phase-space image shown in Figure 3.4, the difference between the operation of the achromatic and monenegetic degraders is plotted. This highlights the importance of selecting the correct degrader properties as the implantation will be either spatially distributed or focused at the final stopper at the end of the FRS depending on the degrader mode chosen.

3.5 Detector Operations

3.5.1 MUlti-Sampling Ionization Chambers (MUSIC)

Two MUlti-Sampling Ionization Chambers (MUSIC) were installed at the exit of the FRS to measure the energy loss of the fragments and determine their atomic numbers, Z. The MUSIC, as shown in figure 3.5, consists of four effective independent anodes each 100 mm long, a cathode and a Frisch grid. The total chamber length was 400 mm with an efficient area of (276 x 150) mm^2. The chamber was filled with

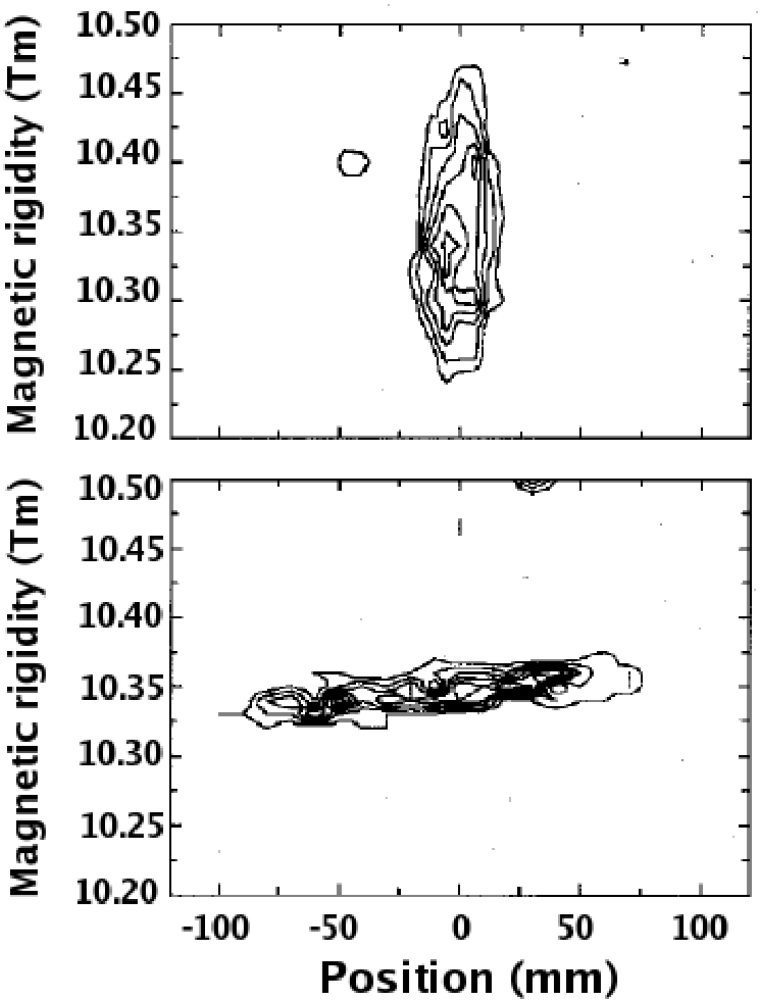

Figure 3.4: Schematic outline of the phase-space image at $S2$-position when the FRS is operated in achromatic (upper) and monoenergetic (lower) modes, taken from [105].

a mixture of 90% argon and 10% CH_4 gas at atmospheric pressure and continuously pumped to preserve the detection qualities. The entrance and exit windows of the chamber were made of 25 μm Kapton foils and each foil was covered by an aluminium layer of 40 (g/cm^2) to decrease the secondary interactions of the fragments [106].

The MUSIC operates like any ionization chamber in generating electron-ion pairs when ionizing radiation passes through the gas filled space between the electrodes. Each of the four energy loss signals through the four anodes was coupled to a charge sensitive preamplifier. The output signal of each preamplifier received a further amplification and these were averaged with the resulting value corresponding to the energy loss in the chamber.

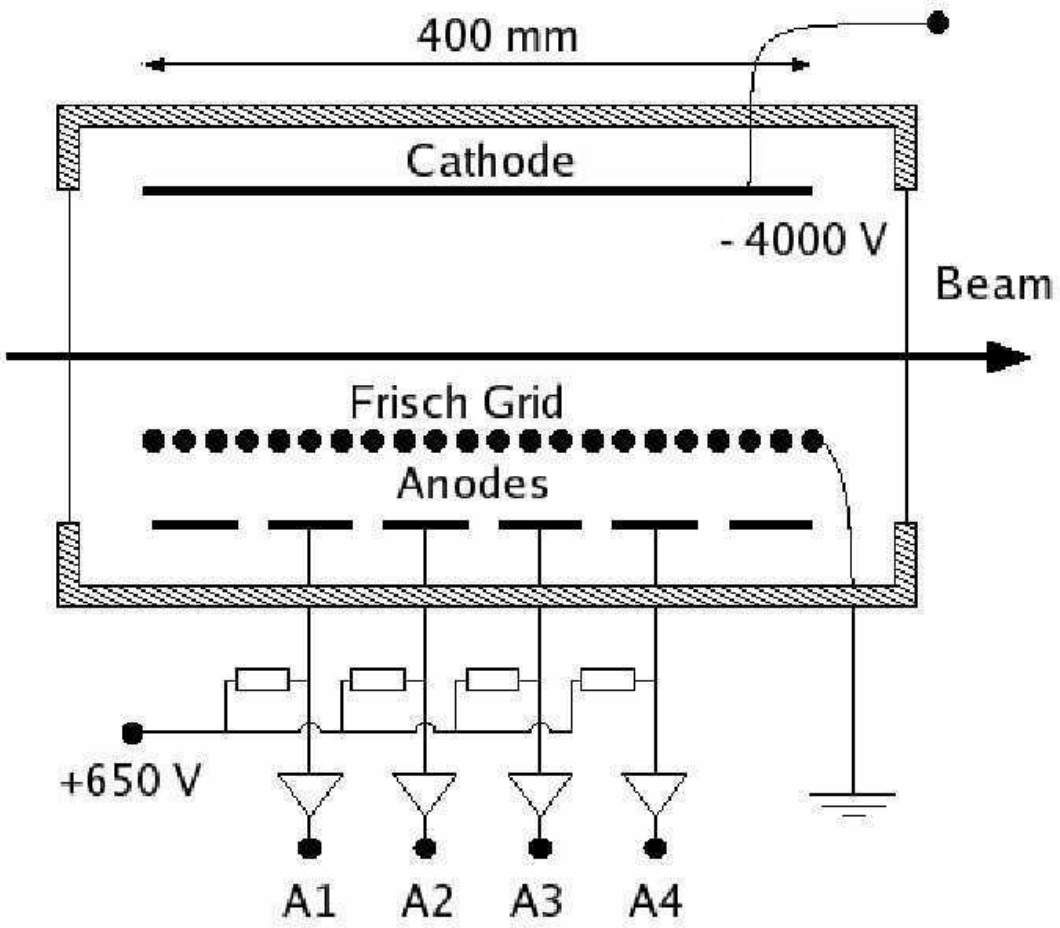

Figure 3.5: Schematic outline of a Multiple-Sampling Ionization Chamber (MUSIC), taken from [106].

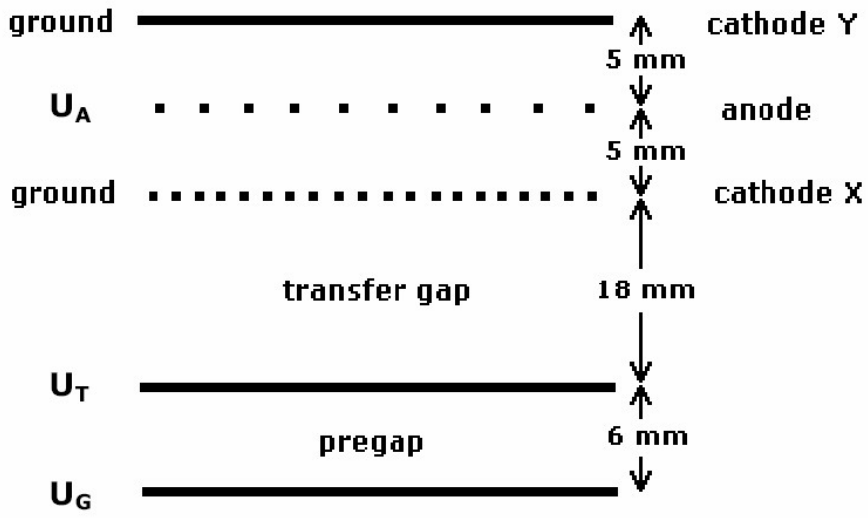

Figure 3.6: Schematic outline of a MultiWire Proportional Counter (MWPC), taken from [108].

3.5.2 The Multi Wire Chamber (MW)

The Multi-Wire detector is a proportional counter which consists of five parallel sets of wires, as shown in figure 3.6. The active area of the MW detector is (200 × 200) mm^2 and the window is made of a thin Kapton. The planar anode A, was 20 μm thick and made of gold-plated tungsten while the cathodes X and Y were 50 μm thick and made of the same material. Two planar electrodes G and T were added with a spacing between them of 6 mm and used with light ions. The chamber was filled with a gas mixture of Argon, CO_2 and alcohol at atmospheric pressure. In the work described in this thesis, two Multi Wire chambers were used and positioned in the last stage of the FRS [107].

When the charge particles pass through the MW chamber, the anode A collects the electron avalanche and generates positive signals in the adjacent wires of the X and Y cathodes. The readout of signals are used to determine the x and y position of the fragments using the following equations:

$$x = \alpha_x(t_{xL} - t_{xR}) + \beta_x, \qquad y = \alpha_y(t_{yU} - t_{yD}) + \beta_y \tag{3.7}$$

where t_{xL} (t_{yD}) and t_{xR} (t_{yU}) are the charge collections from the x-left and x-right (y-up and y-down) ends of the cathode wires, and α and β are the calibration factors and offsets respectively. Note, the MW detector is only used in the primary beam

calibration stage of the experiment as its wire structure can cause inhomogeneities in the secondary beam.

3.5.3 The Plastic Scintillators

The scintillators used in the current work consist of a plastic organic material called $BC420$ (from the Bicron company) which is characterized by high light output and a fast time response of 1.5 ns [109]. The light signals produced by the charged particles are guided to two photomultipliers (Hamamatsu $HM2431$) which are mounted to the left and right of the beam direction. In the current work, four scintillator detectors (Sci21, Sci41, Sci42 and Sci43) were placed at the intermediate and the final focal planes. These scintillators provided time of flight (TOF) and position information from the time differences of the signals of the corresponding left and right photomultiplier tubes. Figure 3.7 gives a schematic diagram of the scintillator detectors used in the current work.

The output signal from the two photomultiplier tubes were used to start and stop a time-to-amplitude-converter (TAC). The analog output of the TAC was then read by an analog-to-digital-converter (ADC). When the ions signals pass through Sci21 (at time $T2$) and through Sci41 (at time $T4$), the distance between these two detectors ($\sim$35 m) can be used to determine the time of flight (TOF) for each ion. However, there are some delays in the arriving signals from the Sci21 due to travel through longer electronic cables. This delay time (T_0) is chosen in such a way that $T2 + T_0 > T4$.

The time of flight (TOF^*) measurement is taken as the average of the right and left times of flight TOF^*_L and TOF^*_R as follows:

$$TOF^* = \frac{(TOF^*_L \cdot \alpha_L) + (TOF^*_R \cdot \alpha_R)}{2} = T_{S2} + T_0 - T_{S4} \tag{3.8}$$

where α_L and α_R are calibration factors which transform the left and right T from raw amplitude to nanoseconds. The true time of flight (TOF) is then equal to:

$$TOF = T_0 - TOF^* = T_{S4} - T_{S2} = \frac{d_0}{v} \tag{3.9}$$

where d_0 and v are the path length and velocity of the fragment respectively.

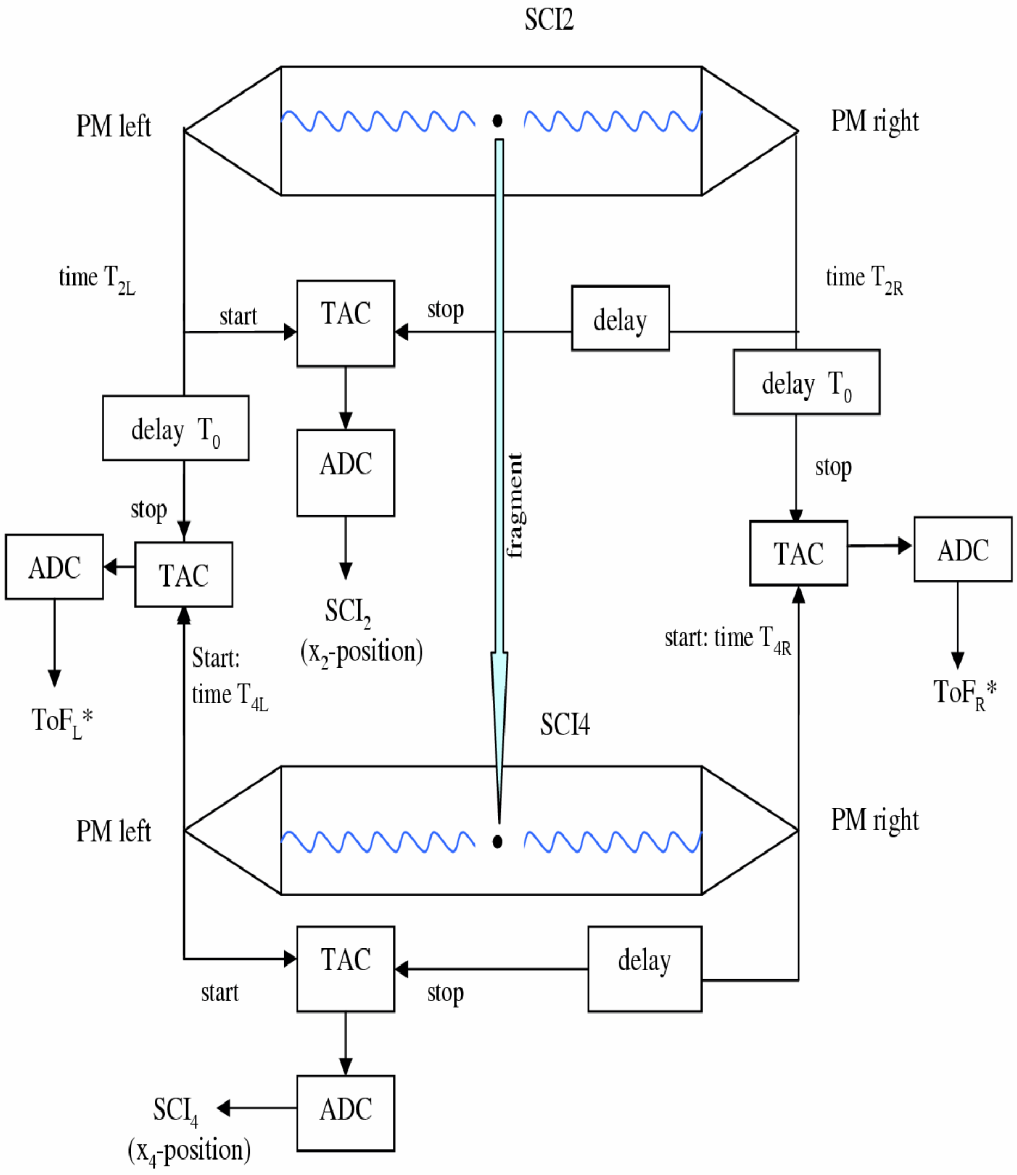

Figure 3.7: Schematic diagram of the main components of the scintillator detector, taken from reference [110].

3.6 Gamma-ray Spectroscopy

3.6.1 Semiconductor Materials

A semiconductor material is packed into separate energy bands and an electron must be confined to one of these bands [111]. The lowest energy band is called the valence band which, in a perfect idealized semiconductor is full of electrons that are bound to the lattice sites within the crystal. The next highest energy band is called the conduction band and in a perfect semiconductor represents an empty band (at temperature T=0 K) where the electrons are free to migrate through the crystal. These two energy bands are separated by energy gap, called the bandgap. The size of this gap is the main factor of classifying the material as semiconductor or as insulator which is about 1 eV in a semiconductor and 5 eV in insulator [91].

If gamma-ray photon enters the detector and is photoelectrically absorbed by the semiconductor detector crystal, this will produce a photoelectron that jumps from the valence band (leaving a vacancy or hole) to the conduction band of the crystal. This means that an extra electron is still in the conduction band and an extra hole in the valence band. Applying an electric field across the region causes the negatively charged electrons to move in the opposite direction to the effective movement of the positively charged holes. Then the charge released by the ionization can be collected and the presence of gamma rays recorded [91].

The value of the energy gap is not constant and changes with temperature [91]. As a general rule for semiconductor materials, the energy gap initially increases linearly as the temperature decreases. However, at very low temperatures, the energy gap reaches a constant value. Therefore, when the temperature is greater than absolute zero, the electrons in the crystal lattice will share thermal energy, giving a probability that an electron can be thermally excited across the band gap into the conduction band. The probability per unit time that an electron-hole pair thermally generated is given by a Boltzmann function [112]:

$$P(T) = CT^{\frac{3}{2}} exp\left(-\frac{E_g}{2\kappa T}\right) \tag{3.10}$$

where T is the absolute temperature in kelvin, E_g is the energy band gap, κ is $Boltzmann's$ constant (=1.38 $\times 10^{-23} JK^{-1}$) and C is a probability constant charac-

teristic of the material.

In the case of semiconductor materials, the energy gap is small and gives a large probability of thermal excitation, creating unwanted noise at room temperature ($\sim$ 300 K). This thermal noise can be significantly reduced by cooling the semiconductor crystal to the liquid nitrogen temperature ($\sim$ 77 K) [113].

To control the electrical conduction in semiconductors, a small a mount of impurities are added to the lattice in a process called *doping*. The idea of this process is to increase the number of the charge carriers (electrons or holes) by adding a material with free charge carriers. If the negative charge carriers (electrons) in the semiconductor atoms are more than the positive charge carries (holes), the material is called an *n-type* semiconductor. The inverse situation is called an p-type semiconductor. When n-type and p-type materials are combined together, the electrons from the n-type will diffuse from the n-type to the p-type and the holes will diffuse to the opposite direction. This diffusion produce an equilibrium of the charge carriers concentration, creating a volume called the depletion region.

3.6.2 Germanium Detectors

Germanium is the most common semiconductor material used for gamma spectroscopy. In the 1960, the lithium drift technique started because of the impurity of the Ge at that time which led to small depth for the depletion region. The main disadvantage of that type of detector was that it had to be kept cold at all times otherwise the lithium migrated outside the crystal lattice. By decreasing the impurity in the germanium crystal, an active volume can be obtained that was comparable and even larger to those available in Ge(Li) detector. These detectors are called intrinsic germanium or high purity germanium detectors. The major advantage of this type of detector is that room-temperature storage is now acceptable because of the absence of lithium drifting [113].

The energy required to create an electron-hole pair in HPGe detectors is typically 3-4 eV which is ten times less than the energy required to create ion pair in typical gas-filled detectors [111]. This has two consequences. Firstly, there is a small statistical fluctuation in the number of charge carriers per pulse. Secondly, as a result of the large number of charges, there is an excellent signal to noise ratio and therefore a good

energy resolution [91].

3.6.3 Photon Interaction in Matter

Gamma rays can interact with matter via three main interaction mechanisms: photoelectric effect, Compton scattering and pair production.

Photoelectric effect

The incident photon interacts with the absorber atom especially with the bounding atomic electrons in the inner K and L shells [91, 113]. As a result, the photon disappears and its energy transfers to the electron which is ejected as free electron with kinetic energy E_e:

$$E_e = h\nu - E_b \tag{3.11}$$

where E_b is the binding energy of the electron, h is the Planck's constant and ν is the frequency of the incident photon.

The vacancy of that electron is directly filled by another electron from outer shell. Therefore an X-ray or Auger electron will be emitted because of the different energy between these two shells. The photoelectric effect is the major interaction of γ rays of relativity low (<200 keV) energy [91]. In addition, the photoelectric effect cross section τ depends on the atomic number of the absorber material Z and the photon energy E_γ:

$$\tau \approx \frac{Z^n}{E^{3.5}} \tag{3.12}$$

where Z is the atomic number and n is a number between 4 and 5 [91].

Compton Scattering

This interaction is a collision between a γ photon and a free atomic electron. The γ-ray photon transfers a part of its energy to that electron and scattering at lower energy in various angles. The photon energy after scattering depends on the angle of scattering and can be defined by the following equation:

$$E_{\gamma'} = \frac{E_\gamma}{1 + \frac{E_\gamma}{m_0 c^2}\left(1 - cos\theta\right)} \tag{3.13}$$

where E_γ and $E_{\gamma'}$ are the energies of the γ-ray before and after the collision, m_0 is the rest mass of an electron, c is the speed of the light in a vacuum and θ is the scatter angle of the γ ray. Therefore, the kinetic energy E_e of the recoil electron is given by the following equation [91]:

$$E_e = E_\gamma - E_{\gamma'} \tag{3.14}$$

The minimum and maximum energies of the scattered photon are obtained when $\theta = \pi$ and 0 respectively. Furthermore, the cross section, σ, of the Compton scattering decreases with increasing the photon energy. The Compton-scattering cross section is also increased when the number of the available scattering target electrons (the atomic number Z) is increased [91, 113].

The Klein-Nishina formula for the differential cross section provides an accurate prediction of the probability for the photon to scatter at an angle θ into the solid angle dΩ [91]:

$$\frac{d\sigma}{d\Omega} = Z r_0^2 \left(\frac{1}{1 + \alpha\left(1 - cos\theta\right)}\right)^2 \left(\frac{1 + cos^2\theta}{2}\right) \left(1 + \frac{\alpha^2\left(1 - cos\theta\right)^2}{\left(1 + cos^2\theta\right)\left[1 + \alpha\left(1 - cos\theta\right)\right]}\right) \tag{3.15}$$

where α is the photon energy in units of the electron rest mass ($\alpha = E_\gamma$ / m_0 c^2) and r_0 is the classical electron radius.

Pair Production

For incident γ rays of energies greater than 1.02 MeV (in practice the photon's energies should be several MeV), pair production is possible [91]. In the interaction, the photon disappears and a pair of electron-positron is produced. Each of these two particles is shared the photon energy as described by the following equation:

$$E_{e^-} + E_{e^+} = E_\gamma - 2m_0 c^2 \tag{3.16}$$

where, m_0 is the rest mass of an electron or positron. The positron will subsequently annihilate (i.e. combine with an atomic electron) and two photons are produced

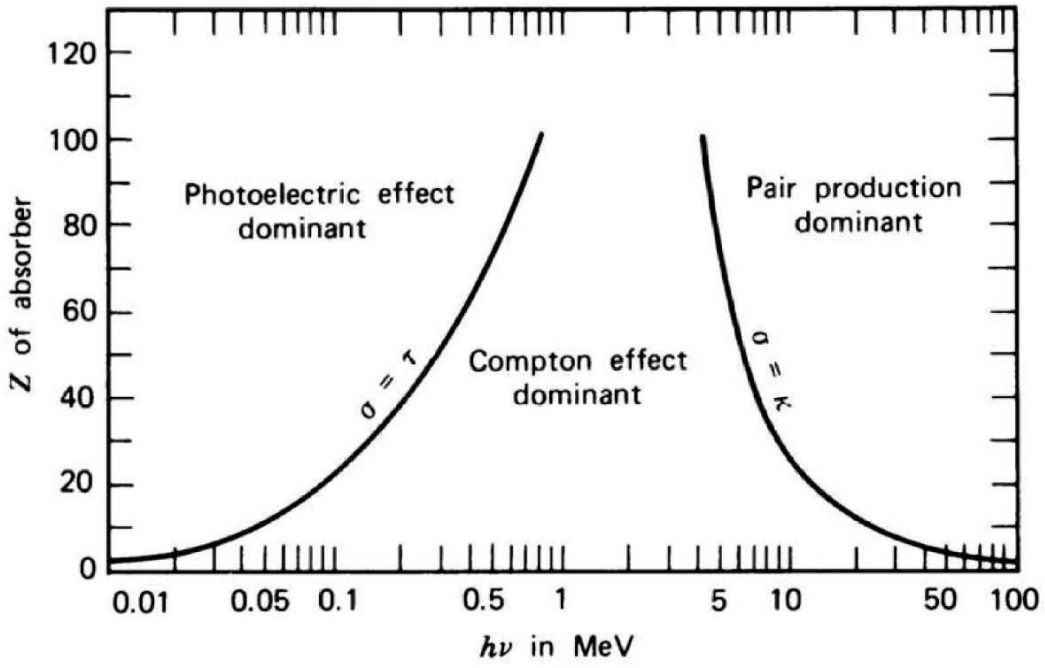

Figure 3.8: The relative importance of the three major gamma interactions, taken from reference [91].

with an energy 511 keV.

The relative importance of these three main interactions for different absorber materials and gamma-ray energies is illustrated in figure 3.8. The left-handside line reflects the energy at which the probability of photoelectric and Compton scattering interactions are equally probable as a function of the absorber atomic number. Above the line the probability of photoelectric effect is dominant and below it the Compton scattering is dominant. The right-handside line reflects the energy at which the probability of Compton scattering and pair production interactions are equally probable [91, 113].

The attenuation coefficient or cross-section gives the probability of removal of the gamma photon from the beam by one of the interaction processes (photoelectric effect, Compton scattering and pair production) per unit path length [91]. The sum of these probabilities of interactions per unit length is called the linear attenuation coefficient (μ), i.e;

$$\mu = \tau(photoelectric) + \sigma(Compton) + \kappa(Pair - Production) \tag{3.17}$$

The linear attenuation coefficient, μ varies with the absorber density even for the

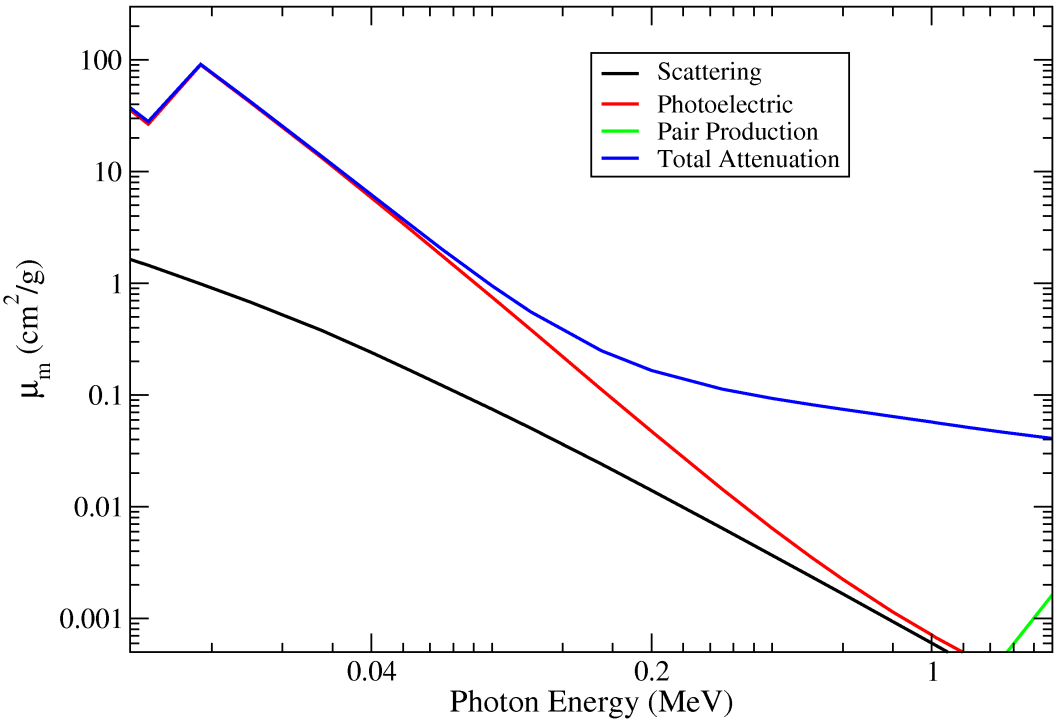

Figure 3.9: Photon interaction cross section for germanium at energies from 0.01 to 2 MeV. The data are taken from reference [115].

same material [91], therefore, the mass attenuation coefficient (μ_m) is also widely used:

$$\mu_m = \frac{\mu}{\rho} \tag{3.18}$$

where ρ is the absorber density. Figure 3.9 shows the photon cross sections for scattering, photoelectric absorption and pair production, as well as the total attenuation coefficient for the germanium (Z=32) within range of photon energies from 0.01 to 2 MeV [115].

3.6.4 RISING Array

RISING (Rare ISotope INvestigation at GSI) [116] is a combination of the FRS at GSI and the 15 former EUROBALL CLUSTER germanium detectors [19]. This project is supported by an International *Memorandum of Understanding* between centres in the UK, Germany, France, Sweden, Denmark, Poland, Belgium and Italy. Figure 3.10 is a photograph of the RISING Stopped Beam Germanium array at the final focal plane of the FRS.

The RISING array consists of 15 CLUSTER detectors, each consisting of seven

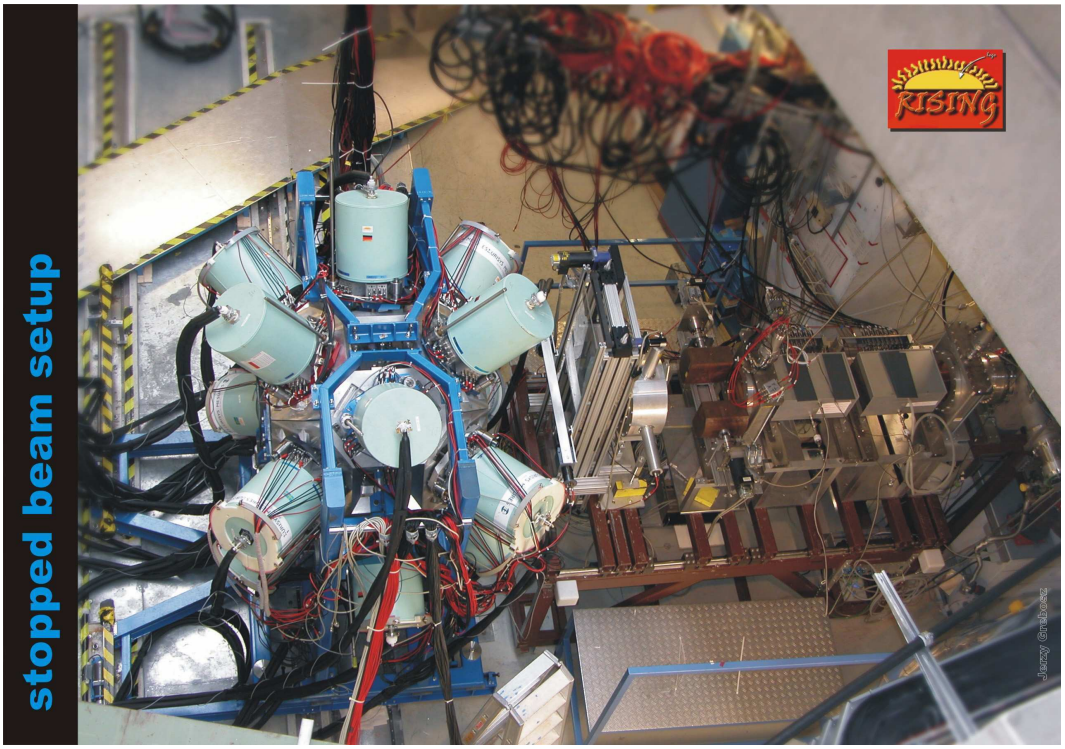

Figure 3.10: Photograph of the Stopped RISING array coupled to the RISING beamline at the focal plane of the FRS.

high efficiency individual germanium crystals. The detectors were positioned in a compact configuration of three rings of five detectors at three different angles 51^0, 90^0 and 129^0 relative to the secondary beam axis. The intrinsic photopeak efficiency of these crystals was measured using two sources positioned in the centre of the array. One was a mixed source of ^{241}Am,^{137}Cs and ^{60}Co, while the other was a ^{133}Ba source. The intrinsic photopeak efficiency found to be approximately 14% for the ^{137}Cs decay line at 662 keV (see figure 3.11). In the current work, these detectors surrounded an active stopper of three silicon detectors [117]. Each germanium crystal was connected with two parallel output preamplifiers which were sent to two separate branches of the data acquisition. The first output was a fully digital branch which provides the input signal from 105 channels within the 30 digital Gamma Finder (DGF-4C) modules [43]. The second preamplifier in each crystal provided the timing output signals [43].

Electronics

For each RISING germanium crystal, there were two individual preamplifiers connected with two separate data acquisition branches [19, 118]. One processed the

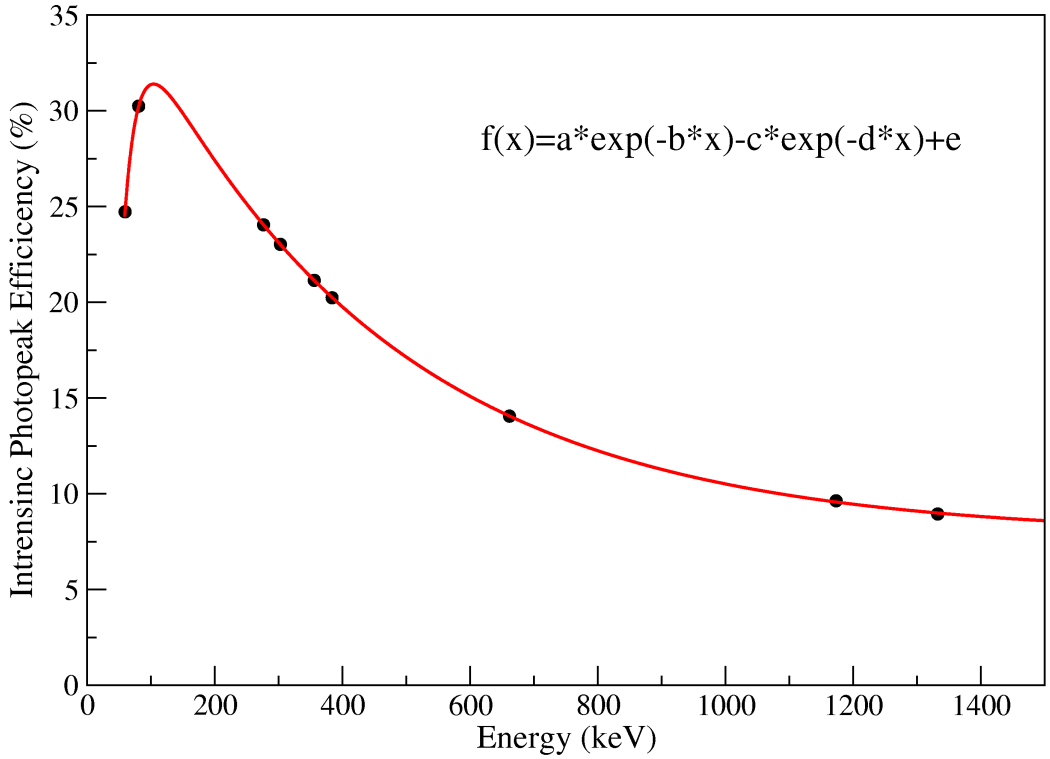

Figure 3.11: The measured intrinsic photopeak efficiency for the germanium detectors used in the Stopped RISING array at GSI.

energy signals using 30×4 channel Digital Gamma Finder (DGF-4C) modules [119]. The timing signal of each DGF channel trigger was validated by a fast timing plastic scintillator detector positioned at the final focal plan of the FRS. The internal clock of the DGF provided a 25 ns timing resolution and the maximum coincidence window between the fast plastic scintillator and subsequent γ ray was 400 μs.

The output signal of the second RISING preamplifier was sent to an analogue timing branch of a standard TFA-CFD-TDC timing circuit. Two ranges of TDC timing were used, a short range (1 s full range with a 0.31 ns/channel step) and a long range (up to 800 s with a 0.73 ns/channel step). The short range timing provided the ability of identifying shorter-lived isomers (τ ∼10 ns) [19, 118].

3.7 The RISING Active Stopper

A new beta counting system was used in the experiment described in this thesis which enabled a position correlation between the exotic mother nuclei produced in the fragmentation reaction and the subsequent β^- particles emitted following their decays.

This counter was made up to three Double-Sided Silicon-Strip Detectors (DSSSDs) positioned at the final focus of the FRS to act as an "active" stopper of the secondary beam [42, 120]. Figure 3.12 shows a photograph of the front and back sides of the DSSSD.

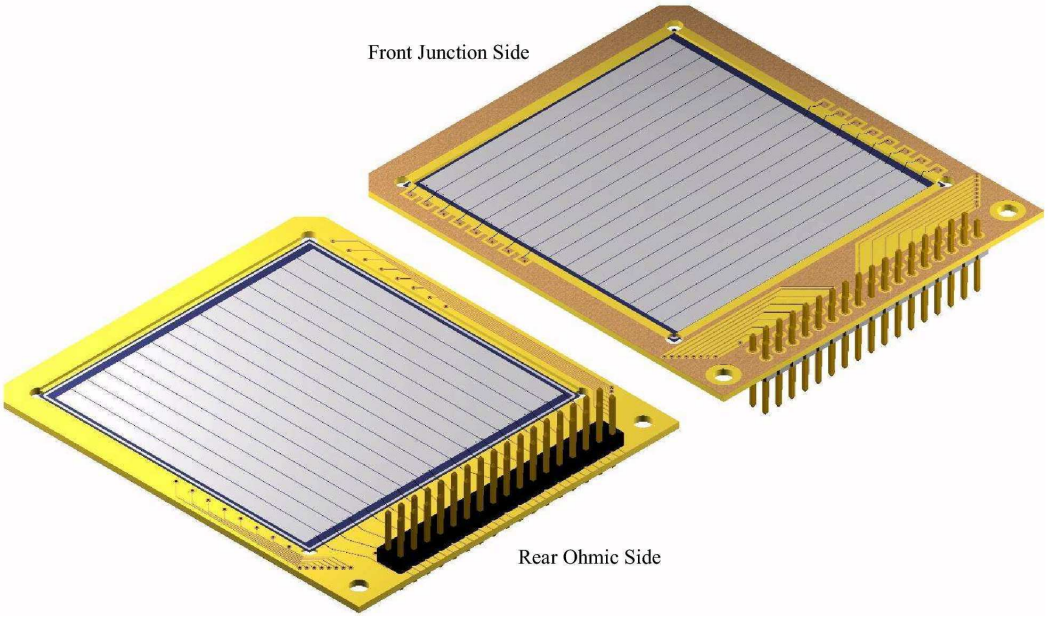

Figure 3.12: Schematic of front and back sides of W1(DS)-1000 double-sided silicon strip detector (DSSSD) from the Micron Semiconductor Ltd, taken from reference [121].

In the experiment described in this thesis, the active stopper consisted of three, 5 cm $\times$ 5 cm, model $W1(DS) - 1000$ DC coupled double-sided silicon strip detector made by Micron Semiconductor LTD [121]. Each single DSSSD consisted of 16 front and back strips, each of 3 mm width. These strips provide a single detector with 256 (=16$\times$16) separate pixels and the three-element full active stopper of 768 pixels in total. The thickness of the DSSSD detectors were 1 mm each, which was enough to ensure stopping all the secondary ions of a specific species when the FRS was operated in the monochromatic mode. Figure 3.13 shows a photograph of three DSSSD detectors positioned in the detector holder. Figure 3.14 shows the active stopper surrounded by the germanium cluster detectors in the current work.

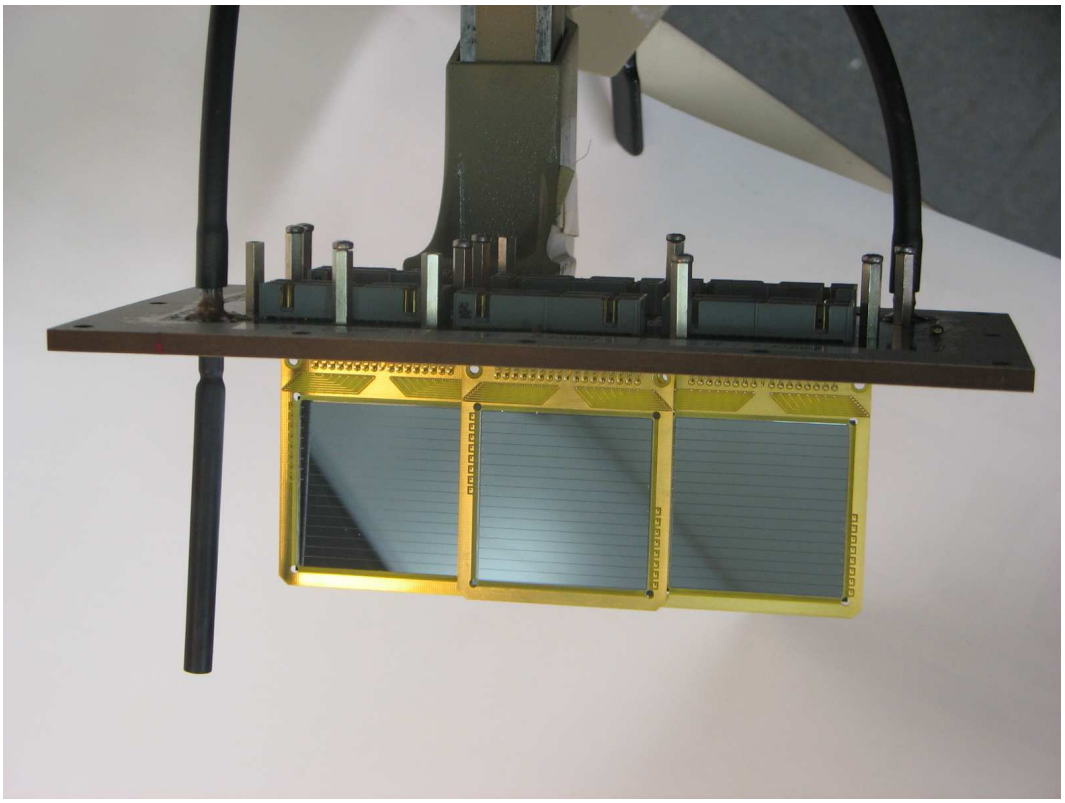

Figure 3.13: A photograph showing how the three DSSSD detectors can be positioned inside the detector holder to ensure a maximum area covered at the final focal plane of the FRS.

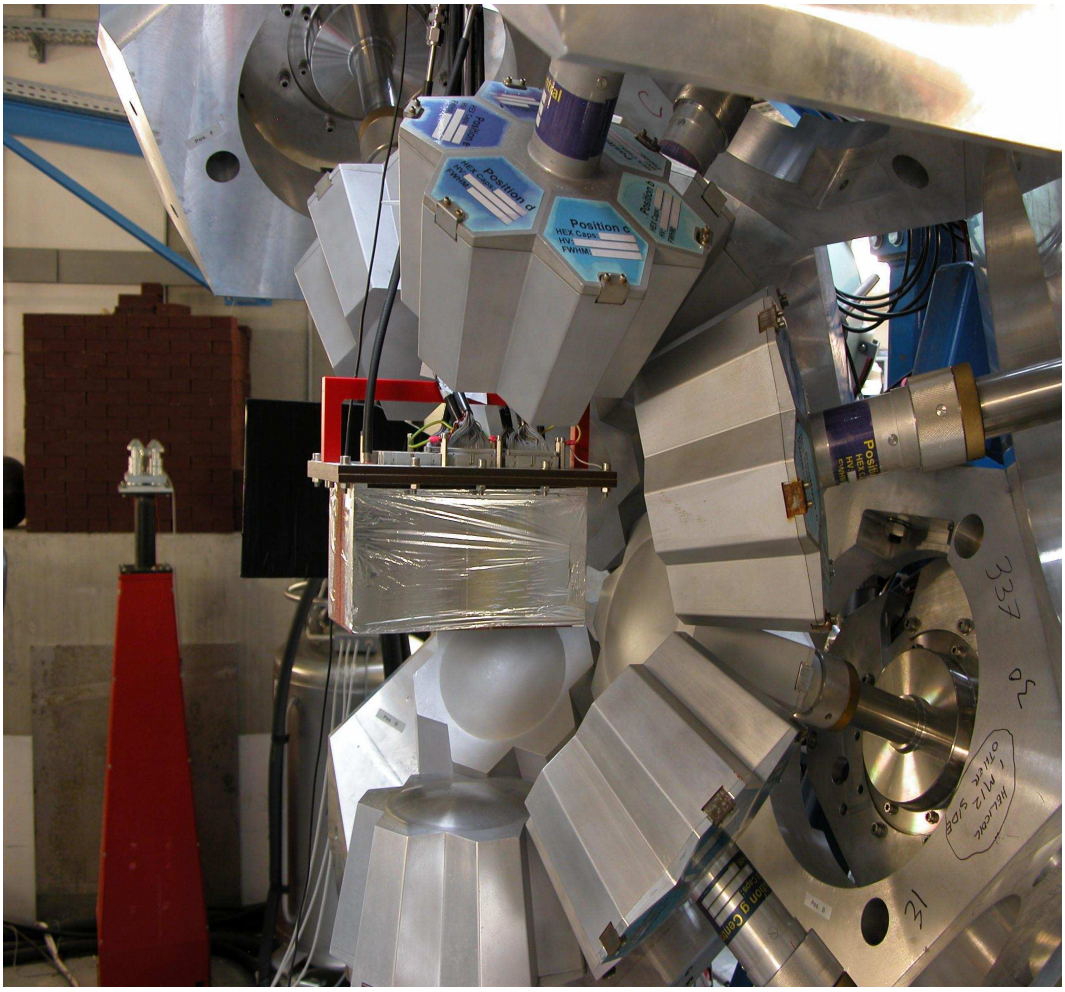

Figure 3.14: A photograph of the active stopper surrounded by the RISING germanium clusters.

Chapter 4

Experimental Details

4.1 Experimental Settings

In the experiment described in this thesis, a primary beam of ^{208}Pb was accelerated to an energy of 1 GeV per nucleon with intensities between 10^8 to 10^9 ion/sec and then impinged on a natural beryllium target of 2446 mg/cm^2 thickness. The typical time length per spill was about 1 second with a typical repetition period varied between 15 to 20 seconds depending on the FRS setting used. During the experiment seven different FRS transmission settings were studied corresponding to centering on the following ion species: ^{190}Ta, ^{192}Ta, ^{194}Re, ^{203}Au, ^{204}Au, ^{198}Ir and ^{202}Ir. Two of these FRS transmission settings are discussed in this thesis, namely those centred on ^{190}Ta and ^{192}Ta ions. Table 4.1 gives a summary of the experimental parameters for these two FRS settings.

Table 4.1: Experimental parameters for the two main FRS settings used in the current work, centred on the transmissions of ^{190}Ta and ^{192}Ta ions.

Setting	Bρ_1 (Tm)	Bρ_2 (Tm)	S2 degrader Thickness (mg/cm^2)	S4 degrader Thickness (mg/cm^2)	Beam Current (p/spill)	Spill Repetition (s)	Total Time of Collection
^{190}Ta	13.0805	9.5915	5050	3320	10^8	20	62 hours
^{192}Ta	13.2285	9.7479	5050	3450	10^9	15	66 hours

4.2 Fragment Cross Sections

To estimate the production rates for the secondary-beam fragments, the EPAX parametrisation was used [122]. Table 4.2 shows an estimate of the Ta isotope production cross sections following projectile fragmentation reactions. These nuclei are the heaviest, neutron-rich Ta isotopes produced to date and their predicted production cross sections drop with increasing mass number. The predicted cross sections of the fully stripped ions (Ta, W and Re) are shown in figure 4.1.

Table 4.2: The cross sections predicted by EPAX [123] for the neutron-rich Ta isotopes between a 1 GeV per nucleon ^{208}Pb on a target ^{9}Be.

Nucleus	Cross section (b)
^{188}Ta	1.2×10^{-06}
^{189}Ta	5.1×10^{-07}
^{190}Ta	2.0×10^{-07}
^{191}Ta	7.2×10^{-08}
^{192}Ta	2.2×10^{-08}
^{193}Ta	6.1×10^{-09}
^{194}Ta	1.4×10^{-09}

4.3 Identification of the reaction products

4.3.1 Selection of projectile fragments

After the interaction of the primary beam (^{208}Pb) with the target (^{9}Be) at the entrance of the FRagment Separator (FRS), a cocktail of secondary beams was produced. The beam reaction products can be broadly classified as either fission fragments or projectile fragments. Figure 4.2 shows the energy loss in one of the MUSIC detectors for these two fragment types which are transmitted to the final focal plane of the FRS for the FRS settings centred on: (i) ^{190}Ta and (ii) ^{192}Ta. The reaction products of interest in the current work were the projectile fragmentation residues. The fission

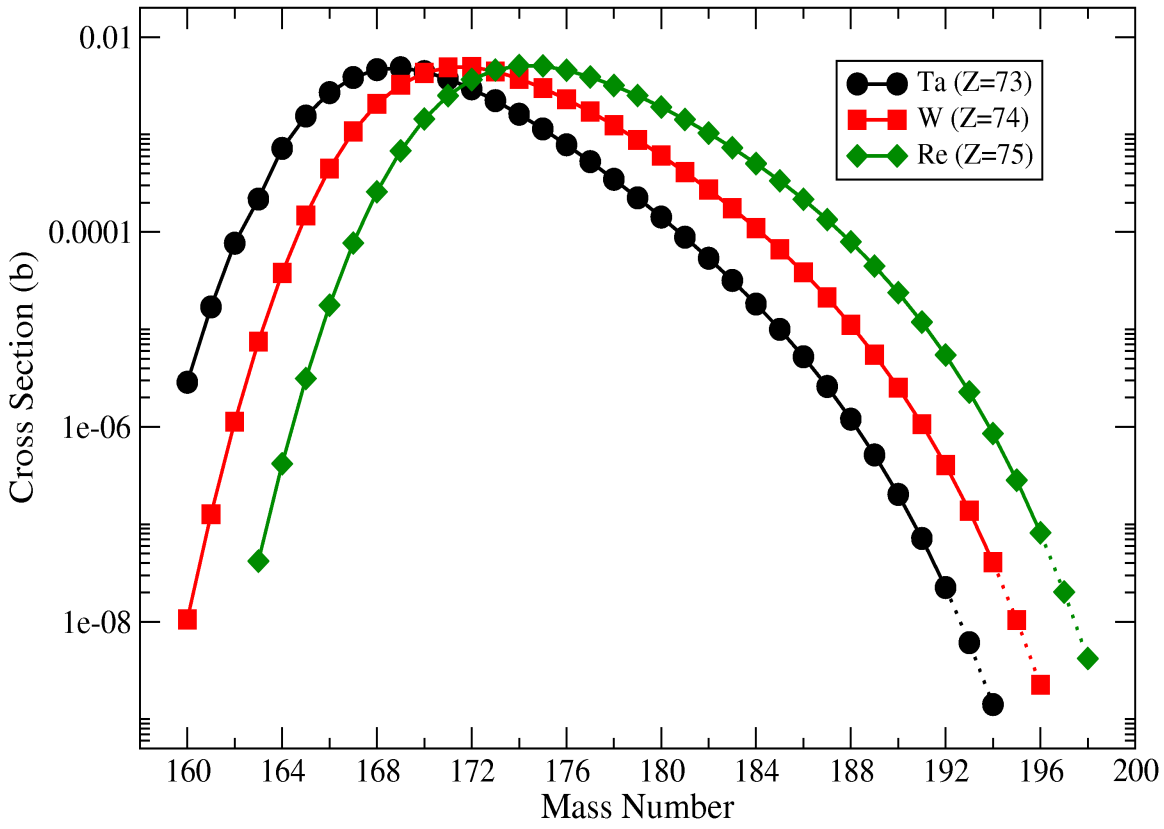

Figure 4.1: Cross sections of the Ta, W and Re isotopes predicted by the EPAX program [123] for a Pb primary beam.

fragments were excluded from the offline analysis using software gates (see later). For the final particle identification process, offline software conditions were applied to the signals from the Multi-Wire detectors (MW41 and MW42) which surrounded the two MUSIC detectors and were used for position calibration. These conditions were applied to both photomultipliers (x and y) of MW41 and MW42 to ensure proper offline corrections and selection of projectile fragments.

4.3.2 Scintillator Sci43 Veto Detector

The scintillator Sci43 detector was positioned behind the active stopper and used as a veto detector to ensure that all the selected ions are stopped in the RISING active stopper. The light particle products (with lower Z) after the interaction with degrader at S4 will pass through the active stopper and register a signal in scintillator Sci43. The interaction of these particles with the active stopper can also produce some prompt gamma rays which are classified as unwanted background events. Therefore,

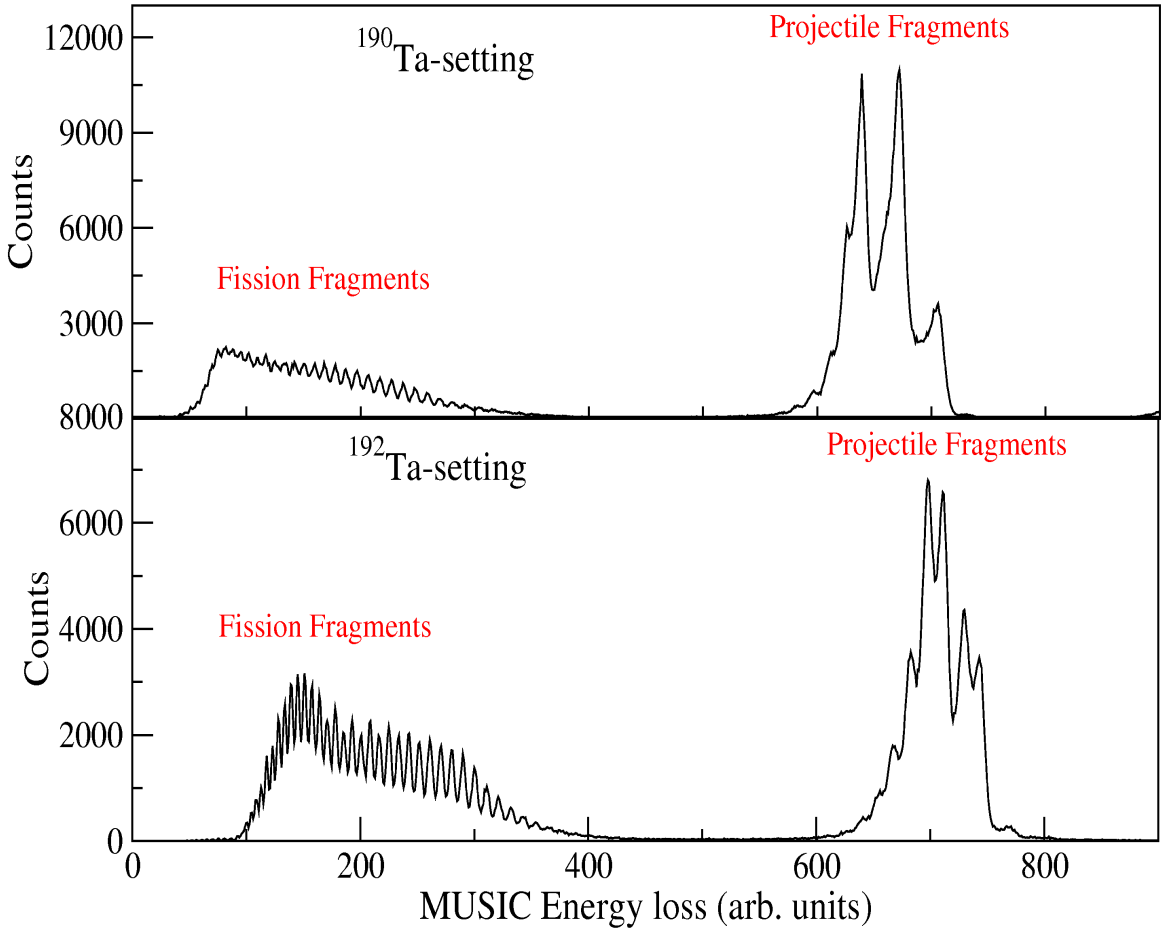

Figure 4.2: Energy loss measurements in the MUSIC detector for the fission and projectile fragments from the ^{190}Ta (upper) and ^{192}Ta (lower) centred settings.

all the gamma rays coming from the interactions associated with these ions should be software vetoed in the offline data analysis. Figure 4.3 shows the energy loss in the scintillator Sci43 "veto" detector. The spike at the beginning of the spectrum arises from the pulser connected to this detector, which gave a signal to show that the veto scintillator detector was working properly.

4.4 Particle Identification

4.4.1 Charge States

The ions transmitted through the FRS are distributed into three main charge state groups: (i) the fully-stripped ions which are assumed to be predominantly ions which are fully stripped in both halves of the FRS; (ii) the H-like ions (i.e. those

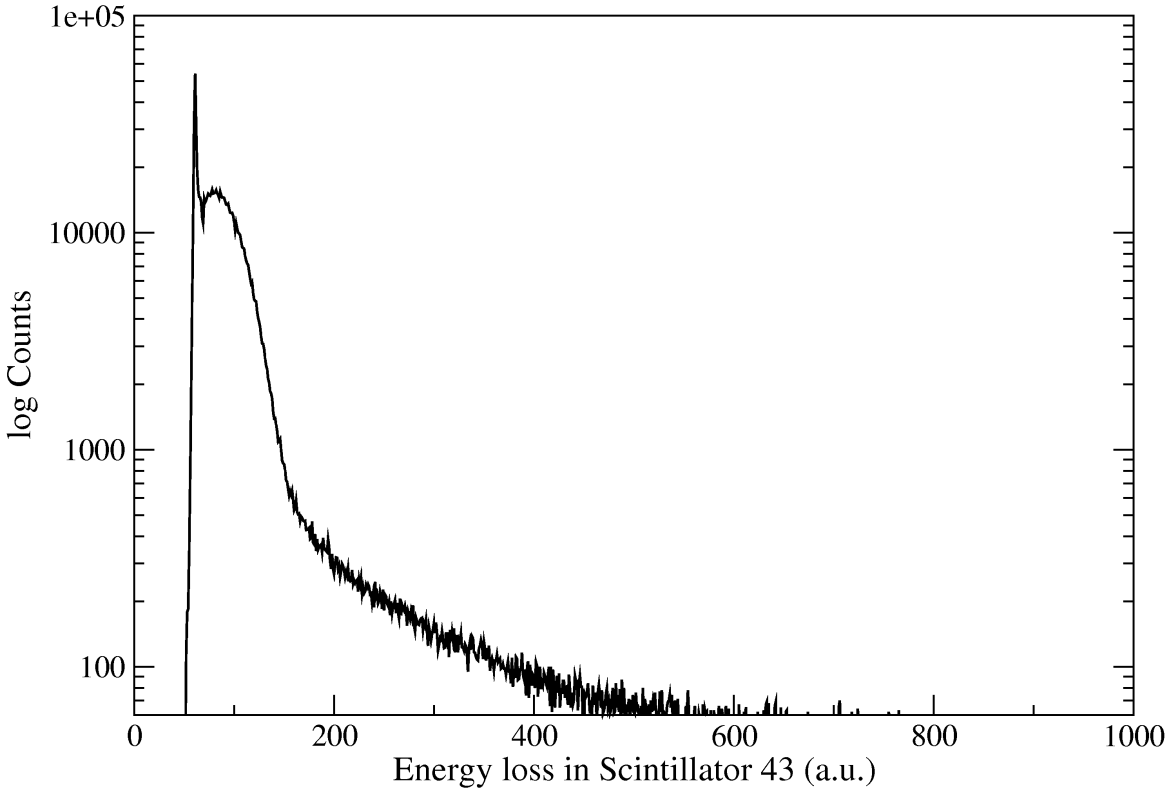

Figure 4.3: Energy loss measurements in the veto scintillator Sci43 at the end of focal plane from the ^{190}Ta and ^{192}Ta settings. The strong peak on the extreme left-hand side arises from a pulser that was connected to scintillator Sci43.

which pick up a single electron), which are assumed to be predominantly ions which are fully stripped in the first part of the FRS and H-like ions in the second half of the FRS; and (iii) the He-like (i.e. pick up of 2-electrons) which are predominantly He-like ions in the second half of the FRS and fully stripped in the first half. A calculation of the predicted charge state distributions was made using the GLOBAL code [126]. Table 4.3 shows the predicted charge state distributions through the FRS for selected transmitted nuclei identified from the ^{190}Ta and ^{192}Ta settings using GLOBAL.

For the separation of different charge states, the energy loss per unit charge ($\frac{\Delta E}{Q}$) in the degrader in the intermediate focal plane of the FRS is used. This can be calculated with respect to the magnetic rigidities ($B\rho$) using the following relation [110]:

$$\frac{\Delta E}{Q} = (\gamma_1 - \gamma_2)\frac{A}{Q}u \tag{4.1}$$

Table 4.3: Calculated ion distribution charge states of some of the transmitted ions in the first and second half of the FRS using the program GLOBAL [126]. Values are percentages of total ions of that species.

	S2			S4		
Nucleus	**Fully-stripped**	**H-like**	**He-like**	**Fully-stripped**	**H-like**	**He-like**
^{186}**Hf**	96.5	3.5	0.03	86.7	12.7	0.52
^{188}**Ta**	96.1	3.7	0.04	85.6	13.7	0.62
^{190}**W**	95.6	4.2	0.04	84.5	14.8	0.73
^{192}**Re**	95.3	4.6	0.05	83.2	15.9	0.86

where $(\frac{A}{Q})$ is the mass-over-charge ratio, u is the atomic mass unit and $\gamma_{1,2}$ are the relativistic parameters for ions in the first and second parts of the FRS respectively. The parameter γ_1 [1] is calculated as follows [110] :

$$\gamma_1 = \sqrt{1 + \left(\frac{B\rho_1}{A/Q}\right)^2 . \left(\frac{e}{uc}\right)^2} \tag{4.2}$$

where e is the electron charge and c is the speed of light in vacuum. The parameter γ_2 is calculated by the measurement of time of flight (TOF) between the Sci21 detector in the S2 position of the FRS and the Sci41 detector at the final focus of the FRS.

Figure 4.4 shows the three charge states of particles after passing through the degrader in S2 by plotting the energy loss in MUSIC41 detector versus energy loss in the degrader. The lower group of these charge states are mostly the fully stripped ions with $q = Z$. The other two are the H-like and He-like charge states in the second half of the FRS which gain one and two electrons respectively. In order to improve the electron stripping of the transmitted heavy ions, two niobium foils were placed behind the Be target and the energy degrader at S2.

4.4.2 Identification of Atomic Number Z

According to Bethe-Bloch formula, as discussed in Section 2.3, the ion energy loss $-\frac{dE}{dX}$ is proportional to the square of atomic number and the inverse of the square of velocity ($\propto \frac{z^2}{v^2}$). In the current work two MUlti Sampling Ionization Chambers

[1] see Appendix B for derivation.

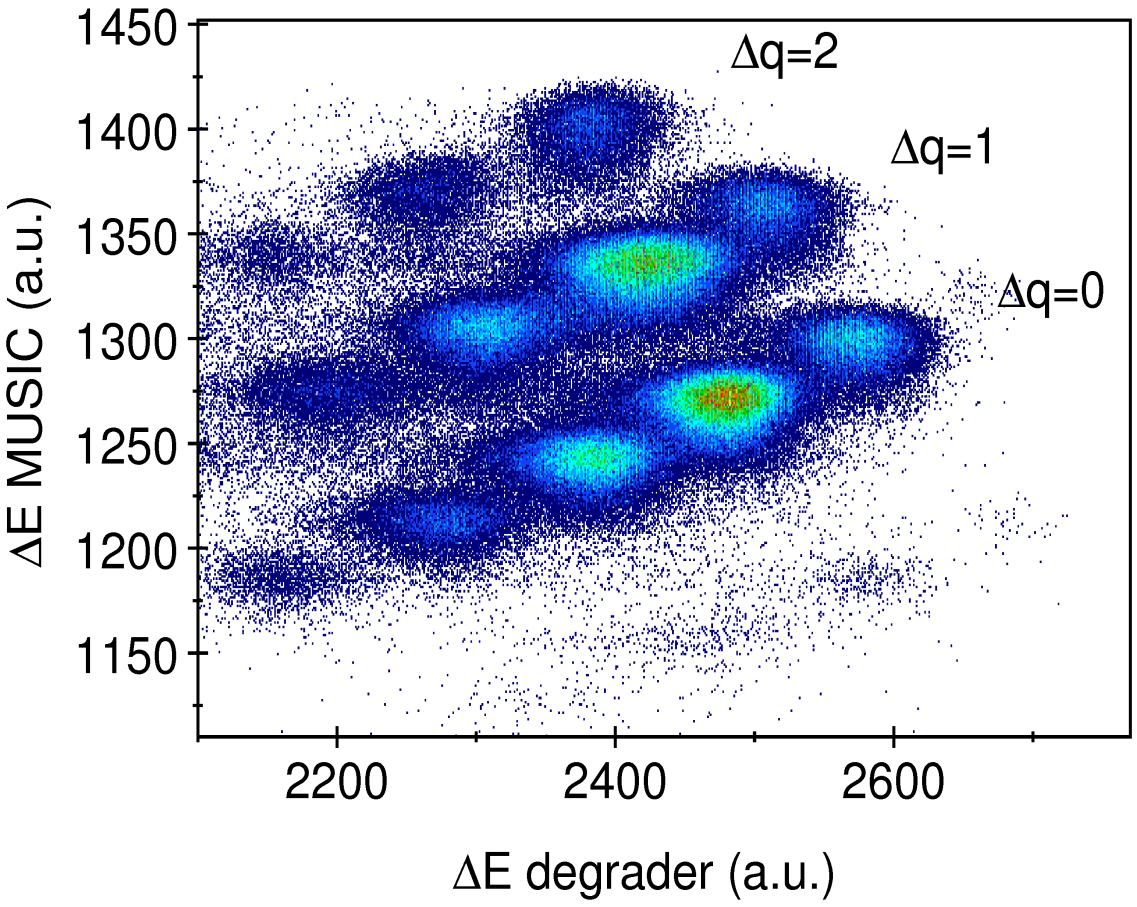

Figure 4.4: The identification of the three charge state groups from the sum of data from both the ^{190}Ta and ^{192}Ta settings using the energy loss in the degrader at position S2. The lower group of Δq=0 corresponds predominantly to the fully stripped charged state. The Δq=1 corresponds to the H-like and the Δq=2 is the He-like ions respectively.

(MUSICs) were positioned at the final focal plane of the FRS for energy loss measurements of the secondary ions and to provide information of their ion atomic numbers. Figure 4.5 shows an example of the energy loss measurements in the second MUSIC chamber. This plot shows the effective use of the energy loss in the chamber gas as it separates the ions with different atomic numbers with good resolution. In addition, by plotting a two dimensional energy loss spectrum of MUSIC41 versus MUSIC42 (see figure 4.6), ions with same atomic number in both chambers are approximately in the same channel. Other events corresponding to nuclear reactions in either detector, can be excluded from the offline analysis by the software gating.

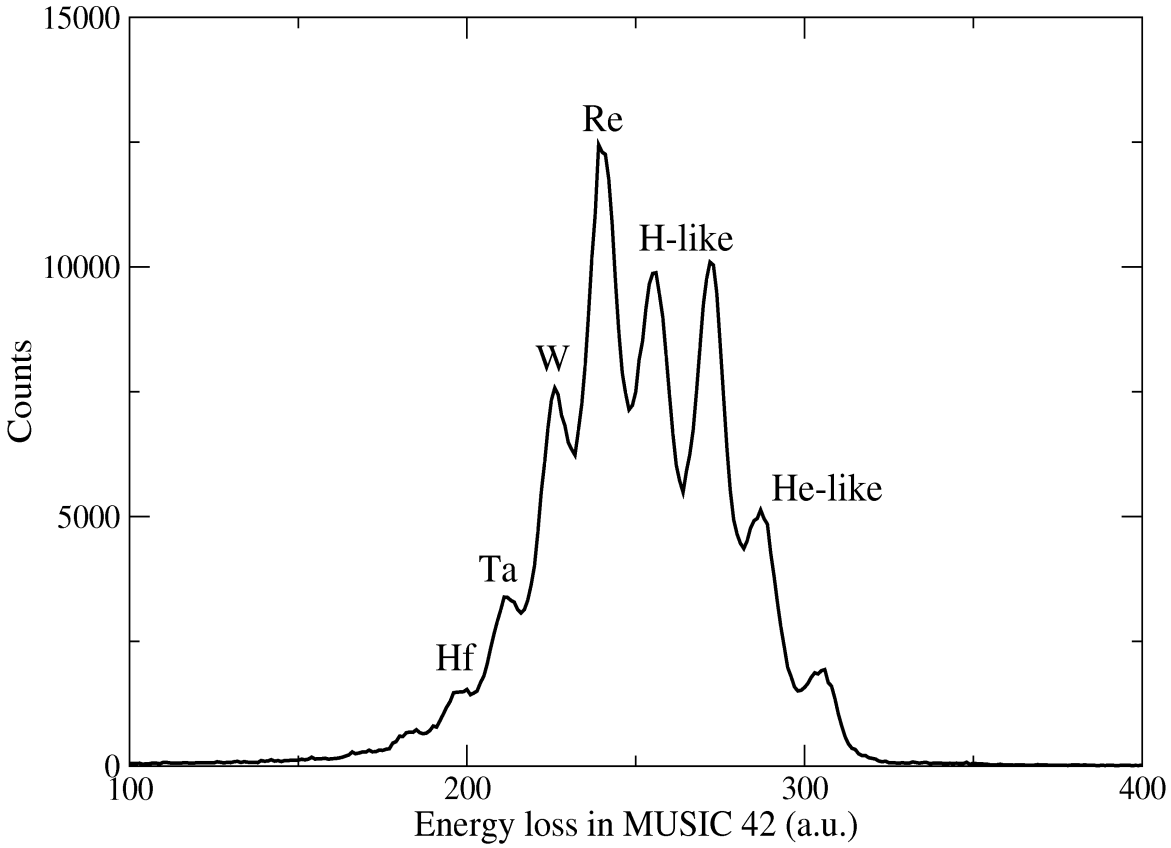

Figure 4.5: Energy loss measurement in the MUSIC42 detector at the end of FRS final focal plane from the ^{190}Ta and ^{192}Ta settings for all charge states. The energy loss in the MUSIC detector was used for the atomic number (Z) identification.

4.4.3 Reactions in Sci42_vs_MUSIC41

The Sci42 detector is positioned directly following the final degrader and can be used to identify changes in energy loss due to nuclear interaction of secondary ions in the degrader. This energy loss in Scintillator Sci42 detector can be used together with the energy loss in MUSIC41 to identify those ions with the same atomic number before and after the interaction with the S4 degrader. The correlation between signals in the MUSIC41 and Sci41 detectors is illustrated in figure 4.7. The ions on the right side of the plot are those ions with the same atomic number before and after the degrader and the events in the left side should be discriminated and removed from the analysis.

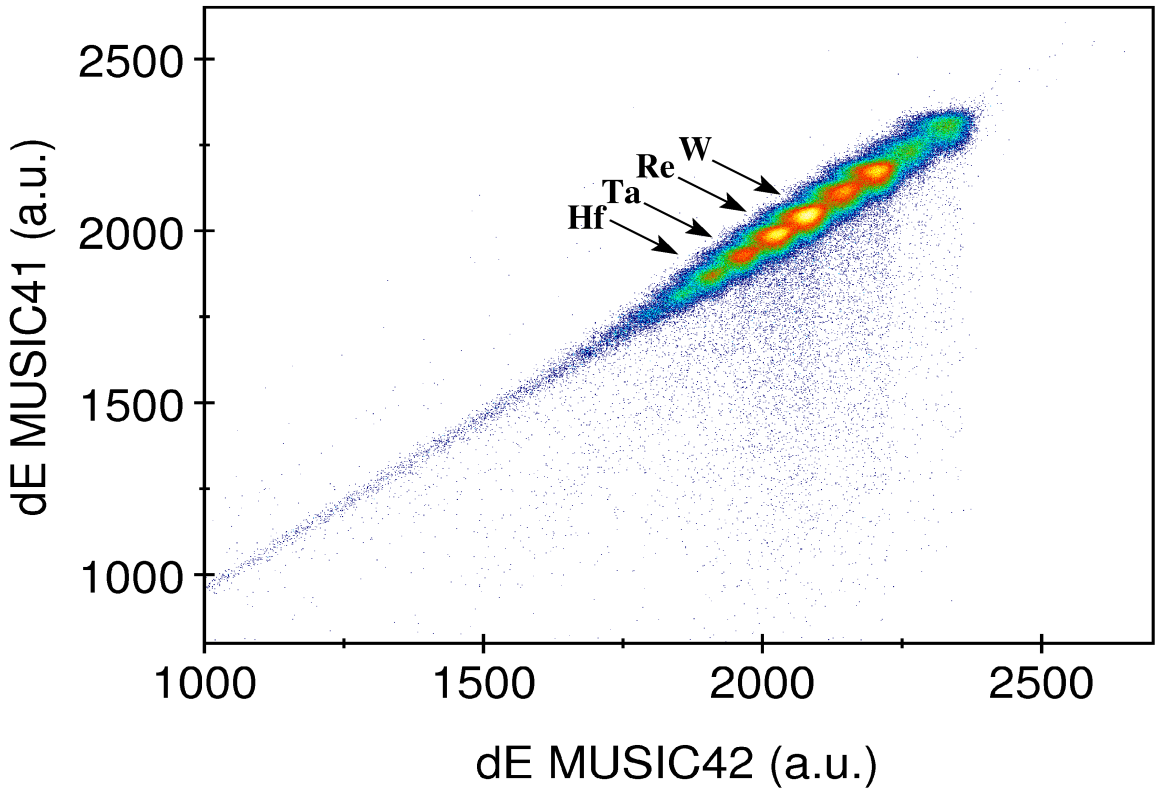

Figure 4.6: Energy loss measurements in both MUSIC detectors (41 and 42) of all fragmentation ions transmitted within the ^{190}Ta and ^{192}Ta settings. Each group represents ions with the same atomic number in both MUSIC detectors. The identified Hf, Ta, W and Re ions in the figure represents those ions in the fully stripped charge state (i.e $\triangle q$ =0).

4.4.4 Particle Identification plot

Figure 4.8 represents the final particle identification plot for fully stripped ions after the combination of the ^{190}Ta and ^{192}Ta centred settings. The atomic number, Z, from the measurement of the energy loss of the fragments in the MUSIC detector is plotted against the time of flight (TOF). This plot shows the fully stripped ions and illustrates the effect of the application of all of the previous conditions on the improvement in the particle identification. Figure 4.9 shows a projection of the particle identification plot onto the x-axis (Time Of Flight TOF) for the Ta isotopes from both ^{190}Ta and ^{192}Ta settings.

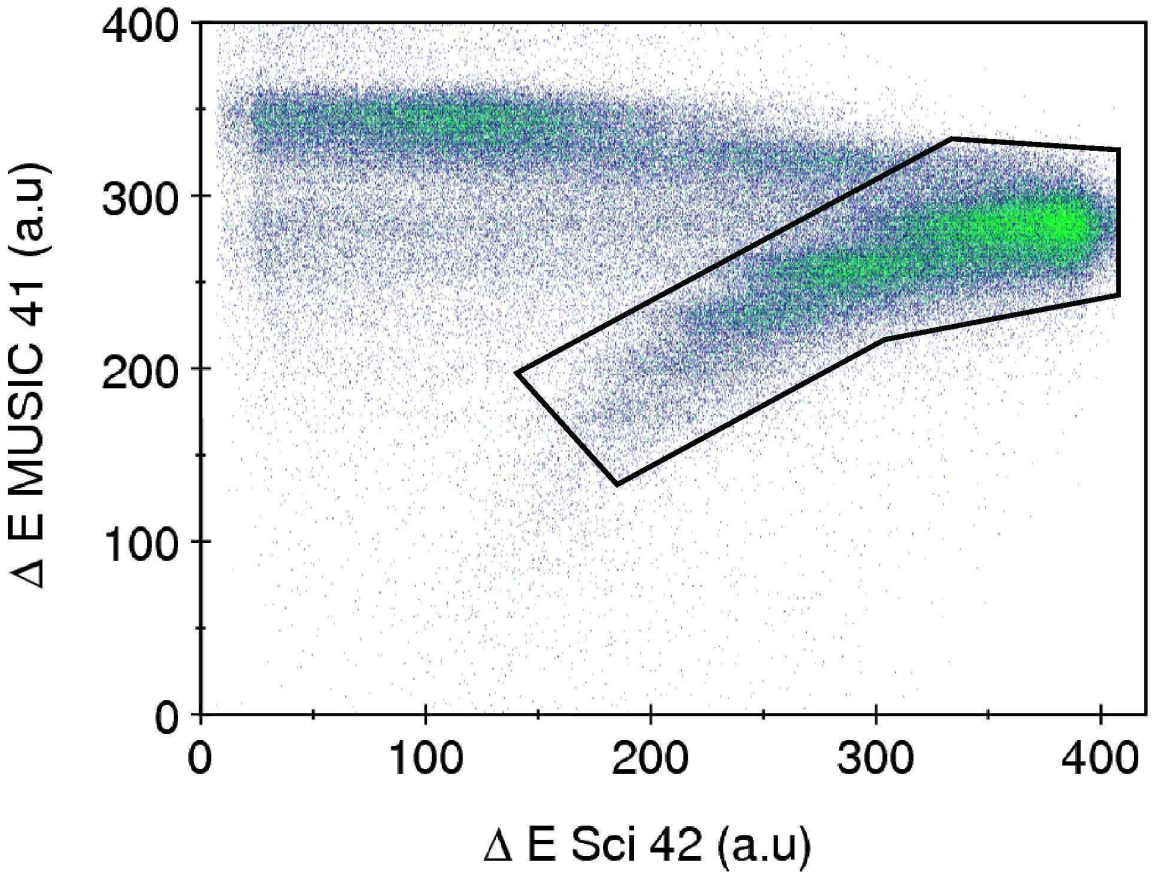

Figure 4.7: Energy loss measurements in the MUSIC 41 versus scintillator Sci42 from the ^{190}Ta and ^{192}Ta settings of the Δq=0 charge state. The events on the right represent those ions with similar atomic numbers before and after interaction with the aluminium degrader at S4.

4.5 Particle Implantations and Beta Decays

This experiment included the measurement of gamma rays emitted after the production of isomeric states and also the subsequent beta decay of implanted ions. In the former, isomeric states were produced during the fragmentation interaction of the primary beam with the target. The typical lifetime of the products should be longer than the time required to traverse the length of the FRS to reach the active stopper (which was approximately 300 ns in the current work), although considerably shorter isomeric half lives have been measured due to suppression of the inflight conversion electron decay branch [11]. The implanted mother nuclei decay to the daughter nuclei by beta particle emission which can be followed by gamma-ray (or internal conversion) decay if the β-decay populates excited states in the daughter nucleus.

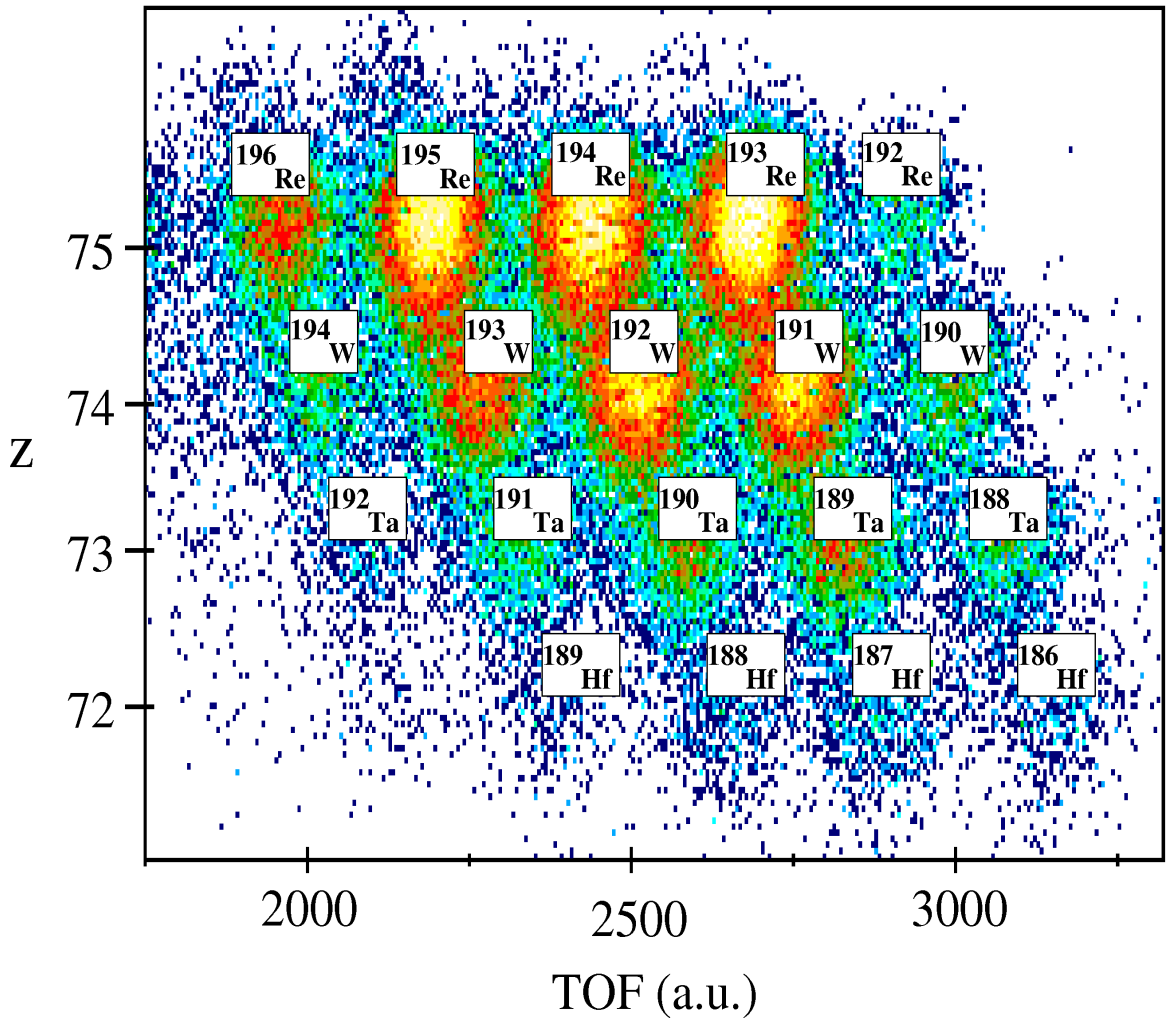

Figure 4.8: Combined data from the ^{190}Ta and ^{192}Ta centred settings showing the final two dimensional identification plot of the fully stripped (Δq=0) ions.

Gamma-ray detection using the RISING array was triggered using two logical signals called the implantion and decay triggers. When selected ions crossed the scintillator Sci41, a signal was passed to the logical electronics of the RISING germanium array to be opened for up to 400 μs, to allow the measurement of γ rays decaying from isomeric decays in the mother nuclei. Then, the gamma-ray array electronics were closed until receiving either a) another Sci41 trigger or b) a signal from the decay trigger of the RISING active stopper. This latter trigger provided a logical signal to the data acquisition electronics to be opened when there were no ions crossing the scintillator Sci41 but following a β^--decay event in the DSSSDs of the active stopper. The decay trigger only fired if the energy signal was above a certain lower threshold. This energy threshold signal was determined to be close to the energy ranges of emitted

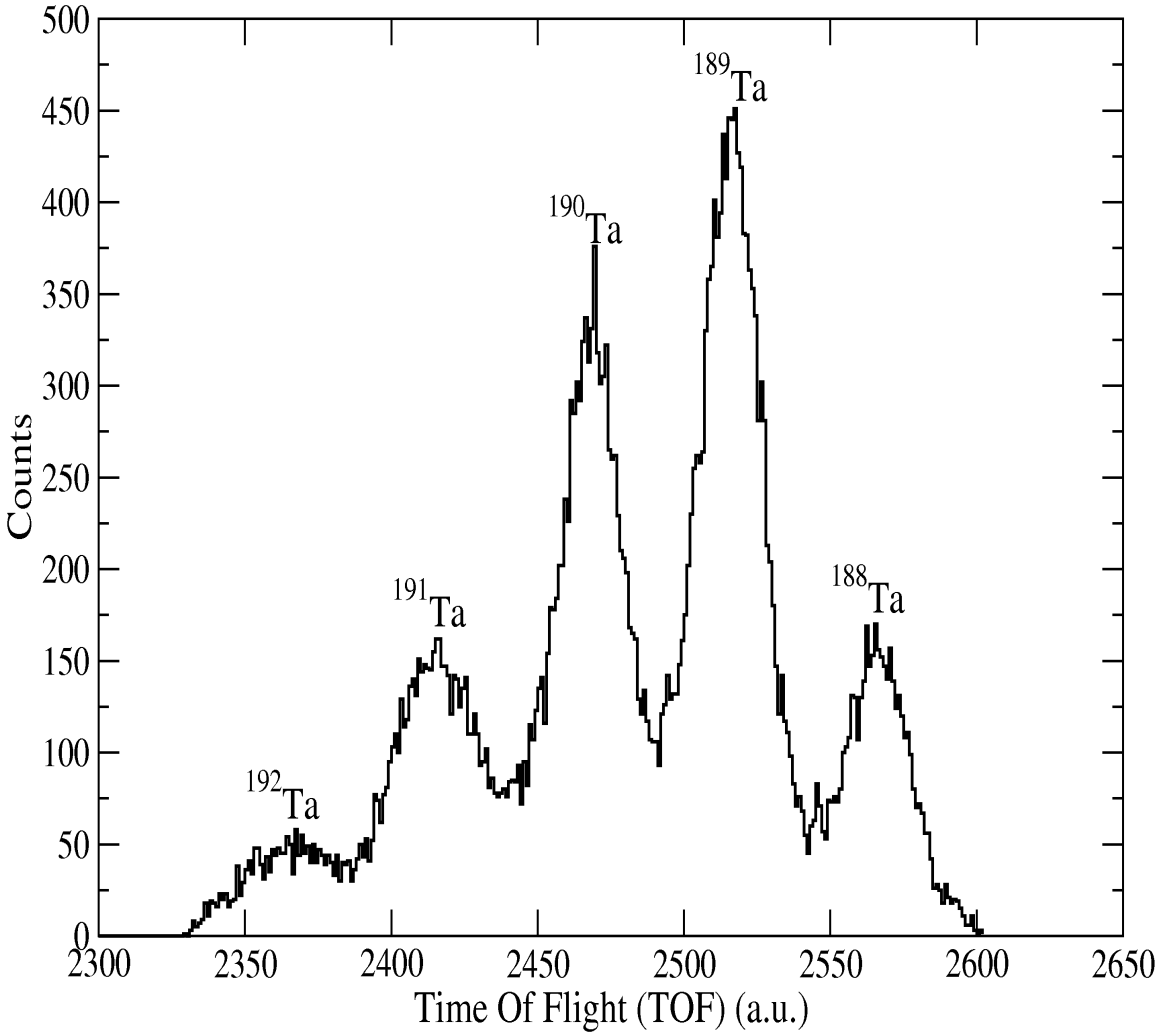

Figure 4.9: Time of flight (TOF)projection for the Ta isotopes identified in the current work from the combined ^{190}Ta and ^{192}Ta centred settings.

beta particles. The DGF electronics for the germanium array in this stage were also opened for up to 400 μs after the initial decay trigger to identify any isomeric decays populated following β^--decay of the secondary ions transmitted through the FRS.

4.5.1 Identification of Decays from Isomeric States

As the secondary beam reached the final focal plane, the fragments were implanted in three Double-Sided Silicon-Strip Detectors (DSSSDs) each of 1 mm thickness. The identification of γ rays following decays from isomeric states was achieved by constructing a two-dimensional matrix of detected gamma-ray energies (as measured by the RISING array) versus the measurement of their decay time from the DGF (Dig-

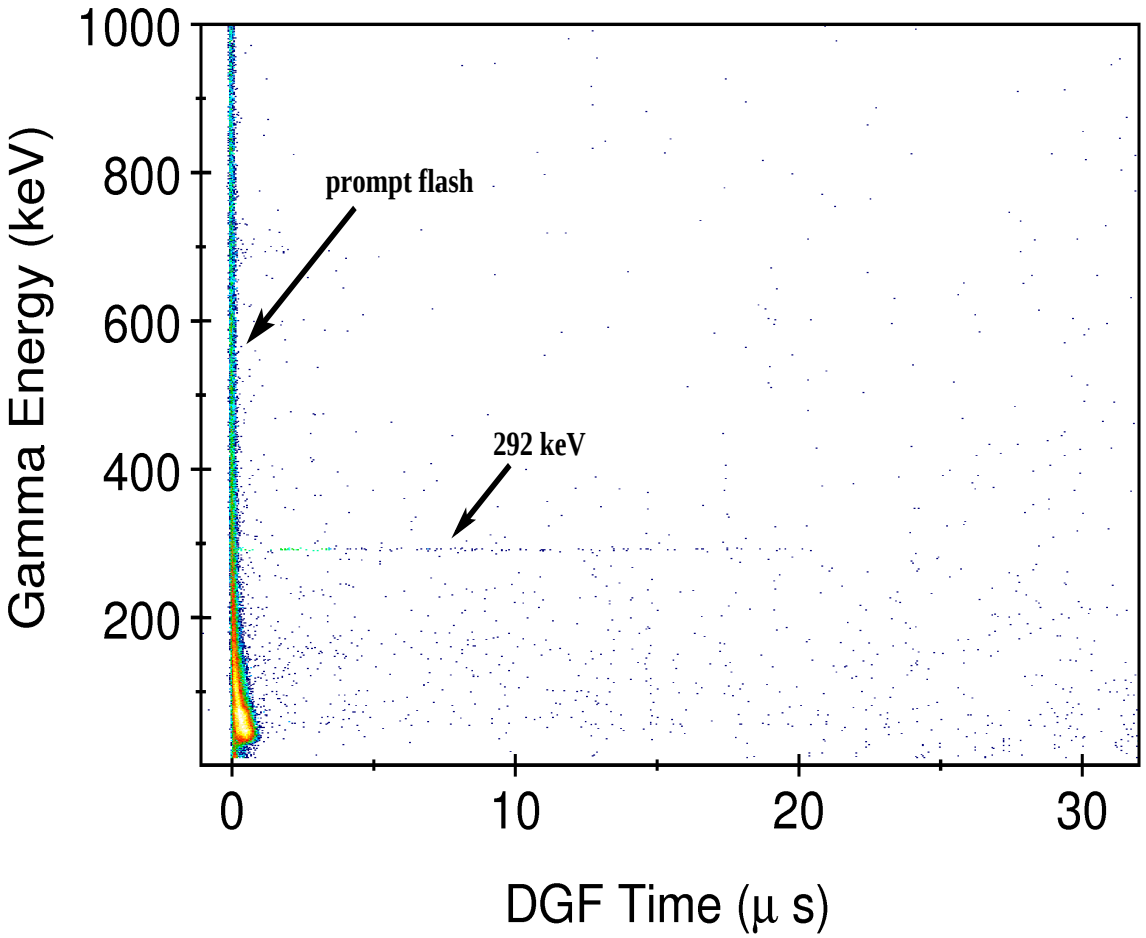

Figure 4.10: Gamma-ray energy versus time matrix for fully stripped ^{188}Ta nuclei. The prompt flash in the left corresponds to the Bremstrahlung events. The 292 keV transition is from the isomeric decay previously identified in this nucleus [11].

ital Gamma Finder) relative to the heavy-ion signal passing through Sci41 detector. Figure 4.10 illustrates this matrix when gated on ^{188}Ta ions and shows the γ-ray line from the isomer in this nucleus which was identified in a previous study [11].

The first observable in the energy versus time matrix is the prompt flash which can be used to define "time zero". This prompt flash is mainly associated with Bremsstrahlung radiation emitted when the high-energy implanted ions slows down and comes to rest in the stopper. The acquisition system can record only one gamma ray per crystal per event, which means that the germanium detectors can be effectively "blocked" by this prompt flash. In another words, this flash reduces the effective efficiency of detecting the isomeric states for a period of time depending on the γ-ray multiplicity of the flash and the granularity of the γ-ray detection system [127].

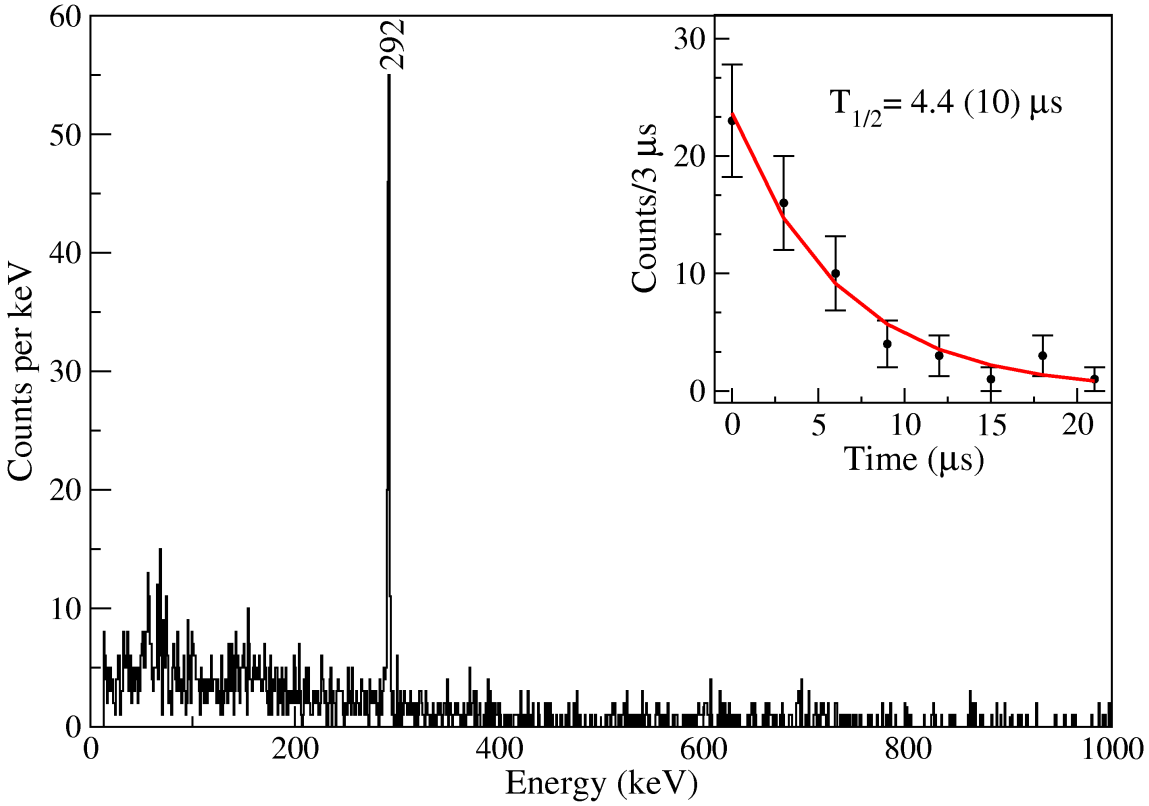

Figure 4.11: The projection of gamma energies of the ^{188}Ta ions within a time range of 0.2-22 μs following the ion implantation in the active stopper. The peak at 292 keV follows the decay of the previously reported isomeric state [11] in this nucleus.

The gamma rays emitted following the decay of isomeric states can be visualised as horizontal lines starting from the prompt flash. Figure 4.11 shows the energy projection of ^{188}Ta with the 292 keV γ ray from the previously reported isomeric decay in this nucleus [11]. The full results of the analysis on the isomeric decays observed in the transmitted secondary fragments are presented and discussed in Chapter 5.

4.6 Active Stopper and β^--Decay Measurements

4.6.1 Experimental configuration

Figure 4.12 shows a schematic of the experimental configuration of the three DSSSDs of the active stopper as used in the current work. As discussed in Chapter 2, the FRS was operated in the monochromatic mode in this study. This operation mode was chosen for two reasons: (i) the implanted ions needed to be implanted in the active

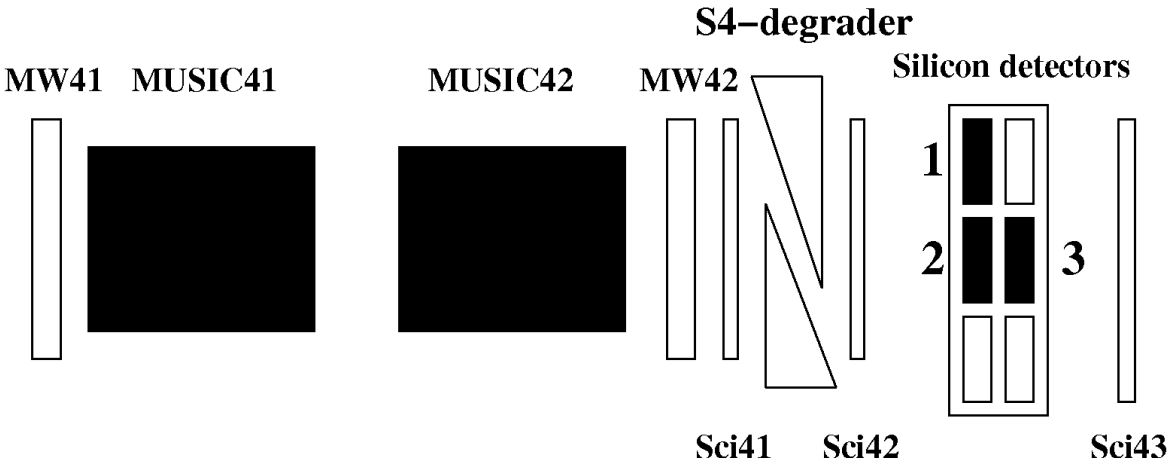

Figure 4.12: Schematic of the experimental arrangement of the three DSSSDs in the RISING stopper for this experiment (see text for details).

stopper with similar energies for a given species. This narrow distribution in the energy ranges between the nuclear species make it possible to identify the implanted ions and subsequently correlate these ions with their subsequent beta decays; and (ii) there was a requirement to distribute the implanted ions across as wide an area as possible of the three active stoppers in order to minimize the probability of having several implanted ions in the same pixel within a typical correlation time.

The active stopper configuration was arranged as in Figure 4.12. This final arrangement was made after the initial calibration setup when it was noticed that most of the implanted ions were in the central and left DSSSDs and almost nothing was implanted on the right hand side position of the final focus. Thus, the right most DSSSD detector was placed behind the central DSSSD and used as a detector to identify those ions not stopped in the first DSSSD.

4.6.2 Measurement of the Energy in the DSSSD using the Mesytec Logarithmic Preamplifier

One of the major issues when implanting nuclei in the active stopper was how to detect both implanted ions (with energies greater than 1 GeV) and their subsequent beta decays (of ∼200 keV→a few MeV) in the same detector. This issue was solved by using a new electronic counting system designed to measure both implanted ions and beta decays in the same system. The Mesytec MPR-32 preamplifier is a new model

which provided combined linear and logarithmic response modes [120]. The application of the logarithmic mode allowed the decay measurement of β-particle energies following the implantion of high energy ions. This mode provided a linear range amplication beta decay events up to 10 MeV, while the logarithmic range measured the implanted ions in the 10 MeV→3 GeV enegy range. Figure 4.13 shows the range of measurements of the Mesytec MPR-32 preamplifier as tested by the GSI electronics team for the RISING collaboration [42].

For the silicon active stopper using the logarithmic preamplifier, the two response sections of the preamplifier needed to be calibrated. The linear part was calibrated using a ^{207}Bi source which emits mono-energetic conversion electrons (see Appendix A.2). This yielded an energy resolution of FWHM∼15-20 keV at 980 keV and a minimum detection threshold of approximately 150 keV. For the logarithmic part, simulated high-energy signals from a pulser were used.

Figure 4.14 shows the total energy spectrum of ions and β^- particles taken from the sum of energies deposited in DSSSD 1 and 2 for the ^{190}Ta and ^{192}Ta settings. The energy from the directly implanted ions when deposited in the silicon detectors, would be enough to saturate the pre-amplifier output signal channels if a standard linear response pre-amplifier was used [110]. The left-hand peak in figure 4.14 shows the decay electrons following the implantion. The two peaks in the centre of the same figure represent the direct ion implantions within the DSSSD 1 and 2 detector pixels. The left-hand peak represents the implantation of the fission fragments while the right-hand grouping represents the projectile fragments of interest (see figure 4.15).

4.6.3 Implant-Decay Correlation Technique

The technique of correlating the implanted ions with their subsequent beta decay depends mainly on identifying of the implantion position in the active stopper and the time of correlation between the implanted ion and subsequent β-particle in the same or neighbouring pixels. As discussed earlier, each of the three DSSSD detectors is double-sided and has 16 individual strips on the front and back sides. The first step of the correlation analysis begins after implantion of the ions in the active stopper. The ions hit the detector and are distributed across the stopper as a result of using the monoenergetic degrader at S2. The ions are then implanted and their strip positions

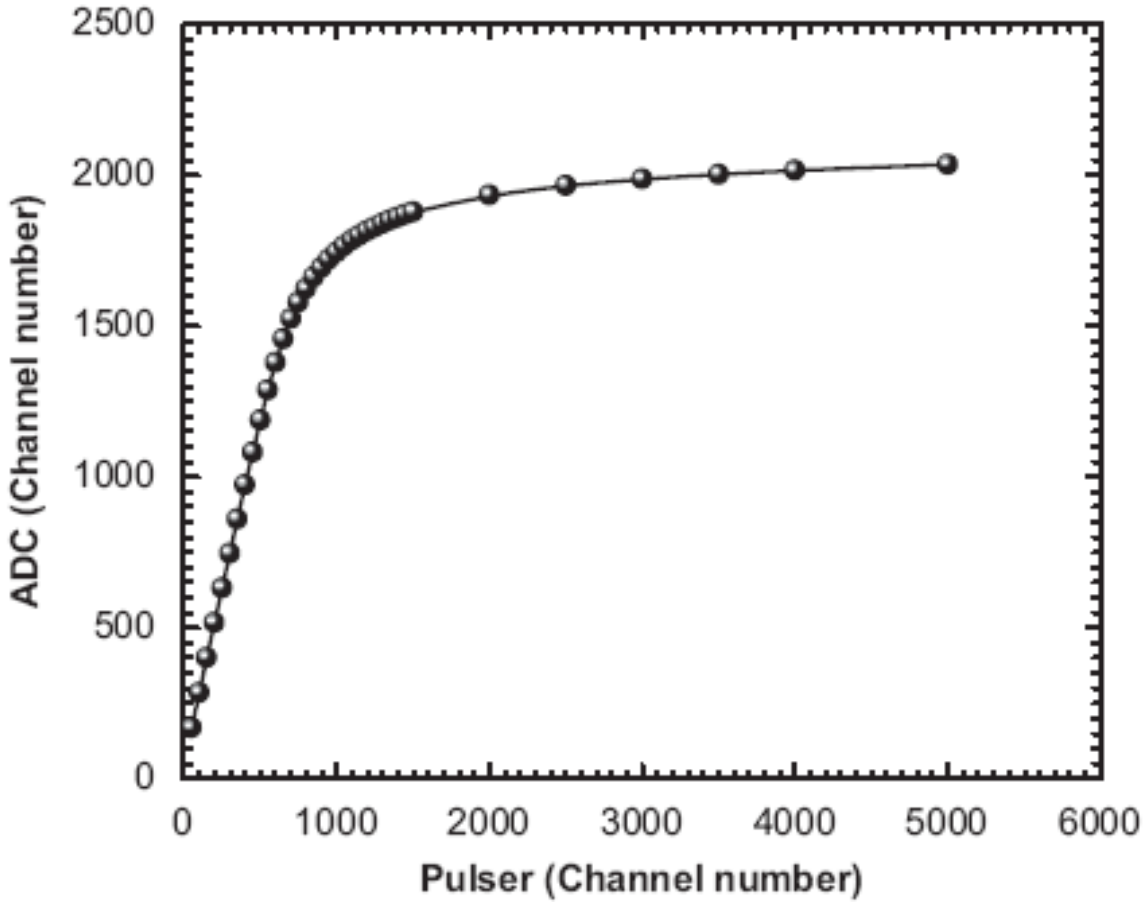

Figure 4.13: The characteristic energy response of the logarithmic MPR-32 preamplifier used with the DSSSDs which provides linear and logarthmic measurements, taken from reference [42].

determined as a coordinate of (x,y) as well as registering the absolute time via a digital, (absolute) time stamp. A valid implanted event is that which produces a high-energy signal in the active stopper (>10 MeV). Moreover, as there is a finite chance of implanting more than a single ion in one pixel, the ion's energy is recorded as shown before in figure 4.14, using the logarithmic part of the preamplifier.

The implant-γ-ray correlation time for an isomer was fixed in this experiment to be no more than 400 μs. The γ-ray electronics (DGF) were then closed and no further implanted ion could be recorded in that event. The decay trigger gave a signal to the γ-ray electronics to be opened again if a subsequent decay signal was detected in the silicon stopper detector. The DGF electronics were then opened for further 400 μs. The linear part of the DSSSDs preamplifier was used to measure the decay signals, which are small compared to the implantation signals. The strip position and time

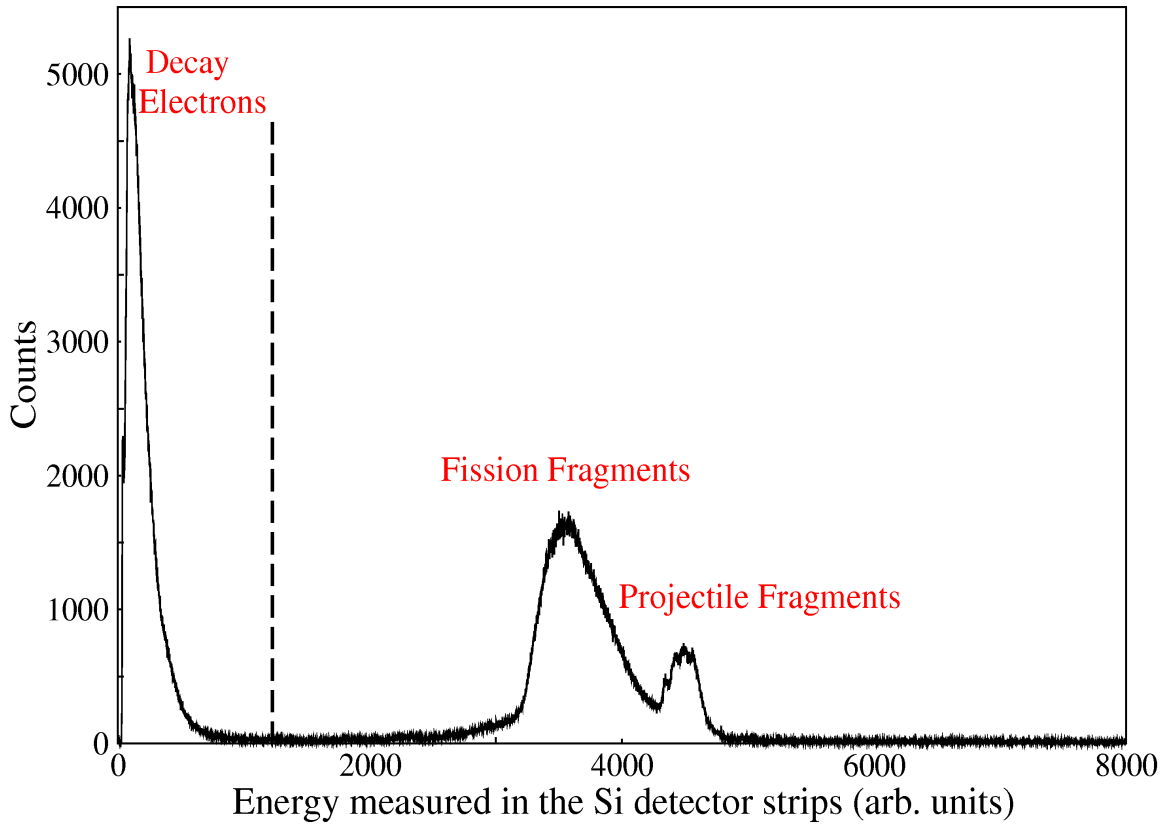

Figure 4.14: Total energy implanted by the nuclei within the silicon active stopper DSSSD 1 and 2 detectors for the ^{190}Ta and ^{192}Ta settings. The double humps in the centre of this figure represent the energy deposited from the direct ion implantions within the active stopper pixels. The deposited energies of beta particles is shown in the left side of the figure.

stamp of the decay signal were noted and correlated with the implantation signal.

The correlation between the implanted ions and their subsequent decay was performed using off-line software analysis. For each implanted pixel and for a period of time after the implantation, the deposited energy above the threshold is considered to arise from the emitted beta particle from the implanted decay in the same pixel. Furthermore, as the beta particles are not always measured in the same pixel as their mother implant, a matching program was developed to also recorded these decays in the neighbouring pixels to that of the original implant. This means that the correlation considered implantations and decays in the same pixel and decays in 8 neighbouring pixels.

Figure 4.16 shows the histograms of the implantion, decay and correlation on

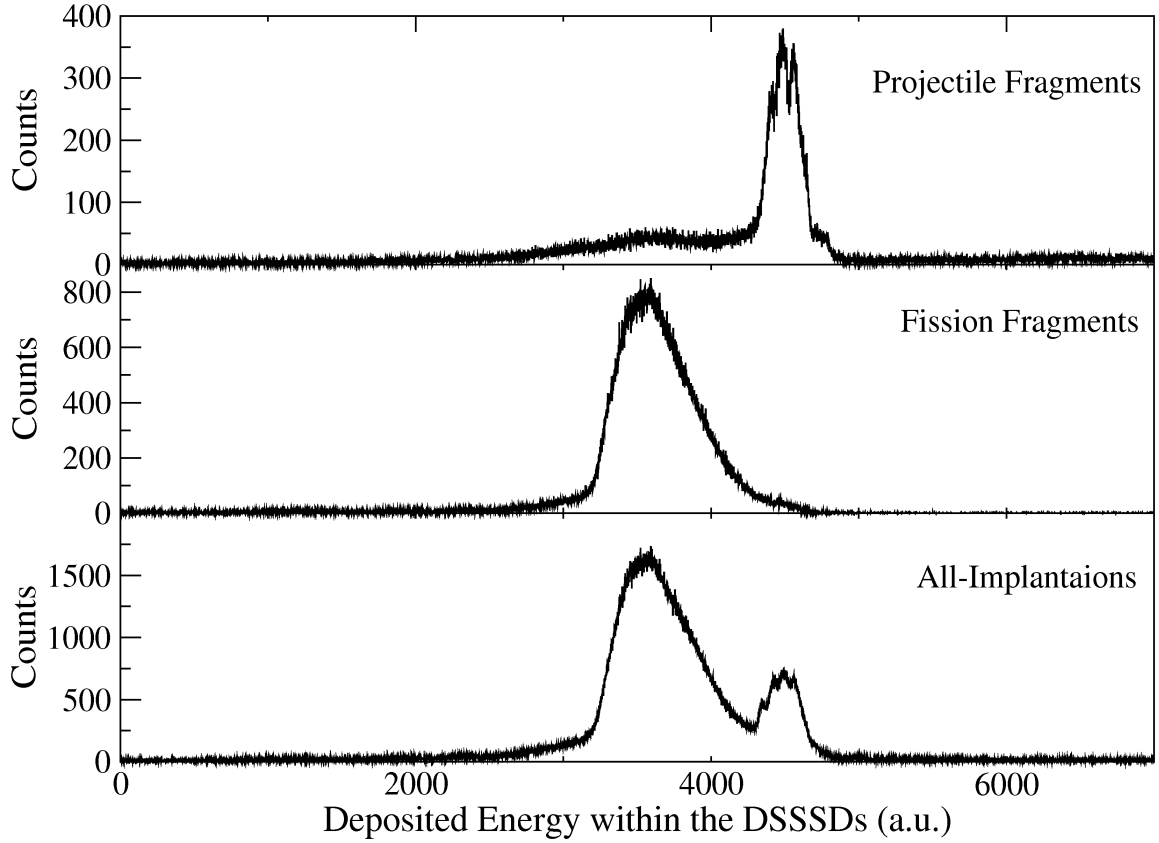

Figure 4.15: (*Lower*:) Total energy spectra within the silicon active stopper DSSSD 1 and 2 detectors for the ^{190}Ta and ^{192}Ta settings; (*Middle*) the energy deposited associated with the transmitted fission fragments; (*Upper*) the energy deposited by the projectile fragments.

the (x-position, y-position) of the three DSSSDs of ^{190}Ta and ^{192}Ta settings. The left-most histogram in figure 4.16 shows the implantions; the central maps are the subsequent β^- decay events; and the right histograms are the heavy-ion-β^- particle correlation histograms for each detector. The majority of the implantations and decays can be seen in these figure to occur in the central and left-handside detectors. DSSSD number 3 was positioned behind the central one, which explains the reduced number of measured events for this detector. Figure 4.17 shows 2-dimensional position histograms of the implantations within the front central DSSSD detectors for ^{188}Ta, ^{190}W and ^{192}Re secondary fragments transmitted in the ^{190}Ta setting.

In principle, the implant-β correlation time can be extended up to hours, but the lifetime of the beta decay puts practical limit on this. Increasing the correlation time will increase the contamination from different ion species increasing the level of the

random background. In the current work, the lifetime of a beta-decaying nucleus was measured as the average time difference between the implanted ion and the subsequent correlated beta particle. This method allowed the construction of an integrated decay time histogram of all events associated with a given implantation species. The life time decay curve can be also obtained from the β-γ coincidence technique. The decay curve using this method is less contaminated by the random β^- background but has fewer statistics.

4.6.4 β-Delayed Gamma-Ray Measurements

As the correlations between the implanted ions with their subsequent beta particle decay are made, the correlation between beta particles and decay γ rays from the daughter nucleus are also possible on an event-by-event basis. The electronics were opened after receiving a signal from the decay trigger that a decay event was detected in the silicon active stopper. A matrix was created of the emitted γ-ray energies versus the time related to the β-particle decay within the DSSSD. Figure 4.18 shows the energy versus the time of the γ-ray decays of ^{190}Ta. Similar results can be obtained by creating the matrix of the γ-ray energies versus the time difference between the implantations and decays.

The projection of the energy versus the time matrix is represented in figure 4.19. This figure shows the projection of γ-ray energies of all correlated, fully-stripped ($\Delta q = 0$) ions in the ^{190}Ta and ^{192}Ta settings with an implant-β correlation time of 1 minute. For a projection of specific ion species, a software gate condition is required on the interesting ions. An example of this projection is illustrated for the decay of the ^{190}Ta to ^{190}W in Figure 4.20. The correlation times for this projection were taken for 30 seconds, 1, 3, and 10 minutes, respectively.

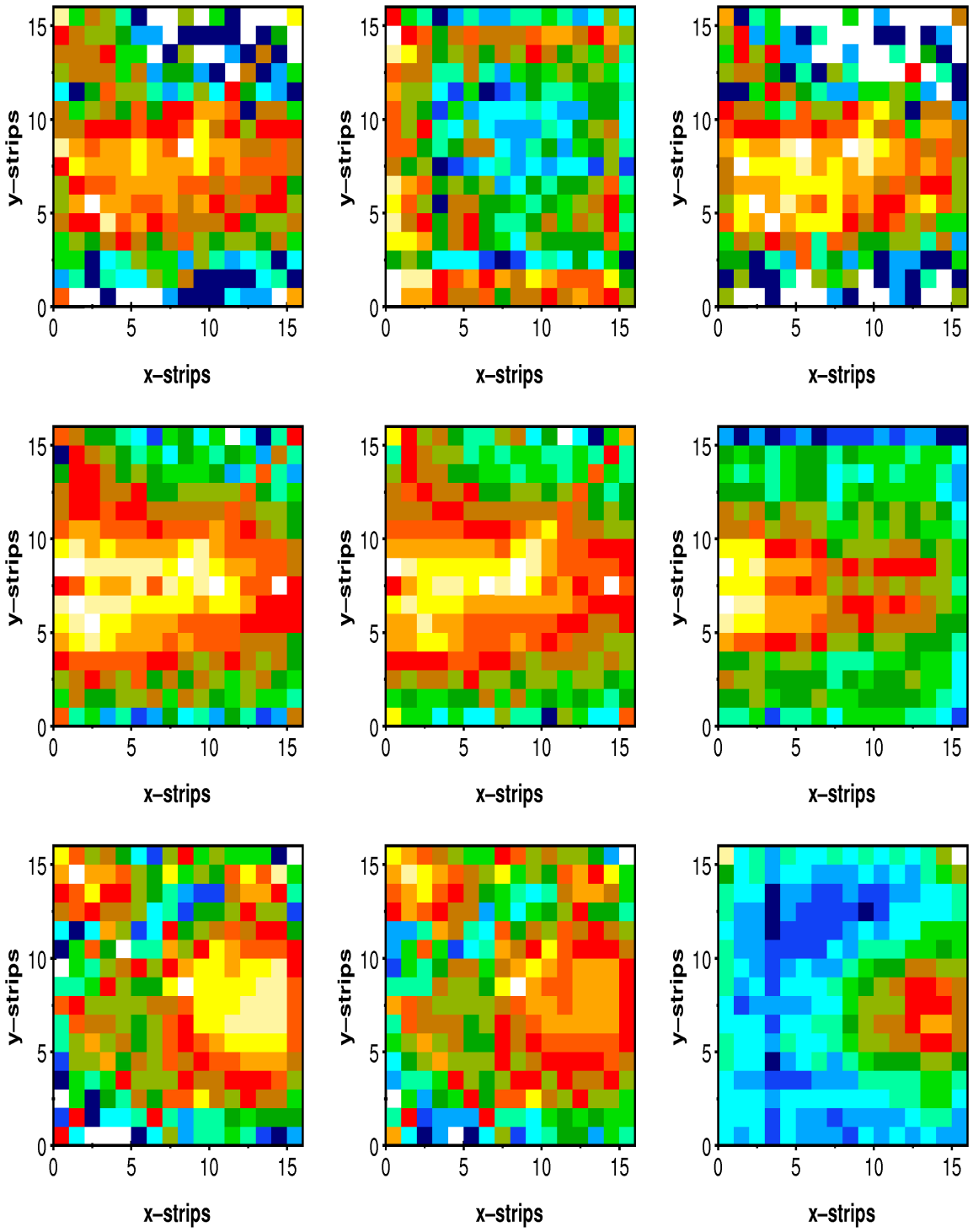

Figure 4.16: **A:** From left to right, the implantion, decay and correlation event maps respectively in the left (*lower*), central (*middle*) and the back (*upper*) DSSSD detectors from the ^{190}Ta and ^{192}Ta settings.

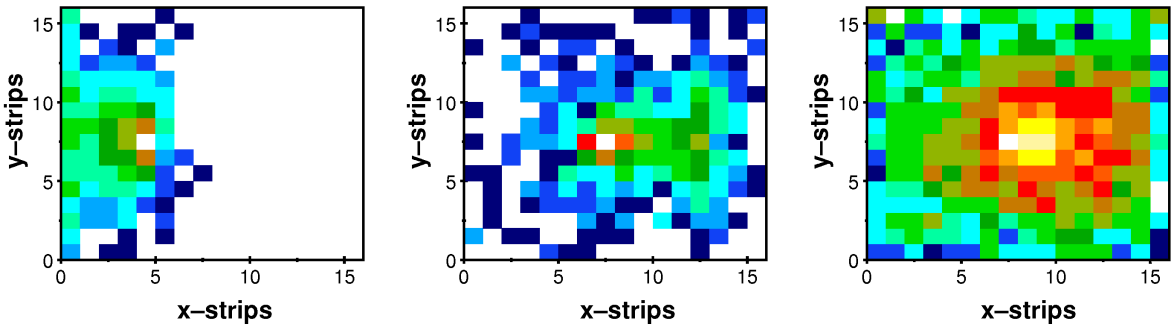

Figure 4.17: The implantion event maps for ^{188}Ta (left), ^{190}W (centre) and ^{192}Re (right) as measured in the DSSSD 2 detector from the ^{190}Ta setting.

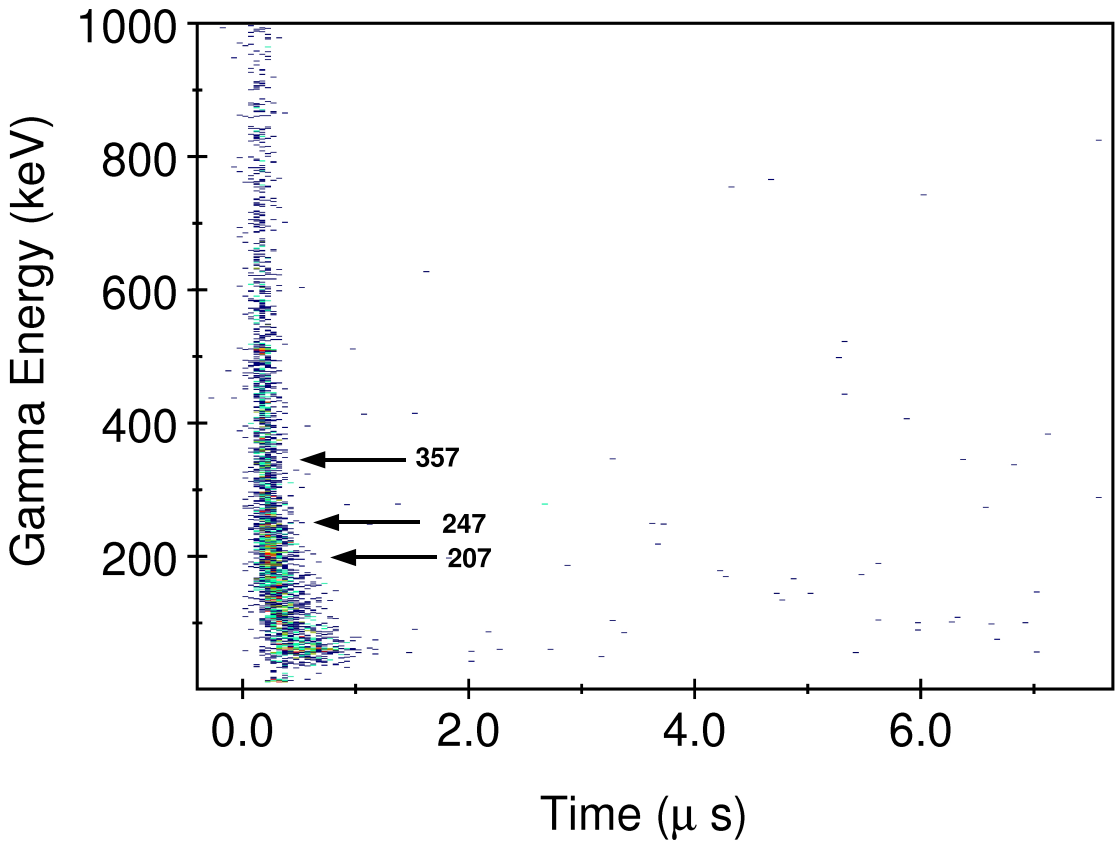

Figure 4.18: γ-ray energy versus time following β-decay correlated with ^{190}Ta ions with a β-ion correlation time of upto one minute.

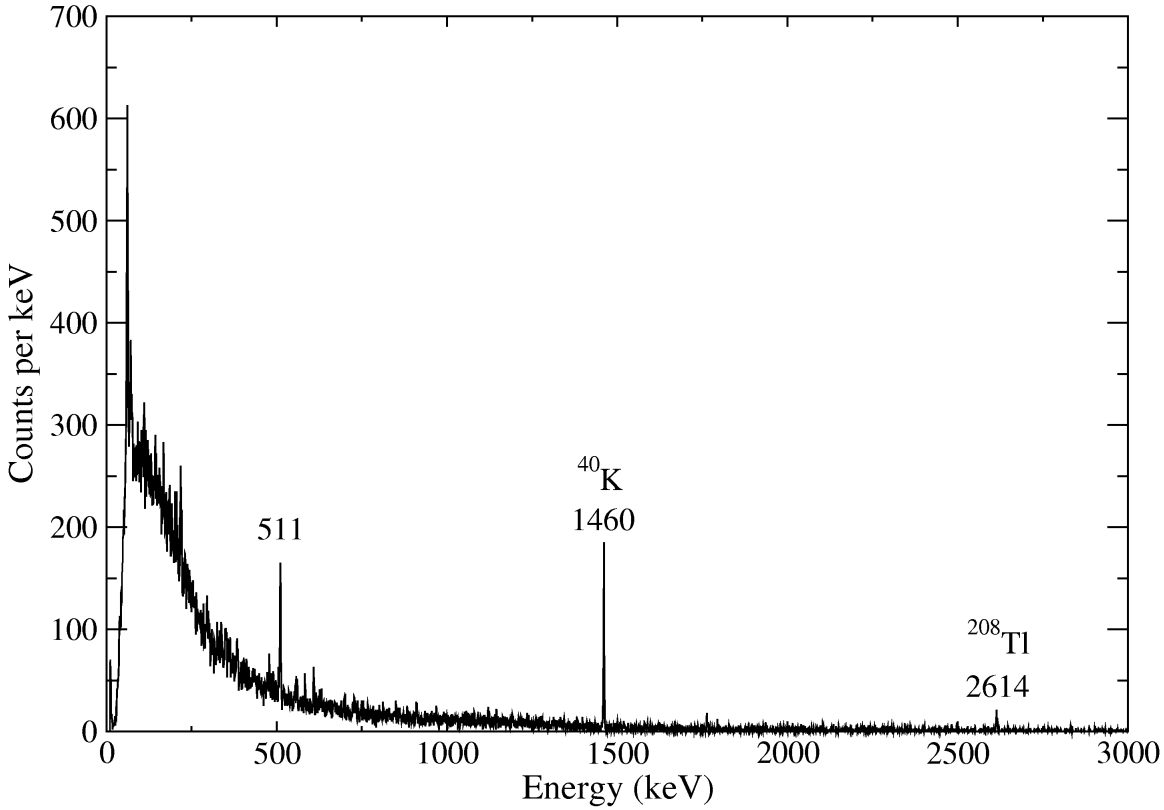

Figure 4.19: The energy projection of the energy versus time difference matrix of all correlated nuclei in the $\Delta q = 0$ charge state for the ^{190}Ta and ^{192}Ta centred settings. The implant-β correlation time for this spectrum was 0→60 seconds.

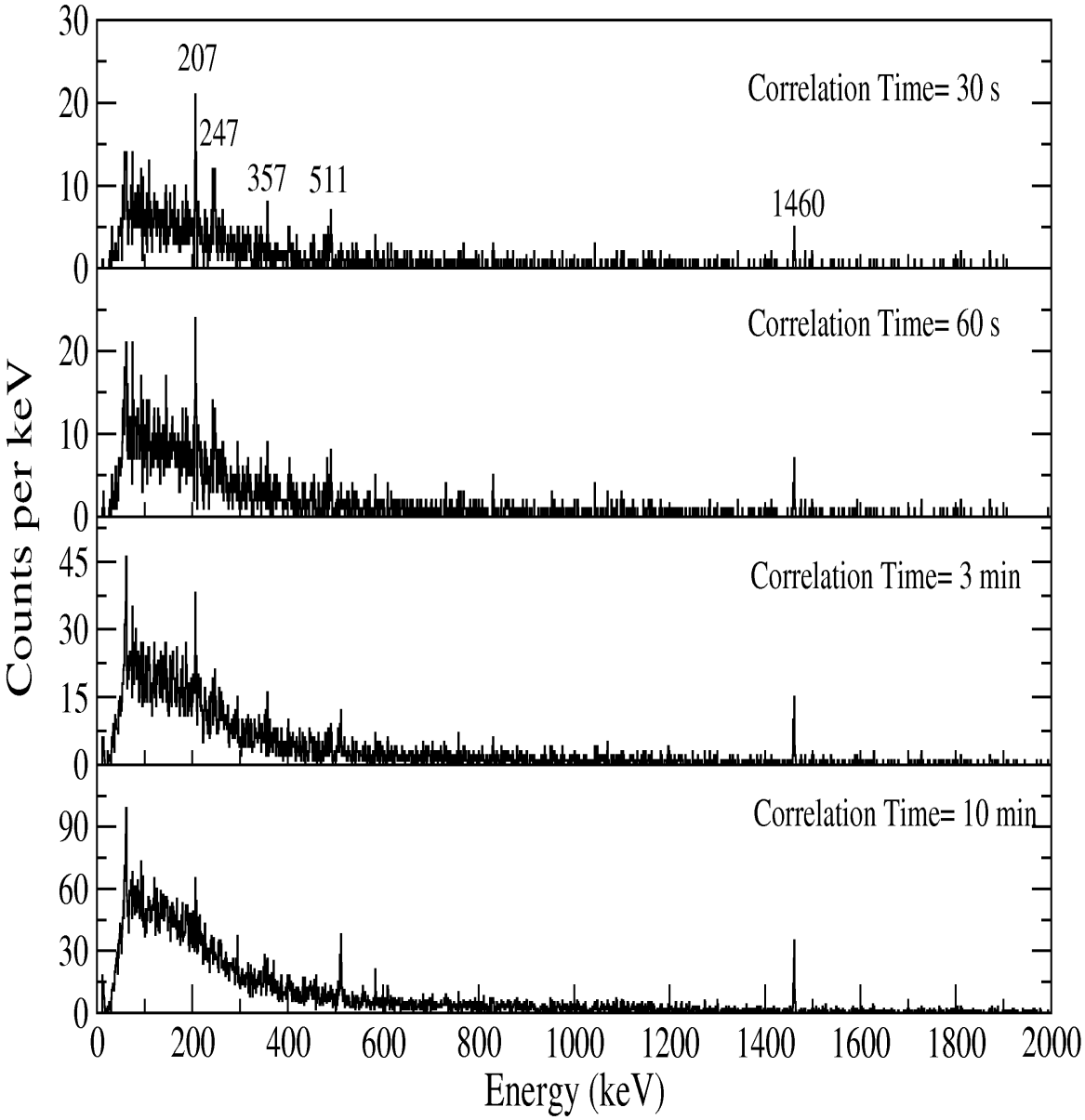

Figure 4.20: The projection of the γ-ray energy versus time difference matrix for correlated ^{190}Ta nuclei from ^{190}Ta and ^{192}Ta settings within different implant-β correlation times.

Chapter 5

Results

The ultimate physics aim of this thesis is to investigate the nuclear structure of the low-lying excited states of the neutron-rich nuclei ^{188}W, ^{190}W and ^{192}W. These isotopes were produced after stopping the secondary products from a Pb beam in three DSSSDs positioned in the centre of the RISING germanium array. As discussed in the previous chapter, the selected mother nuclei were stopped in the RISING active stopper and subsequently decayed by beta particle emissions, followed by the emission of discrete energy γ rays. The ^{188,190,192}Ta isotopes were selected using FRS settings centred on the transmition of ^{190}Ta and ^{192}Ta. Gamma rays following the β-decay of the mother nuclei ^{188,190,192}Ta allowed details of the low-lying level structures in ^{188,190,192}W to be obtained using the ion-β-γ correlation technique. This also allowed a measurement of the decay half lives which are presented here.

5.1 Population of Isomeric States

The decay from isomeric states in the radioactive fragments transmitted through the FRS were measured using the RISING gamma-ray array. These isomers were used as internal checks on the particle identification procedure and analysis and provided an independent validation for the γ-ray energy and timing setups. Figure 5.1 shows the final γ-ray energy spectra and associated decay curves corresponding to decays from isomeric states which were identified in the ^{190}Ta and ^{192}Ta settings. Decays from the previously reported isomers in ^{188}Ta, ^{190}W, ^{192}Re, ^{193}Re [11] are all clearly identified.

The current data also show evidence for isomeric decays in ^{187}Hf, ^{189,190}Ta and ^{191}W. Evidence for the decays in ^{189}Ta and ^{191}W has been previously reported in a

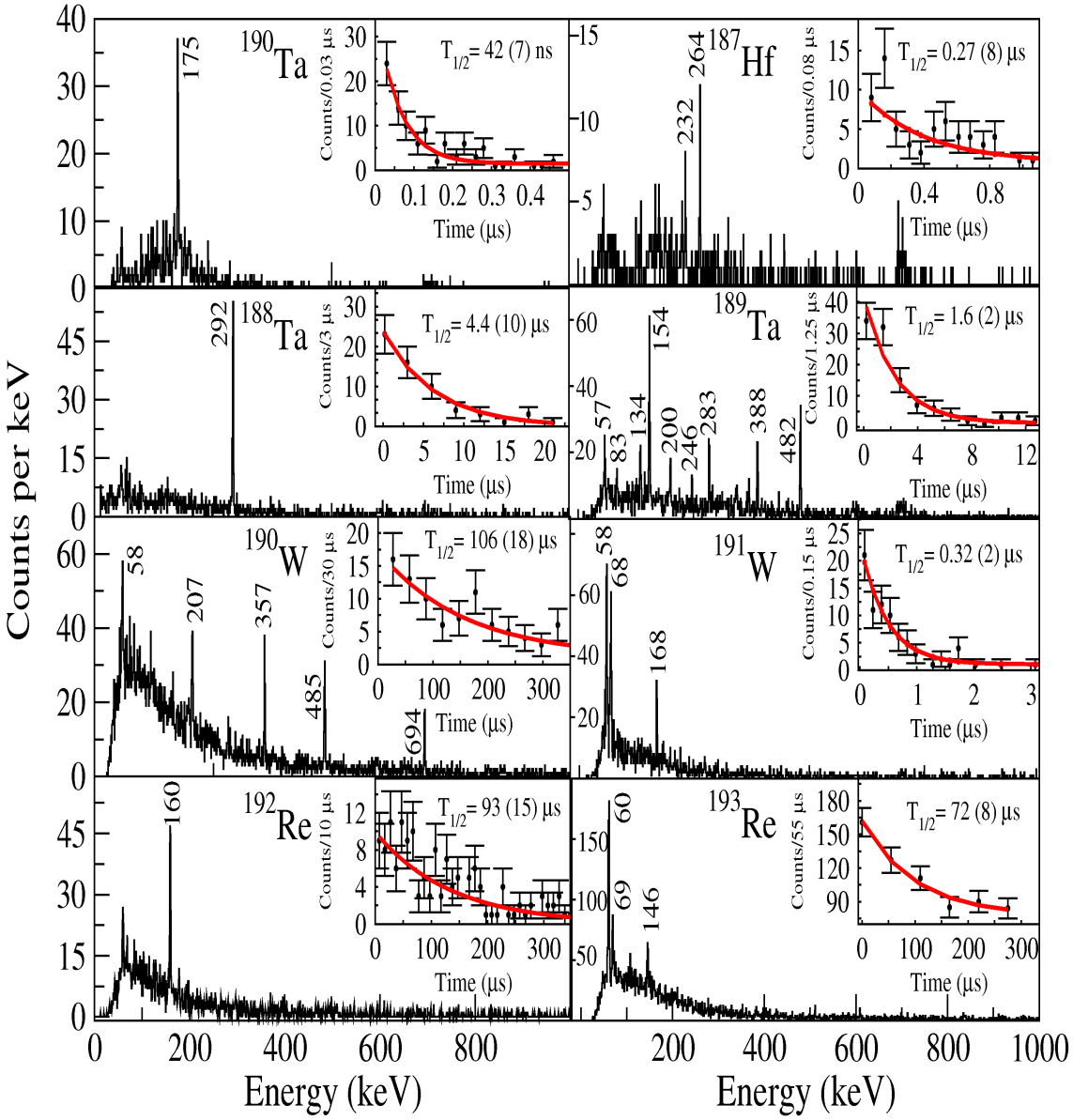

Figure 5.1: Gamma-ray energy and decay-time spectra of delayed events associated with isomeric states identified in ^{188,189,190}Ta (Δt = 0.2→22 μs, 0.2→12 μs and 0.03→0.55 μs respectively); ^{190,191}W (Δt = 2→395 μs and 0.08→3 μs respectively); ^{192,193}Re (Δt = 3→350 μs and 2→350 μs respectively); and ^{187}Hf (Δt = 0.08→1.1 μs).

conference proceeding from the RISING collaboration [44] following a survey of the region using the projectile fragmentation of a ^{208}Pb beam with RISING and a passive stopper. The current data confirm these observation. In addition, previously unreported isomeric decays in ^{187}Hf and ^{190}Ta have been identified for the first time in the current work.

5.2 β^--Decay Half-Life Measurement

The decay half lives of the mother nuclei were determined by measuring the time differences between the implant event times in the DSSSDs and their subsequent correlated β particle events in the same or directly neighbouring pixels gated on the discrete γ rays of the daughter nuclei. The time differences were histogrammed and used to generate a β^--decay curve for that species. This decay curve was then fitted to a single exponential decay assuming a least squares fit to the summed time spectra associated with discrete γ-ray lines. A fit was also made for the entire β^--delayed time spectra in cases where no discrete γ ray was detected following the β^--decay of such nuclei (see Section 5.6). To check the validity of this procedure, a fit was made for the decay time of ^{192}Re to ^{192}Os. The published, adopted half-life value for this decay is 16(1) s [128]. Figure 5.2 shows the fitted decay half life of ^{192}Re using a single-component exponential decay with a least square fitting minimization method and assuming a constant background level. The half-life is measured to be 15.7 (31) s, consistent with the adopted value.

5.3 Beta-Delayed Gamma-ray Spectroscopy of ^{188}Ta $\rightarrow$ ^{188}W

The low lying levels in ^{188}W (N=114, Z=74) have been studied by Podolyak *et. al.* from in-beam studies using deep-inelastic reactions [8]. In that work, the decays from what were interpreted the first three yrast excited states were observed with γ-ray energies of 143, 297 and 432 keV respectively. This interpretation was confirmed by a subsequent study by Shizuma *et. al.* who populated this isotope using a ^{186}W(^{18}O,^{16}O) two-neutron transfer reaction [46]. Figure 5.3 shows the published energy level scheme

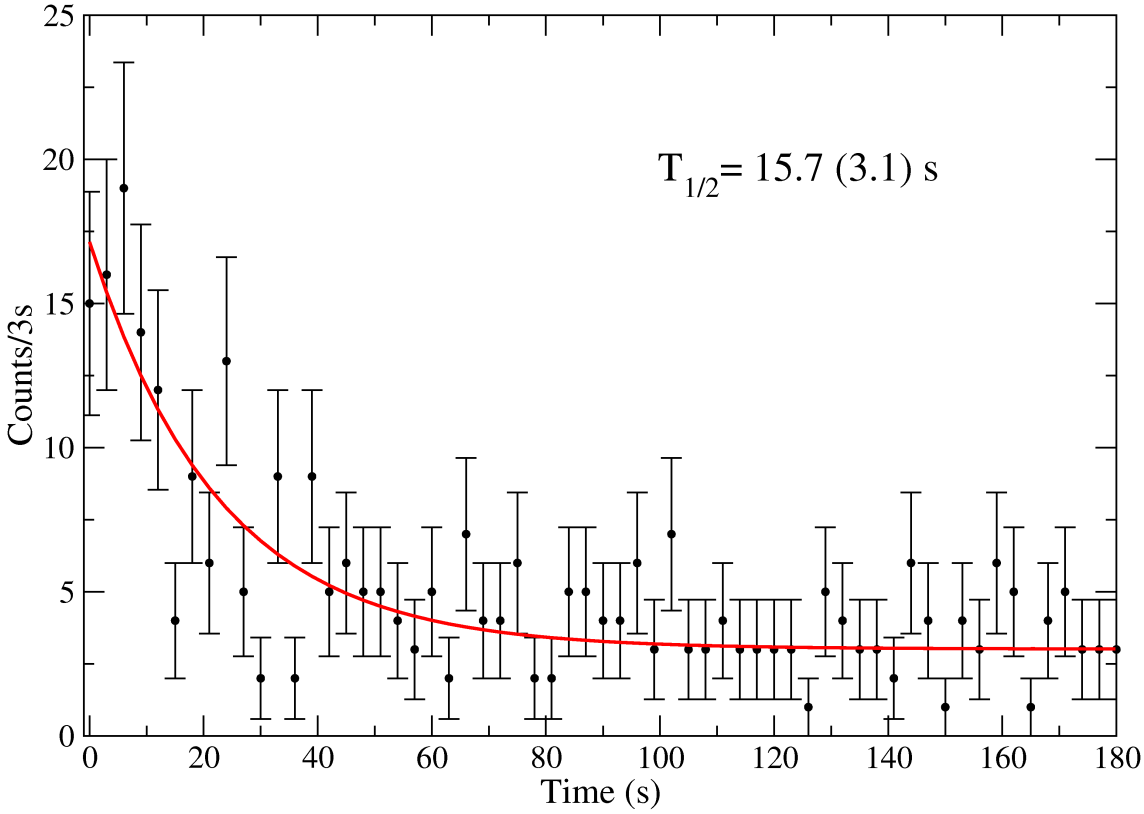

Figure 5.2: Decay time curve for β-decay of ^{192}Re$\rightarrow{}^{192}$Os from the current work. The data fitted with an exponential decay and constant linear background using a least squares fit.

of ^{188}W by Shizuma *et al.* from reference [46]. The ground band states extends up to a spin/parity $I^{\pi}= 8^{+}$ and other states likely to be from a γ-vibrational band were also observed.

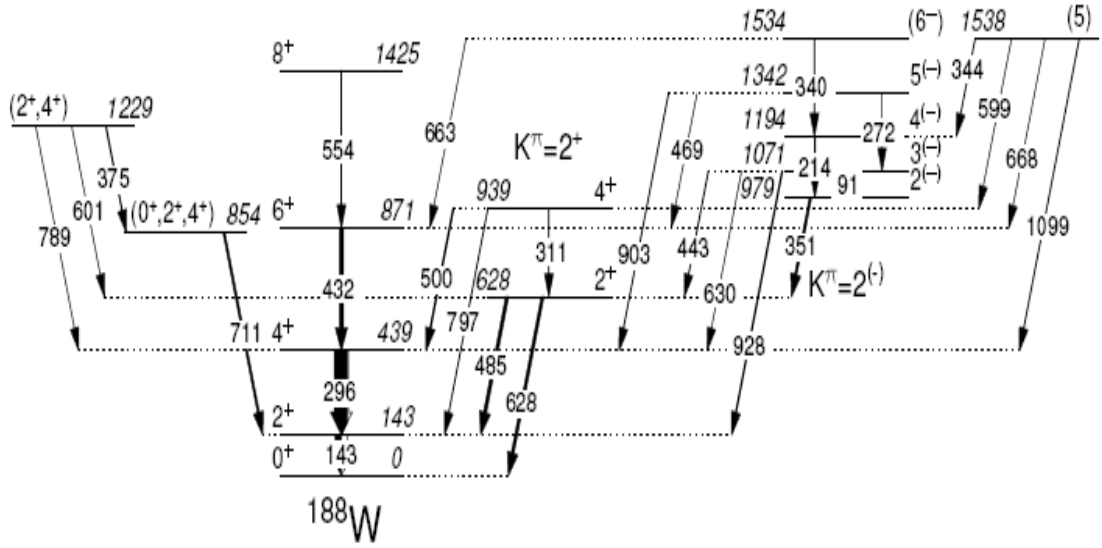

Figure 5.3: The proposed level scheme for ^{188}W as reported in reference [46]. The width of the arrows is proportional to the relative γ-ray intensities (black) and the calculated relative intensities of electron conversion (white).

In the current work, the β-delayed γ-ray spectrum of ^{188}W was generated from the coincidence correlations between the parent nuclei, ^{188}Ta and subsequent β^{-} particles. Figure 5.4 shows the β-delayed γ-ray spectrum for events coming within the first 100 s after the implantation of ^{188}Ta in the current work. The total number of implanted ions of the parent nucleus ^{188}Ta was 4132. A random background was subtracted in Figure 5.4 using a normalization factor to give a background-subtracted spectrum.

Three previously reported peaks at energies 143, 297 and 434 keV were observed, corresponding to the decays from the yrast 2^{+}, 4^{+} and 6^{+} states in ^{188}W respectively. Decays from yrast states with spin/parity of 8^{+} (E_{γ}=554 keV) or higher as reported in reference [46] were not observed in the present work. Information on the yrast γ rays energies and intinsities observed in the current work are summarized in Table 5.1.

Gamma-ray energy peaks at 184, 204 and 401 keV are also identified in the beta-delayed spectrum (figure 5.4). These transitions have been reported by Lane *et al.* [129] following the decay of an isomeric state in ^{188}W with a lifetime in the 100ns regime. The current work does not have sufficient statistics for a gamma-gamma coincidence

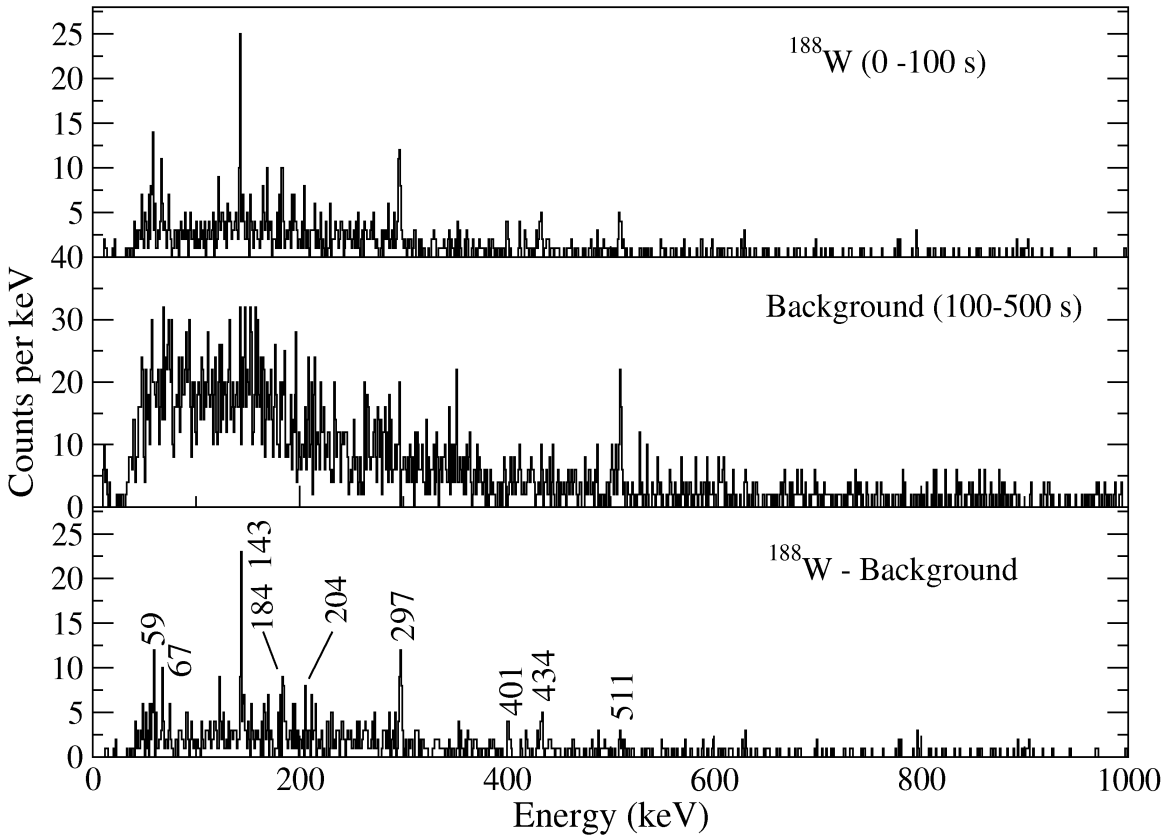

Figure 5.4: (*upper*) Beta-delayed γ-ray spectrum following decay events associated with ^{188}Ta primary fragments which populate ^{188}W. A time condition that the β-particle must be measured within 100 seconds of the secondary beam implant in the active stopper has been applied to this spectrum; (*middle*) the background spectrum associated with the population of ^{188}W for a time period between 120-500 s; (*lower*) Beta-delayed γ-ray background subtracted spectrum of ^{188}W.

analysis of the decays from this recently reported isomer.

The logft values were calculated assuming ground-state mass values taken from reference [2] of 4854(196) keV. For the ^{188}Ta decay, the logft value was estimated assuming a direct β^- feeding branch to the yrast $I^\pi = 6^+$ in ^{188}W. However, the observation of discrete transitions associated with the isomer decay branch reported by Lane *et al.*, suggests some degree of competing direct feeding through a parallel branch in ^{188}W. There is no evidence in the current work that the decays from the reported isomer feed the $I^\pi = 6^+$ yrast state in ^{188}W. Accordingly, it is assumed that the β^- decay feeding from the decay of ^{188}Ta leads to two parallel cascades of gamma rays with 53% of direct feeding to the yrast $I^\pi = 6^+$ state and the remainder feeds to

Table 5.1: Energies, relative intensities, total internal conversion coefficient (α_{tot}), β intensities and deduced logft values associated with γ-ray transitions observed in the β-decay of ^{188}Ta$\rightarrow$ ^{188}W.

E_{level}	E_γ (keV)	I_γ (keV)	α_{tot}[130]	I_{tot}	$I_i \rightarrow I_f$	I_β (%)	logft	$\frac{I_{\beta^- - \gamma}(2^+ \rightarrow 0^+)}{I(\beta^-)}$ (%)
143	143	100(22)	1.03	203(44)	$2^+ \rightarrow 0^+$	-	-	94(36)
440	297	123(31)	0.09	134(35)	$4^+ \rightarrow 2^+$	-	-	-
874	434	80(26)	0.04	83(26)	$6^+ \rightarrow 4^+$	53(20)	5.82(20)	-

the isomeric state. Under these assumptions, it is possible to derive a lower limit for the logft value of 5.82(20) from the direct β^- decay transition to the $I^\pi = 6^+$ state from the measured half-life of ^{188}Ta of 19.8(27)s.

The beta decay half life for this β^--decaying state in ^{188}Ta was also measured using a single exponential decay curve and linear background fit to give a half-life of 19.8(27) s (see the lower panel of figure 5.5). The half life is also determined using the time difference between implantion and decay as shown in the top panel of Figure 5.5. This measurement represents the first measurement of the decay half-life of ^{188}Ta.

5.4 Beta-Delayed Gamma-ray Spectroscopy of ^{190}Ta $\rightarrow$ ^{190}W

The previously reported isomeric state in ^{190}W [11, 29, 131] was populated and observed in the current experiment, as shown in Figure 5.6. Four primary discrete γ-ray lines are observed at energies of 207, 357, 484 and 695 keV in the current work (see Figure 5.6). The results are in the main part consistent with the previous fragmentation study of this nucleus as described in references [11, 29]. However, in the current experiment, the previously reported peak at 591 keV is not apparent. This γ ray was previously reported to be a transition between the yrast 8^+ and 6^+ states in this nucleus [11, 29]. Further study of this ^{190}W isomeric decay and related experiments were discussed elsewhere [131].

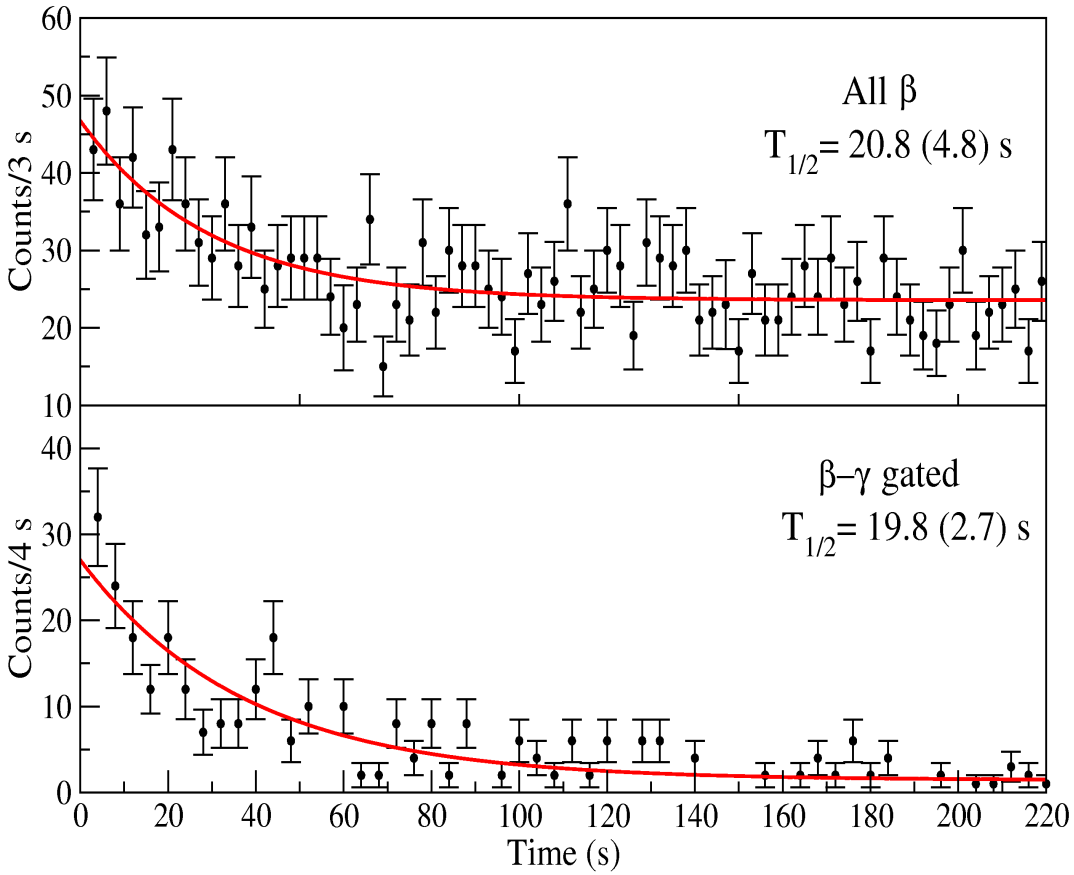

Figure 5.5: (*lower*) The decay time spectrum associated with the decay of ^{188}Ta obtained by gating on 143, 297 and 434 keV discrete γ-ray lines in ^{188}W; and (*upper*) from the time difference between implantion and decay.

The energy spectrum of β-delayed γ-rays from the decay of ^{190}Ta into ^{190}W is shown in Figure 5.7 with a time condition that only events which were registered within 30 s of a heavy-ion implantion are recorded. The upper panel of the figure shows all β-delayed γ-rays occurring within the first 30 s after the implantation of ^{190}Ta ions. The background spectrum associated with a long correlation time (between 30 and 200 s) after the implantation is shown in the middle panel. This random spectrum is normalised and subtracted from the β-delayed γ rays spectrum as shown in lower panel of Figure 5.7. The mother nucleus (^{190}Ta) was populated in the both ^{190}Ta and ^{192}Ta centred settings, providing a total of 8579 unambiguously identified ^{190}Ta ions.

Three main γ-ray lines at 207, 247 and 357 keV are observed in the β-delayed γ-ray spectrum of ^{190}W in current work. The two discrete γ-ray lines at energies of 207

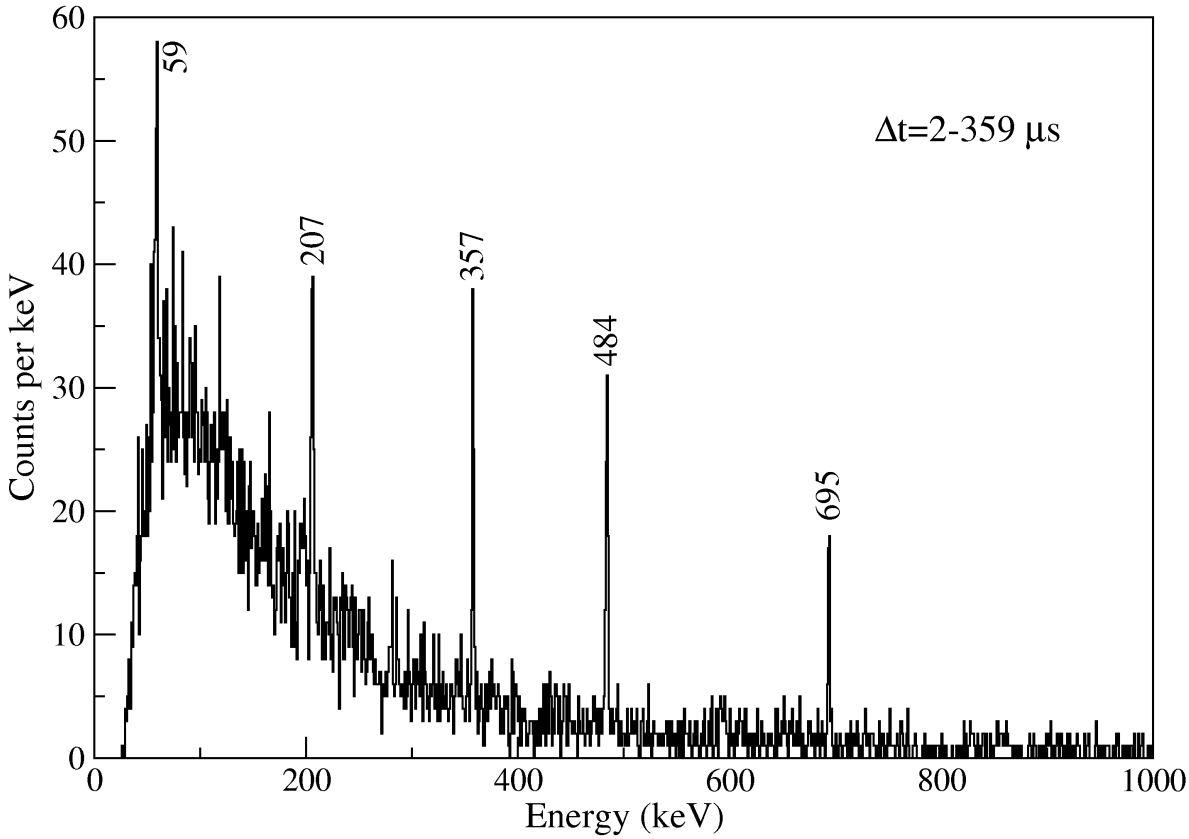

Figure 5.6: Isomeric γ-ray spectrum of the implanted ^{190}W ions in the active stopper detector from the ^{190}Ta and ^{192}Ta settings. It is noted that the data from the current work on the isomeric decay in ^{190}W does not show clear evidence for the 591 keV transition reported in references [29, 11].

and 357 keV have been reported previously in ^{190}W from the decay of the isomeric state in this nucleus (see references [11, 29, 131] and Figure 5.6 of the current work). These transitions were suggested as the decays from the yrast states with $I^{\pi} = 2^{+}$ and 4^{+} in ^{190}W. However, the transitions at 484 and 695 keV reported in the isomeric decay are not observed in the current work following the β^{-}-decay of the mother nucleus, ^{190}Ta. A gamma-gamma coincidence analysis was also performed with the data from this experiment on the isomer-delayed transitions in ^{190}W, which confirmed the mutually coincident nature of the 207 and 357 keV transitions (see Figure 5.8).

In addition to these previously reported transitions in ^{190}W, as shown in Figure 5.7, a previously unreported γ ray at 247 keV is also observed, which was not observed following the decay of the isomer (see Figure 5.6). One plausible possibility is that the 247 keV decay originates from the direct feeding to the 2_2^{+} state in ^{190}W following the

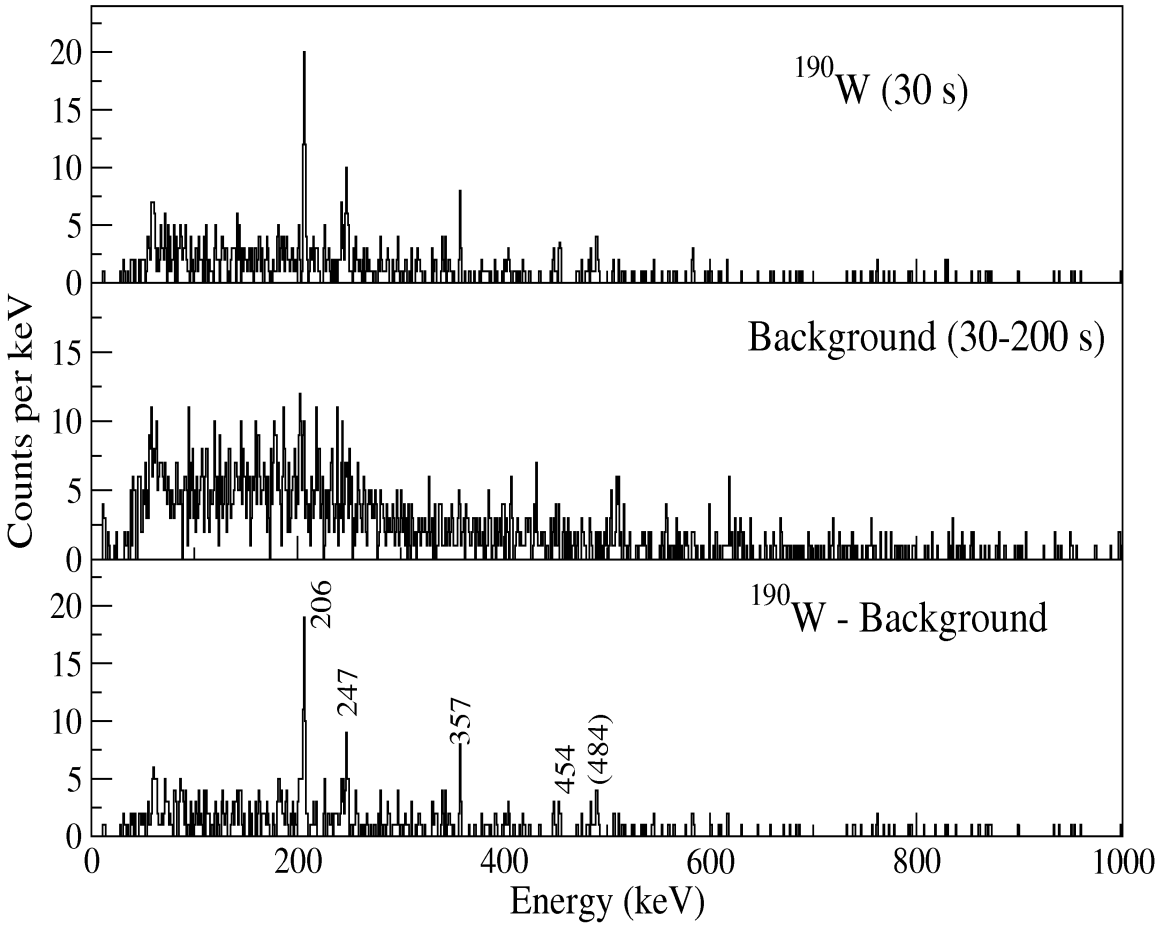

Figure 5.7: Energy spectra of (*upper*) all β-delayed γ rays following decay events associated with ^{190}Ta primary fragments which populate ^{190}W within 30 seconds of the implantation in the DSSSDs; (*middle*) random background spectrum for ion-β^- time correlation gate between 30 and 200 s after implantation; and (*lower*) β-delayed γ-ray spectrum for ^{190}W after the subtraction of the normalised random background.

β^--decay of the mother nucleus, ^{190}Ta. This would represent the $I^\pi = 2^+$ bandhead of the nominal γ vibrational band in this nucleus. The limited statistics in the current beta-delayed data preclude a gamma-gamma coincidence analysis to prove the direct feeding of the 247 keV line into the yrast $I^\pi = 2^+$ state. However, this interpretation can be made using the following arguments:

(i) There are no other gamma-ray transitions of this intensity present in the ^{190}Ta correlated, beta-delayed spectrum shown in Figure 5.7; (ii) There is a notable lack of a 485 keV transition in the beta-decay data. This transition is assumed to decay from the $I^\pi = 6^+$ to $I^\pi = 4^+$ member of the ^{190}W ground state band as reported in references [11, 29, 131] and the current work from the study of the isomeric decay of ^{190}W. This,

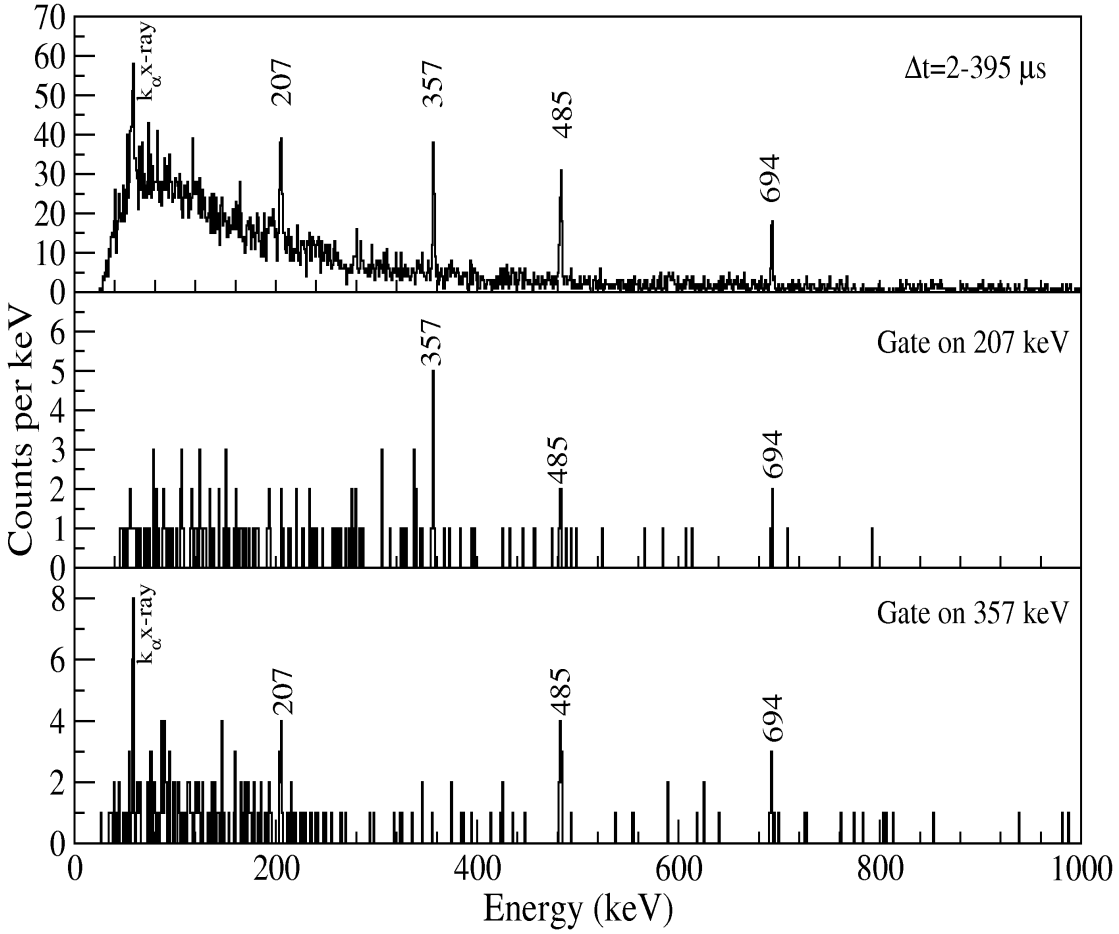

Figure 5.8: The upper spectrum is the gamma single of ^{190}W isomeric transition ions. The lower two spectra are ^{190}W isomer-delayed gamma-gamma coincidence gates on the 207 keV transition and on the 357 keV transition respectively.

together with intensities (see Table 5.2) for the observed decays from the 4^+ and 2^+ yrast states at 564 and 207 keV respectively in Figure 5.7 implies a spin of $3\hbar$ for the beta-decaying state in ^{190}Ta.

The assumption of a spin of $3\hbar$ for the beta-decaying state in ^{190}Ta restricts likely spin/parities (assuming direct population) for the state which decays by the 247 keV transition to 2^+, 3^+ and 4^+. Of these, the 2^+ assignment is favoured on the basis that states of higher spins at excitation energies of 454 keV would be yrast in such a decay scheme. The assumption of a 2_2^+ assignment for this state is further supported by the observation of a weak transition at energy 454 keV in the beta-delayed spectrum for transitions in ^{190}W (see Figure 5.7), which would represent the direct transition from the 2_2^+ state to the 0^+ ground state in ^{190}W.

Table 5.2: Energies, relative intensities, total internal conversion coefficient (α_{tot}), β intensities and log*ft* of the γ-ray transitions observed in the β-decay of ^{190}Ta→ ^{190}W.

E_{level}	E_γ (keV)	I_γ (keV)	α_{tot}[130]	I_{tot} [a]	$I_i \rightarrow I_f$	I_β (%)	log*ft*	$\frac{I_{\beta^- - \gamma}(2^+ \rightarrow 0^+)}{I(\beta^-)}$ (%)
207	207	100(19)	0.29	129(24)	$2^+ \rightarrow 0^+$	$17(^{+21}_{-17})$	$6.3(^{+\infty}_{-0.4})$	97(23)
454	247	60(14)	0.16[a]	69(16)	$2^+_2 \rightarrow 2^+$	61(19)	5.65(24)	-
454	454	24(10)	0.03	25(11)	$2^+_2 \rightarrow 0^+$	61(19)	5.65(24)	-
564	357	30(12)	0.05	32(13)	$4^+ \rightarrow 2^+$	22(8)	6.08(23)	-

[a] Calculated assuming the extremum of a pure E2 multipolarity for the $2^+_2 \rightarrow 2^+_1$ decay.

Figure 5.9 shows the systematics of the low-lying states in even-even tungsten isotopes with A=180→192 including the 2^+_2 state, which is usually associated with the bandhead of the K^π=2^+ γ-vibrational band. It is noted that the assumption of the second 2^+ state in ^{190}W at an excitation energy of 454 keV is in line with the trend expected for this region, with the ongoing, systematic decrease in the energy of the 2^+_2 state relative to the yrast 4^+ states in this isotopic chain approaching the N=116 isotone, ^{190}W.

The half life measurement for the β^--decay of ^{190}Ta is shown in Figure 5.10. This shows the decay curve of ^{190}Ta using the data fitted for the time difference between implantion and β-decay (upper) and gated on discrete γ-ray lines identified in ^{190}W daughter nuclei. The log*ft* values were calculated (see Table 5.2) assuming a Q_{β^-} value of 5634(466) keV taken from reference [2]. The proposed level scheme of ^{190}W populated following the decay of ^{190}Ta is shown in Figure 5.11.

5.5 Beta-Delayed Gamma-ray Spectroscopy of ^{192}Ta → ^{192}W

The β-delayed γ-ray spectrum for ^{192}W is shown in Figure 5.12 within an ion-β^- correlation time of upto 15 s. The total number of implanted mother nucleus ^{192}Ta

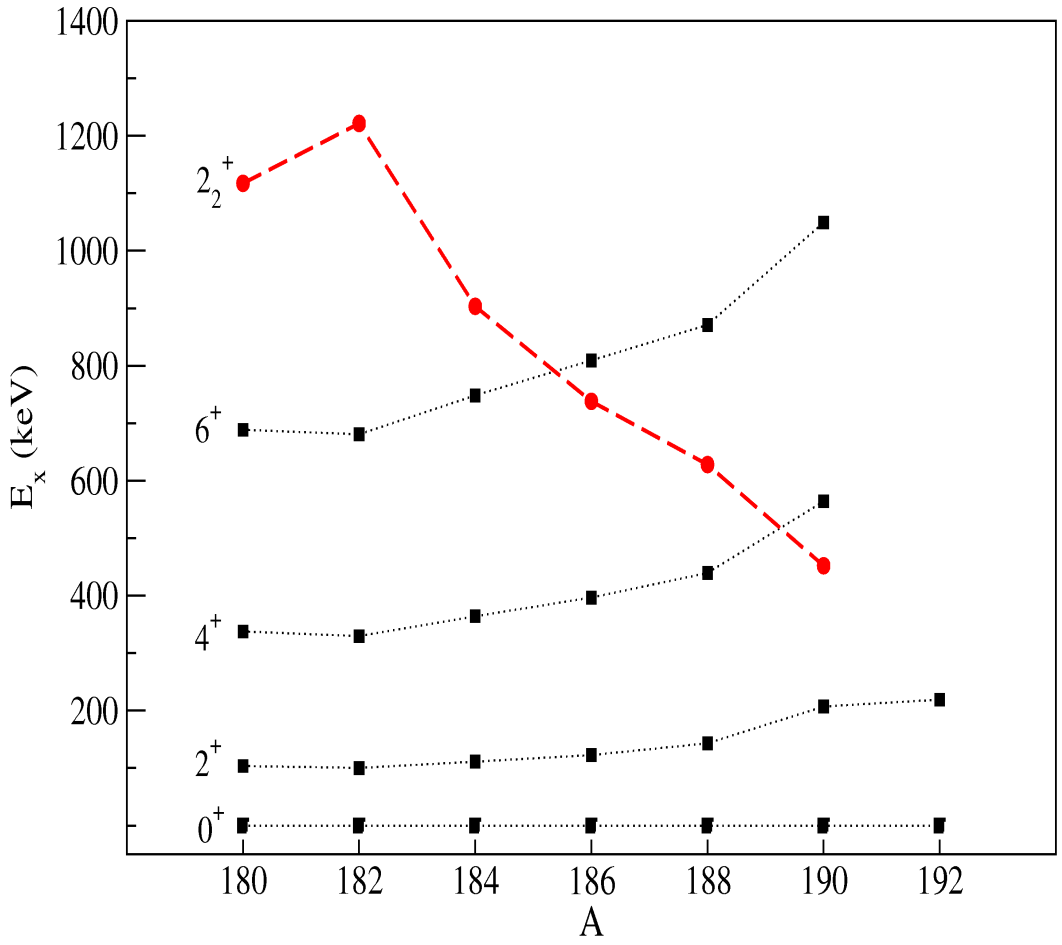

Figure 5.9: Systematic behaviour of the low-lying states of even-even W-isotopes A=180→192. The red dashed levels correspond to the second excited 2^+ states. The data taken from Ref. [3] and the current work.

was 1722 ions. A single peak at a γ-ray energy of 219 keV is evident in the β-delayed γ-ray spectrum for the daughter nucleus ^{192}W. The characteristics of this peak are summarized in Table 5.3. This line is interpreted as the yrast $2^+ \rightarrow 0^+$ transition in ^{192}W.

The half-life measurement for ^{192}Ta was determined gating on the 219 keV γ-ray line to be 2.6 (0.9) s (see Figure 5.13). This was consistent with a value derived from the time difference between implantion and β-decay as shown in Figure 5.13. The Q_{β^-}= 6501 keV is an extrapolated value taken from reference [132]. The likely spin of the decaying state in the ^{192}Ta parent nucleus can be restricted to 1 or 2$\hbar$ on the basis of the expected β^- decay selection rules and the lack of any apparent line associated with the $4^+ \rightarrow 2^+$ transition in ^{192}W. However, it is noted that on the basis of the

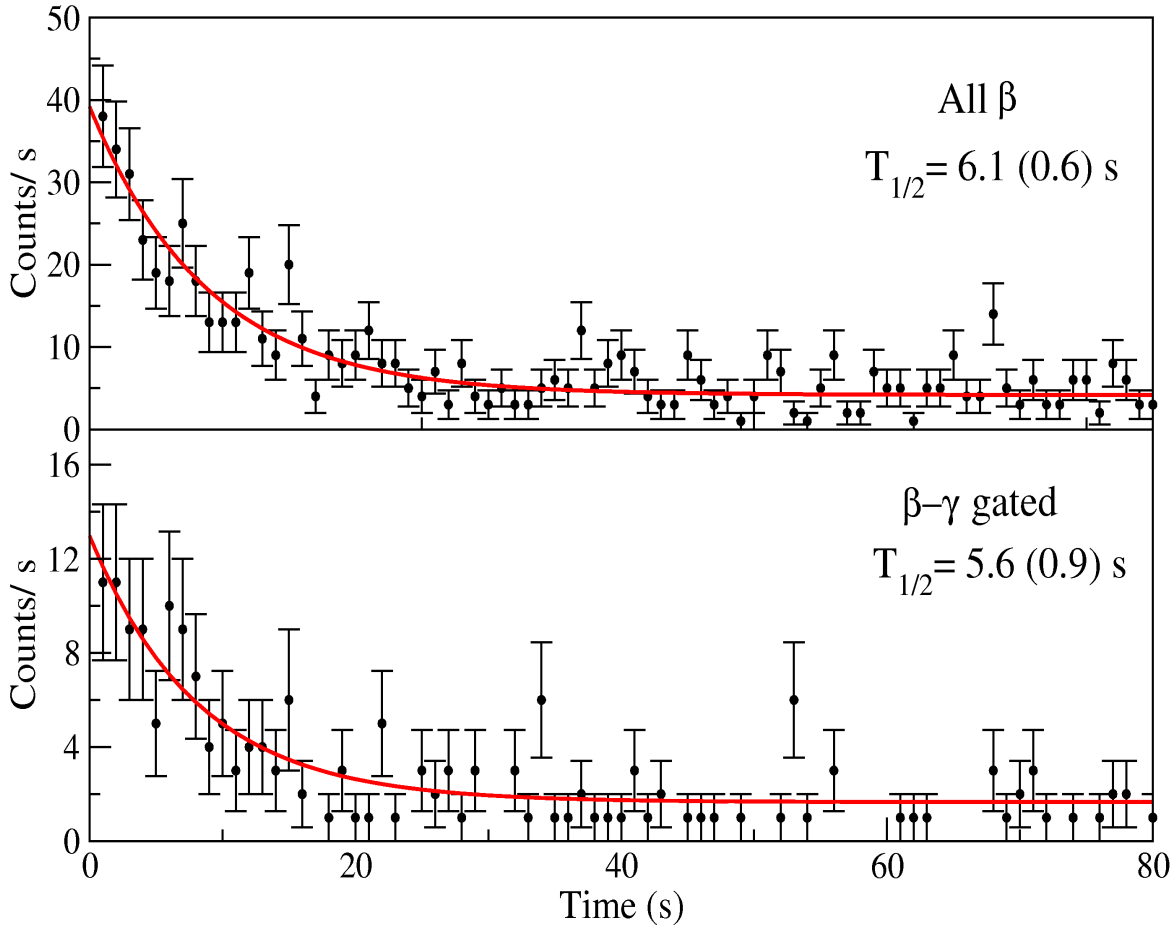

Figure 5.10: (*upper*) Decay time curve for ^{190}Ta obtained from the time difference between implantation and β-decay of ^{190}Ta; and (*lower*) from gating on the discrete γ-ray line transitions of the daughter nucleus ^{190}W. The data were fitted with a single exponential decay plus a linear random background.

statistics in the current work as shown in Figure 5.12, we can not rule out the possible population of higher spin states in the yrast cascade in ^{192}W and thus a higher spin for the beta-decaying state. From a comparison of the number of implants and associated β^-- γ-ray coincident event (see Table 5.3), there is no strong evidence of direct feeding from the β^- decay of ^{192}Ta to the ground state of ^{192}W, although such a branch can not be exclusively ruled out in the current work. The lower limit for the $\log ft$ for this decay given in Table 5.3 assumes 100% feeding in the β^- decay to the proposed yrast $I^\pi = 2^+$ state in ^{192}W.

It is noted that the 219 keV is almost the same energy as the yrast $2^+ \rightarrow 0^+$ transition in the $N = 118$ isotone, ^{194}Os ($E(2^+) = 218$ keV) [133]. Indeed similar,

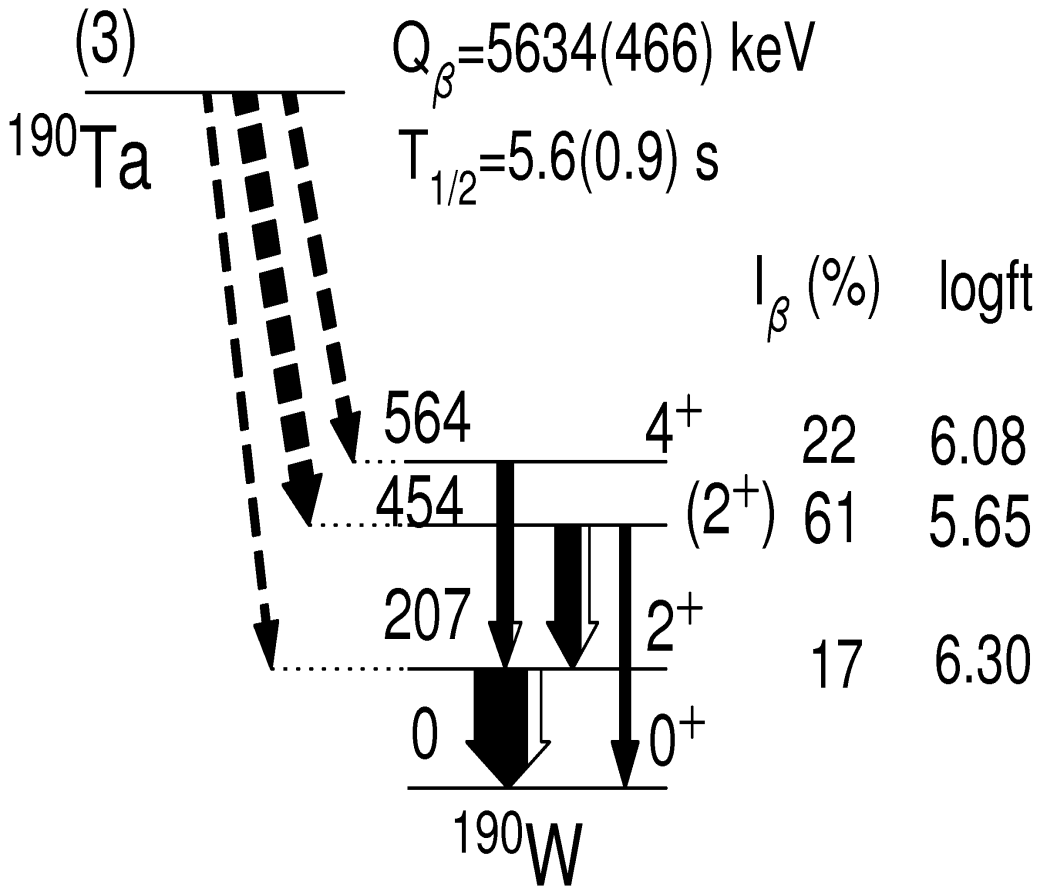

Figure 5.11: Proposed level scheme for ^{190}W populated following the β-decay of ^{190}Ta. The Q_β value was deduced from reference [2]. The β-feeding and $\log ft$ values are given in the right side of the level scheme.

near-isospectral behaviour is also evident for the $N = 116$ isotonic doublet ^{190}W and ^{192}Os ($E(2^+)\approx$207 keV) [41]. The possibility that the 219 keV transition observed in the present work is the result of a mis-assignment of the beta-decay of ^{194}Re into ^{194}Os can be discounted as this decay has been studied in the same data set, with multiple other transitions observed resulting from decays from higher spin states in ^{194}Os [134] evident for this decay, which are not observed in the current ^{192}W analysis.

5.6 Half-Life Distributions

For N radioactive nuclei present at time t, the number of decaying nuclei dN during a time dt is proportional to original nuclei number N. This relation can be expressed by:

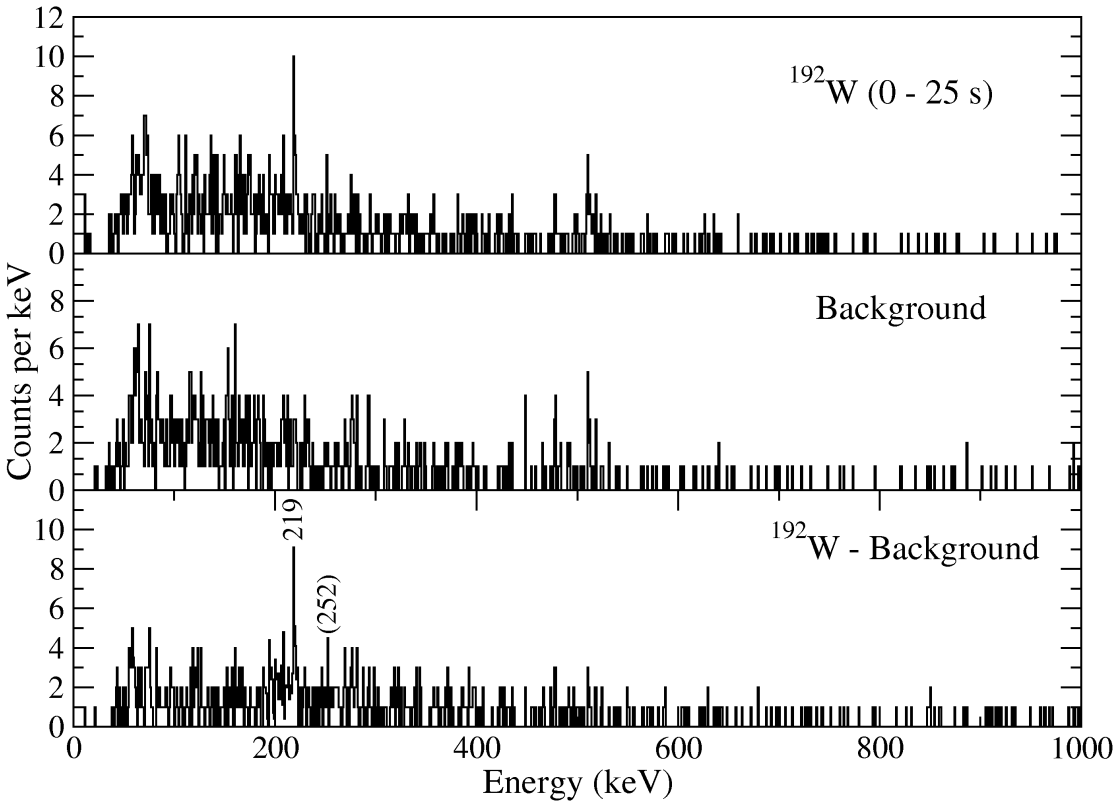

Figure 5.12: (*upper*) Beta-delayed γ-ray spectrum following decay events associated with ^{192}Ta primary fragments which populate ^{192}W within 15 seconds of the ^{192}Ta implantation; (*middle*) associated random background spectrum within a time window of 15→200 s; and (*lower*) β-delayed γ-ray spectrum of ^{192}W after the subtraction of the normalised random background.

$$\lambda = -\frac{(dN/dt)}{N} \tag{5.1}$$

where λ is the decay constant. Integrating this equation leads to the exponential radioactive decay law:

$$N(t) = N_0 e^{-\lambda t} \tag{5.2}$$

where N_0 is the original number of nuclei at time=0. The time necessary for half of the nuclei to decay is the half life, $t_{1/2}$, and is related to the decay constant λ by:

$$t_{1/2} = \frac{0.693}{\lambda} \tag{5.3}$$

In the current work, the decay half lives of the implanted mother nuclei were determined by measuring the time differences between the implant event times in the

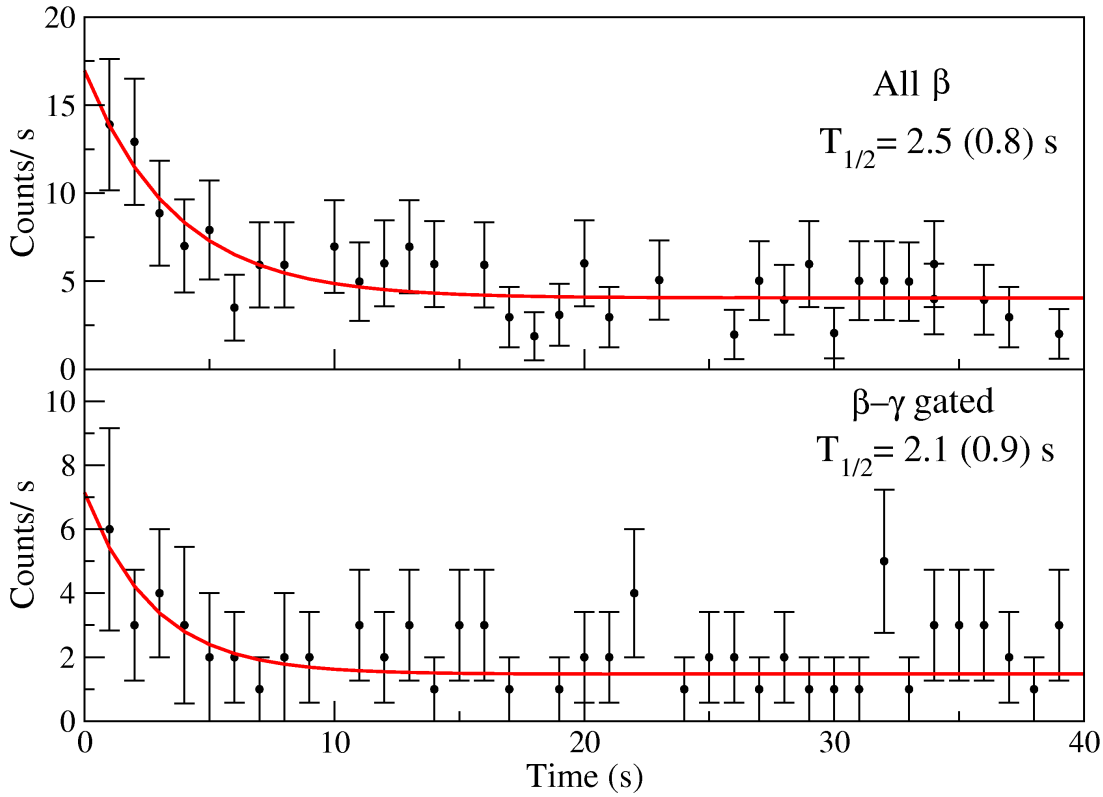

Figure 5.13: Decay time curve of ^{192}Ta showing (*upper*) fragments-β correlation time difference; and (*lower*) beta-decay curve gated on the 219 keV of the daughter nucleus ^{192}W. The data were fitted with a single exponential decay plus a linear background.

DSSSDs and their subsequent correlated β particle events in the same or directly neighbouring pixels. The decay curve was fitted to a single exponential decay plus a constant contribution for the random background, i.e;

$$N(t) = N_0 e^{-\lambda t} + c \tag{5.4}$$

where c is the level of random background. Least-squares fits to the decay curves associated with the β^--delayed events were used for fitting the decay time spectra. The β^--decay spectra for the implanted Hf, Ta, W and Re ions in the current work from the ^{190}Ta and ^{192}Ta settings are shown in Figures 5.14, 5.15, 5.16 and 5.17 respectively. Systematics of the experimental half lives of these nuclear species are shown in Figures 5.18 and 5.19 against the mass number, A, and Q_{β^-} values respectively. The Q_{β^-} values for all the nuclei measured in the current work are derived from systematic trend taken from taken from references [2, 132].

Table 5.3: Energy, relative intensity, total internal conversion coefficient (α_{tot}), β intensity and logft of the γ-ray transition observed in the β-decay of ^{192}Ta $\rightarrow$ ^{192}W.

E_{level}	E_γ (keV)	I_γ (keV)	α_{tot}[130]	I_{tot}	$I_i \rightarrow I_f$	I_β (%)	logft	$\frac{I_{\beta^- - \gamma}(2^+ \rightarrow 0^+)}{I(\beta^-)}$ (%)
219	219	100(26)	0.23	123(32)	$2^+ \rightarrow 0^+$	100	5.40	96(37)

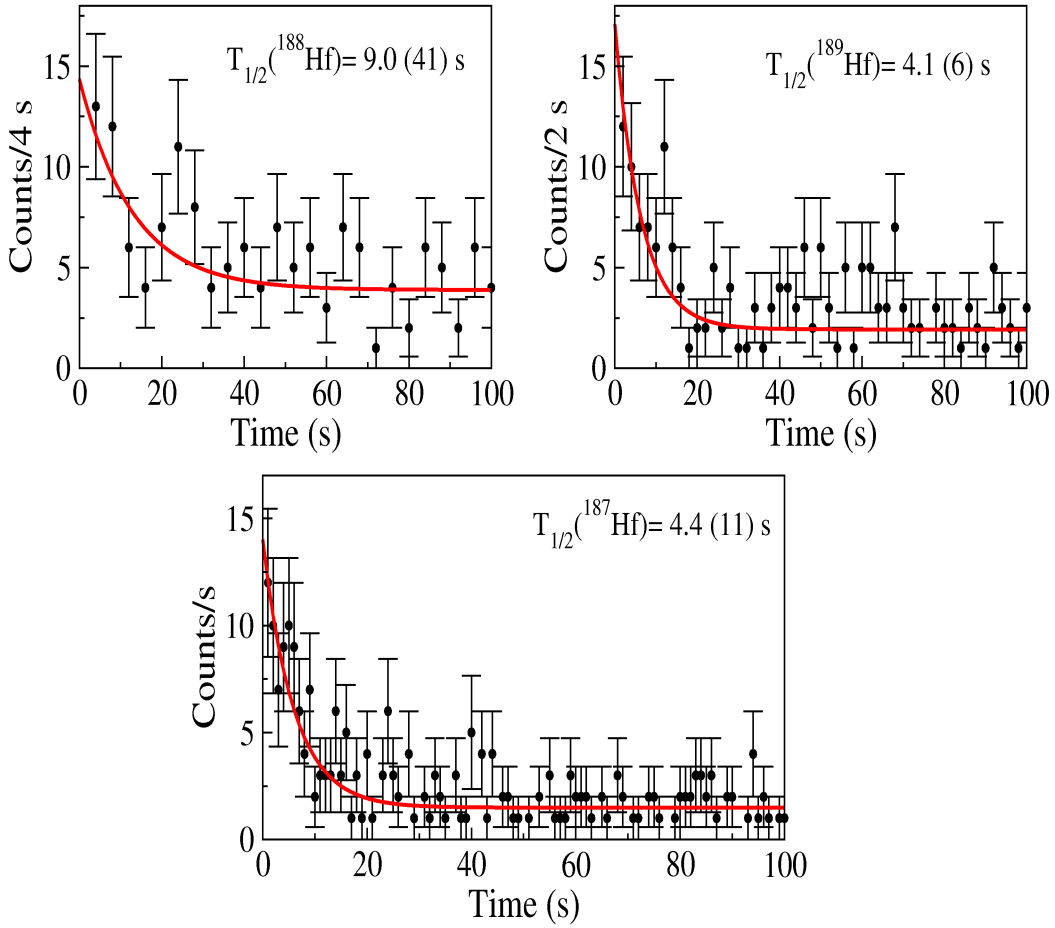

Figure 5.14: β-decay time spectra for ^{187,188,189}Hf isotopes populated in the current work from the two settings centred on the transmition of ^{190}Ta and ^{192}Ta.

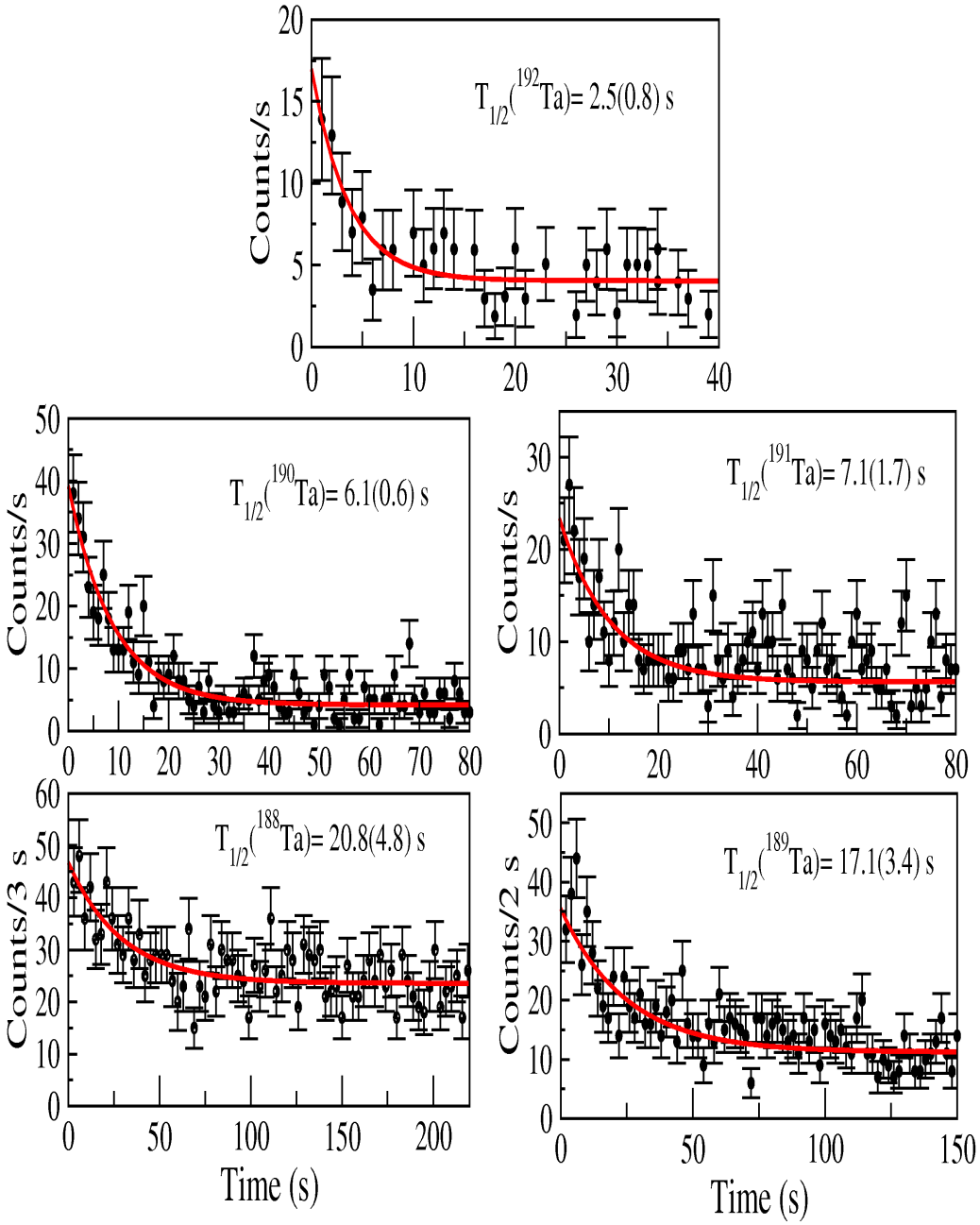

Figure 5.15: β-decay time spectra for ^{188,189,190,191,192}Ta isotopes populated in the current work from the two settings centred on the transmition of ^{190}Ta and ^{192}Ta.

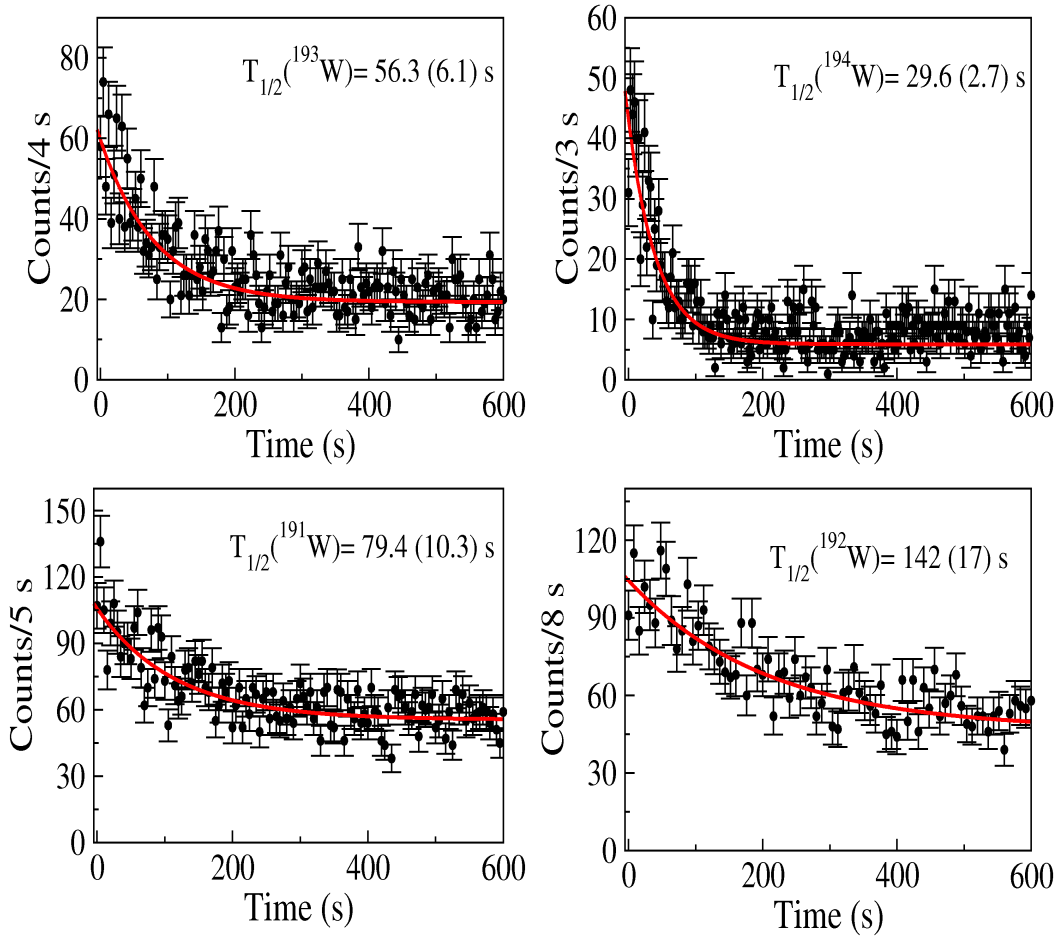

Figure 5.16: β-decay time spectra for ^{191,192,193,194}W isotopes populated in the current work from the two settings centred on the transmition of ^{190}Ta and ^{192}Ta.

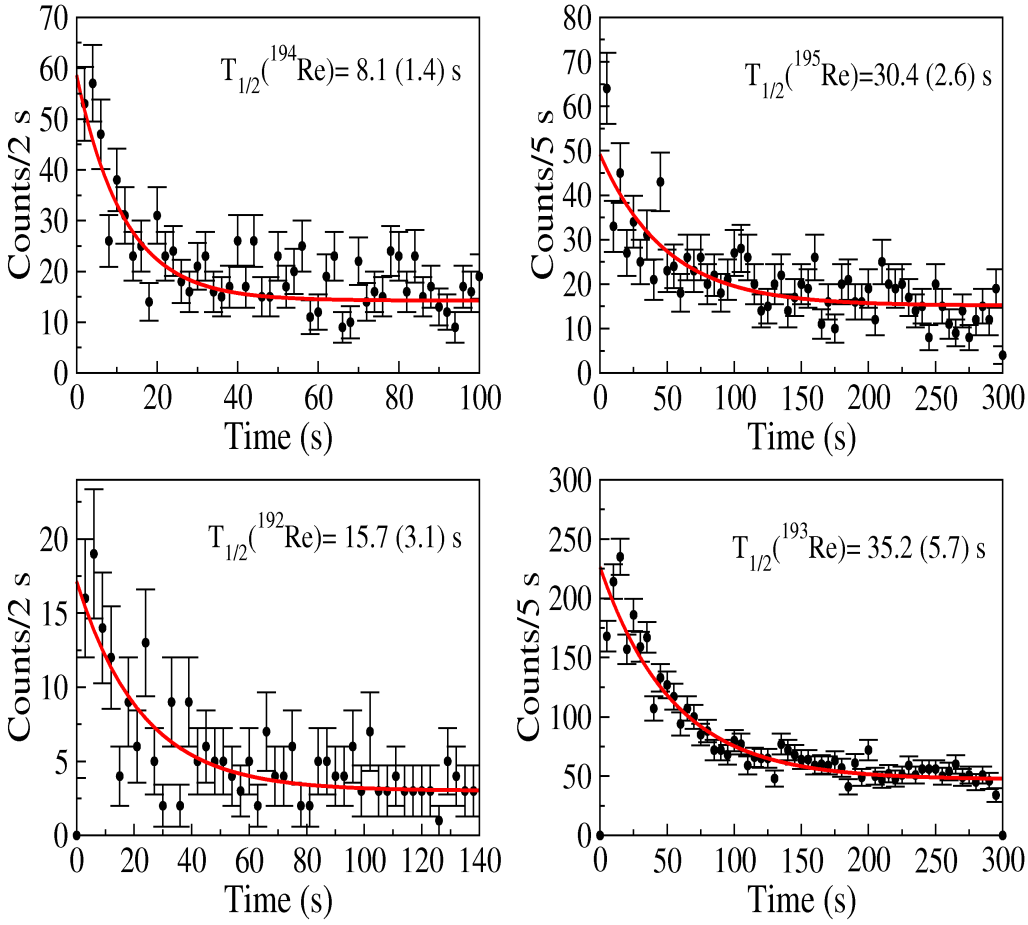

Figure 5.17: β-decay time spectra for ^{192,193,194,195}Re isotopes populated in the current work from the two settings centred on the transmition of ^{190}Ta and ^{192}Ta.

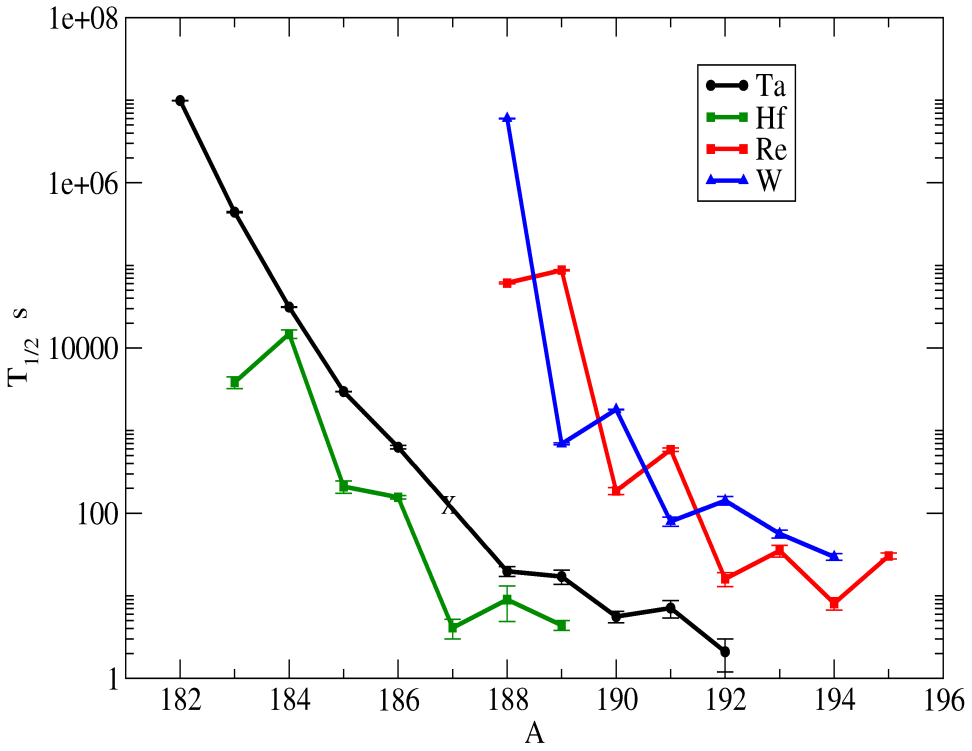

Figure 5.18: Experimental half lives values of β^--decay nuclear species Hf, Ta, W and Re isotopes versus the mass number, A including the half life results obtained from the current work. The symbol X indicates ^{187}Ta which does not have a current experimental value of its decay half life.

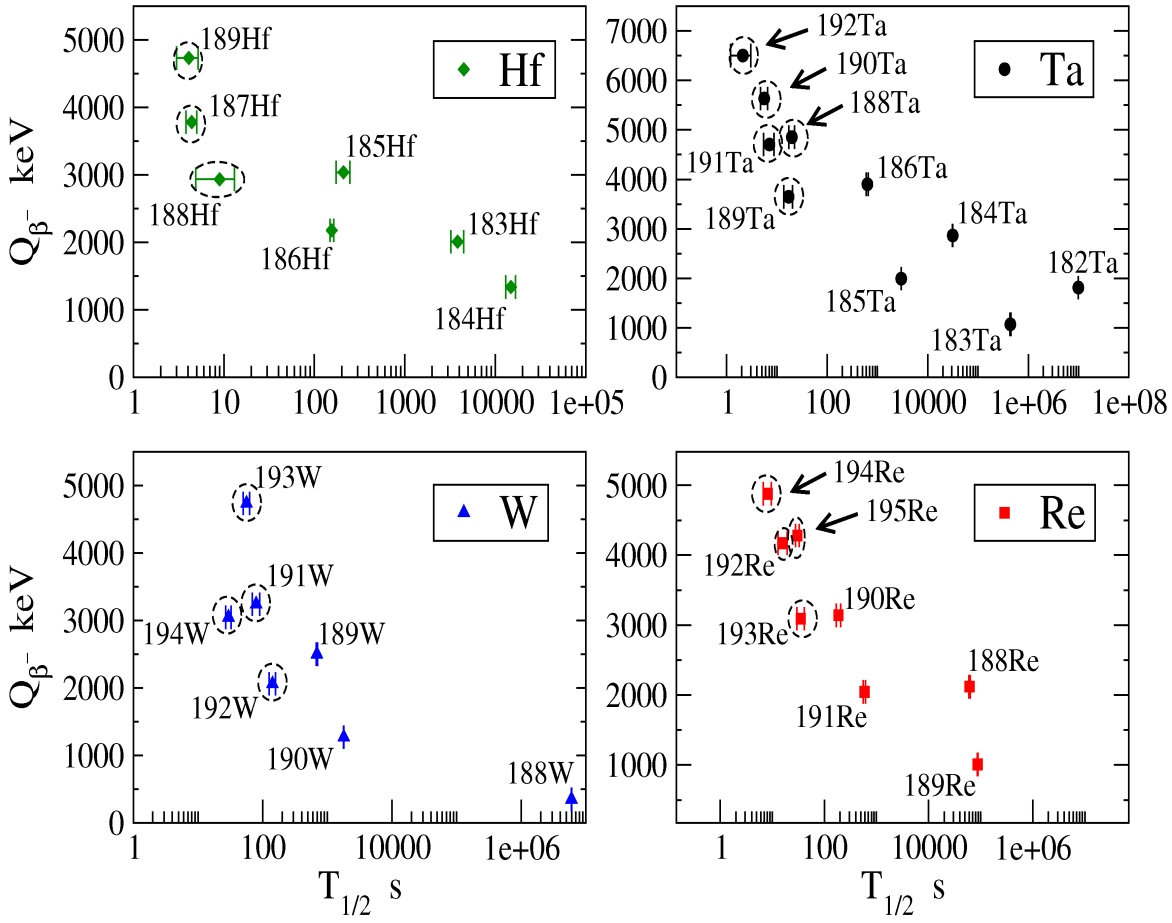

Figure 5.19: Systematics of β^--decay half lives for Hf, Ta, W and Re isotopes against Q_{β^-} values including the half life results obtained from the current work. The nuclei with half lives obtained from the current work are indicated by dashed circles. The Q_{β^-} values were taken from references [2, 132].

Chapter 6

Nuclear Structure and Interpretation of Results

6.1 Discussion of Possible Sub-Shell Closure for the A∼190 Region?

The energy ratio R(4/2)= E(4^+)/E(2^+) is arguably the best indicator of changes in low-lying nuclear structure [27]. It has a limiting value of 2.00 for a perfect harmonic quadrupole vibrator [135] and an idealized value of 3.33 for a perfect symmetric rotor. A value of R(4/2)≈2.5 is indicative of a γ-soft rotor [25]. The energy ratio R(4/2) against the proton number for even-even nuclei in this region with N=98 to N=118 is shown in Figure 6.1. This systematics show a gradual decrease in the value of the R(4/2) for tungsten isotopes with increasing the neutron number from $^{182}W_{108}$ (R(4/2)= 3.29) to $^{188}W_{114}$ (R(4/2)= 3.07). This is followed by a very dramatic decrease at $^{190}W_{116}$ to a value of R(4/2)= 2.72 approaching the γ-soft limit of R(4/2)= 2.5.

One explanation for this sudden deviation of the energy ratio R($4^+/2^+$) in ^{190}W compared to ^{188}W is a possible proton sub-shell closure in this region. These excitation energy systematics as shown in Figure 6.1 indicate a different pattern for ^{190}W compared with lighter tungsten isotopes. Also, this pattern is different from that observed for other nearby γ-soft nuclei $^{192}Os_{116}$ [41] and $^{196}Pt_{118}$ [40]. The energy systematics evidence for the possibility of a sub-shell effect for the A∼190 region is similar to that reported at Z = 64 for the N=78→88 (see references [136, 137]). The systematics for the Z=64 shell closure are also shown on the right side of the same figure for a

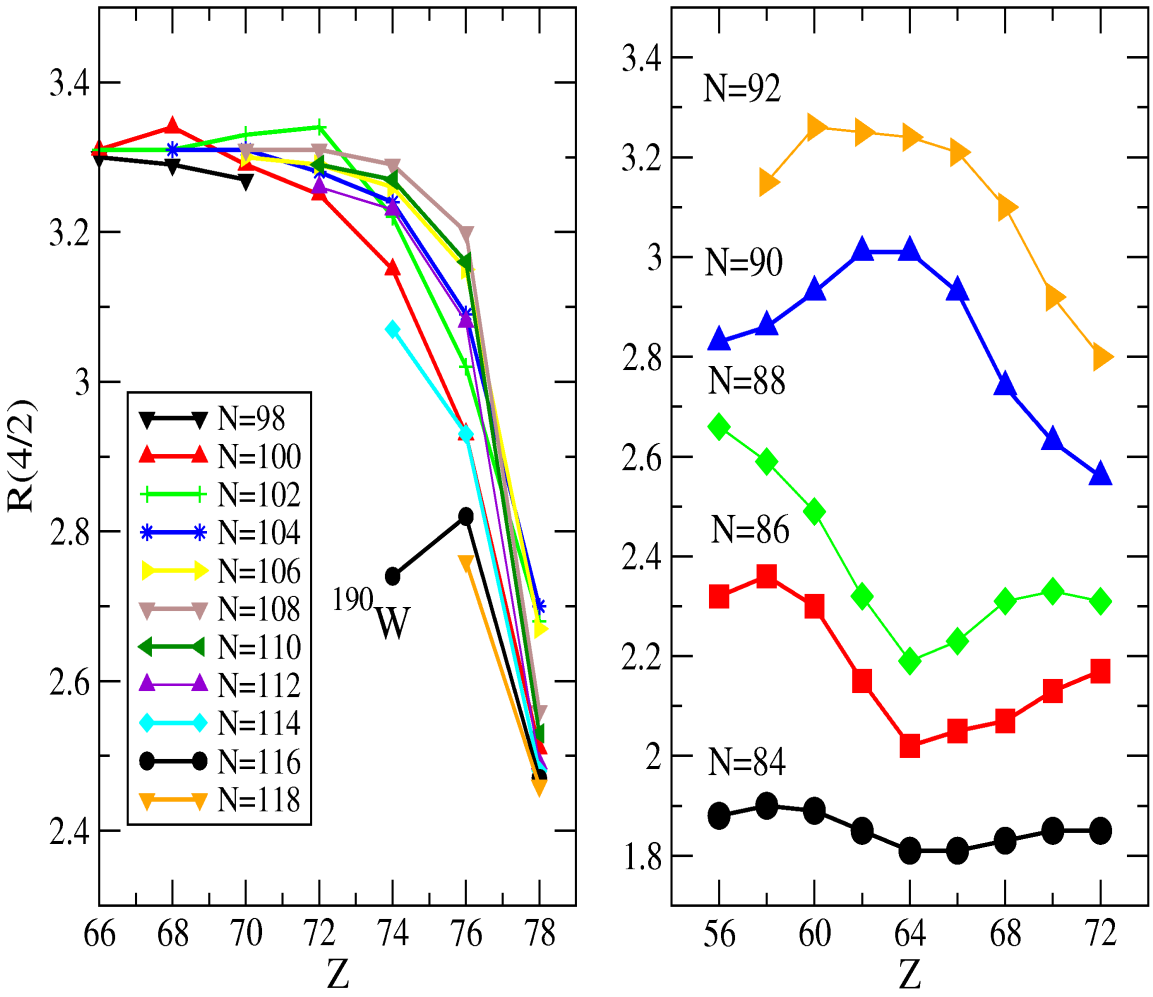

Figure 6.1: Experimental ratio of the excitation energies of the yrast $I^{\pi}=4^{+}$ and 2^{+} states R(4/2) for the even-even nuclei with Z=68→78 and for N >98 (Left). Similar plot (right) for Z=56→72 and for N=84→92, showing the effect of the sub-shell closure at Z=64. These data taken from reference [3] and the current work.

comparison.

6.1.1 $1/E(2_1^+)$ Systematics

The energy ratio R(4/2) is a key signature for changes in low-lying nuclear structure. However, for many new exotic nuclei, only energy of the first 2^+ state is measured. Therefore, Cakirli and Casten [22] have suggested a signature related to the R(4/2) value, which uses the inverse value of the energy of the first 2^+ state. In general, the energy of the first 2^+ decreases as the number of the valence nucleons increases (i.e. the collectivity increases). This general trend is opposite to the R(4/2) and thus the

$1/\mathrm{E}(2_1^+)$ systematics should follow similar behaviour to R(4/2).

Figure 6.2 shows the experimental values of the inverse of first 2^+ state energy for the A$\sim$190 region. The $1/\mathrm{E}(2_1^+)$ value is plotted versus the neutron (left) and proton (right) numbers. The left panel (for the neutrons between N=110 and N=122) exhibits a "crossing" pattern [22]. The crossing seems to occur between the N= 116 (for W and Os) and N= 120 (for Pt and Hg). The same panel also shows what is referred to in reference [22] as a "bubble" pattern (i.e. a pattern of concave and convex curves) for the same elements but for neutron number between N= 100 and 112. This "bubble" is used as potential evidence for a sub-shell effect around neutron number N=108 [138, 139]. In the right panel of the figure, the same data is plotted but as a function of proton numbers between Z=72 and 80. This systematics shows a possible beginning of the effect of localised proton sub-shell for the A$\sim$190 region which supported by the data for ^{192}W from the current work.

6.1.2 δ R(4/2) Systematics

Evidence of such a sub-shell effect and/or dramatic shape evolution with the addition/removal of two nucleons can also be seen from the *difference* in $R(4/2)$ between neighbouring even-even isotopes, i.e., $\delta R(4/2) = R(4/2)_{Z,N} - R(4/2)_{Z,N+2}$ [140]. Figure 6.3 shows this quantity for the Hf, W, Os and Pt isotopes with neutron numbers ranging from the mid-shell at $N = 104$ up to $N = 118$. The value for $\delta R(4/2)$ of > 0.3 between ^{188}W (R(4/2)= 3.07) to ^{190}W (R(4/2)= 2.72) represents one of the largest $\delta R(4/2)$ differences away from closed shells in the entire Segré chart. This provides compelling evidence for a dramatic change in the ground state structure for W isotopes in going from $N = 114$ to $N = 116$.

6.2 Discussion of γ-softness around N=116

The energy of the first excited state, $\mathrm{E}(2^+)$, and the energy ratio R(4/2) are standard signatures of the collectivity in even-even nuclei [27]. Figure 6.4 shows these empirical indicators for the even-even W and Os isotopes plotted against neutron number with N=90 to N=118, including data obtained in the current work for ^{188,190,192}W. The systematics for R(4/2) as described in Section 6.1, show a slow decrease with neu-

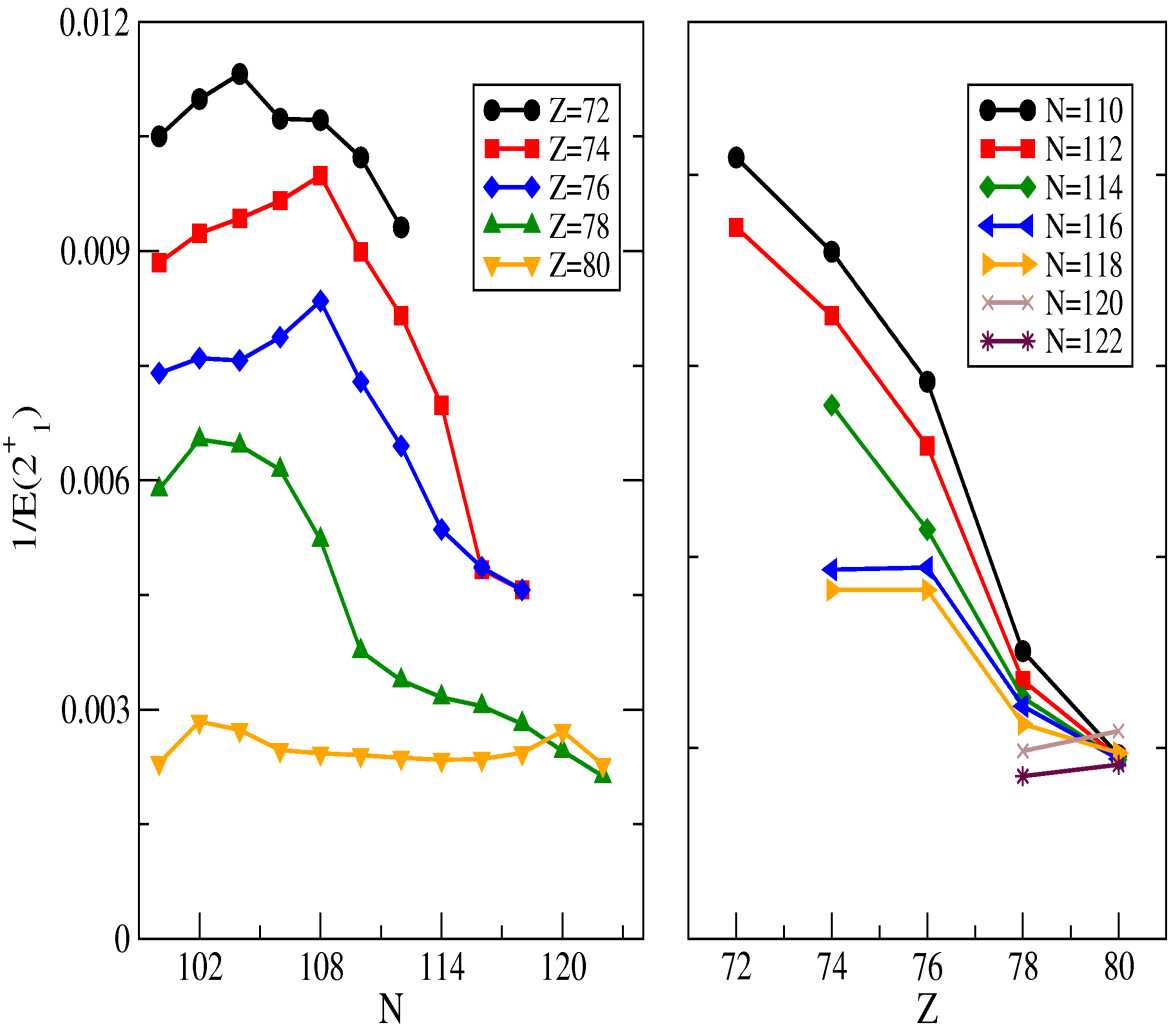

Figure 6.2: The empirical $1/E(2_1^+)$ values plotted against neutron number, N, for (left) A$\sim$150 region and as a function of the proton number between 72 and 80 (right). These data taken from reference [3] and the current work.

tron number from ^{182}W (with a value of 3.29) to 3.07 for ^{188}W (N= 108). A sudden decrease is then notable for the ^{190}W isotope which has R(4/2)= 2.7.

The E(2^+) systematics are expected to increase as the neutron number is increased in this region as the N=126 shell closure is approached. This increase in $E(2_1^+)$ seems to be continued for the heavier tungsten isotopes using the new data for the 2_1^+ energy in the N=118 isotone, ^{192}W. In the same sequence, the estimated quadrupole deformation which can be inferred from an empirical relationship with the energy of the first $I^+ = 2_1^+$ state as described by Raman *et. al.* [21] ($\beta_2 = (466 \pm 41)\ E^{-1/2}\ A^{-1}$), shows a decrease in deformation with increasing the neutron number. This general behaviour of a reduction in R(4/2) and parallel increase in the energy of the first 2^+ state in these

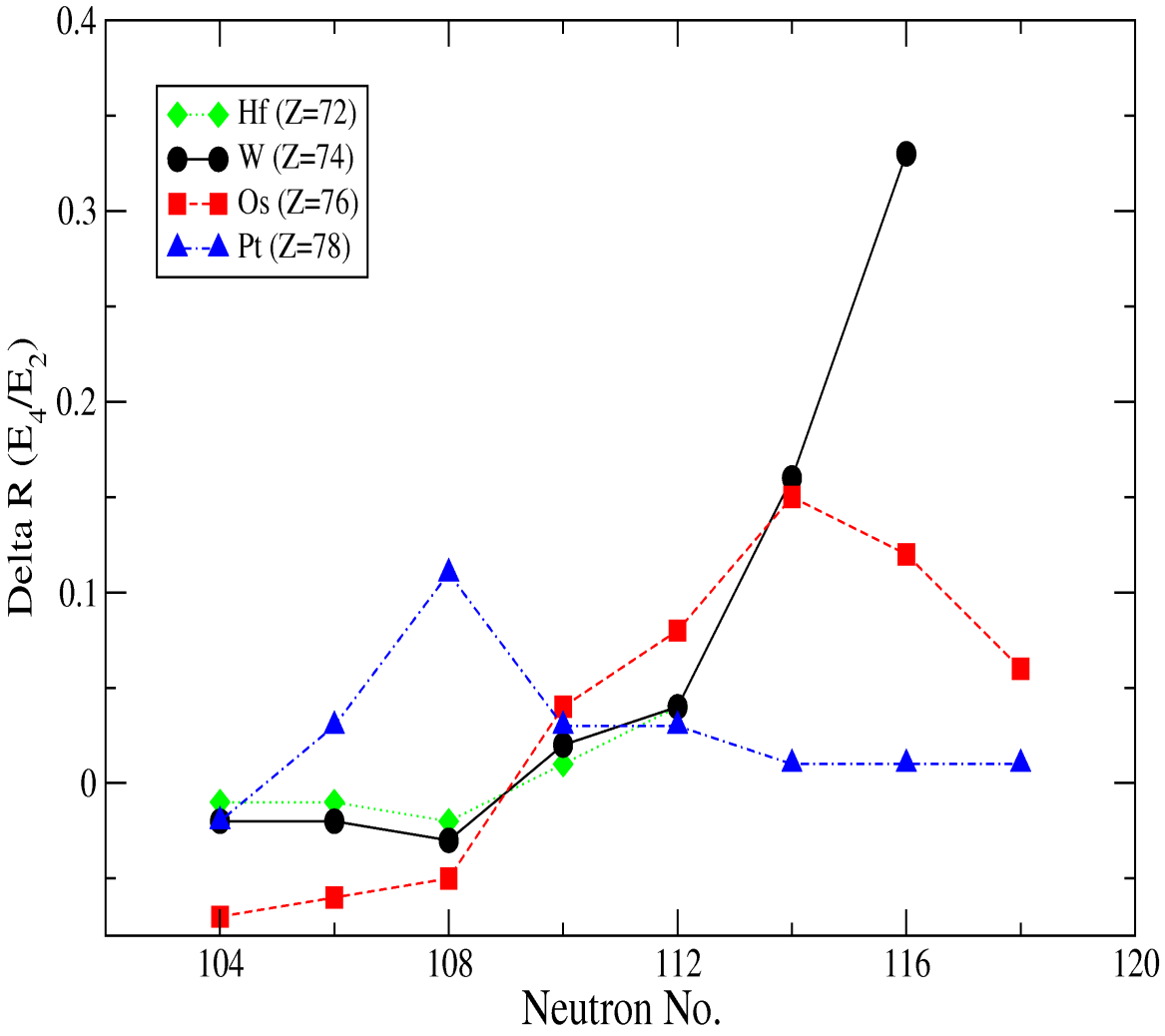

Figure 6.3: Systematics of the excitation energy difference between the energy ratio R(4/2) for heavy even-even neutron rich-nuclei with N = 104→118. These data are taken from reference [3] and the present work.

elements are indicative of the expected reduction in collectivity as the neutron number approaches the N=126 closed shell.

6.2.1 IBA-1 Calculation

The energy ratio R(4/2) in ^{190}W (E(2^+)=207 keV and E(4^+)=564 keV) can plausibly be explained as a feature of γ-softness. Jolie and Linnemann [28] have suggested the region of nuclei between ^{180}Hf and ^{200}Hg exhibits prolate-oblate deformations and phase shape transitions. A prolate to oblate phase transition is represented by the O(6) symmetry in the Interacting Boson Approximation (IBA) [35, 36, 37, 38, 39].

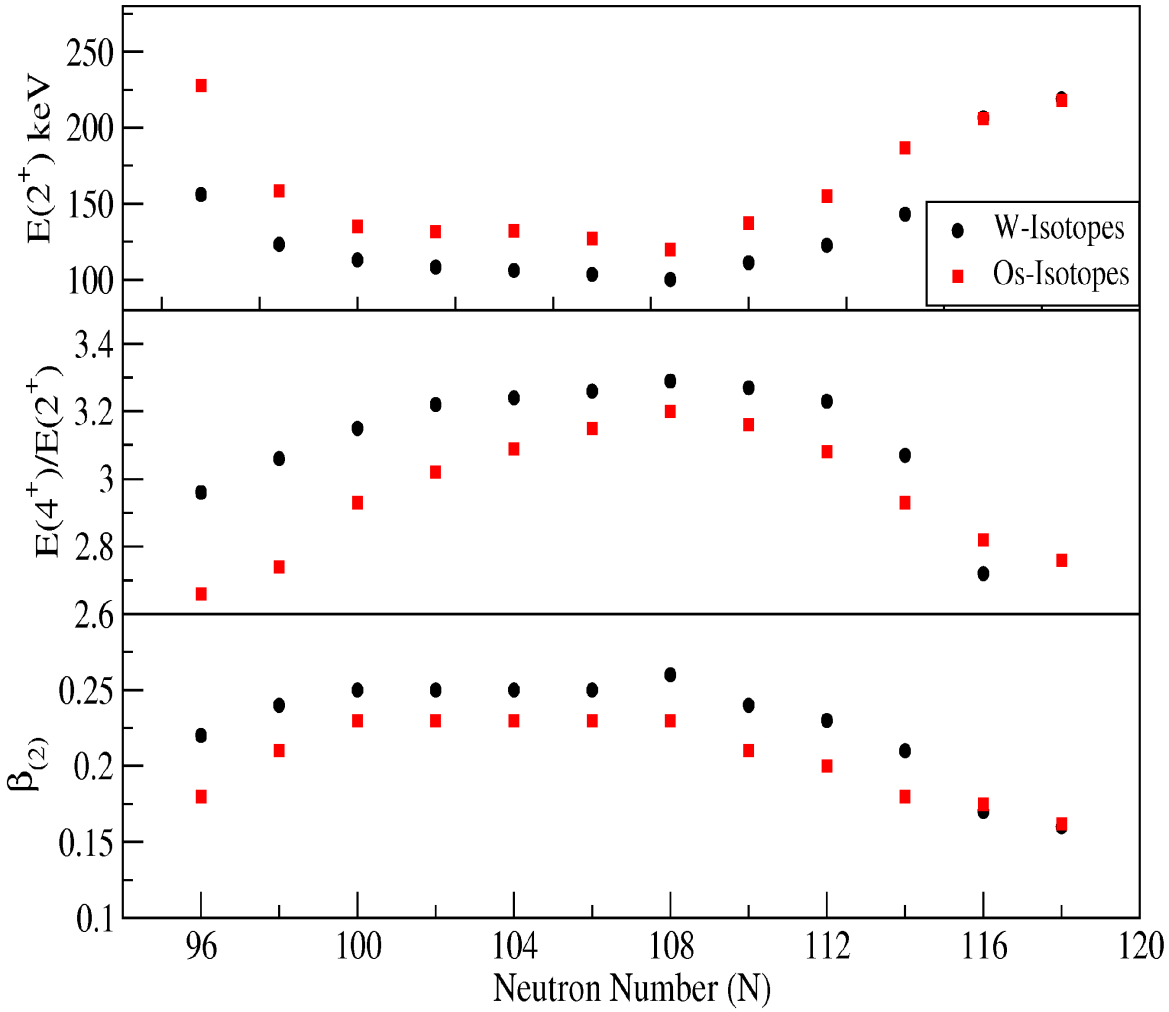

Figure 6.4: Energy systematics of the first 2^+ and the energy ratio R(4/2) for even-even W and Os isotopes, including data from the current work. The deformation parameter, β_2, is inferred from the empirical relation proposed by Raman [21].

The ^{194,196}Pt nuclei representing the idealised experimental examples of the O(6) symmetry limit, within the description of the Interacting Boson Approximation [24, 40]. The N=116 isotone, ^{192}Os, is also reported [41] to exhibit such behaviour. It therefore is interesting to apply the IBA to the tungsten isotopes, particularly to the N=116 isotone, ^{190}W, to look for further supportive evidence of prolate-oblate phase transition in this region.

To study the structure of ^{190}W, an IBA-1 [35, 36, 37, 38, 39] calculation was performed in which the Hamiltonian can be written as [141]:

$$H(\zeta) = c\left[(1-\zeta)\hat{n}_d - \frac{\zeta}{4N}\hat{Q}^{\chi}.\hat{Q}^{\chi}\right] \tag{6.1}$$

where $\hat{n}_d = d^\dagger \cdot \tilde{d}$, $\hat{Q}^\chi = (s^\dagger \tilde{d} + d^\dagger s) + \chi(d^\dagger \tilde{d})$ and N is the number of valence bosons.

This Hamiltonian has two parameters ζ and χ plus an overall scaling factor c. In this Hamiltonian, there are limiting values of these parameters which give the three dynamical symmetries: (i) ζ= 0 (for any χ) for U(5) (the $\hat{n}_d$ term); (ii) ζ= 1 and $\chi = -\frac{\sqrt{7}}{2}$=-1.32 for SU(3); and ζ=1 and χ =0 for O(6). Variation values of ζ and χ allow one to span a wide range of collective structures along the IBA symmetry triangle.

The technique for a correct position of a nucleus inside the symmetry triangle based on the Orthogonal Cross Contour (OCC) method [142]. In this method two contours of two observables will cross inside the symmetry triangle. The most useful experimental observables to obtain these contours are: (i)R(4/2); and (ii) $\frac{E(0_2^+)-E(2_\gamma^+)}{E(2_1^+)}$. These observables are chosen as they are crossing in a point inside the symmetry triangle. However, only one of these observables is available from the current data for ^{190}W, R(4/2).

The current work provides evidence for the second 2^+ state in ^{190}W (i.e., K$^\pi$=2^+, γ bandhead state) at an excitation energy of 454 keV. This observable is used with the R(4/2) to get the best fit for the IBA-1 parametrisation for ^{190}W. The values of E(2_2^+) are calculated along the R(4/2)= 2.72 contour as shown in Figure 6.5 and the results are compared with the experimental values for the low-lying states observed experimentally in ^{190}W.

The IBA-1 predicted value of I$^\pi$= 2_2^+ state in ^{190}W indicates that the yrast state 4^+ is located higher in energy than this state. However, it should be noted that in the O(6) limit, E(2_2^+)=E(4_1^+) due their common membership in the τ=2, O(5) multiplet. For any other situation the E(4_1^+) is lower than the E(2_2^+). Therefore, it is impossible to obtain a precise fit using IBA-1 for ^{190}W since the experimental value for ^{190}W has E(2_2^+)<E(4_1^+).

The energy ratio R(4/2)= 2.72 for ^{190}W does not uniquely establish this nucleus to have a γ-soft structure since this value can be also obtained for an axially symmetric rotor as shown in the inset of Figure 6.5. However, while the 2-parameters of the IBA-1 Hamiltonian of equation 6.1 cannot fit a 2_2^+ energy as low as observed experimentally, the best fit is obtained for a γ-soft structure very close to O(6). The theoretical level scheme obtained from this procedure is compared with the experimental data in Figure

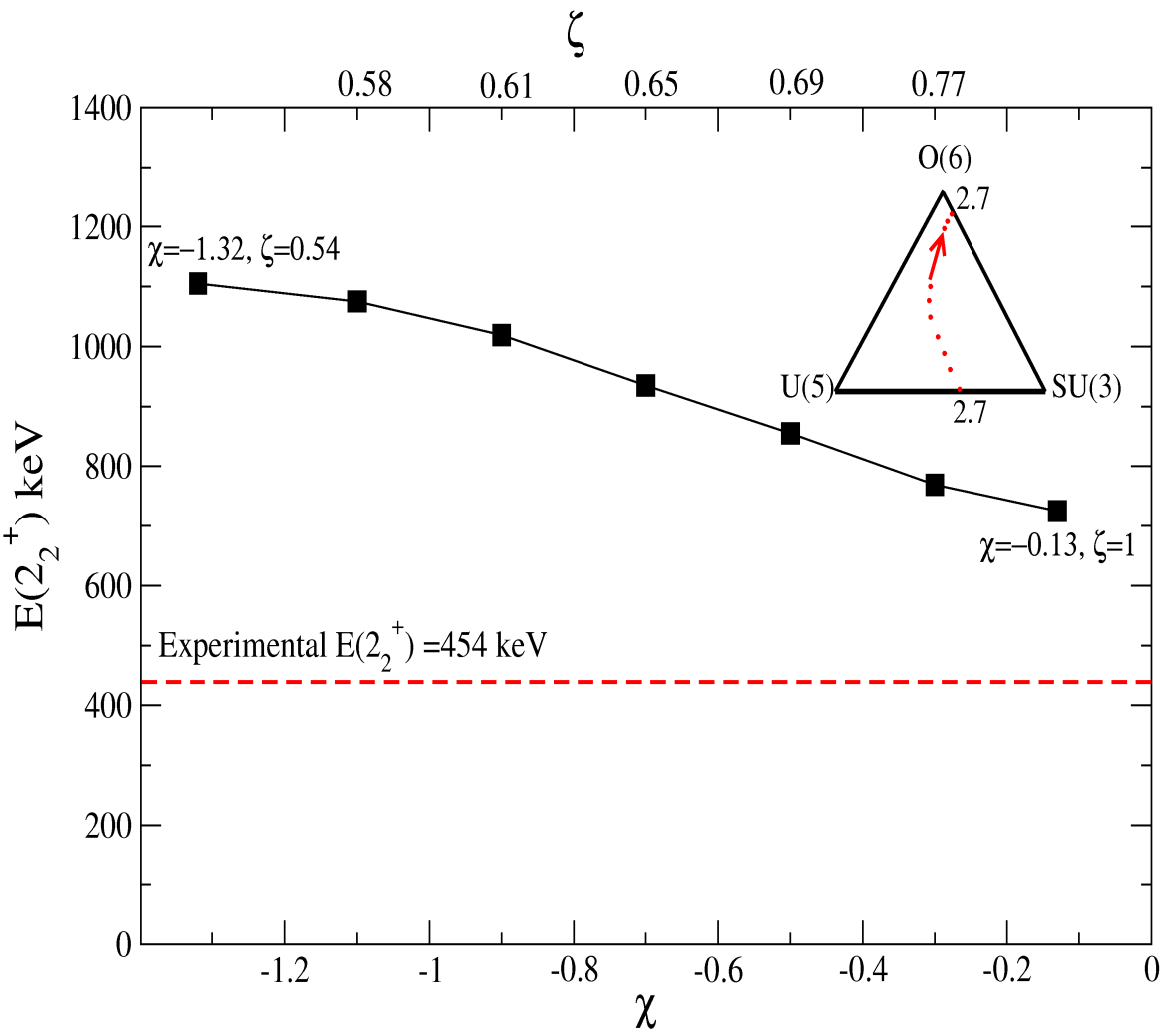

Figure 6.5: IBA-1 calculations for $E(2_2^+)$ ^{190}W along the contour in the IBA-1 symmetry triangle (red contour in the triangle). The closest calculated result to the experimental $E(2_2^+)$ value is the one near to the O(6) geometrically limit.

6.6.

The identification of a weakly populated peak at energy of 454 keV in ^{190}W suggests a direct transition from the 2_2^+ state to the ground state 0^+ in ^{190}W. In the pure, idealised O(6) limit, such a transition is forbidden [35, 36, 37, 38, 39], however, in realistic, finite nuclear systems, such hindered transitions have been observed. The statistics in the current work preclude an angular distribution analysis to establish the M1/E2 mixing ratio of the unstretched $2_2^+ \rightarrow 2_1^+$ transition in ^{190}W (247 keV). However, if one assumes a pure E2 decay for this decay, the evaluated branching ratio from the gamma-ray intensities, corrected for E2 internal conversion, would give a value for $\frac{B(E2:2_2^+ \rightarrow 2_1^+)}{B(E2:2_2^+ \rightarrow 0_1^+)} = 63 \pm 30$, consistent with the expected hindrance of the 2_2^+ state direct

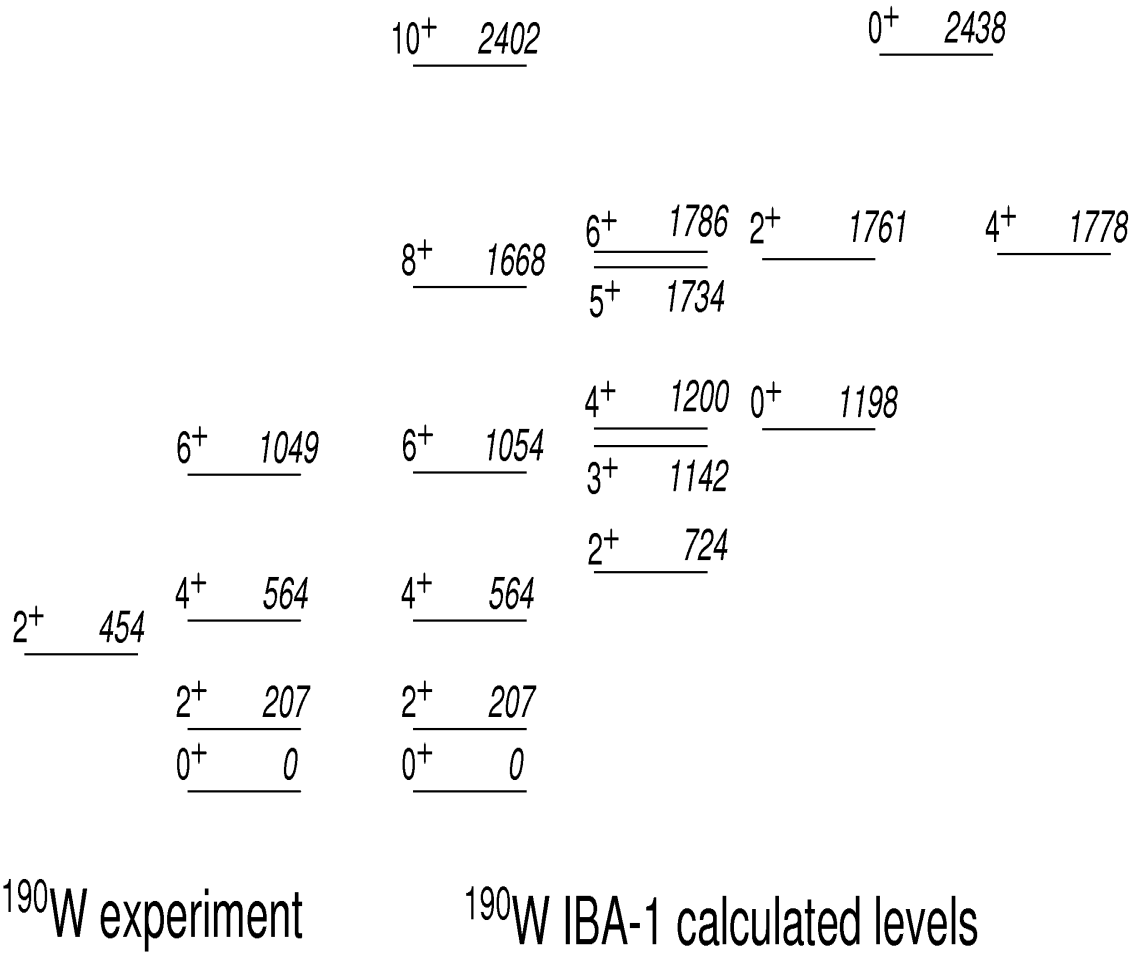

Figure 6.6: Results of IBA-1 calculations for ^{190}W and comparison with the experimentally measured low-lying energy levels for this nucleus. The fitted IBA-1 Hamiltonian was used the two parameters ζ= 1 and χ= -0.13.

decay to the ground state. The IBA-1 calculations for ^{190}W predict $\frac{B(E2:2_2^+ \rightarrow 2_1^+)}{B(E2:2_2^+ \rightarrow 0_1^+)} =$ 14 for this decay branching. Therefore, both the experimental data (assuming a pure E2 transition) and the IBA predictions suggest that only a small degree of mixing is present between the first and second 2^+ states in ^{190}W. This small mixing is responsible for the non-vanishing nature of the $2_2^+ \rightarrow 0_1^+$ transition in ^{190}W and is consistent with a nucleus that has only small deviations in its wavefunction from the O(6) symmetry limit.

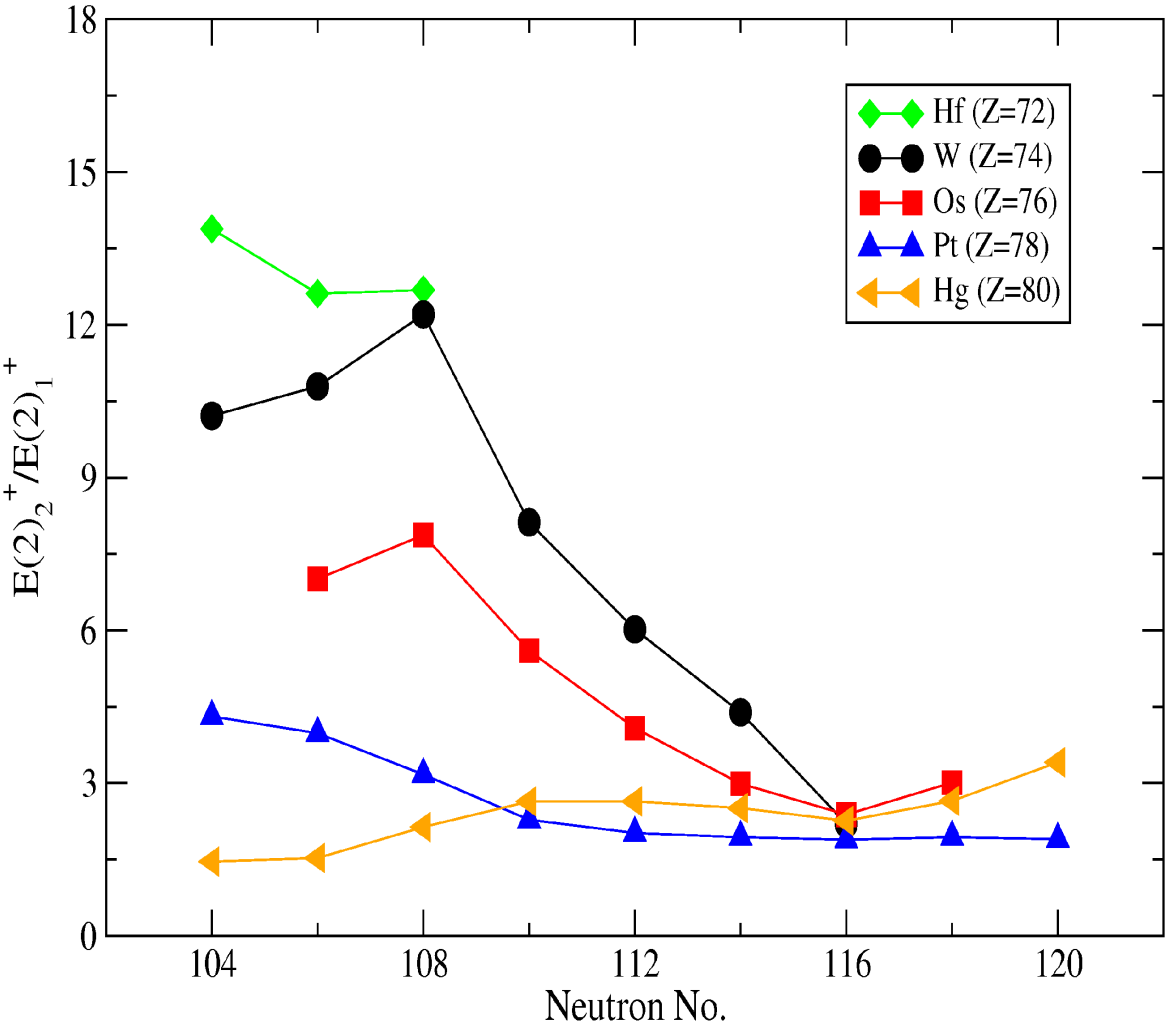

Figure 6.7: The ratio of the excitation energies of the $I^{\pi}=2_2^+$ and $I^{\pi}=2_1^+$ states for heavy even-even neutron rich-nuclei with N=104→120. These data are taken from reference [3] and the current work.

6.2.2 $E(2_2^+)/E(2_1^+)$ Systematics

An empirical quantity which can be used to infer prolate-oblate shape transitions is the energy ratio $E(2_2^+)/E(2_1^+)$ [143] as a function of nucleon number. Figure 6.7 shows a systematic of this ratio versus neutron number for even-even Hf-Hg (Z=72→80) nuclei between N=104 and N=120. The neutron number N=116 appears as the transitional point with a maximization of the γ-softness for the Pt, Os, Hg and possibly for W isotopes with the new data from the current work.

6.2.3 Estimate of γ-softness Deformation Parameter

An estimate of the value of the static or average triaxial deformation parameter, γ, can be extracted using the energy ratio $E(2_2^+)/E(2_1^+)$ from the Davydov model [61]. Although the Davydov model represents an asymmetric nucleus with a rigid shape, this parameter can provide a simple prediction of a static γ value which can be compared with the average γ value associated with γ-soft potentials. The expression as described in reference [27] is used to extract the γ value as follows:

$$\frac{E(2_2^+)}{E(2_1^+)} = \frac{[1+X]}{[1-X]} \tag{6.2}$$

where,

$$X = \sqrt{1 - \frac{8}{9} sin^2(3\gamma)} \tag{6.3}$$

Therefore, when X=1 (i.e. for γ=0°), the energy ratio $E(2_2^+)/E(2_1^+) \rightarrow \infty$. While for X=1/3, γ= 30°. Assuming the result for the 2_2^+ state in ^{190}W from the current work, the ratio of $E(2_2^+)/E(2_1^+)$ is equal to 2.19 for this nucleus and therefore $\gamma \approx$26° using equations 6.2 and 6.3. Table 6.1 gives the energy ratio $E(2_2^+)/E(2_1^+)$ for some deformed and transitional nuclei and their calculated extrapolated γ values [27]. The γ value of ^{190}W is comparable with other γ-soft nuclei in the same region such as ^{192}Os and ^{196}Pt. In addition, Figure 6.8 shows the static γ values extracted using this method for the even-even Hf-Hg isotones between N=104 and N=120.

Table 6.1: The energy ratio of $E(2_2^+)/E(2_1^+)$ for some deformed and transitional nuclei and their associated static γ values, taken from reference [27].

Nucleus	$E(2_2^+)/E(2_1^+)$	γ-value
^{168}Er	10.3	13°
^{176}Hf	15.2	10°
^{182}W	12.2	12°
^{184}Os	7.9	14°
^{192}Os	2.4	25°
^{196}Pt	1.94	30°

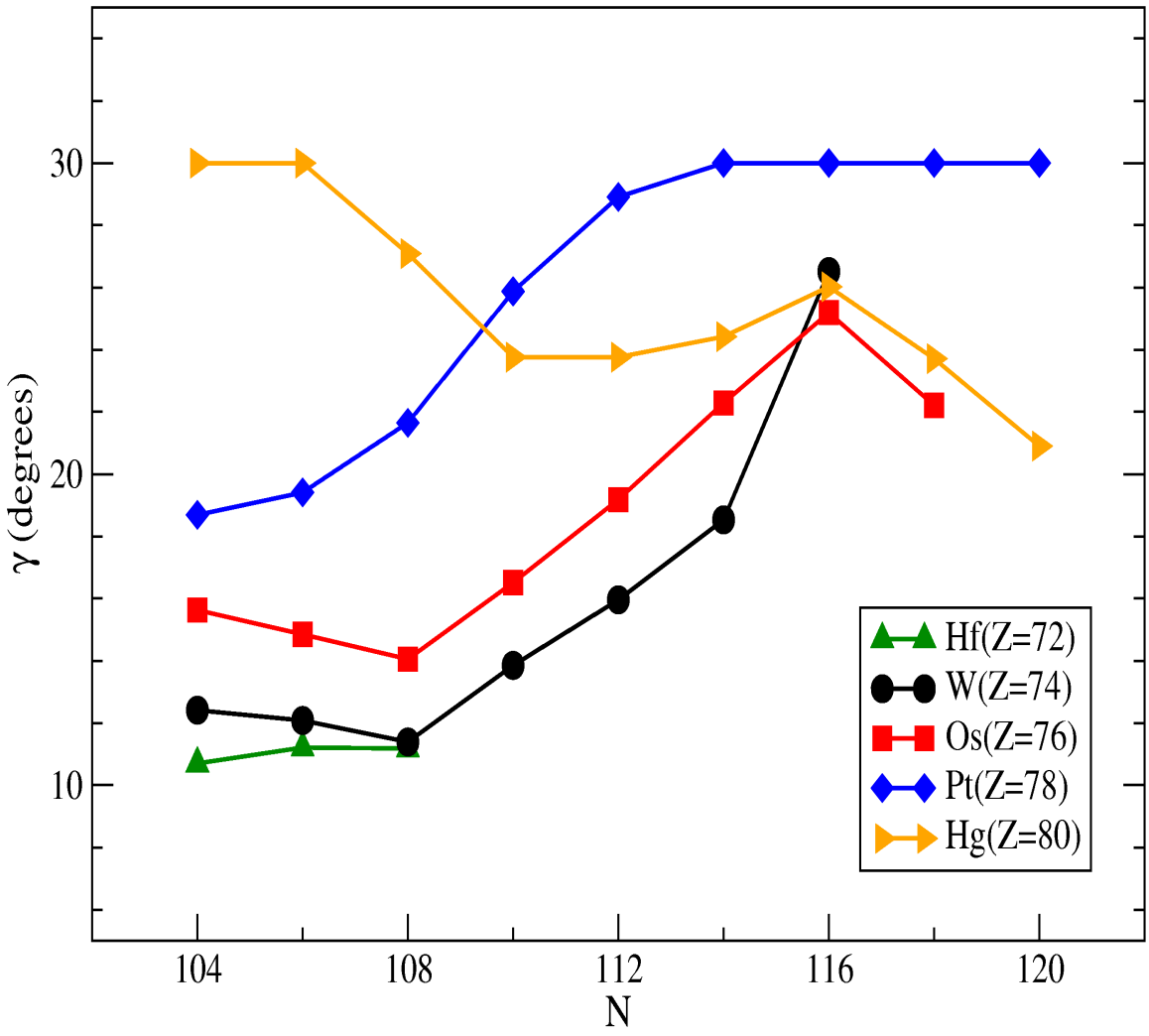

Figure 6.8: Static γ values for Hf→Hg even-even nuclei with N=104→120 using equations 6.2 and 6.3 of the Davydov model (see text for more details).

6.2.4 E(2_2^+)-E(4_1^+) Systematics

According to Kumar [144], a negative value of E(2_2^+)- E(4_1^+) (i.e. the second 2^+ state lying lower in energy than the yrast 4^+ state) is a good indicator of a region of prolate-oblate phase transition. This factor results in a negative value in the energy difference between the prolate and oblate minima of the potential energy of deformation. Thus, a positive value of the quantity E(2_2^+)- E(4_1^+) indicates an axially symmetric prolate or oblate shape while the negative value is a signature of γ-soft limit.

Figure 6.9 shows the systematics of the energy difference between the E(2_2^+) and E(4^+) for the even-even Hf→Hg nuclei between N=104 to N=120. The systematics show similar characteristics of the previous E(2_2^+)/E(2_1^+) systematics (see Figure 6.7).

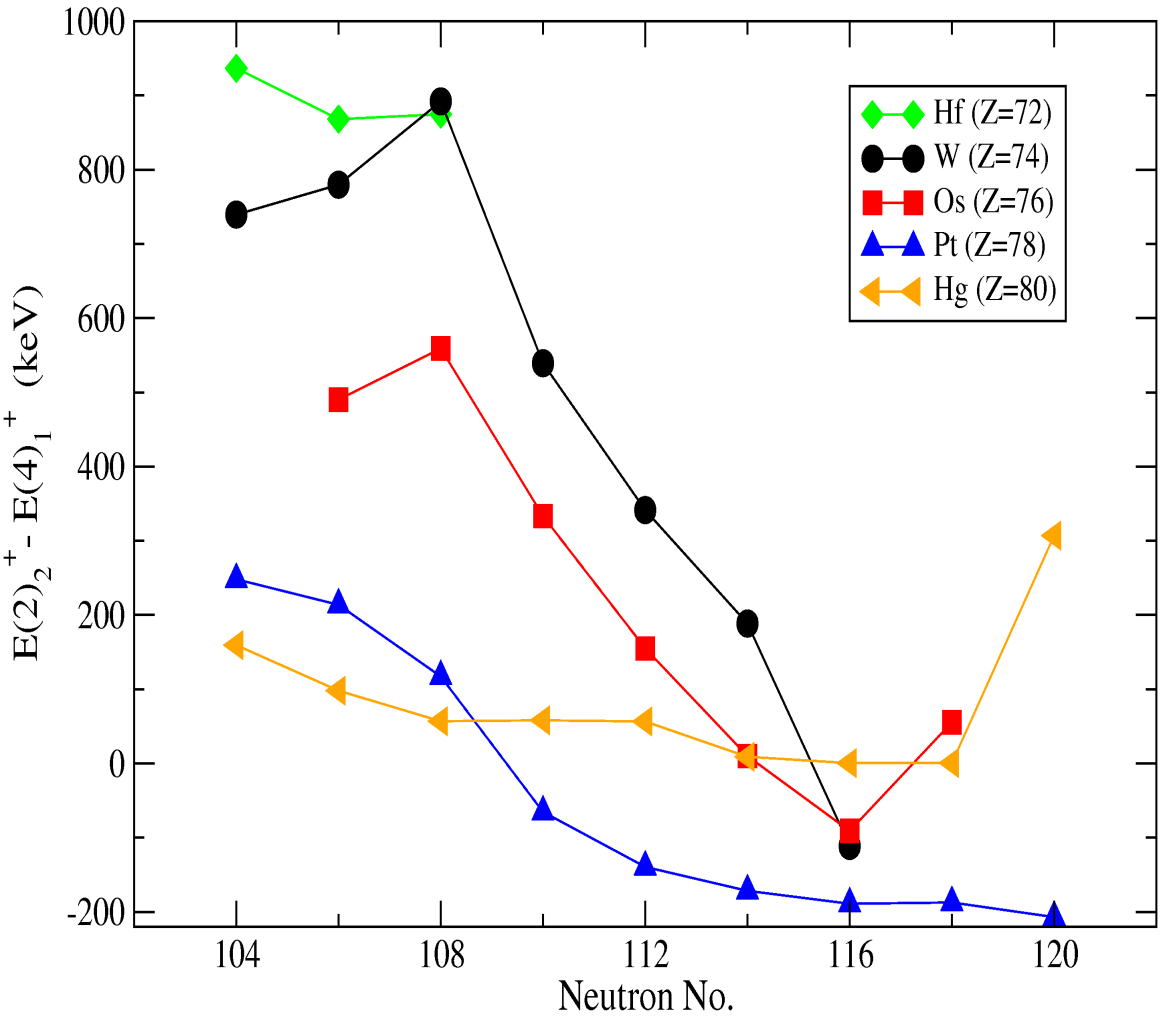

Figure 6.9: Systematics of the excitation energy difference between the $I^{\pi}=2_2^+$ and $I^{\pi}=4^+$ states for the even-even Hf-Hg nuclei as a function of the neutron number for N=104→120. These data are taken from reference [3] and the current work.

It shows an apparent of maximization of γ softness around neutron number N=116 for Os and Hg isotopes. The E(2_2^+)- E(4_1^+) value decreases smoothly for heavy W-isotones, moving to a negative value assuming the proposed level scheme for $^{190}W_{116}$, in the current work.

6.2.5 Total-Routhian-Surface (TRS) Calculations for ^{188,190,192}W

In order to predict the ground state quadrupole deformations of ^{188,190,192}W, Total-Routhian-Surface (TRS) calculations using the prescription described in references [145] have been performed. The results of these are shown in Figure 6.10. In

these calculations the potential energy is shown as a function of β deformation and γ degree of freedom. The value of γ=0° corresponds to a prolate axially symmetric shape, while γ=60° corresponds to an axially symmetric oblate shape.

The calculations predict an evolution from a prolate gamma-soft potential in ^{188}W, to a very γ-soft potential for ^{190}W and ^{192}W. Indeed, the very flat energy change associated with the γ-degree of freedom for $\beta_2 \approx$0.15 can be linked to a clear predicted region of prolate/oblate shape co-existence associated with an O(6)-like potential.

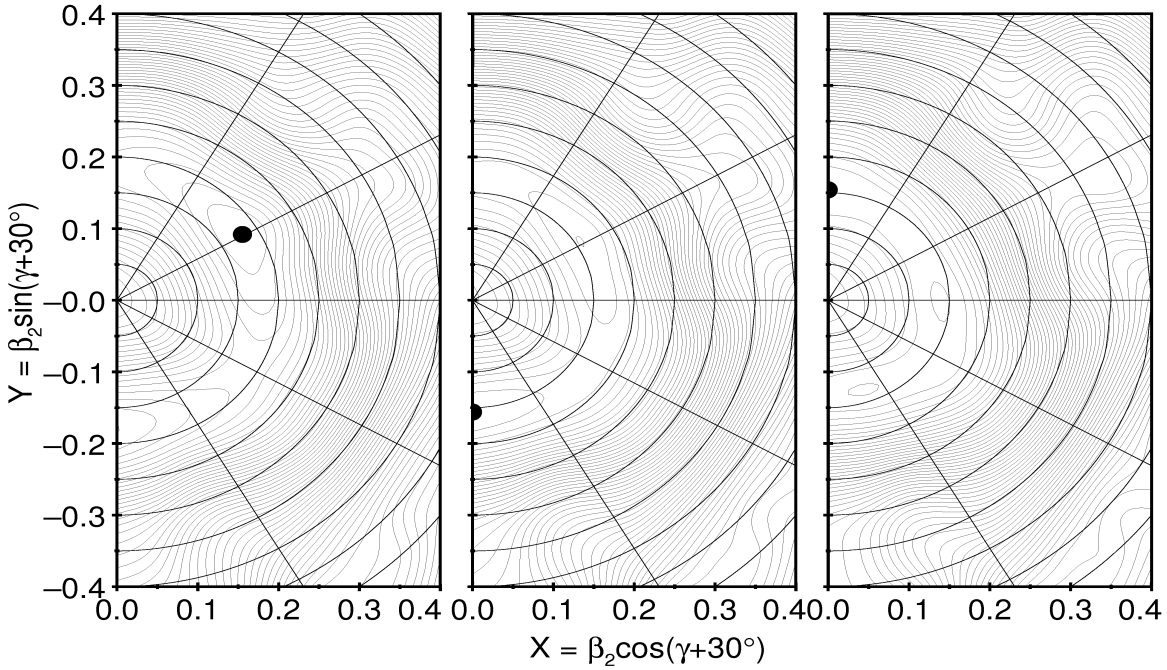

Figure 6.10: Total-Routhian-Surface (TRS) calculations performed by Xu *et. al.* [145, 146] for the ground state configurations of: (left) ^{188}W with β_2 = 0.178 and γ = 1.3°; (centre) ^{190}W with β_2 = 0.158 and γ = -120.0° and (right) ^{192}W with β_2 = 0.136 and γ = -24.1°. The energy contours in this figure are separated by 200 keV.

6.2.6 Mean Field Calculations

In their recent theoretical work on this region using a Skyrme Hartree-Fock plus BCS pairing approach, Sarriguren *et. al.*, [32] predict that ^{190}W lies on the near-critical point between prolate and oblate shapes in this region, with a prediction of a very shallow triaxial minimum for the ground state shape. Figure 6.11 shows the contour plot of their potential energy surface calculation for the N=116, ^{190}W, with a predicted γ =25° for this nucleus. Sarriguren *et. al.* also point out that neutron number N =

116 appears to be a 'saddle point' for the the Yb, Hf, W and Os isotopes with respect to maximum γ-softness at the transition between axially-symmetric prolate and oblate ground states for $N \leq 114$ and $N \geq 118$, respectively.

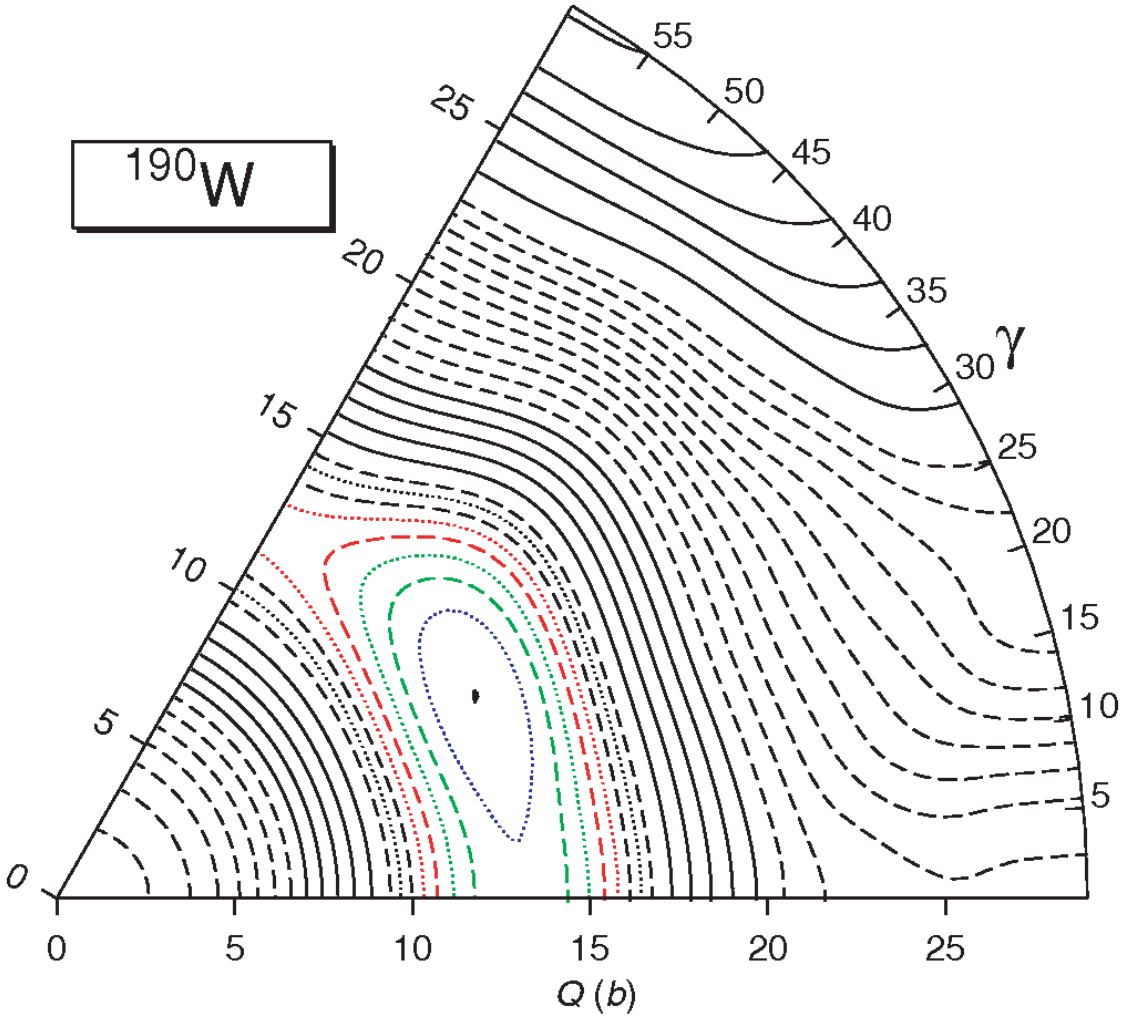

Figure 6.11: Contour plot using potential energy surface calculation of ^{190}W in a two-dimensional β-γ plane representation performed by Sarriguren *et. al.* and taken from reference [32].

Chapter 7

Summary

Spectroscopic information on heavy neutron-rich nuclei around A$\sim$190 has been investigated following projectile fragmentation reactions using a 1 GeV per nucleon, ^{208}Pb primary beam on a ^{9}Be target. For the first time within the RISING experimental campaign at GSI, a technique has been developed to measure the β-decay half-lives and γ rays from low-lying states of exotic nuclei in complex background conditions, using position and time correlations between the implantation of the fragments and their subsequent β-decay. This was achieved by using the RISING active stopper of three 5cm x 5cm Double Sided Silicon Strip Detectors (DSSSDs). The low-lying states of ^{188,190,192}W have been investigated following the β^- decay of their tantalum mother nuclei. In addition, β^- decay half lives of ^{187,188,189}Hf, ^{188,189,190,191,192}Ta, ^{191,192,193,194}W and ^{193,194,195}Re nuclei have been established for the first time in this work.

The β^--decay of ^{188}Ta showed the previously reported γ rays associated with decays of levels in the yrast states of ^{188}W daughter nucleus up to a spin/parity of 6^+. The results support the previously reported assignments for the first 2^+ and 4^+ states in ^{190}W and provide a candidate of the second 2^+ state corresponding to the γ-bandhead in this nucleus. In addition, the excitation energy of the yrast 2^+ state in ^{192}W is also reported for the first time in the current work.

The interpretation of the results is mainly based on the systematics for the region around A$\sim$190. An interpretation of a beginning of a new localised subshell closure is supported by the confirmation of the R(4/2) energy ratio for ^{190}W and the excitation energy systematics arising from the first observation of the yrast $I^{\pi}= 2^+$ state in ^{192}W. The observation of the second 2^+ in ^{190}W with energy lower than the energy of the yrast

4^+ state supports the interpretation of large γ softness in this nucleus. Investigation of the low lying structure of ^{190}W using a simple two-parameters Hamiltonian of the Interacting Boson Approximation model (IBA-1) obtains a best fit that is very close the O(6) limit. This interpretation is consistent with Total Routhian Surface (TRS) and mean field calculations which predict a large γ softness in the low-lying states of ^{190}W.

Appendix A

Calibration

A.1 Energy Calibration of RISING Germaniums

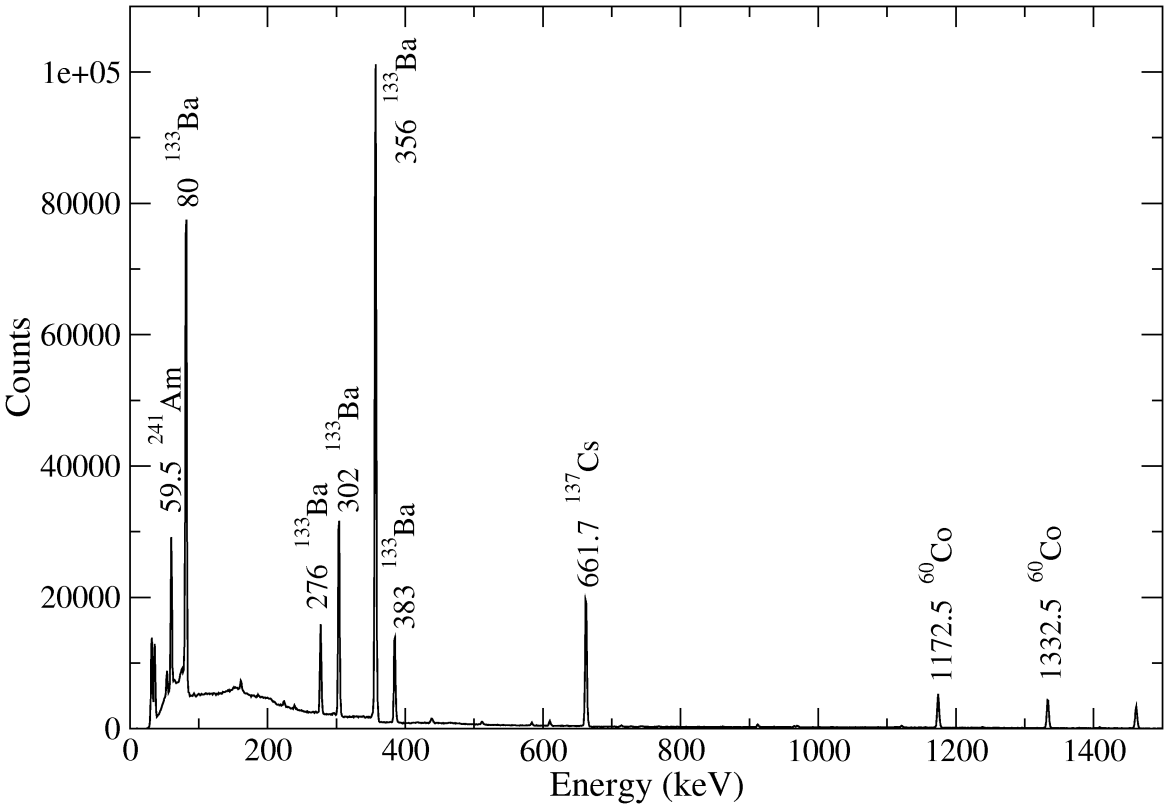

Figure A.1: Gamma rays energies of the sources used for the energy calibration of the RISING germanium crystals. The calibration used two sources: (i) A mixed source of ^{241}Am, ^{137}Cs and ^{60}Co; and (ii) a ^{133}Ba source.

A.2 Energy Calibration of Silicon Detectors

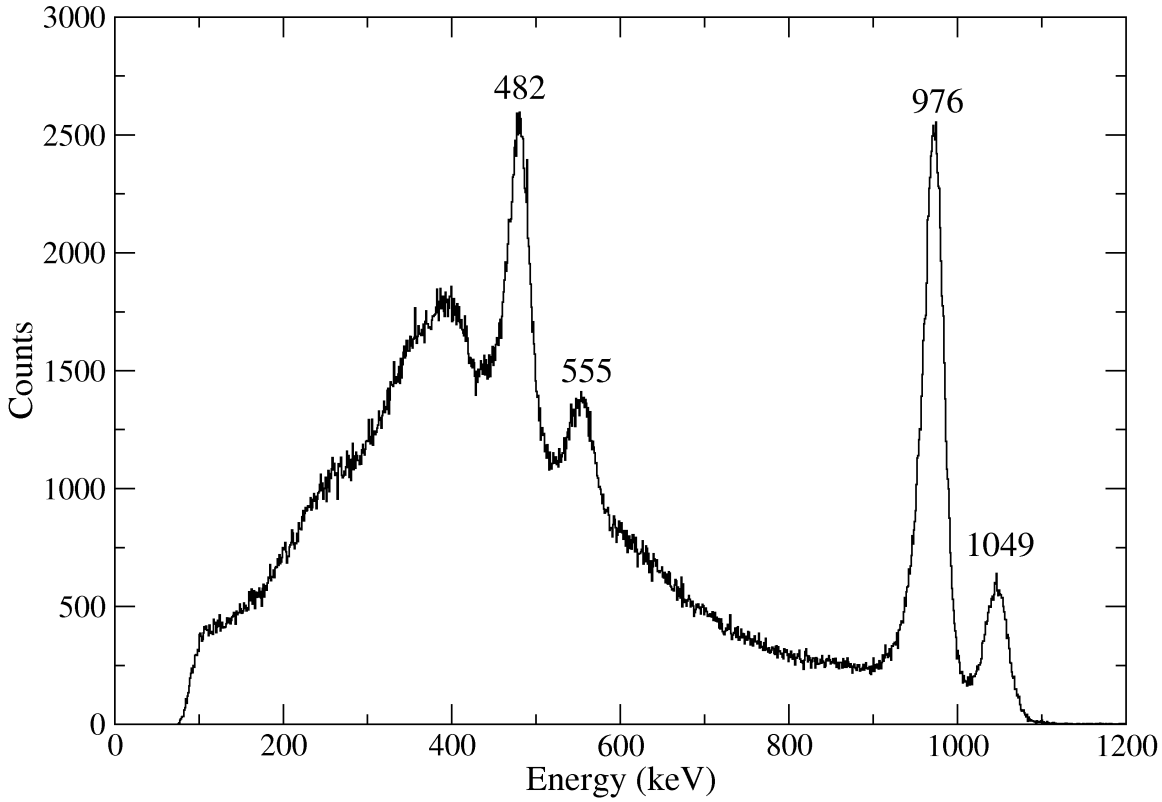

Figure A.2: Energy calibration spectrum of the ^{207}Bi electron conversion source. This source was used for energy calibration of the linear preamplier part of the silcion active stopper.

Appendix B

Numerical Calculation of the Relativistic Parameter, γ_1

The relativistic parameter γ_1 for the calculation of the energy loss ($\frac{\triangle E}{Q}$) in the intermediate degrader is given by:

$$\gamma_1 = \sqrt{1 + \left(\frac{B\rho_1}{A/Q}\right)^2 . \left(\frac{e}{uc}\right)^2} \tag{B.1}$$

This formula should equal to the relativistic definition of γ, which is expressed as:

$$\gamma = \sqrt{\frac{1}{1 - \frac{v^2}{c^2}}} \tag{B.2}$$

To improve that $\gamma_1 = \gamma$, we used the definition of the $\frac{A}{Q}$:

$$B\rho = \frac{A}{Q}\beta\gamma\frac{uc}{e} \tag{B.3}$$

using $\gamma = \sqrt{\frac{1}{1-\beta^2}}$, we can write equation B.3 as:

$$B\rho = \frac{A}{Q}\frac{\beta}{\sqrt{1-\beta^2}}\frac{uc}{e} \tag{B.4}$$

$$B\rho Q\sqrt{1-\beta^2} = A\beta\frac{uc}{e} \tag{B.5}$$

Taking the square of both sides:

$$(B\rho)^2Q^2 - (B\rho)^2Q^2\beta^2 = A^2\beta^2(\frac{uc}{e})^2 \tag{B.6}$$

$$(B\rho)^2Q^2 = A^2\beta^2(\frac{uc}{e})^2 + (B\rho)^2Q^2\beta^2 \tag{B.7}$$

Thus, the relativistic parameter β can be defined as:

$$\beta^2 = \frac{(B\rho)^2Q^2}{A^2(\frac{uc}{e})^2 + (B\rho)^2Q^2} \tag{B.8}$$

using the relation of β^2 into equation B.2:

$$\gamma = \sqrt{\frac{1}{1-\beta^2}} = \sqrt{\frac{A^2(\frac{uc}{e})^2 + (B\rho)^2Q^2}{A^2(\frac{uc}{e})^2 + (B\rho)^2Q^2 - (B\rho)^2Q^2}} \tag{B.9}$$

Therefor

$$\gamma = \sqrt{1 + \left(\frac{B\rho_1}{A/Q}\right)^2 . \left(\frac{e}{uc}\right)^2} = \gamma_1 \tag{B.10}$$

Appendix C

Publications

C.1 List of Publications

N. Alkhomashi, P.H. Regan, Zs. Podolyàk *et al.*,
β^- Decays from ^{188,190,192}Ta: Shape Evolution in Neutron-Rich Tungsten Isotopes,
Phys. Rev. ***C80*** *(2009) 064308.*

N. Alkhomashi, P.H. Regan, Zs. Podolyàk et al.,
β-Delayed and Isomer Spectroscopy of Neutron-Rich Ta and W Isotopes,
Acta Physica Polonica ***B40*** *(2009) 875.*

P.H. Regan, N. Alkhomashi, N. Al-Dahan, Zs. Podolyàk et al.,
First Results With The RISING Active Stopper,
International Journal of Modern Physics ***E17*** *(2008) 8.*

P.H. Regan, N. Alkhomashi, N. Al-Dahan, Zs. Podolyàk et al.,
New Insights into the Structure of Exotic Nuclei Using the RISING Active Stopper ,
American Institute of Physics (AIP), ***1090*** *(2008) 122.*

N. Al-Dahan, Zs. Podolyàk, P. H. Regan, S. J. Steer, N. Alkhomashi et al.,
Structure of N>=126 nuclei produced in fragmentation of ^{238}U*,*
American Institute of Physics (AIP), ***1090*** *(2008) 145.*

N. Al-Dahan, Zs. Podolyàk , P.H. Regan , S.J. Steer , A.M. Denis Bacelar, N. Alkhomashi et al.,
Isomeric States in ^{208}Hg *and* ^{209}Tl *Populated in Fragentation of* ^{238}U*,*
Acta Physica Polonica ***B40*** *(2009) 871.*

A.I. Morales, J. Benlliure, P.H. Regan, Z. Podolyàk, M. Górska, N. Alkhomashi et al.,

β-Delayed γ-Ray Spectroscopy of Heavy Neutron Rich Nuclei South of Lead,
Acta Physica Polonica ***B40*** *(2009) 867.*

A.M. Denis Bacelar, A.M. Bruce, Zs. Podolyàk, S. Lalkovski, S. Pietri, N. Al-Dahan, M. Górska, A. Algora, N. Alkhomashi et al.,
Angular Momentum Population in Fragmention Reactions,
Acta Physica Polonica ***B40*** *(2009) 889.*

Zs. Podolyàk, G.F. Farrelly, P.H. Regan, A.B. Garnsworthy, S.J. Steer, M. Górska, J. Benlliure, E. Casarejos, S. Pietri, J. Gerl, H.J. Wollersheim, R. Kumar, F. Molina, A. Algora, N. Alkhomashi et al.,
Proton hole excitation in the closed shell nucleus ^{205}Au*,*
Phy. Lett. ***B672*** *(2009) 116.*

N. Al-Dahan, Zs. Podolyàk , P.H. Regan, M. Górska, H. Grawe, K.H. Maier, J. Gerl, S.B. Pietri, H.J. Wollersheim, N. Alkhomashi et al.,
Nuclear structure 'southest' of ^{208}Pb*: isomeric states in* ^{208}Hg *and* ^{209}Tl*,*
Phys. Rev. ***C80*** *(2009) 061302(R).*

C.2 List of Oral Presentations and Posters

Institute of Physics Annual Conference 2008, Oral Presentation,
β⁻ Decay studies of $^{188,190,192}Ta$ *using Projectile Fragmentation Reactions*
University of Liverpool, UK, (April, 2008).

50th Anniversary Symposium on Nuclear Size and Shapes,Poster Presentation,
β-Delayed Spectroscopy of W Isotopes,
University of Surrey, UK, (June 2008).

42st Conference on Nuclear Physics, Oral Presentation
β-Delayed and Isomer Spectroscopy of Neutron-Rich Ta and W Isotopes,
Zakopane, Poland, (September, 2008).

Institute of Physics Annual Conference 2009, Oral Presentation,
β⁻ Decays from $^{188,190,192}Ta$*: Shape Evolution in Neutron-Rich Tungsten Isotopes*
University of Birmigham, UK, (April, 2009).

7th WNSL Workshop, Oral Presentation,

Decays from ^{188,190,192}Ta: Shape Evolution in Neutron-Rich Tungsten Isotopes,
Yale University, USA, (June, 2009).

Gordon Conference, Poster Presentation,
Decays from ^{188,190,192}Ta: Shape Evolution in Neutron-Rich Tungsten Isotopes,
New London, USA, (June, 2009).

RISING Celebration Day, Oral Presentation,
Shapes and Structural Transitions around N$\sim$116,
Darmstadt University, Germany, (October, 2009).

Bibliography

[1] *E. M. Baum, H. D. Knox and T. R. Miller, Chart of The Nuclides, 16^{th} Edition, Lockheed Martin (2002).*

[2] *G. Audi et al., Nucl. Phys.* ***A729*** *(2003) 337.*

[3] *Evaluated Nuclear Structure Data File (ENSDF), online database, National Nuclear Data Center, http://www.nndc.bnl.gov/ensdf/, (Site Visited: October, 2008).*

[4] *Nuclear Physics Group, University of York, http://npg.york.ac.uk/images/segrechart-new.gif, (Site Visited: October, 2007).*

[5] *W. Gelletly, proceedings of the American Philosophical Society,* ***145*** *(2001) 4.*

[6] *R. DAlarcao et al., Phys. Rev.* ***C59*** *(1999) 1227(R).*

[7] *C. Wheldon et al., Phys. Rev.* ***C63*** *(2000) 011304(R).*

[8] *Zs. Podolyak et al. , Int. J. Mod. Phys.* ***E13*** *(2004) 123.*

[9] *J. Benlliure et al., Nucl. Phys.* ***A660*** *(1999) 87.*

[10] *M. Pfützner et al., Phys. Lett.* ***B444*** *(1998) 32.*

[11] *M. Caamano et al., Eur. Phys. J.* ***A23*** *(2005) 201.*

[12] *T. Enqvist et al., Nucl. Phys.* ***A658*** *(1999) 47.*

[13] *P. H. Regan et al., Laser Phys. Lett.* ***1*** *(2004) 317.*

[14] *R. Broda et al., Eur. Phys. J.* ***A20*** *(2004) 145.*

[15] *J. Benlliure et al., Erratum Nucl. Phys.* ***A674*** *(2000) 578.*

[16] *K. Krumbholz et al., Z. Phys.* ***A351*** *(1995) 11.*

[17] *Zs. Podolyak et al., Phys.Rev.* ***C79*** *(2009) 031305.*

[18] *H. Geissel, G. Münzenberg and K. Riisager, Annu. Rev. Nucl. Sci.* ***45*** *(1995) 163.*

[19] *S. Pietri, et al., Nucl. Inst. Meth.* ***B261*** *(2007) 1079.*

[20] A. Bohr and B. R. Mottelson, Kgl. Danske Videnskab Selskab Mat -fys Medd, **27** (1953) 16.

[21] S. Raman et al., At. Data Nucl. Data Tables **78** (2001) 1.

[22] R. B. Cakirli and R. F. Casten, Phys. Rev. **C78** (2008) 041301(R).

[23] R. F. Casten Private Communications (2009).

[24] G. Sharff-Goldhaber and J. Weneser, Phys. Rev. **98** (1995) 212.

[25] R. F. Casten, Phys. Lett. **B152** (1985) 145.

[26] A. Bohr Mat. Fys. Medd. K. Dan. Vidensk. Selsk. **26** (1952) 14.

[27] R. F. Casten, Nuclear Structure from a Simple Perspective, 2^{nd} Edition, Oxford University Press (2000).

[28] J. Jolie and A. Linneman, Nucl. Phys. **C68** (2003) 031301(R).

[29] Zs. Podolyak et al., Phys. Letts. **B491** (2000) 225.

[30] P. M. Walker and F. R. Xu, Phys. Letts. **B635** (2006) 286.

[31] Y. Sun et al., Phys Lett **B659** (2008) 165.

[32] P. Sarriguren et al., Phys. Rev. **C77** (2008) 064322.

[33] P. D. Stevenson et al., Phys. Rev. **C72** (2005) 047303.

[34] L. M. Robledo et al., J. Phys. G: Nucl. Part. Phys. **36** (2009) 115104.

[35] A. Arima and F. Iachello, Phys. Rev. Lett. **35** (1975) 1069.

[36] F. Iachello and A. Arima, The Interacting Boson Model, Cambridge University Press (1987).

[37] F. lachello and A. Arima, Phys. Lett. **B53** (1974) 309.

[38] A. Arima and F. Iachello, Ann. of Phys. **99** (1976) 253.

[39] A. Arima and F. Iachello, Phys. Rev. Lett. **40** (1978) 385.

[40] J. A. Cizewski et al., Phys. Rev. Lett. **40** (1978) 167.

[41] R. F. Casten et al., Nucl. Phys. **A309** (1978) 206.

[42] R. Kumar et al., Nucl. Inst. Meth. Phys. **A598** (2009) 754.

[43] S. Pietri, et al., Acta Phys. Pol. **B38** (2007) 1255.

[44] S. Steer et al., Int. J. Mod. Phys. **E18** (2009) 1002.

[45] Zs. Podolyak et al., Phys. Letts. **B672** (2009) 116.

[46] T. Shizuma et al., Eur. Phys. J. **A30** (2006) 391.

[47] K.Rykaczewski et al., Univ. Mainz, 1983 Ann.Rept., (1984) 72

[48] K. L. G. Heyde, Basic ideas and concepts in nuclear physics, 3^{rd} Edition, Institute of Physics Pub, Bristol (2004).

[49] D. Bohm, Quantum Theory, Courier Dover Publications (1989).

[50] K. S. Krane, Introductory Nuclear Physics, John Wiley & Sons Inc. (1988).

[51] R. D. Woods and D. S. Saxon, Phys. Rev. **95** (1954) 577.

[52] M. Goeppert-Mayer, Phys. Rev. **75** (1949) 1969L.

[53] O. Haxel, J. H. D. Jensen and H. E. Suess, Phys. Rev. **128** (1950) 295.

[54] W. Pauli, Z. Phys. **31** (1925) 765.

[55] C. J. Gallagher and S.A. Moszkowski, Phys. Rev. **111** (1958) 1282.

[56] A. Andreyev et al., CERN Courier **47** (2007) 7.

[57] S. B. Patel, Nuclear Physics: An Introduction, New Age Publishers (1991).

[58] I. Talmi, Simple Models of Complex Nuclei: The Shell Model and Interacting Boson Model, Taylor and Francis (1993).

[59] D. L. Hill and J. Wheeler, Phys. Rev. **89** (1953) 1102.

[60] A. B. Garnsworthy, Neutron-Proton Interactions in Heavy Self-Conjugate Nuclei, PhD Thesis, University of Surrey, UK (2007).

[61] A. S. Davydov and G. F. Filippov, Nucl. Phys. **8** (1958) 237.

[62] M. A. Preston and R. K. Bhaduri, Structure of the Nucleus, Addison-Wesley, Reading (1975).

[63] L. Wilets and M. Jean, Phys. Rev. **102** (1956) 3.

[64] S. G. Nilsson, Dan. Mat. Fys. Medd. **29** (1955) 3.

[65] J. Y. Zhang et al., Phys. Rev. **C39** (1989) 714.

[66] B. Singh et al., Nucl. Data Sheets **97** (2002) 241.

[67] W. D. Myers and W.J. Swiatecki, Annals of Physics, **55** (1969) 395.

[68] V. M. Strutinski, Nucl. Phys. **A95** (1967) 420.

[69] W. Nazarewicz et al., Nucl. Phys. **A512** (1990) 61.

[70] W. Nazarewicz et al., Nucl. Phys. **A435** (1985) 397.

[71] H. C. Pradhan, Y. Nogami, and J. Law, Nucl. Phys. **A201** (1973) 357.

[72] C. F. von Weizsacker, Z. Phys. **96** (1935) 431.

[73] E. Fermi, Z. Phys. **88** (1934) 161.

[74] G. Gamow and E. Teller, Phys. Rev. **49** (1936) 895.

[75] I. Feister, Phys. Rev. **78** (1950) 4.

[76] N.B. Gove and N.J. Martin, At. Data and Nucl. Data Tables **10** (1971) 205.

[77] C.S. Wu and S. A. Moszkowski, Beta Decay, John Wiley & Sons (1966).

[78] *B. Rubio and W. Gelletly, Lecture notes, Beta Decay of Exotic Nuclei, unpublished.*

[79] *B. Singh et al., Nucl. Data Sheets* **84** *(1998) 487.*

[80] *W. N. Cottingham and D. A. Greenwood, An Introduction to Nuclear Physics, Cambridge University Press (2001).*

[81] *W. E. Burcham, Nuclear Physics An Introduction, 2^{nd} Edition, Longman Group Limited (1973).*

[82] *P. Ring and P. Schuck, The Nuclear Many-Body Problem, Springer-Verlag, New York (1980).*

[83] *J. Kantele, Heavy Ions and Nuclear Structure, Nuclear Science Research Conference Series, Edited by B. Sikora and Z. Wilhelmi Harwood,* ***5*** *(1984) 391.*

[84] *F. Rosel et al., At. Data Nucl. Data Tables* ***21*** *(1978) 91.*

[85] *I. M. Band et al., At. Data Nucl. Data Tables* ***81*** *(2002) 1-334.*

[86] *A. Bohr and B. R. Mottelson, Nuclear Structure, W. A. Benjamin, New York (1969).*

[87] *P. M. Walker and J. J. Carroll, Physics Today* ***58*** *(2005) 39.*

[88] *P. M Walker and G.D Dracoulis, Nature* ***399*** *(1999) 35.*

[89] *C. Chandler et al., Phys. Rev.* ***C56*** *(1997) 2924(R).*

[90] *J. J. Ressler et al., Phys. Rev.* ***C69*** *(2004) 034317.*

[91] *G. F. Knoll, Radiation Detection and Measurement, 3^{rd} Edition, John Wiley & Sons (2000).*

[92] *M. Pfützner et al., Phys. Rev.* ***C65*** *(2002) 064604.*

[93] *H. Bethe, Ann. Phys.* ***5*** *(1930) 325.*

[94] *F. Bloch, Z. Phys.* ***81*** *(1933) 363.*

[95] *C. Iliadis , Nuclear Physics of Stars. Wiley-VCH, Germany (2007).*

[96] *GSI, Accelerator, UNILAC,*
http://www-inj.gsi.de/index.php?section=3&subsection=2,
(Site Visited: October, 2008).

[97] *GSI, Accelerator, SIS-18,*
http://www.gsi.de/beschleuniger/sis18/sis_e.html,
(Site Visited: October, 2008).

[98] *J. Hüfner, K. Schafer and B. Schurmann, Physics Review* ***C12****, (1975) 1888.*

[99] *H. Geissel, Nucl. Inst. Meth. Phys. Res.* **B70** *(1992) 286.*

[100] *M. N. Mineva, A new μs Isomer in ^{136}Sb Produced in the Projectile Fission of ^{238}U, PhD Thesis, Lund University, Sweden (2003).*

[101] *A. B. Garnsworthy et al., in press Phys. Rev.* ***C*** *(2009).*

[102] *J. D. Jackson, Classical Electrodynamics, John Willey & Sons, New York (1986).*

[103] C. Scheidenberger and H. Geissel, Nucl. Instr. Meth. **B135**, (1998) 25.

[104] H. Folger et al., Nucl. Instr. Method. **A303** (1991) 24.

[105] G. Münzenberg, Nucl. Instr. Method. **B70** (1992) 265.

[106] M. Pfützner et al, Nucl. Instr. and Meth. **B86** (1994) 213.

[107] H. Stelzer et al., Nucl. Inst. and Meth. **A310** (1991) 103.

[108] http://www-linux.gsi.de/weick/frs/mwpc.html,
(Site Visited: October, 2008).

[109] M. V. Ricciardi, High-resolution measurements of light nuclides produced in 1 A GeV ^{238}U-induced reactions in hydrogen and in titanium, PhD Thesis, Universidad de Santiago de Compostela, Spain (2005).

[110] T. Kurtukian Nieto, Production and β decay half-lives of heavy neutron-rich nuclei approaching the stellar nucleosynthesis r-process path around A=195, PhD Thesis, Universidad de Santiago de Compostela, Spain (2007).

[111] N. Tsoulfanidis, Measurement and Detection of Radiation, Hemisphere Publishing Corporation, USA (1983).

[112] P. H. Regan, Post Graduate Nuclear Experimental Techniques, Course Notes, Univesity of Surrey (2002) unpublished,
http://personal.ph.surrey.ac.uk/ phs1pr/lecture_notes,
(Site Visited: November, 2009).

[113] C. F. G. Delaney and E. C. Finch, Radiation Detectors, Oxford Science Publishers, New York (1992).

[114] G. Gordon and D. John, Practical Gamma-Ray Spectroscopy, John Wiley & Sons (1995).

[115] XCOM: Photon Cross Sections Database,
http://physics.nist.gov/PhysRefData/Xcom/Text/XCOM.html,
(Site Visited: November, 2008).

[116] M. Górska et al, Acta Phys. Pol **B38** (2007) 1219.

[117] P. H. Regan, et al., Int. J. Mod. Phys. **E17** (2008) 8.

[118] S. Pietri, et al., Acta Phys. Pol. **B38** (2007) 1255.

[119] M. Pfützner et al, Nucl. Instr. and Meth, **A493** (2002) 155.

[120] mesytec, www.mesytec.com,
(Site Visited: September 2007).

[121] Micron Semiconductor ltd www.micron,
http://www.micronsemiconductor.co.uk,
(Site Visited: September 2007).

[122] K. Summerer and B. Blank, Phys. Rev. **C61** (2000) 034607.

[123] GSI Webserver, EPAX Version 2.1,
http://www-w2k.gsi.de/hellstr/asp/gsi/epaxv21m.asp,
(Site Visited: October, 2008).

[124] D. Bazin, et al., Nucl. Inst. and Meth. **A482** (2002) 307.

[125] O. B. Tarasov and D. Bazin, Nucl. Phy. **A746** (2004) 411.

[126] C. Scheidenberger, et al., Nucl. Inst. and Meth. **B142** (1998) 441.

[127] Zs. Podolyak et al., Nucl. Phy. **A722** (2003) 273.

[128] C. M. Baglin, Nucl. Data Sheets **84** (1998) 717.

[129] G. Lane et al., Private Communications (2009).

[130] T. Kibédi et al., Nucl. Inst. and Meth. **A589** (2008) 202.

[131] G. Farrely et al., Acta Phys. Pol. **B40** (2009) 885.

[132] P. Möller et al., At. Data Nucl. Data Tab. **59** (1995) 185.

[133] R. F. Casten et al., Phys. Lett. **B76** (1978) 3.

[134] P. H. Regan et al., American Ins. of Phys. **1090** (2008) 122.

[135] G. Sharff-Goldhaber and J. Weneser, Phys. Rev. **98** (1995) 212.

[136] R. F. Casten et al., Phys. Rev. Lett. **47** (1981) 1433.

[137] P. Federman and S. Pittel, Phys. Lett. **B69** (1977) 385.

[138] R. F. Casten Nucl. Phys. **A443** (1985) 1.

[139] V. R. Green et al., Phys. Lett. **B173** (1986) 115.

[140] R. B. Cakirli and R. F. Casten, Private Communications (2009).

[141] V. Werner et al., Phys. Rev. **C61** (2000) 021301(R).

[142] E. A. McCutchan and R. F. Casten, Phys. Rev. **C74** (2006) 057302.

[143] R. F. Casten et al., Phys. Lett. **B76** (1978) 280.

[144] K. Kumar, Phys. Rev. **C1** (1970) 369.

[145] F. R. Xu, Phys. Lett. **B435** (1998) 257.

[146] F. R. Xu, Private Communications (2009).

β^--delayed spectroscopy of neutron-rich tantalum nuclei: Shape evolution in neutron-rich tungsten isotopes

N. Alkhomashi,[1,*] P. H. Regan,[1] Zs. Podolyák,[1] S. Pietri,[1] A. B. Garnsworthy,[1] S. J. Steer,[1] J. Benlliure,[2] E. Caserejos,[2] R. F. Casten,[3] J. Gerl,[4] H. J. Wollersheim,[4] J. Grebosz,[5] G. Farrelly,[1] M. Górska,[4] I. Kojouharov,[4] H. Schaffner,[4] A. Algora,[6,7] G. Benzoni,[8] A. Blazhev,[9] P. Boutachkov,[4] A. M. Bruce,[10] A. M. Denis Bacelar,[10] I. J. Cullen,[1] L. Cáceres,[4] P. Doornenbal,[4] M. E. Estevez,[2] Y. Fujita,[11] W. Gelletly,[1] R. Hoischen,[4,12] R. Kumar,[13] N. Kurz,[4] S. Lalkovski,[10] Z. Liu,[14] C. Mihai,[15] F. Molina,[6] A. I. Morales,[2] D. Mücher,[9] W. Prokopowicz,[4] B. Rubio,[6] Y. Shi,[16] A. Tamii,[17] S. Tashenov,[4] J. J. Valiente-Dobón,[18] P. M. Walker,[1] P. J. Woods,[14] and F. R. Xu[16]

[1]*Department of Physics, University of Surrey, Guildford GU2 7XH, United Kingdom*
[2]*Universidad de Santiago de Compostela, E-15706 Santiago de Compostela, Spain*
[3]*WNSL, Yale University, New Haven, Connecticut 06520, USA*
[4]*GSI, Plankstrasse 1, D-64291 Darmstadt, Germany*
[5]*The Henryk Niewodniczànski Institute of Nuclear Physics, PL-31-342 Kraków, Poland*
[6]*IFIC, CSIC-Universidad de Valencia, E-46071 Valencia, Spain*
[7]*Institute of Nuclear Research of the Hungarian Academy of Sciences, Debrecen H-4001, Hungary*
[8]*INFN, Università degli Studi di Milano, I-20133 Milano, Italy*
[9]*IKP, University of Cologne, D-50937 Cologne, Germany*
[10]*School of Environment and Technology, University of Brighton, Brighton BN2 4GJ, United Kingdom*
[11]*Department of Physics, Osaka University, Osaka, Japan*
[12]*Department of Physics, Lund University, S-22100 Lund, Sweden*
[13]*IUAC, New Delhi, India*
[14]*School of Physics and Astronomy, University of Edinburgh, Edinburgh EH9 3JZ, United Kingdom*
[15]*Horia Hulubei National Institute of Physics and Nuclear Engineering, R-76900 Bucharest, Romania*
[16]*Department of Technical Physics, Peking University, Beijing 100871, People's Republic of China*
[17]*Research Center for Nuclear Physics, Osaka University, Osaka, Japan*
[18]*INFN-Laboratori Nazionali di Legnaro, I-35020 Legnaro, Italy*

(Received 18 September 2009; published 8 December 2009)

The low-lying structure of ^{188,190,192}W has been studied following β decays of the neutron-rich mother nuclei ^{188,190,192}Ta produced following the projectile fragmentation of a 1-GeV-per-nucleon ^{208}Pb primary beam on a natural beryllium target at the GSI Fragment Separator. The β-decay half-lives of ^{188}Ta, ^{190}Ta, and ^{192}Ta have been measured, with γ-ray decays of low-lying states in their respective W daughter nuclei, using heavy-ion β-γ correlations and a position-sensitive silicon detector setup. The data provide information on the low-lying excited states in ^{188}W, ^{190}W, and ^{192}W, which highlight a change in nuclear shape at ^{190}W compared with that of lighter W isotopes. This evolution of ground-state structure along the W isotopic chain is discussed as evidence for a possible proton subshell effect for the $A \sim 190$ region and is consistent with maximization of the γ-softness of the nuclear potential around $N \sim 116$.

DOI: 10.1103/PhysRevC.80.064308 PACS number(s): 21.10.−k, 23.40.−s, 27.80.+w, 29.38.Db

I. INTRODUCTION

Nuclei with $A \sim 190$ for the elements between Hf ($Z = 72$) and Pt ($Z = 78$) exhibit a wide variation of nuclear structural properties, including well-deformed prolate shapes with rotational band structures [1], K-isomeric states associated with axial symmetry in a deformed nuclear potential [2], and shape transitions across isotopic and isotonic chains [3,4]. The evolution from axially symmetric deformed prolate shapes around the valence maximum nucleus at ^{170}Dy [5] toward spherical, single-particle–like excitations close to the doubly magic nucleus ^{208}Pb is predicted to pass through a region of triaxial γ-soft and oblate nuclei [6–8]. Nuclei that are predicted to lie on the boundary between regions of prolate and oblate deformation have been described by Jolie and Linneman as prolate-oblate phase-transitional systems [9]. The phase-transitional region between axially symmetric, deformed prolate and oblate shapes is also relevant to the limits of geometric symmetry within the interacting boson model (IBM) [10–13]. Platinum isotopes with $N = 116$ and 118 represent the best cases thus far for the experimental realization of the O(6) symmetry limit of the IBM, which can be associated with a nuclear potential that is flat in the triaxial degree of freedom [14–16].

Evidence of increased γ-softness in the nuclear potential can be inferred from a number of simple experimental signatures. These signatures include a decrease in the excitation energy of the second $I^\pi = 2^+$ state [17] relative to the yrast $I^\pi = 2^+$ state and a reduction in the ratio of the excitation

*n.alkhomashi@surrey.ac.uk

TABLE I. Experimental parameters for the two FRS settings studied in the current work.

Setting	Magnetic rigidity $B\rho_1$ (Tm)	Magnetic rigidity $B\rho_2$ (Tm)	S2 degrader thickness (mg/cm^2)	S4 degrader thickness (mg/cm^2)	Beam current (p/spill)	Spill repetition (s)	Total collection time (h)
^{190}Ta	13.0805	9.5915	5050	3320	10^8	20	62
^{192}Ta	13.2285	9.7479	5050	3450	10^9	15	66

energies of the yrast $I^\pi = 4^+$ and 2^+ states, $R(4/2)$, compared to the perfect axial rotor limit of 3.33. Evidence for such behavior has been reported in a number of nuclei in this region, including ^{192}Os [18] and ^{194,196}Pt [15,19].

One focus of the current work is to extend the spectral knowledge of heavy, neutron-rich nuclei, with the specific aim of studying the predicted evolution from prolate-deformed, through γ-soft, to oblate-deformed shapes in neutron-rich tungsten ($Z = 74$) isotopes [7].

The heaviest stable tungsten isotope is $^{186}W_{112}$. Experimental information on the neutron-rich isotopes of tungsten with $N \geqslant 116$ is sparse because of the neutron-rich nature of these systems. To investigate the change of structure with increasing neutron number and the expected evolution toward a more γ-soft and possibly oblate shape, the nuclei of interest must be studied by either deep-inelastic collisions [20–22] or projectile fragmentation reactions. Prior to this work, the heaviest even-N tungsten isotopes for which even the most rudimentary spectral information had been reported were ^{188}W and ^{190}W. In-beam spectroscopy of $^{188}W_{114}$ was studied previously using deep-inelastic [22] and two-nucleon transfer reactions [23], which provided information on the structure of the yrast sequence up to a spin of $8\hbar$. Transitions populating the ground-state band of $^{190}W_{116}$ were identified via isomer-delayed γ-ray spectroscopy following relativistic projectile fragmentation of a ^{208}Pb beam [24–26]. The inferred $R(4/2)$ value for ^{190}W showed a sudden decrease in value compared to the systematics in the region [24].

The present work primarily investigates the low-lying nuclear structure of ^{188}W, ^{190}W, and ^{192}W following β-delayed spectroscopy of their mother nuclei, ^{188}Ta, ^{190}Ta, and ^{192}Ta, respectively. The data confirm the previously reported $R(4/2)$ value in ^{190}W and also provide evidence for the observation of the second 2^+ state in this nucleus. The excitation energy of the yrast 2^+ state in ^{192}W is also reported for the first time in the current work. Preliminary results from this study have been reported in a series of conference papers [27–29]; this article provides the complete analysis of this work.

II. EXPERIMENTAL DETAILS

The nuclei of interest were produced following projectile fragmentation reactions between a primary beam of ^{208}Pb impinging on a natural beryllium target of thickness 2446 mg/cm^2. The 1 GeV/nucleon beam was provided by the SIS-18 heavy-ion synchrotron at GSI, Germany, with primary beam intensities of up to 10^9 ions/spill. The duration of each primary beam spill was approximately 1 s with a typical repetition period of 15–20 s. The secondary fragmentation reaction residues were separated and identified event-by-event using the GSI Fragment Separator (FRS) [30], operated in monochromatic mode with an aluminum wedge-shaped degrader positioned in the intermediate focal plane. Two specific FRS settings were used in the current work, one centered on fully stripped (i.e., $Q = Z$) ions of ^{190}Ta and the second centered on fully stripped ^{192}Ta ions. Table I gives a summary of the experimental parameters for the FRS in these two settings.

A. Detector configuration at the FRS focal plane

A schematic of the experimental configuration used in the current work is shown in Fig. 1. The secondary ions were implanted into the RISING active stopper, which consisted of a series of double-sided silicon strip detectors (DSSSDs; see Refs. [28,31] for details). In the current work, the stopper configuration was positioned as shown in Fig. 1 and consisted of three 5 cm × 5 cm × 1 mm DSSSDs [32], each with 16 individual 3-mm-width strips on the front and back faces. The DSSSDs were used to determine the position of the implanted ion and to correlate it with its subsequent β^- decay detected in the same or neighboring pixels of the DSSSD.

The correlation of low-energy (typically hundreds of keV) β particles with significantly higher energy (typically a few GeV) implanted ions was afforded by the use of Mesytec semilogarithmic preamplifiers applied to the energy outputs of the DSSSDs [31]. These preamplifiers allowed a linear

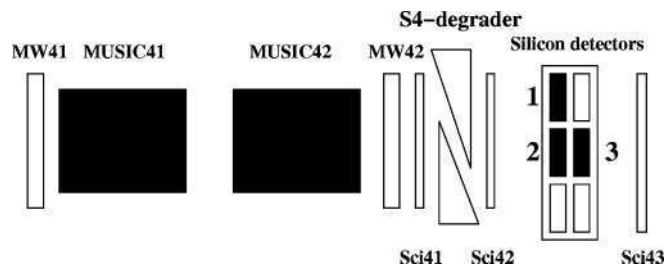

FIG. 1. Schematic of the detector configuration at the final focus of the GSI FRS for the current work. Three of the possible six positions (black boxes) in the active stopper were occupied by DSSSDs in this particular experiment. MW = multiwire position detectors; Sci = plastic scintillator detectors; MUSIC = multiple sampling ionization chamber detectors. The number 4 corresponds to the detectors being placed at the final focus (i.e., after the fourth dipole magnet) of the GSI FRS. The secondary ions are transmitted from left to right on this schematic.

amplification of the DSSSD signal for energies of up to 10 MeV, whereas a logarithmic amplification range was used for implantation energies of between 10 MeV and 3 GeV. The linear region of the preamplifier response was calibrated using the monoenergetic internal conversion electrons emitted using a standard ^{207}Bi calibration source, which yielded a measured energy full width at half maximum (FWHM) of 20 keV at 980 keV and a minimum detection threshold of approximately 150 keV. This level of electron energy resolution was used to select delayed internal conversion electron lines following decays that were observed in other FRS settings from the same experiment (for example, in the internal conversion decay of a long-lived isomer in ^{205}Au [33]). For the logarithmic portion of the preamplifier energy response, simulated signals from a pulser were used for the initial energy calibration, which was then checked by comparing the experimental data to simulations from the LISE3 code [34,35].

The active stopper was viewed by the stopped RISING γ-ray spectrometer array, which consists of 15 seven-element germanium cluster detectors with a measured total photopeak efficiency of ∼15% at 662 keV [36,37]. Previously, the RISING array has been used to detect γ-ray transitions emitted following the decay of isomeric states in secondary fragments produced by projectile fragmentation and fission, using the techniques described in Refs. [24,25,38–42]. This experiment represents the first time that the RISING array was also used to correlate γ-ray transitions arising from the decays of states populated following the β decay of secondary fragmentation products.

B. Data reduction and particle identification process

The identification of the projectile fragments was based on the time-of-flight (TOF) position and energy loss techniques described in Ref. [43]. The TOF in the second stage of the FRS was determined by measuring the time difference between the ions passing between two plastic scintillators mounted (i) before the degrader at the intermediate focal plane (after region S2) and (ii) at the final focal plane (after region S4). Two multiwire proportional chambers and two multiple sampling ionization chambers (MUSICs) provided position determination and energy loss information of the fragments at the final focal plane, respectively. The secondary ions of interest were then slowed down in a variable-thickness aluminum degrader (see Table I) before coming to rest in the RISING active stopper. Two plastic scintillators were placed before and after the active stopper to act as veto detectors for reactions in the final degrader and to remove events that produced light particles from nuclear reactions in the final degrader.

1. Charge-state selection of secondary ions

Charge-state anomalies in the transmitted secondary ions can cause problems with particle identification and the subsequent tagging of a β decay from specific neutron-rich isotopes. In particular, hydrogen-like (i.e., $q = Z - 1$) ions of a given element can have a similar mass-to-charge ratio, A/q, as fully stripped ($q = Z$) ions. Thus, heavier neutron-rich isotopes of the same element can cause problems in the selection process. Such so-called A/q anomalies can be partially resolved using the technique described in Ref. [43]. The difference in the magnetic rigidity of the ions, $B\rho$, before and after the intermediate focal plane degrader can be used to estimate the energy loss of the transmitted ions. This value can be correlated with the measured energy loss of the same ions in the two MUSICs at the final focus of the FRS to give loci of ions associated with different *changes* in charge state through the first and second halves of the FRS [30,37]. Niobium foils were placed after the target and the intermediate degrader to improve the atomic electron stripping efficiency. The ions transmitted through the FRS degrader were distributed into three main charge-state groups: (i) The group in which $\Delta q = 0$ is assumed to include predominantly ions that are fully stripped in both halves of the FRS. We note that there is a finite probability that the $\Delta q = 0$ condition could be satisfied by ions that are hydrogen-like in both halves of the FRS. However, the expected charge-state distributions for the ions using the GLOBAL code [44] suggest that the transmission of such events is highly suppressed compared to the fully stripped species. (ii) The group $\Delta q = +1$ is assumed to include predominantly ions that are fully stripped in the first part of the FRS and hydrogen-like ions (i.e., with one attached electron) in the second half of the FRS (i.e., after the intermediate focal plane degrader). (iii) The group $\Delta q = +2$ involves predominantly helium-like ions (two electrons) in the second half of the FRS and fully stripped in the first half. The GLOBAL code [44] gives a prediction that 96.7% of the ^{190}Ta ions were fully stripped in the first half of FRS and 81.7% in the second half. Figure 2 shows the charge-state change groups of the transmitted ions by plotting the energy loss in a MUSIC detector versus energy loss in the intermediate degrader.

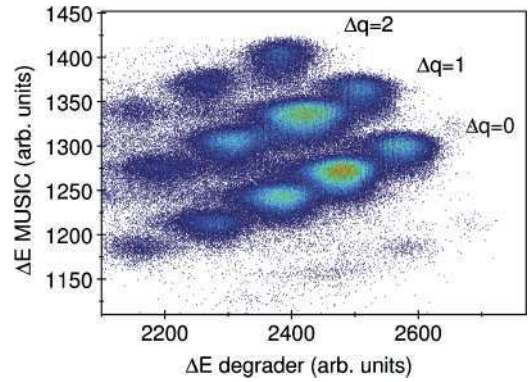

FIG. 2. (Color online) The identification of the three charge-state change groups determined using the energy loss in the intermediate degrader and the MUSIC detector at the final focal plane of the FRS. These data are taken from both the ^{190}Ta- and ^{192}Ta-centered settings. The lower group of $\Delta q = 0$ corresponds predominantly to the fully stripped charge-state transmitted through the FRS (i.e., fully stripped ions in both the first and second halves of the FRS).

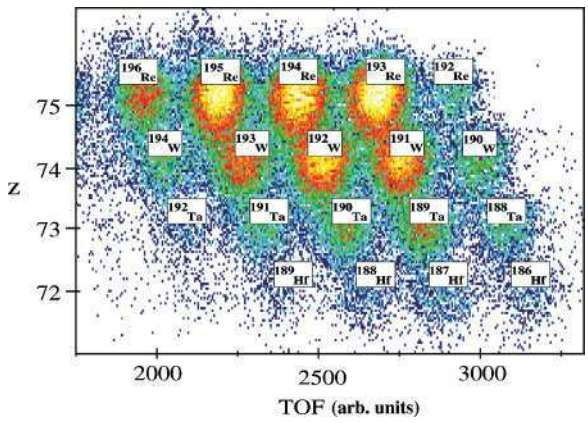

FIG. 3. (Color online) Two-dimensional particle identification plot associated with $\Delta q = 0$ (i.e., fully stripped) ions from both ^{190}Ta- and ^{192}Ta-centered settings.

2. *Particle identification*

The particle identification procedure was based on selecting the ions with $\Delta q = 0$, as illustrated in Fig. 2. Figure 3 shows the particle identification plot for $\Delta q = 0$ ions in terms of the atomic number, Z, as derived from the measured energy loss of the fragments in the MUSIC detector, versus the measured TOF in the second half of the FRS, which is related via the magnetic rigidity to the mass-over-charge ratio of the transmitted ions.

A two-dimensional matrix of detected γ-ray energies, as measured by the RISING array, versus their detection time relative to the signal from the heavy ion passing through the scintillation detector (Sci41) was created for all identified species in Fig. 3. The germanium γ-ray timing signal was recorded using the XIA DGF modules for each germanium channel, which gave an absolute time measurement with a resolution of 25 ns (see Refs. [37–41] for details). γ-rays from decays of previously reported isomeric states were used as internal checks on the particle identification procedure and to provide an independent validation of the γ-ray energy and timing measurement calibrations. Figure 4 shows selected γ-ray energy spectra and associated decay curves corresponding to γ-ray decays from isomeric states identified in the current work. Decays from the previously reported isomers in ^{188}Ta, ^{190}W,[1] ^{192}Re, and ^{193}Re [25] are all clearly identified.

The current data also show evidence for isomeric states in ^{187}Hf, ^{189,190}Ta, and ^{191}W. Evidence for the decays in ^{189}Ta and ^{191}W was previously reported in a conference proceeding from our Collaboration [45] following a survey of the region using the projectile fragmentation of a ^{208}Pb beam with RISING and a passive stopper. The current data confirm these observations. In addition, previously unreported isomeric decays in ^{187}Hf

[1]We note that the data from the current work on the isomeric decay in ^{190}W do not show any clear evidence for the 591 keV transition reported in Refs. [24,25]. This is discussed further in Ref. [26].

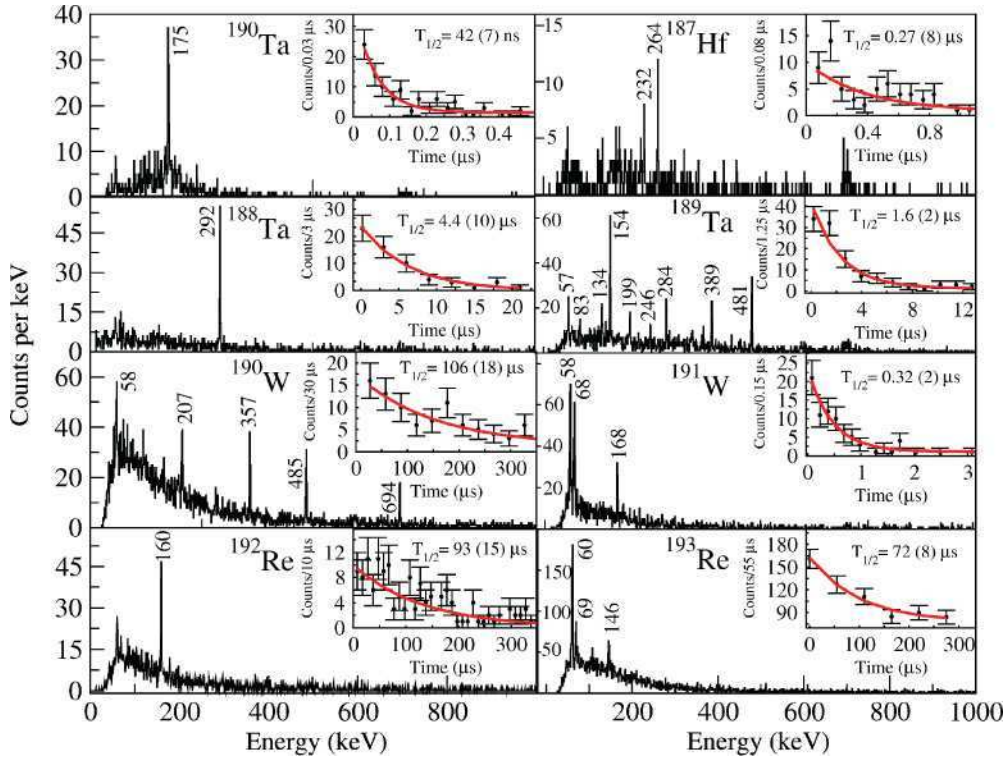

FIG. 4. (Color online) γ-ray energy and decay-time spectra of delayed events associated with isomeric states identified in ^{188,189,190}Ta (Δt $= 0.2 \rightarrow 22$, $0.2 \rightarrow 12$, and $0.03 \rightarrow 0.55\,\mu$s, respectively), ^{190,191}W ($\Delta t = 2 \rightarrow 395$ and $0.08 \rightarrow 3\,\mu$s, respectively), ^{192,193}Re ($\Delta t = 3 \rightarrow 350$ and $2 \rightarrow 350\,\mu$s, respectively), and ^{187}Hf ($\Delta t = 0.08 \rightarrow 1.1\,\mu$s).

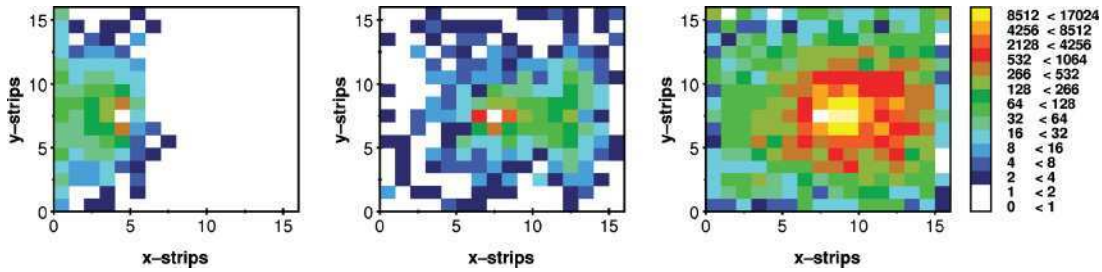

FIG. 5. (Color online) The implantion event maps for ^{188}Ta (left), ^{190}W (center), and ^{192}Re (right) as measured in the front central DSSSD from the ^{190}Ta setting.

and ^{190}Ta have been identified for the first time in the current work.

C. Implant-decay correlation technique

The technique of correlating the implanted ions with their subsequent β decay is based on the identification of the implantation position in the active stopper and the time of correlation between the implanted ion and subsequent β particle in the same or neighboring pixels of the DSSSD. The FRS was operated in monochromatic mode [46] in this experiment, which had the effect of distributing the implanted ions across a relatively wide area on the active stopper silicon detectors. This approach was required so that the probability of having multiple implantations of nuclei in the same pixel within a typical correlation time would be minimized. The use of the monochromatic mode also had the advantage of minimizing the range distribution of ions of a given species within the active stopper; thus, in general, selected isotopes of interest were stopped in a single layer of a given DSSSD. The radioactive ions were implanted in the DSSSD, with the implantation strip positions determined and an absolute measurement of the implantation time made via a digital, absolute time stamp. A valid implanted event was selected with the criterion that it produced a high-energy signal in the active stopper (>10 MeV) using the logarithmic region of the preamplifier response. Figure 5 shows two-dimensional position histograms of the implantations within one of the DSSSDs for ^{188}Ta, ^{190}W, and ^{192}Re from the ^{190}Ta setting.

The strip position, energy deposited, and time stamp for β^--decay signals in the DSSSD were correlated with the most recent implantation signal in the same or near-neighboring pixel. Figure 6 shows the energy spectrum of ions and β particles taken from the sum of energies deposited in DSSSD 1 and 2 (see Fig. 1). For each secondary ion of interest implanted in a well-defined DSSSD pixel, any energy above the threshold identified in that or neighboring pixels was considered a candidate for β^- events from the implanted mother nucleus. The time differences between the implanted events and their correlated β particle were then used to generate the β-decay time curves.

III. RESULTS

A total of 4132, 8579, and 1722 implantation events were identified for ^{188}Ta, ^{190}Ta, and ^{192}Ta ions, respectively. The β-delayed γ rays associated with these events are shown in Fig. 7, which provides spectral information on the daughter nuclei, ^{188}W, ^{190}W, and ^{192}W. Implant-β time differences of up to 100, 30, and 15 s for ^{188}Ta, ^{190}Ta, and ^{192}Ta, respectively, were used in this analysis. These γ-ray spectra have all had random, normalized γ-ray spectra subtracted from them, with the random spectra generated from long correlation times after the implantation and normalized to the time range of the original time gate. The insets of Fig. 7 show the time spectra associated with β decays of ^{188}Ta, ^{190}Ta, and ^{192}Ta, gated on discrete γ-ray lines identified in the tungsten daughter nuclei. The quoted decay half-lives were determined using a single-component exponential decay with a least-squares-fit minimization method and assuming a constant background level. A summary of the results from this γ-ray analysis for the decays identified in ^{188}W, ^{190}W, and ^{192}W in the present work is given in Table II.

A. Decay of ^{188}Ta to ^{188}W

Figure 7(a) shows discrete transitions at γ-ray energies of 143, 297, and 434 keV following the β decay of ^{188}Ta to excited states in ^{188}W. A half-life of 19.6(20) s for this β^--decaying

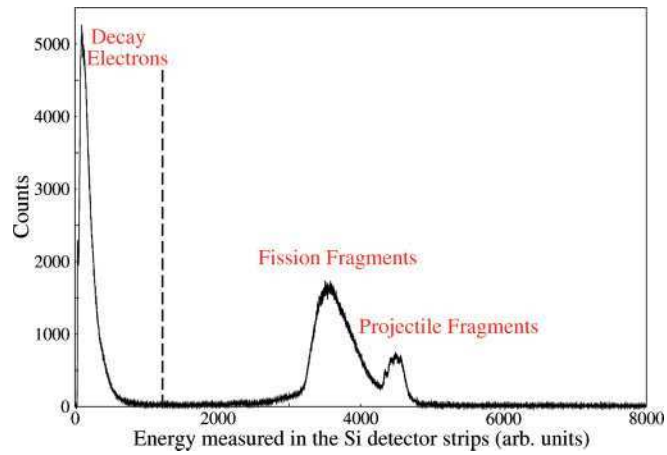

FIG. 6. (Color online) Total energy implanted by the nuclei within the silicon active stopper detector for the ^{190}Ta and ^{192}Ta settings. The double-peaked structure represents the energy deposited from both the direct implantations and for fission fragments, which are also transmitted through the FRS and pass through the active stopper. The deposited energies of β particles is shown on the left-hand side of the figure.

TABLE II. Energies, relative intensities, total internal conversion coefficient (α_{tot}), β intensities, and deduced log *ft* values associated with the γ-ray transitions observed in the β decay of ^{188,190,192}Ta.

Nucleus	E_{level} (keV)	E_γ (keV)	I_γ	α_{tot} [47]	I_{tot}[a]	$I_i \rightarrow I_f$	I_β (%)	log *ft*
^{188}Ta $\rightarrow$ ^{188}W	143	143	100(22)	1.03	203(44)	$2^+ \rightarrow 0^+$	–	–
$Q_\beta = 4854(196)$ keV	440	297	123(31)	0.09	134(35)	$4^+ \rightarrow 2^+$	–	–
	874	434	80(26)	0.04	83(26)	$6^+ \rightarrow 4^+$	53(20)	5.82(20)
	207	207	100(19)	0.29	129(24)	$2^+ \rightarrow 0^+$	$17(^{+21}_{-17})$	$6.3(^{+\infty}_{-0.4})$
^{190}Ta $\rightarrow$ ^{190}W	454	247	60(14)	0.16[a]	69(16)	$2^+_2 \rightarrow 2^+$	61(19)	5.65(24)
$Q_\beta = 5634(466)$ keV	454	454	24(10)	0.03	25(11)	$2^+_2 \rightarrow 0^+$	61(19)	5.65(24)
	564	357	30(12)	0.05	32(13)	$4^+ \rightarrow 2^+$	22(8)	6.08(23)
^{192}Ta $\rightarrow$ ^{192}W	219	219	100(26)	0.23	123(32)	$2^+ \rightarrow 0^+$	100	5.40
$Q_\beta = 6501$ keV[b]								

[a]Calculated assuming the extremum of a pure $E2$ multipolarity for the $2^+_2 \rightarrow 2^+_1$ decay.
[b]Extrapolated value, taken from Ref. [48].

state in ^{188}Ta was deduced in the current work [see the inset in Fig. 7(a)].[2]

These γ-ray energies correspond to previously observed decays from the first three excited states in the ground-state band of ^{188}W, reported following in-beam studies using both deep-inelastic reactions [22] and two-neutron transfer reactions [23]. By contrast, the transition from the yrast 8^+ state in ^{188}W ($E_\gamma = 554$ keV) as reported in Ref. [23] is not apparent in this spectrum. γ-ray energy peaks at 184, 204, and 401 keV are also identified in the β-delayed spectrum. These transitions were reported by Lane *et al.* [49] following the decay of an isomeric state in ^{188}W, with a lifetime in the 100-ns regime. The current work does not have sufficient statistics for a γ-γ coincidence analysis of the decays from this isomer.

The log *ft* values were calculated assuming ground-state mass values taken from Ref. [50]. For the ^{188}Ta decay, the log *ft* value was estimated assuming a direct β^--feeding branch to the yrast $I^\pi = 6^+$ in ^{188}W. It should be noted, however, that the observation of discrete transitions associated with the isomer decay branch reported by Lane *et al.* suggests some degree of competition in the direct feeding through a parallel branch in ^{188}W. From the observed γ-ray intensities in Fig. 7(a), an estimate of the direct β feeding to the yrast $I^\pi = 6^+$ state has been made, which in turn has been used to extract a value for log *ft* for the decay of ^{188}Ta to the yrast 6^+ state in ^{188}W, given in Table II.[3] There is no evidence

[2]Note that this discussion assumes that a single β-decaying state is observed in the present work. The presence of two parallel, low-lying, β-decaying states in ^{188}Ta with similar half-lives cannot be ruled out in the current work.

[3]Because the complete feeding intensity into the tungsten daughter is not established in the current work, we note that the log *ft* values given in Table II should be regarded as lower limits rather than precise values.

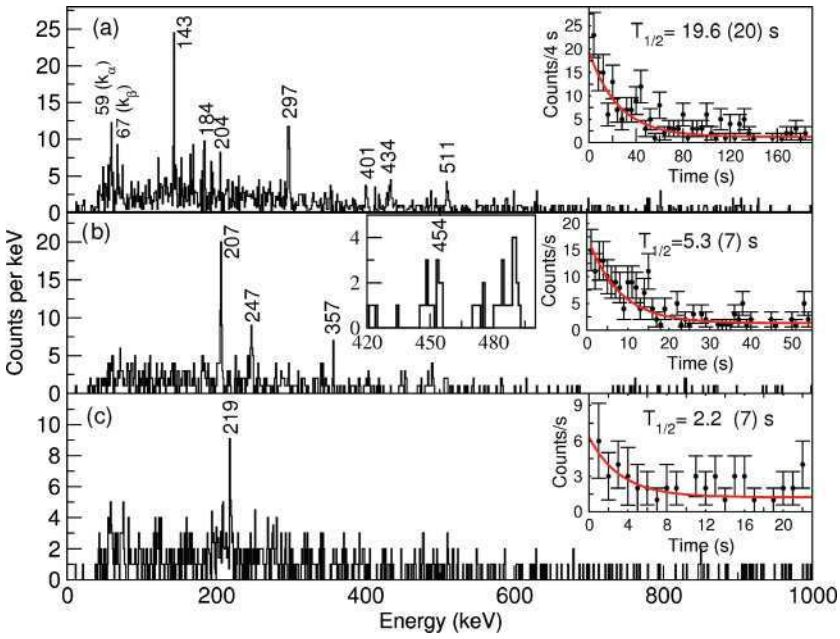

FIG. 7. (Color online) β-delayed γ-ray spectra to populate excited states in (a) ^{188}W ($\Delta t_{implant-\beta} = 100$ s); (b) ^{190}W ($\Delta t_{implant-\beta} = 30$ s), with the insert showing the enlargement of the 420→500 keV region; and (c) ^{192}W ($\Delta t_{implant-\beta} = 15$ s). A normalized random background has been subtracted from each γ-ray spectrum.

in the current work that the decays from the reported isomer feed the $I^\pi = 6^+$ yrast state in ^{188}W. Accordingly, we assume that the β^--decay feeding from the decay of ^{188}Ta leads to two parallel cascades of γ rays with 53% of direct feeding to the yrast $I^\pi = 6^+$ state and the remainder feeding to the isomeric state. Under these assumptions, it is possible to derive a lower limit for the log ft value of 5.82(20) from the direct β^--decay transition to the $I^\pi = 6^+$ state from the measured half-life of ^{188}Ta of 19.6(20) s.

B. Decay of ^{190}Ta to ^{190}W

The β-delayed γ-ray spectrum for transitions in ^{190}W is shown in Fig. 7(b). The previously reported isomeric state in ^{190}W [24–26] was also directly populated via projectile fragmentation in the current work, as shown in Fig. 4. Following population by the β^- decay of ^{190}Ta, two discrete γ-ray lines at energies of 207 and 357 keV are observed, establishing these as the decays from the yrast states with $I^\pi = 2^+$ and 4^+, respectively, in ^{190}W. A γ-γ coincidence analysis was also performed with the data from this experiment on the isomer-delayed transitions in ^{190}W, which confirmed the mutually coincident nature of the 207- and 357-keV transitions (see Fig. 8).

In addition to these previously reported transitions in ^{190}W, a transition at 247 keV is also observed in the β-delayed coincidence spectra following the decay of ^{190}Ta. This transition is interpreted as arising from the decay of the 2_2^+ state in ^{190}W, which feeds directly into the yrast $I^\pi = 2^+$ state. The limited statistics in the current β-delayed data preclude a γ-γ coincidence analysis to prove the direct feeding of the 247-keV line into the yrast $I^\pi = 2^+$ state; however, this interpretation is made on the following basis: (i) There are no other γ-ray transitions of similar intensity present in the ^{190}Ta correlated, β-delayed spectrum shown in Fig. 7(b); (ii) The 485-keV transition (which is assumed to decay from the $I^\pi = 6^+$ member of the ^{190}W ground-state band [24–26]) is not apparent in the β-decay data. (Note that the population of the yrast 6^+ state in ^{190}W is observed following the isomeric decay of the same nucleus in the current work; see Fig. 8.) Thus, it is suggested that $I^\pi = 2^+$ is the most likely spin-parity assignment for this level. (iii) An $I^\pi = 4^+$ assignment would make the 454-keV state yrast, in which case it would have been expected to have been populated in the decay of the isomeric state previously reported in ^{190}W, which it is not. An $I^\pi = 3^+$ assignment would imply that it is a collective state and built on the $I^\pi = 2^+$ bandhead of the γ-band, which can be ruled out on the basis of a lack of observation of a candidate for the required $3_\gamma^+ \rightarrow 2_2^+$ transition. (iv) Assignments of either 1^+ or 1^- at this energy in an even-even nucleus are inherently unlikely. The assumption of a 2_2^+ assignment for this state is further strengthened by the observation of a weak transition at 454 keV energy in the β-delayed spectrum for transitions in ^{190}W [see inset in Fig. 7(b)], which would represent the direct transition from the 2_2^+ state to the 0^+ ground state in ^{190}W.

The preceding arguments, together with the measured intensities (see Table II) for the observed decays from the 4^+ and 2^+ yrast states at 564 and 207 keV, respectively, in Fig. 7(b) imply a spin of $3\hbar$ for the β-decaying state in ^{190}Ta. The assumption of a spin of $3\hbar$ for the β-decaying state in ^{190}Ta is consistent (assuming direct population) with the previously discussed $I^\pi = 2^+$ assignment for the 454-keV level.

Figure 9 shows the systematics of the low-lying states in even-even tungsten isotopes with $A = 180 \rightarrow 192$ including the proposed 2_2^+ state in ^{190}W. Such states in deformed nuclei usually are associated with the bandhead of the $K^\pi = 2^+\gamma$-vibrational band. We note that the assumption of the second 2^+ state in ^{190}W at an excitation energy of 454 keV is in line with the trend expected for this region, with the ongoing, systematic decrease in the energy of the 2_2^+ state relative to the yrast 4^+ states in this isotopic chain approaching the $N = 116$ isotone, ^{190}W.

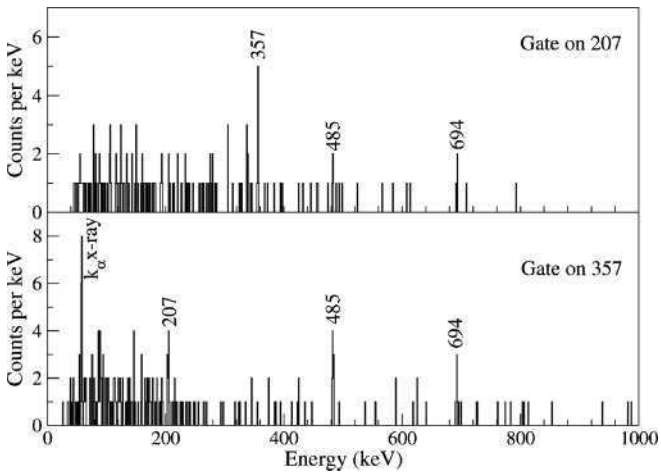

FIG. 8. Isomer-delayed γ-γ coincidence gate on (upper panel) the 207-keV transition in ^{190}W and (lower panel) the 357-keV transition in ^{190}W. The time gate condition was selected from 2→ 395 μs following the ion implantation in the active stopper.

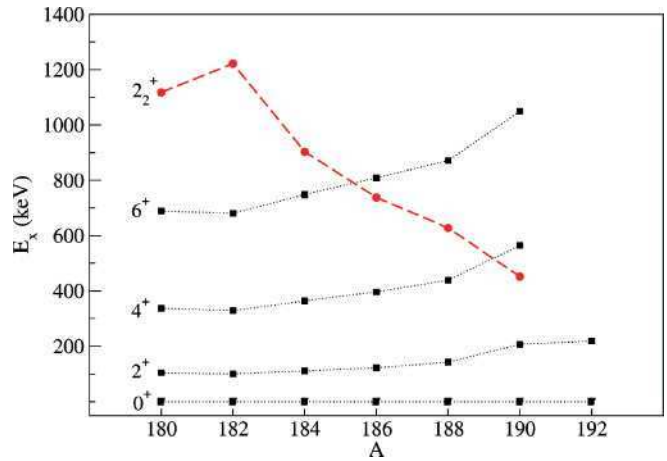

FIG. 9. (Color online) Systematic behavior of the low-lying states of even-A tungsten isotopes with $A = 180 \rightarrow 192$. The dashed lines correspond to the second $I^\pi = 2^+$ states. The data are taken from Ref. [51] and the current work.

If it is assumed that the β^- decay of the ^{190}Ta ground state feeds only the 207, 454 and 564 keV levels, then the logft values for the β^- feeding of these levels given in Table II can be derived using the half-life measured in the present work and a Q_{β^-} value of 5.634 MeV [50].

C. Decay of ^{192}Ta to ^{192}W

The β-delayed γ-ray spectrum showing transitions in ^{192}W following the decay of ^{192}Ta is shown in Fig. 7(c). A single γ-ray line at an energy of 219 keV is evident and is interpreted as arising from the yrast $2^+ \rightarrow 0^+$ transition in ^{192}W. The decay half-life measurement for ^{192}Ta gated on the 219-keV γ-ray photopeak is 2.2 ± 0.7 s. We note that 219 keV is almost the same energy as the $2^+ \rightarrow 0^+$ transition in the $N = 118$ isotone, ^{194}Os [$E(2^+) = 218$ keV], and indeed the same, near-isospectral behavior is also evident for the $N = 116$ isotonic doublet ^{190}W and ^{192}Os [$E(2^+) \approx 207$ keV]. The possibility that the 219-keV transition observed in the present work is the result of a misassignment of the β decay of ^{194}Re into ^{194}Os can be discounted as this specific decay has also been studied in the same data set, with multiple other transitions observed resulting from decays from higher spin states in ^{194}Os [27].

The likely spin of the decaying state in the ^{192}Ta parent nucleus can be restricted to $1\hbar$ or $2\hbar$ on the basis of the expected β^--decay selection rules and the lack of any apparent line associated with the $4^+ \rightarrow 2^+$ transition in ^{192}W. However, it should be noted that, on the basis of the statistics in the current work as shown in Fig. 7(c), the possible population of higher spin states in the yrast cascade in ^{192}W and thus a higher spin for the β-decaying state cannot be ruled out. From a comparison of the number of implants and associated β^--γ-ray coincident event, there is no strong evidence of direct feeding from the β^- decay of ^{192}Ta to the ground state of ^{192}W, although such a branch cannot be exclusively ruled out in the current work. The lower limit for the logft value for this decay given in Table II assumes 100% feeding in the β^- decay to the proposed yrast $I^\pi = 2^+$ state in ^{192}W.

IV. DISCUSSION

A. Subshell closure for the $A \sim 190$ region?

The systematics of the energy ratio $R(4/2) = E(4^+)/E(2^+)$ is arguably the best indicator of changes in low-lying nuclear structure [17]. However, for the most exotic nuclei, often only the energy of the first 2^+ state is known. In general, the energy of the first 2^+ state has been shown to decrease as the number of the valence nucleons (and related quadrupole collectivity) increases [52]. This general trend is opposite to the magnitude of the energy ratio and, thus, the $1/E(2_1^+)$ systematics should follow behavior similar to that for the $R(4/2)$ ratio. Cakirli and Casten [53] have recently used these empirically derived observables to demonstrate evidence for subshell closures in different regions of the nuclear chart. They also noted that the behavior of the $R(4/2)$ and $1/E(2_1^+)$ observables appear to scale with each other in regions of shape evolution and that evidence of subshell closures can be seen in the appearance of a "bubble" in the evolution of such plots as a function of proton or neutron number.

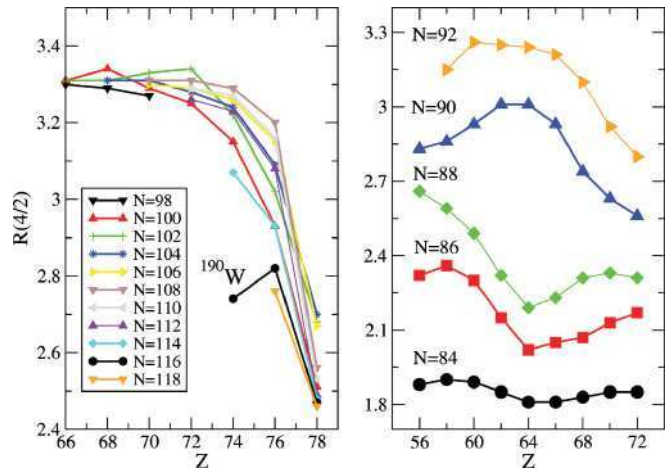

FIG. 10. (Color online) Experimental ratio of the excitation energies of the yrast $I^\pi = 4^+$ and 2^+ states [$R(4/2)$] for the even-even nuclei with (left) $Z = 66 \rightarrow 78$ and for $N > 98$ and (right) similar plot for $Z = 56 \rightarrow 72$ and for $N = 84 \rightarrow 92$, showing the effect of the subshell closure in this region. These data are taken from Ref. [51] and the present work.

The energy ratios in Fig. 10 show a gradual, systematic decrease in the value of $R(4/2)$ with neutron number from $^{182}W_{108}$ [$R(4/2) = 3.29$] to $^{188}W_{114}$ [$R(4/2) = 3.07$]. This is followed by a very dramatic decrease at the $N = 116$ isotone, ^{190}W, for which the ratio drops to a value of $R(4/2) = 2.7$, approaching the triaxial-rotor limit of $R(4/2) = 2.5$. This gives rise to what appears to be the onset of the bubble effect described by Cakirli and Casten. With the data point for ^{192}W from the current work, this behavior is even more dramatically demonstrated by the behavior of the $1/E(2_1^+)$ observable, as shown in Fig. 11, which shows the beginning of a gap/bubble pattern for the $A \sim 190$ region. Evidence for such a subshell effect or dramatic shape evolution with the addition or removal of two nucleons can also be seen from the *difference*

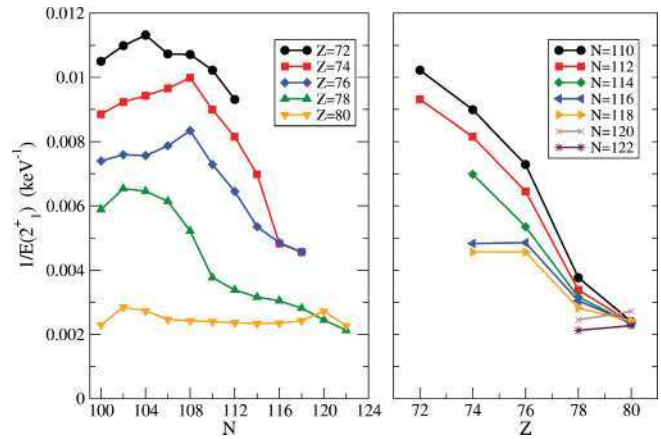

FIG. 11. (Color online) The empirical $1/E(2_1^+)$ values plotted (left) against the proton number for the $A \sim 190$ region and (right) as a function of neutron number, N, between 100 and 122. These data are taken from Ref. [51] and the present work.

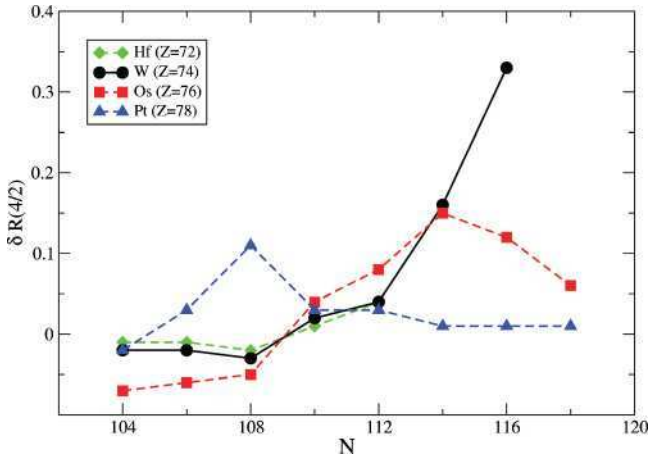

FIG. 12. (Color online) Systematics of the difference in the excitation energy ratio, $\delta R(4/2)$, for heavy even-even neutron-rich nuclei with $N = 104 \rightarrow 118$. These data are taken from Ref. [51] and the present work.

in $R(4/2)$ between neighboring even-even isotopes; that is, $\delta R(4/2) = R(4/2)_{Z,N} - R(4/2)_{Z,N-2}$ [54]. Figure 12 shows this quantity for the Hf, W, Os, and Pt isotopes with neutron numbers ranging from the midshell at $N = 104$ up to $N = 118$. The value for $\delta R(4/2)$ of greater than 0.3 between ^{188}W and ^{190}W represents one of the largest $\delta R(4/2)$ differences in the entire Segré chart. This provides compelling evidence for a dramatic change in the ground-state structure for W isotopes in going from $N = 114$ to $N = 116$.

B. Triaxial softness around $N = 116$

Evidence for triaxial (or γ-soft) collective behavior in nuclei can be obtained by using a number of basic experimental observables. These include (i) $R(2_2/2_1)$, the excitation energy ratio between the second and first spin-parity 2^+ states; (ii) the $R(4/2)$ ratio; and (iii) the ratio of the reduced matrix probabilities between the second and the first 2^+ states and from the second 2^+ state to the ground state, $R_2 = \frac{B(E2:2_2^+ \rightarrow 2_1^+)}{B(E2:2_2^+ \rightarrow 0_1^+)}$ [17]. The $E(2_1^+)$ energy is expected to increase with increasing neutron number as the $N = 126$ shell closure is approached. This increase seems to be continued for the heavier tungsten isotopes using the data for the 2_1^+ energy in the $N = 118$ isotone, ^{192}W, from the current work. This general behavior of a reduction in the energy ratio $R(4/2)$ and parallel increase in the energy of the first 2^+ state in these isotopes is indicative of the expected reduction in quadrupole collectivity as the neutron number approaches the $N = 126$ closed shell.

The $R(4/2)$ value in ^{190}W can be explained as a general feature of a γ-soft potential. Jolie and Linnemann [9] suggested that the region of nuclei between ^{180}Hf and ^{200}Hg exhibits prolate-oblate deformations and phase-shape transitions between these two shapes. There have also been theoretical predictions of a ground-state/low-lying shape transition from prolate to oblate shapes in this mass region using a variety of mean-field models (see Ref. [7] and references therein). This phase transition occurs at the O(6) symmetry in the interacting boson approximation (IBA) [10–13]. It is useful to apply the IBA model to ^{190}W, because it allows one to investigate the γ dependence of the potential appropriate for this nucleus. To study ^{190}W, we used a simple, two-parameter IBA-1 Hamiltonian suitable for most collective nuclei. This Hamiltonian can be written as [55,56]

$$H(\zeta) = c\left[(1-\zeta)\hat{n}_d - \frac{\zeta}{4N}\hat{Q}^\chi \cdot \hat{Q}^\chi\right], \qquad (1)$$

where N is the number of valence bosons, $\hat{n}_d = d^\dagger \cdot \tilde{d}$, and $\hat{Q}^\chi = (s^\dagger \tilde{d} + d^\dagger s) + \chi(d^\dagger \tilde{d})$.

This Hamiltonian has two parameters, ζ and χ, with an overall scaling factor. In this Hamiltonian, $\zeta = 0$ gives a U(5) or a quadrupole vibrator spectrum (the $\hat{n}_d$ term) while $\zeta = 1$ gives a rotor (the $\hat{Q} \cdot \hat{Q}$ term). In this latter case, one has an axial rotor for $\chi = -\frac{\sqrt{7}}{2} = -1.32$ and a γ-soft [O(6)] for $\chi = 0$. Intermediate values of ζ and χ allow one to span a wide range of collective structures.

To use Eq. (1), a technique was used based on the orthogonal cross-contour method [57]. In this approach, one can place a nucleus in the symmetry triangle for the IBA by using a contour of constant values of a pair of observables. With the data available, we used $R(4/2)$ and $E(2_2^+)$. In the O(6) limit, $E(2_2^+) = E(4_1^+)$ due to their common membership in the $\tau = 2$, O(5) multiplet. For any other situation, the IBA-1 Hamiltonian [55,56] of Eq. (1) gives $E(2_2^+) > E(4_1^+)$. Therefore, it is impossible to obtain a precise fit for the ^{190}W data, because the experimental values have $E(2_2^+) < E(4_1^+)$.

Experimentally, $R(4/2) = 2.72$ for ^{190}W. The contour for this value for $N = 9$ is shown in the inset of Fig. 13. To investigate the structure further, another observable is required, and so the $E(2_2^+)$ values are calculated along the $R(4/2) = 2.72$ contour. The results for $E(2_2^+)$ are compared with experimental value, as shown in Fig. 13.

The experimental value of $R(4/2)$ is consistent with a γ-soft [$R(4/2) \approx 2.5$] structure but does not establish it because a

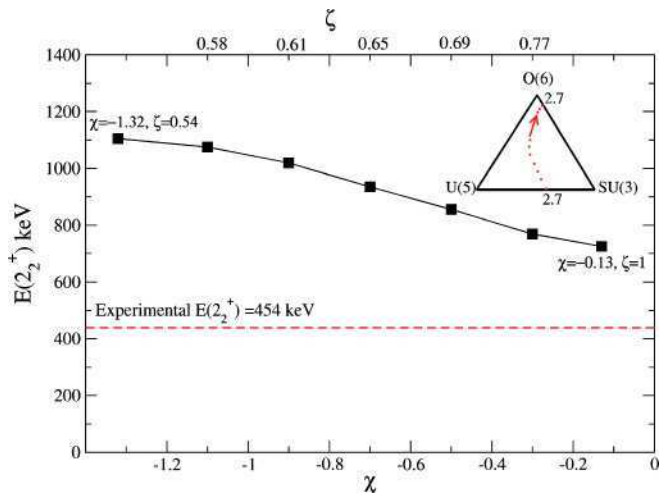

FIG. 13. (Color online) IBA-1 calculations for $E(2_2^+)$ ^{190}W along the contour in the IBA-1 symmetry triangle (dotted-line contour in the triangle) corresponding to $R(4/2) = 2.72$. The closest calculated result to the experimental $E(2_2^+)$ value is the one near the O(6) geometrically limit.

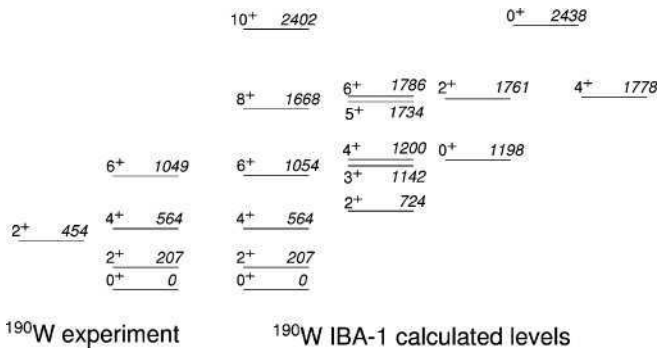

FIG. 14. Results of IBA-1 calculations for ^{190}W and comparison with the experimentally measured low-lying energy levels for this nucleus.

value of 2.7 can also be obtained for an axially symmetric quasirotor, as seen the inset of Fig. 13. Because the two parameters of the IBA-1 Hamiltonian of Eq. (1) cannot fit a 2_2^+ energy as low as observed experimentally, the best fit is obtained for a γ-soft structure very close to O(6). The theoretical-level scheme obtained from this procedure is compared with the experimental data in Fig. 14.

From a consideration of O(6) and also of the IBA calculations on the right-hand side of Fig. 14, one characteristic feature is a staggering in the γ-band energies, and in particular a near degeneracy of the 3_γ^+ and 4_γ^+ levels. Experimentally identifying these levels would provide a good future test of these ideas.

The identification of a weakly populated peak at 454 keV energy in ^{190}W suggests a direct transition from the 2_2^+ state to the ground state 0^+ in ^{190}W. In the pure, idealized O(6) limit, such a transition is forbidden [10–13]; however, in realistic, finite nuclear systems, such hindered transitions have been observed. The statistics in the current work preclude an angular distribution analysis to establish the $M1/E2$ mixing ratio of the proposed, unstretched $(2_2^+) \rightarrow 2_1^+$ transition in ^{190}W ($E_\gamma =$ 247 keV).

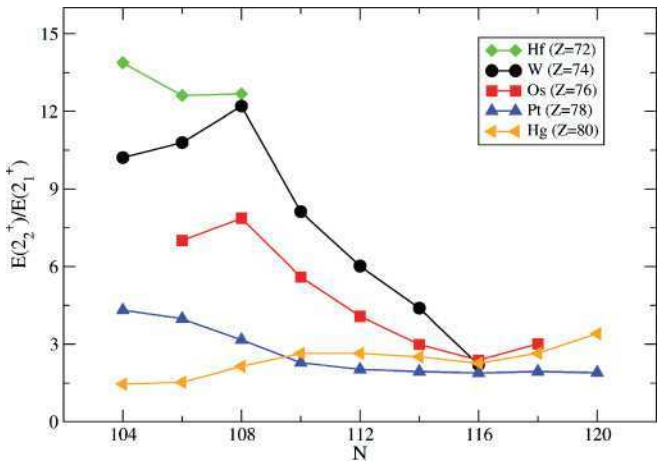

FIG. 15. (Color online) The ratio of the excitation energies of the $I^\pi = 2_2^+$ and $I^\pi = 2_1^+$ states for heavy even-even neutron-rich nuclei with $N = 104 \rightarrow 120$. These data are taken from Ref. [51] and the current work for ^{190}W.

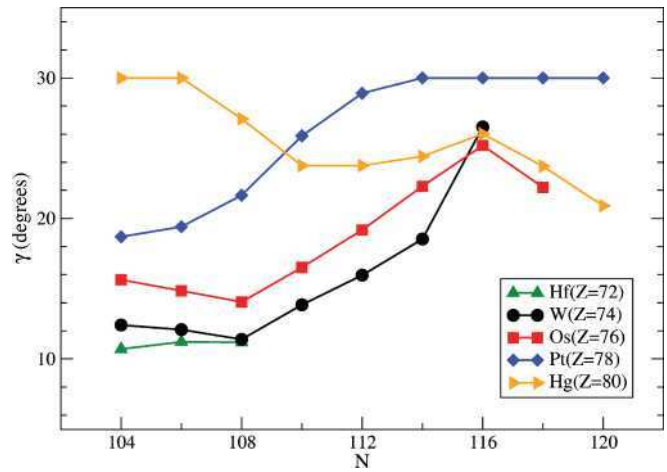

FIG. 16. (Color online) Empirically deduced γ values for heavy Hf $\rightarrow$ Hg even-even neutron-rich nuclei with $N = 104 \rightarrow 120$ using Eqs. (2) and (3) of the Davydov model (see text for details).

Another empirical quantity, which has been used to infer the prolate-oblate shape-transition regions, is the energy ratio $E(2_2^+)/E(2_1^+)$ [58]. Figure 15 shows a systematic of this ratio versus the neutron number of even-even Hf $\rightarrow$ Hg ($Z = 72 \rightarrow$ 80) isotopes $N = 104 \rightarrow 120$. The figure shows an apparent maximization of the γ softness for Os, Pt, and Hg at neutron number $N = 116$ in which the new data point for ^{190}W from the current work is consistent with this trend.

An estimate of the value of the static or average triaxial deformation parameter, γ, can be extracted from the Davydov model [59] using the energy ratio $E(2_2^+)/E(2_1^+)$. Although the Davydov model represents an asymmetric nucleus with a rigid shape, this parameter can provide a simple prediction of a static γ value that can be compared with the average γ value associated with γ-soft potentials. The expression described in

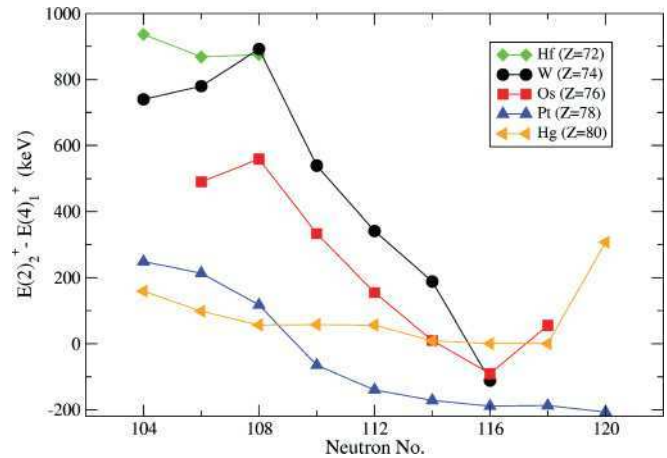

FIG. 17. (Color online) Systematics of the excitation energy difference between the $I^\pi = 2_2^+$ and $I^\pi = 4^+$ states for the even-even Hf $\rightarrow$ Hg nuclei as a function of the neutron numbers for $N = 104 \rightarrow$ 120. These data are taken from Ref. [51] and the present work.

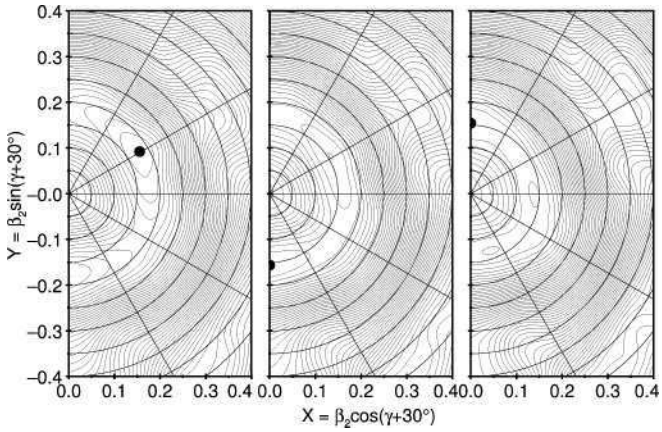

FIG. 18. (Color online) TRS calculations for the ground-state configurations of (left) ^{188}W with $\beta_2 = 0.178$ and $\gamma = 1.3°$, (middle) ^{190}W with $\beta_2 = 0.158$ and $\gamma = -120.0°$, and (right) ^{192}W with $\beta_2 = 0.136$ and $\gamma = -24.1°$. The energy contours in this figure are separated by 200 keV.

Ref. [17] is used to extract the γ value as follows:

$$\frac{E(2_2^+)}{E(2_1^+)} = \frac{[1+X]}{[1-X]}, \tag{2}$$

where

$$X = \sqrt{1 - \frac{8}{9}\sin^2(3\gamma)}. \tag{3}$$

Therefore, when $X = 1$ (i.e., for $\gamma = 0°$), the energy ratio $E(2_2^+)/E(2_1^+) \rightarrow \infty$, whereas for $X = 1/3$, $\gamma = 30°$. For ^{190}W the ratio of $E(2_2^+)/E(2_1^+)$ is equal to 2.19, leading to a value of $\gamma \approx 27°$. Figure 16 shows the γ values extracted for the even-even Hf $\rightarrow$ Hg isotopes with $N = 104 \rightarrow 120$ using Eqs. (2) and (3). The maximum γ-value appears to be reached at $N = 116$ for W, Os, and Hg.

A second quantity used to infer prolate-oblate shape-transition regions is the energy difference between the $E(2_2^+)$ and $E(4^+)$ levels [58]. According to Kumar [60], a negative value of $E(2_2^+) - E(4^+)$ (i.e., the second 2^+ state lying lower in energy than the yrast 4^+ state) is a good indicator of a region of prolate-oblate phase transition. Figure 17 shows this energy difference versus the neutron number for the region of interest. These systematics display similar characteristics to the $E(2_2^+)/E(2_1^+)$ systematics shown in Fig. 15. The neutron number $N = 116$ again appears to be associated with maximum γ softness for the low-lying states in the Os, Hg, and possibly W isotopic chains.

In their recent theoretical studies of this region using a Skyrme Hartree-Fock plus BCS pairing approach, Sarriguren *et al.* [7,61] predicted that ^{190}W lies on the near-critical point between prolate and oblate shapes in this region, with a prediction of a very shallow triaxial minimum for the ground-state shape with a predicted $\gamma = 25°$. These authors also point out that neutron number $N = 116$ appears to be a "saddle point" for the Yb, Hf, W, and Os isotopes with respect to maximum γ softness at the transition between axially symmetric prolate and oblate ground states for $N \leqslant 114$ and $N \geqslant 118$, respectively.

Total Routhian surface (TRS) calculations using the prescription described in Ref. [62] for the ground-state configurations of ^{188,190,192}W have been performed as shown in Fig. 18. The calculations predict an evolution from a prolate (albeit) γ-soft potential in ^{188}W to a very γ-soft potential for ^{190}W and ^{192}W. Indeed, the very flat energy change associated with the γ degree of freedom for $\beta_2 \approx 0.15$ can be linked to a clear predicted region of prolate/oblate shape coexistence associated with an O(6)-like potential.

V. CONCLUSIONS

The low-lying states of ^{188}W, ^{190}W, and ^{192}W have been investigated following the β^- decay of their tantalum mother nuclei populated in relativistic projectile fragmentation reactions. The results support the previously reported assignments for the first 2^+ and 4^+ states in ^{190}W and provide candidates for decays from the second 2^+ state in this nucleus and the first 2^+ state in ^{192}W. The results are consistent with the fact that $N = 116$ represents a maximum value of γ softness in this region at the intersection between prolate and oblate deformations for lighter and heavier isotopes, respectively. A direct link between the emergence of a localized proton subshell closure at $Z \leqslant 74$ for $N \geqslant 116$ and the apparent maximum values of γ softness around $N \sim 116$ is not clear at the present time.

ACKNOWLEDGMENTS

The excellent work of the GSI accelerator staff is acknowledged. This work is supported by the EPSRC/STFC (UK), King Abdulaziz City for Science and Technology (Saudi Arabia), AWE plc. (UK), the EU Access to Large Scale Facilities Programme (EURONS, EU Contract No. 506065), the Swedish Research Council, the Polish Ministry of Science and Higher Education, the Bulgarian Science Fund, the US Department of Energy under Grant No. DE-FG02-91ER-40609, the Spanish Ministerio de Educación y Ciencia, the German BMBF under Grant No. 06KY205I, the Hungarian Science Foundation, the Italian INFN, and CNCSIS under Contract No. ID-180.

[1] R. F. Casten, Nucl. Phys. **A443**, 1 (1985).
[2] P. M. Walker and G. Dracoulis, Nature (London) **399**, 35 (1999).
[3] C. Y. Wu *et al.*, Nucl. Phys. **A607**, 178 (1996).
[4] C. Wheldon, J. Garcés Narro, C. J. Pearson, P. H. Regan, Zs. Podolyák, D. D. Warner, P. Fallon, A. O. Macchiavelli, and M. Cromaz, Phys. Rev. C **63**, 011304 (2000).
[5] P. H. Regan, F. R. Xu, P. M. Walker, M. Oi, A. K. Rath, P. D. Stevenson *et al.*, Phys. Rev. C **65**, 037302 (2002).
[6] P. D. Stevenson, M. P. Brine, Zs. Podolyák, P. H. Regan, P. M. Walker, and J. R. Stone, Phys. Rev. C **72**, 047303 (2005).
[7] P. Sarriguren, R. Rodríguez-Guzmán, and L. M. Robledo, Phys. Rev. C **77**, 064322 (2008).

[8] Zs. Podolyák *et al.*, Phys. Rev. C **79**, 031305(R) (2009).
[9] J. Jolie and A. Linnemann, Phys. Rev. C **68**, 031301(R) (2003).
[10] F. Iachello and A. Arima, *The Interacting Boson Model* (Cambridge University Press, Cambridge, 1987).
[11] F. lachello and A. Arima, Phys. Lett. **B53**, 309 (1974).
[12] A. Arima and F. Iachello, Phys. Rev. Lett. **40**, 385 (1978).
[13] A. Arima and F. lachello, Phys. Rev. Lett. **35**, 1069 (1975).
[14] R. F. Casten and J. A. Cizewski, Phys. Lett. **B185**, 293 (1987).
[15] J. A. Cizewski, R. F. Casten, G. J. Smith, M. L. Stelts, W. R. Kane, H. G. Borner, and W. F. Davidson, Phys. Rev. Lett. **40**, 167 (1978).
[16] N. V. Zamfir, W.-T. Chou, and R. F. Casten, Phys. Rev. C **57**, 427 (1998).
[17] R. F. Casten, *Nuclear Structure from Simple Perspective* (Oxford University Press, Oxford, 2000), pp. 240–252.
[18] R. F. Casten, H. G. Borner, J. A. Pinston, and W. F. Davidson, Nucl. Phys. **A309**, 206 (1978).
[19] G. Berrier-Ronsin, M. Vergnes, G. Rotbard, J. Kalifa, J. Vernotte, and R. Seltz, Phys. Rev. C **23**, 2425 (1981).
[20] R. D'Alarcao *et al.*, Phys. Rev. C **59**, R1227 (1999).
[21] C. Wheldon, J. Garcés Narro, C. J. Pearson, P. H. Regan, Zs. Podolyák, D. D. Warner, P. Fallon, A. O. Macchiavelli, and M. Cromaz, Phys. Rev. C **63**, 011304(R) (2000).
[22] Zs. Podolyák *et al.*, Int. J. Mod. Phys. E **13**, 123 (2004).
[23] T. Shizuma *et al.*, Eur. Phys. J. A **30**, 391 (2006).
[24] Zs. Podolyák *et al.*, Phys. Lett. **B491**, 225 (2000).
[25] M. Caamano *et al.*, Eur. Phys. J. A **23**, 201 (2005).
[26] G. F. Farrelly *et al.*, Acta Phys. Pol. B **40**, 885 (2009).
[27] P. H. Regan *et al.*, AIP Conf. Proc. **1090**, 122 (2008).
[28] P. H. Regan *et al.*, Int. J. Mod. Phys. E **17**, 8 (2008).
[29] N. Alkhomashi *et al.*, Acta Phys. Pol. B **40**, 875 (2009).
[30] H. Geissel *et al.*, Nucl. Instrum. Methods Phys. Res. B **70**, 286 (1992).
[31] R. Kumar *et al.*, Nucl. Instrum. Methods Phys. Res. A **598**, 754 (2009).
[32] Micron Semiconductor Ltd, Marlborough Road, Lancing Sussex, England, http://www.micronsemiconductor.co.uk (2009).
[33] Zs. Podolyák *et al.*, Phys. Lett. **B672**, 116 (2009).
[34] D. Bazin, O. Tarasov, M. Lewitowicz, and O. Sorlin, Nucl. Instrum. Methods Phys. Res. A **482**, 307 (2002).
[35] O. B. Tarasov and D. Bazin, Nucl. Phys. **A746**, 411 (2004).
[36] S. Pietri *et al.*, Nucl. Instrum. Methods Phys. Res. B **261**, 1079 (2007).
[37] S. Pietri *et al.*, Acta Phys. Pol. B **38**, 1255 (2007).
[38] A. B. Garnsworthy *et al.*, Phys. Lett. **B660**, 326 (2008).
[39] S. J. Steer *et al.*, Phys. Rev. C **78**, 061302(R) (2008).
[40] D. Rudolph *et al.*, Phys. Rev. C **78**, 021301(R) (2008).
[41] M. Gorska *et al.*, Acta Phys. Pol. B **38**, 1219 (2007).
[42] L. Caceres *et al.*, Phys. Rev. C **79**, 011301(R) (2009).
[43] J. Benlliure, K.-H. Schmidt, D. Cortina-Gil, T. Enqvist, F. Farget, A. Heinz, A. R. Junghans, J. Pereira, and J. Taieb, Nucl. Phys. **A660**, 87 (1997).
[44] C. Scheidenberger, Th. Stöhlker, W. E. Meyerhof, H. Geissel, P. H. Mokler, and B. Blank, Nucl. Instrum. Methods Phys. Res. B **142**, 441 (1998).
[45] S. J. Steer *et al.*, Int. J. Mod. Phys. E **18**, 1002 (2009).
[46] G. Münzenberg, Nucl. Instrum. Methods Phys. Res. B **70**, 265 (1992).
[47] T. Kibédi, T. W. Burrows, M. B. Trzhaskovskaya, P. M. Davidson, and C. W. Nestor Jr., Nucl. Instrum. Methods Phys. Res. A **589**, 202 (2008).
[48] P. Möller, J. R. Nix, W. D. Myers, and W. J. Swiatecki, At. Data Nucl. Data Tables **59**, 185 (1995).
[49] G. Lane *et al.* (private communication, 2009).
[50] G. Audi, A. H. Wapstra, and C. Thibault, Nucl. Phys. **A729**, 337 (2003).
[51] Evaluated Nuclear Structure Data File, ENSDF, online database, National Nuclear Data Center, 2008.
[52] R. F. Casten and N. V. Zamfir, Phys. Rev. Lett. **70**, 402 (1993).
[53] R. B. Cakirli and R. F. Casten, Phys. Rev. C **78**, 041301(R) (2008).
[54] R. B. Cakirli and R. F. Casten (private communication, 2009).
[55] V. Werner, N. Pietralla, P. von Brentano, R. F. Casten, and R. V. Jolos, Phys. Rev. C **61**, 021301(R) (2000).
[56] P. O. Lipas, P. Toivonen, and D. D. Warner, Phys. Lett. **B155**, 295 (1985).
[57] E. A. McCutchan and R. F. Casten, Phys. Rev. C **74**, 057302 (2006).
[58] R. F. Casten, A. I. Namenson, W. F. Davidson, D. D. Warner, and H. G. Borner, Phys. Lett. **B76**, 280 (1978).
[59] A. S. Davydov and G. F. Filippov, Nucl. Phys. **8**, 237 (1958).
[60] K. Kumar, Phys. Rev. C **1**, 369 (1970).
[61] L. M. Robledo, R. Rodríguez-Guzmán, and P. Sarriguren, J. Phys. G: Nucl. Part. Phys. **36**, 115104 (2009).
[62] F. R. Xu, Phys. Lett. **B435**, 257 (1998).

β^--DELAYED AND ISOMER SPECTROSCOPY OF NEUTRON-RICH Ta AND W ISOTOPES* **

N. Alkhomashi[a], P.H. Regan[a], Zs. Podolyák[a], S.B. Pietri[a]
A.B. Garnsworthy[a], S.J. Steer[a], J. Benlliure[b], E. Caserejos[b], M. Górska[c]
J. Gerl[c], H.J. Wollersheim[c], J. Grebosz[d], N. Kurz[c], I. Kojouharov[c]
H. Schaffner[c], A. Algora[e,p], G. Benzoni[f], A. Blazhev[g], P. Boutachkov[c]
A.M. Bruce[h], L. Caceres[c], P. Doornenbal[c], A.M. Denis Bacelar[h]
I.J. Cullen[a], M.E. Estevez[b], G. Farrelly[a], Y. Fujita[i], W. Gelletly[a]
R. Hoischen[j], R. Kumar[k], S. Lalkovski[h], Z. Liu[l], C. Mihai[m], F. Molina[e]
D. Mücher[g], B. Rubio[e], A. Tamii[n], S. Tashenov[c], J.J. Valiente-Dobón[o]
P.M. Walker[a], P.J. Woods[l]

[a]Department of Physics, University of Surrey, Guildford GU2 7XH, UK
[b]Universidad de Santiago de Compostela, Santiago de Compostela, Spain
[c]Gesselschaft für Schwerionenforschung mbH, 64291 Darmstadt, Germany
[d]H. Niewodniczanski Institute of Nuclear Physics PAN, Krakow, Poland
[e]IFIC Valencia, Spain
[f]INFN, Universita degli Studi di Milano, 20133 Milano, Italy
[g]IKP, University of Cologne, 50937 Cologne, Germany
[h]School of Environment and Tech., Univ. of Brighton, Brighton BN2 4GJ, UK
[i]Department of Physics, Osaka University, Osaka, Japan
[j]Department of Physics, Lund University, 22100 Lund, Sweden
[k]UFAC, New Delhi, India
[l]University of Edinburgh, UK
[m]National Inst. for Phys. & Nucl. Engineering, 077125 Magurele, Romania
[n]Research Center for Nuclear Physics (RCNP), Osaka University, Japan
[o]INFN-Laboratori Nazionali di Legnaro, Padova, Italy
[p]Inst. of Nucl. Research of the Hungarian Academy of Sciences, Hungary

(Received October 30, 2008)

Decays of neutron-rich $A \sim 190$ nuclei have been studied following projectile fragmentation of a ^{208}Pb beam on a ^{9}Be target at the GSI Fragment Separator. Gamma-ray decays from previously reported isomeric states in ^{188}Ta, ^{190}W and ^{192,193}Re were used as internal calibrations for the particle identification analysis, together with the identification of previously unreported isomeric decays in ^{189}Ta and ^{191}W. The current work also identifies β-delayed γ rays following the decay of ^{188}Ta to ^{188}W for the first time.

PACS numbers: 25.70.Mn, 21.60.–n, 29.30.Kv

* Presented at the Zakopane Conference on Nuclear Physics, September 1–7, 2008, Zakopane, Poland.

** This work is supported by King Abdulaziz City for Science and Technology (KACST), Saudi Arabia; EPSRC/STFC(UK); EURONS, EU contract 506065; The Spanish Ministerio de Educacion y Ciencia; and The German BMBF.

1. Introduction

Little spectroscopic information is currently available on the structure of heavy neutron-rich nuclei with $A \sim 190$ due to the difficulties in populating such systems for experimental study. Relativistic-energy projectile fragmentation reactions [1,2] can however provide a means by which such nuclei can be accessed in the laboratory. Structural studies can then be made using the high efficiency gamma-ray detection available with the Stopped RISING gamma-ray spectrometer array [3]. This device enables the measurement of spectroscopic information from the decays of both isomeric states and β^--delayed decays [4] of ions which have been synthesised in projectile fragmentation reactions at the GSI facility in Darmstadt, Germany. This short conference paper presents some preliminary results from β^--delayed γ-ray spectroscopic study of heavy projectile fragments to investigate the low-lying states of neutron-rich W isotopes.

2. Experimental setup

A primary beam of ^{208}Pb at an energy of 1 GeV/nucleon from the SIS-18 synchrotron at GSI was fragmented on a 2.45 g/cm^2 Be target with the resulting ions being separated and identified using the GSI Fragment Separator (FRS) [5]. Two MUlti Sampling Ionization Chamber detectors were used at the final focal plane of the FRS to measure the energy loss of the individual ions. This, together with the time-of-flight of the ions enabled an event-by-event particle identification for the ions transmitted through the FRS. The ions of interest were brought to rest at the end of the FRS in an array of three 5 cm $\times$ 5 cm $\times$ 1 mm Double-Sided Silicon Strip Detectors (DSSSDs) each segmented into 16 strips in both the horizontal and vertical directions [4]. The DSSSDs used logarithmic preamplifiers [6] to enable the measurement of both the total implantation energy *and* the energy deposited by the subsequent β^- particle for each decay event for each pixel. This was used to determine the implantation positions of the transmitted secondary ions and correlate them with their subsequent β-decay signals in the same or neighbouring pixels of the DSSSDs. Coincident γ-rays following either isomeric decays or β-delayed emission were measured using the 15 germanium cluster detectors of the RISING γ-ray array [3].

3. Experimental results and summary

The fragment particle identification was achieved by creating standard two dimensional spectra of the energy loss in the MUSIC chamber detector (which is related to the atomic number, Z, of the ions) *versus* the time-of-flight, TOF (which is related to the mass-over-charge ratio of the transmitted ions), on an event-by-event basis for each ion. Reference [5] provides more details on the particle identification used in the current work.

Fig. 1 shows gamma-ray spectra associated with decays from previously reported [2] isomeric states in ^{188}Ta, ^{190}W and ^{192,193}Re as observed in the present work. These isomers were used as checks for the particle identification analysis and provided an independent validation for the γ-ray energy and timing setups. Decays from two previously unreported isomers were observed associated with the ^{189}Ta and ^{191}W nuclei. Fig. 2 shows the β-delayed gamma-ray spectra for ^{188}W following decays from the parent nucleus ^{188}Ta. The γ-ray transitions observed in ^{188}W have been reported previously from in-beam studies using deep-inelastic [7] and two-neutron transfer reactions [8]. Three discrete transitions were identified at energies of 143, 297 and 434 keV. These correspond to the decays from the yrast 2^+, 4^+ and 6^+ states, respectively. The transition from the previously identified [8] yrast 8^+ state ($E_\gamma = 554$ keV) is not observed here, suggesting that the β^- decaying state has a tentative spin of ($I = 5$).

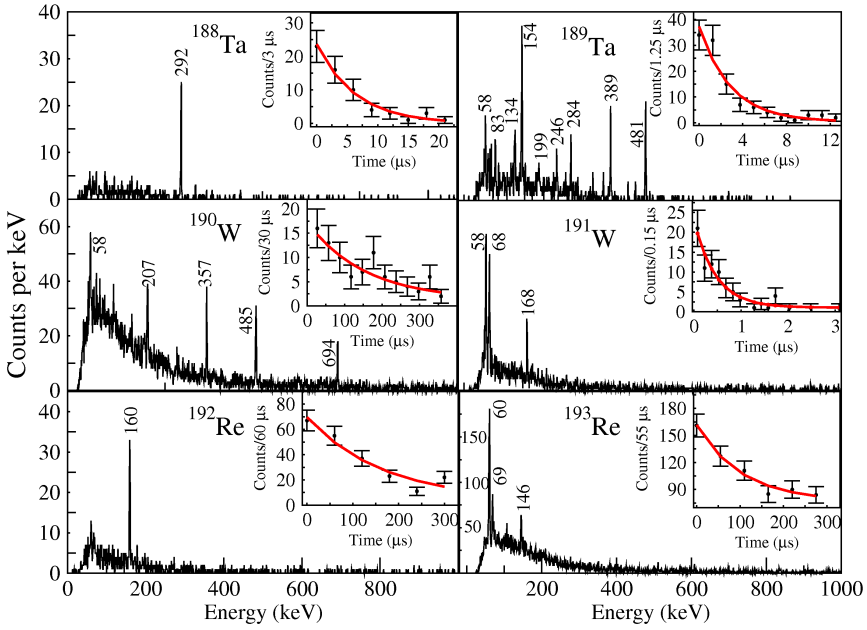

Fig. 1. Gamma-ray energy and decay time spectra for decays from isomeric states observed in the current work.

In conclusion, the RISING active stopper has been used to obtain spectroscopic information on heavy neutron-rich nuclei around $A \sim 190$ which were populated following projectile fragmentation reactions using a 1 GeV per nucleon, ^{208}Pb primary beam. Isomeric and β-delayed γ-ray spectroscopy have both been used to provide new spectral information on the

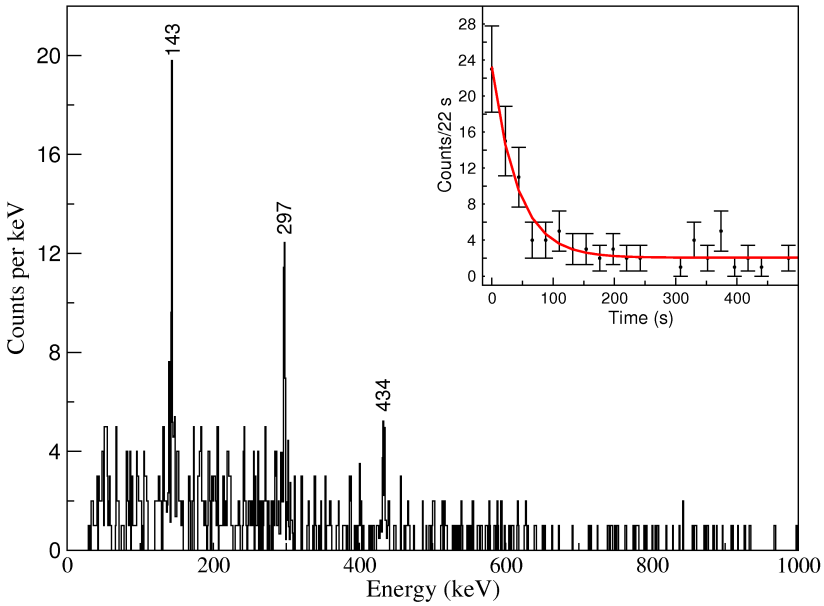

Fig. 2. Beta-delayed γ-ray spectrum following decay events associated with ^{188}Ta primary fragments which populate ^{188}W. A time condition that the β-particle must be measured within 120 seconds of the secondary beam implant in the active stopper has been applied to this spectrum. The inset shows the decay time spectrum associated with this decay half-life obtained by projecting the decay times of β-delayed gamma-ray coincidence events relative to the ^{188}Ta implantation time.

low-lying internal states in Ta and W nuclei. The spectra for the β^--decay of ^{188}Ta show the previously reported γ rays associated with decays of levels in the ^{188}W daughter nucleus up to a spin-parity of 6^+. Data on heavier Ta $\rightarrow$ W decays, which were studied in the same experiment, are currently under analysis and the preliminary results are reported elsewhere [4].

REFERENCES

[1] J. Benlliure *et al.*, *Nucl. Phys.* **A660**, 87 (1999).
[2] M. Caamano *et al.*, *Eur. Phys. J.* **A23**, 201 (2005).
[3] S. Pietri *et al.*, *Nucl. Instrum. Methods Phys. Res.* **B261**, 1079 (2007).
[4] P.H. Regan *et al.*, *Int. J. Mod. Phys.* **E**, in press.
[5] H. Geissel *et al.*, *Nucl. Instrum. Methods Phys. Res.* **B70**, 286 (1992).
[6] R. Kumar *et al.*, *Nucl. Instrum. Methods Phys. Res.* **A598**, 754 (2009).
[7] Zs. Podolyák *et al.*, *Int. J. Mod. Phys.* **E13**, 123 (2004).
[8] T. Shizuma *et al.*, *Eur. Phys. J.* **A30**, 391 (2006).